PARTICLE-TO-WALL HEAT TRANSFER IN CIRCULATING FLUIDIZED BEDS

by

Michael C. Lints

Submitted to the Department of
Mechanical Engineering in Partial
Fulfillment of the Requirements
for the Degree of

Doctor of Science in Mechanical Engineering

at the
Massachusetts Institute of Technology

February, 1992

Signature of Author_____
Department of Mechanical Engineering
January 29, 1992

Certified by_____
Leon R. Glicksman
Professor of Building Technology
Thesis Supervisor

Accepted by_____
Ain A. Sonin
Chairman, Graduate Committee
Department of Mechanical Engineering

Particle-to-Wall Heat Transfer
in Circulating Fluidized Beds

by

Michael C. Lints

Submitted to the Department of Mechanical Engineering
on January 29, 1992 in partial fulfillment
of the requirements for the Degree of
Doctor of Science in Mechanical Engineering

ABSTRACT

Since their development at MIT in 1938, circulating fluidized beds (CFBs) have found use in many applications which require good mixing of solid particles with a gas. Interest has been recently renewed in CFBs due to their ability to burn a wide variety of fuels, especially coal, both cleanly and efficiently. However, development of commercial-scale plants using CFB combustion has been hindered by a lack of understanding concerning the basic mechanisms of heat transfer. This thesis examines those mechanisms by a review of previous work in the literature and the experimental measurement of particle motion near (< 1mm) the wall of a CFB.

The wall of a CFB is alternately covered by a dense phase of particle clusters and a dilute phase comprised of mostly gas. A mechanistic model of the convective heat transfer process leads to five parameters related to the motion of the particle clusters. A particle impact probe was developed to measure one of these parameters, the distance of the clusters from the wall (δ), with an accuracy of order 10 μm. Measurements in a cold model CFB using 182 μm sand show δ to be between 0.2 and 1.0 particle diameters, and to vary inversely with the bed density between 8 and 40 kg/m^3. Each of the other four parameters is also examined using the impact probe data and the results of other researchers.

Relationships are provided for each of the five heat transfer parameters which depend only on the bed density and other known operating conditions. Heat transfer coefficients predicted by these equations compare well with heat transfer measurements in the literature. Suggestions are made for future work to address areas of uncertainty.

Thesis Supervisor: Leon R.Glicksman
Professor of Building Technology

Dedicated to my teachers

Acknowledgements

First and foremost, I would like to thank Prof. Leon R. Glicksman for his support and guidance during the preparation of this thesis. I am also grateful to all my friends and fellow students in the Heat Transfer Laboratory at MIT for many useful discussions of the work, but mostly for making the long hours, days, and years spent at MIT seem so much shorter.

I am obliged to the colleagues who provided details of their work in this area, including Drs. Hongder Chang and Michel Louge of Cornell University, and Dr. Clive Brereton of the University of British Columbia. Special thanks are due Dr. Peter J. Huber of MIT for his generous assistance with the statistical treatment of the data.

Finally, I wish to express sincere thanks to my wife, Diane, for her unfailing love and understanding during the past twelve months.

Financial support for this work was provided by the National Science Foundation, under grants CTS-8615549 and CTS-9022199.

Table of Contents

List of Tables

List of Figures

Nomenclature

Roman Letters

A - Cross-sectional area of CFB riser [m^2]
c - Volumetric solid concentration (1-ε)
$\overline{c}$ - Cross-section average volumetric solid concentration
$\overline{c}_c$ - Average cluster volumetric solid concentration
$c_{c,min}$ - Minimum cluster volumetric solid concentration
c_d - Dilute phase volumetric solid concentration
$c_{p,s}$ - Specific heat of the solid [J/kg-K]
c_{tr} - Concentration of tracer particles
D_b - Bed diameter [m]
d_p - Particle diameter [μm]
f - Fraction of wall covered by clusters
f - Friction factor (in Eq. 3.7)
f_i - Fractional wall coverage of point i at x_i^+
f_0 - Maximum value of fractional wall coverage in statistical model (Section 5.1)
G_s - Solid circulation rate [kg/m^2-s]
h - Overall heat transfer coefficient at the wall [W/m^2-K]
h_c - Heat transfer coefficient from the wall to a cluster [W/m^2-K]
h_d - Heat transfer coefficient from the wall to the dilute phase [W/m^2-K]
h_e - Heat transfer coefficient due to conduction within a cluster [W/m^2-K]
h_w - Heat transfer coefficient due to conduction through gas layer [W/m^2-K]
h_0 - Extrapolated heat transfer coefficient at zero bed density [W/m^2-K]
k_c - Thermal conductivity of cluster [W/m-K]
k_d - Thermal conductivity of dilute phase [W/m-K]
k_g - Thermal conductivity of gas [W/m-K]
k_s - Thermal conductivity of solid [W/m-K]
L_h - Length of heat transfer surface [m]
l - Location of cluster at the wall (Eq. 3.1) [m]
l_d - Distance between clusters at the wall [m]
Nu - Nusselt number
Pr - Prandtl number
q - Heat flux due to conduction within a cluster [W/m^2]
R - Radius of the bed [m]
Re - Reynolds number
R_w - Thermal resistance due to conduction through gas layer [m^2-K/W]
r - Radial distance from the center of the bed [m]
s - Sample standard deviation
s^* - Normalized sample standard deviation
ΔT - Temperature difference for conduction within a cluster [K]
t - Time of contact between wall and cluster
U_c - Velocity of cluster at wall [m/s]
U_g - Superficial gas velocity [m/s]
V_{bed} - Volume of bed [m^3]

x - Radial distance away from the wall into the bed [μm]
x^+ - Non-dimensional radial distance from the wall into the bed (x/d_p)
x_i^+ - Non-dimensional radial distance from the wall of point i

Greek Letters

α - Thermal diffusivity [m^2/s]
δ - Non-dimensional gas layer thickness between wall and clusters
δ' - Non-dimensional distance from wall where cluster coverage reaches f_0
ε - Volumetric void fraction
ε_c - Volumetric void fraction of cluster
ρ_{bed} - Cross-sectional average bed density [kg/m^3]
ρ_s - Solid particle density [kg/m^3]
σ - Population standard deviation
σ_i - Population standard deviation of point i
σ_{max} - Maximum population standard deviation
σ_{min} - Minimum population standard deviation
χ^2 - Weighted least-squares likelihood estimator

Blank page

Chapter 1

Introduction

A circulating fluidized bed is a reactor which has gas introduced at the bottom of a bed of solid particles at a velocity many times the terminal velocity of a single particle. Since entrained particles are continuously carried out the top of the reactor, they must be separated from the exhaust gas stream and continuously added at the bottom in order to maintain steady conditions in the reactor. By maintaining a high flow rate of solids, solids recirculate in the bed and have a much higher residence time than solids in a pneumatic conveying system. The circulating fluidized bed (CFB) was originally developed at MIT in 1938 for the catalytic cracking of hydrocarbon gas [Jahnig et al. (1980)]. Since then, other applications for CFBs have been found in the petroleum, chemical processing and metallurgical industries where good mixing of solid particles with a gas is required.

Recent interest in CFBs have focused on their ability to burn a wide variety of fuels cleanly and efficiently. In particular, when high sulfur coal is burned in a bed of fluidized limestone particles, much of the sulfur is captured by the limestone. This prevents its release to the atmosphere as sulfur dioxide, without the necessity of scrubbers or other expensive pollution control devices. Because combustion in a CFB occurs at a lower temperature than in conventional coal boilers, production of nitrogen oxides is also reduced. Both of these factors are important for new power plants and process heating

plants in the United States in view of the damage due to acid rain which may be caused by emissions from conventional coal-fired plants.

Development of commercial-scale plants using CFB combustion has been hindered by a lack of understanding concerning the basic mechanisms of heat transfer. In order for the fluidized bed to function properly, its temperature must remain within narrow limits during either full or part load operation. Also, the ability of a CFB boiler to respond to changing heating loads will be governed by the way in which the heat transfer coefficient varies with different operating conditions. An accurate understanding of the heat transfer to the bed walls and to any immersed heat transfer surfaces is required in order to properly size and design such equipment. The wall heat transfer can also be important in determining temperature and metallurgical limits of the wall materials.

Although the situation has improved significantly in the past few years, there still exists a scarcity of heat transfer measurements in CFBs, especially at elevated temperatures. Measurements made in CFB combustors [Kobro and Brereton (1986); Andersson, Johnsson and Leckner (1987); Wu et al. (1989b)] generally show heat transfer coefficients in the range of 100 - 300 W/m^2-K; this compares to a single-phase heat transfer coefficient for air flow at similar conditions of about 10 W/m^2-K [Petukhov (1970)]. A recent review [Glicksman (1988)] of published work in CFB heat transfer points out the following trends in the available heat transfer data:

1) h increases with increasing bed density

2) h decreases with increasing particle size

3) h increases with increasing temperature

4) h decreases with increasing length of the heat transfer surface

Although these trends are listed here approximately in decreasing order of significance, the predominance of one or another seems to vary according to operating conditions. There is no correlation available which adequately predicts the heat transfer coefficient for the range of operating conditions seen in the literature. It is clear that a better fundamental understanding of CFB heat transfer is needed.

Attempts have been made to describe the heat transfer processes in CFBs in a mechanistic way (e.g. Martin (1984)). One of the models most successful at explaining the observed trends in the available heat transfer data is a surface renewal model [Subbarao and Basu (1986), Glicksman (1988)], similar to one proposed for bubbling fluidized beds [Mickley and Fairbanks (1955)]. However, the usefulness of this model is limited by a lack of knowledge regarding flow conditions at the heat transfer surface. This thesis examines the flow-dependent hydrodynamic parameters which govern the heat transfer process, especially those mechanistic effects occurring within a few particle diameters of the wall.

Within this thesis, the surface renewal model as it applies to heat transfer in CFBs is reviewed in Chapter 2, and the unknown parameters associated with the model are described. Chapter 3 contains an in-depth look at each of the heat transfer parameters in turn, including a review of the relevant work in the literature. The experimental work of this thesis is described in Chapter 4, along with details of the data analysis. In Chapter 5, recommended values for each of the heat transfer parameters are provided based on the

results of the experimental work. The heat transfer model is re-examined in view of the observed phenomena. Predictions are made of the heat transfer coefficient for a variety of cases, and comparisons to experimental measurements of heat transfer from the literature are provided. Finally, Chapter 6 presents the conclusions and recommendations for further work.

Chapter 2

CFB Heat Transfer Model

2.1 CFB Hydrodynamics

It is apparent that the motion of the gas and particles in a CFB will play a dominant role in the wall heat transfer process. It is therefore necessary to consider briefly the behavior of the gas and particles in the bed before describing the heat transfer mechanism governed by their behavior.

The gas-solid suspension in CFBs has been observed to consist of two distinct phases: a dilute phase, made up primarily of gas but which may contain scattered individual particles; and a dense phase, in which the volumetric concentration of particles in the gas may approach the close-packed condition [Horio et al. (1988); Hartge, Rensner and Werther (1988)]. The use of this two-phase description may be due in part to earlier work in bubbling fluidized beds, in which a sharp boundary between the dilute phase bubbles and the dense emulsion can be seen clearly [Leva et al. (1948); Rowe, Partridge and Lyall (1962)]. While it is obvious from the studies on CFBs cited above that local variations in solids concentration also exist within a circulating fluidized bed, a precise division between these two phases has not been established. Wu (1989), among others, has measured wide variations in the void fraction of the dense phase, although the size of the measurement volume used may have obscured finer details of the flow structure. No direct measurements of the void fraction in the dilute phase are known to this author.

These facts notwithstanding, the two-phase description of CFBs often appears justified by experimental observations, and has proven useful in previous work. Its use will be continued here, with the understanding that the division between the two phases is imperfectly known. A more complete discussion of the dense-phase structure in CFBs will be postponed to Chapter 3.

2.1.1 Fluidization Regimes

A circulating fluidized bed can contain one or more different fluidization regimes depending upon the superficial gas velocity, particle recirculation rate, and height above the distributor. The different regimes of gas-particle fluidization have been described by Yerushalmi, Turner and Squires (1976), among others. As a stream of gas is directed through a quiescent bed of solid particles from the bottom, a drag force is exerted on the particles by the flowing gas. When the gas velocity reaches the minimum fluidization velocity, the drag force on the particles equals the gravitational force and the particles behave in many ways similar to a liquid. For many types of particles (groups A, B and D in Geldart's (1973) classification system), if the gas velocity is increased beyond minimum fluidization, bubbles will form and pass up through the fluidized bed. If the bed is sufficiently deep and its diameter small enough, the bubbles will coalesce as they rise until they occupy the entire cross-section. This transition from the bubbling regime to the slugging regime is marked by alternating slugs of dense phase and dilute phase rising in the bed [Hovmand and Davidson (1971)].

As the gas velocity is further increased, Kehoe and Davidson (1971) observed a breakdown of the slugging regime into "a state of continuous coalescence - virtually a channeling state with tongues of fluid darting in zig-zag fashion through the bed." This is the turbulent fluidization regime, in which both dense phase and dilute phase appear as continuous, intertwined streams. The turbulent regime extends to the transport velocity [Yerushalmi and Cankurt (1979)], at which point the gas flow is sufficiently rapid to entrain the particles and carry them out of the bed. The bed empties in a short period of time unless particles are continuously supplied to it. If this solids flow rate is sufficiently large, then as Yerushalmi and Cankurt (1979) point out, "it is possible to maintain in the vessel a high solid concentration typical of the fast fluidized bed".

In contrast to the bubbling and turbulent fluidization regimes, the bed density in fast fluidization is a function not only of gas velocity, but also of the solids flow rate. If the gas velocity is large enough or the solids rate low enough, then the bed will enter the pneumatic transport regime, in which the dense wall layer disappears and the bed becomes all dilute phase flowing in same direction as the gas. The up-flowing clusters which may be present in the core region of fast fluidization also disappear, and the bed develops a more or less uniform high void fraction throughout its cross-section.

It is not unusual to have more than one flow regime in evidence simultaneously in different portions of a CFB. A common operating condition is to have turbulent fluidization in the lower portions of the bed, with fast fluidization in the upper portions. The S-shaped density profile corresponding to this condition was described by Li and

Kwauk (1980), and is a common sight in the literature, e.g. Kato et al. (1991); Zhang et al. (1991); Arena et al. (1988); and Hartge, Li and Werther (1986). Figure 2.1, taken from Kunii and Levenspiel (1991b), shows an idealized example of the density profile corresponding to the different flow regimes. In the figure, ε_s is their notation for solid concentration, and refers to the cross-section average. The vertical axis represents increasing height in the bed, corresponding to the adjoining sketch of a CFB riser. Although they use a different terminology, level A marks the transition from turbulent to fast fluidization.

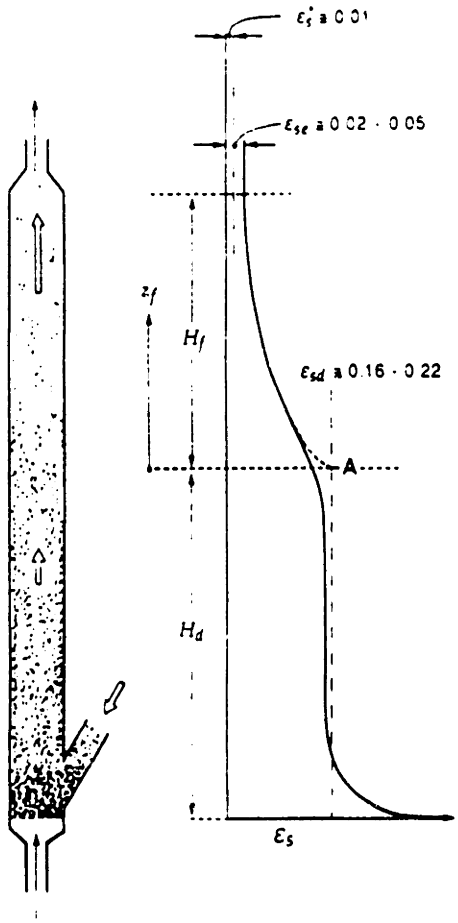

Figure 2.1 - Typical Profile of the Pressure Gradient (Bed Density) in a CFB

2.1.2 Fast Fluidization

Recent studies have shown that the fast fluidization regime has a core-annulus structure [Hartge, Li and Werther (1986); Horio et al. (1988)]. A representation of the dynamics of particle motion in fast fluidization is shown in Figure 2.2 [Yang (1988)]. The core is mostly upward-flowing dilute phase, with some entrained clusters [Bader, Findlay and Knowlton (1988); Horio et al. (1988)]. Of primary importance to the heat transfer at the wall is the annulus of alternating dilute phase and dense phase clusters adjoining the wall. The existence of these predominantly down-flowing clusters has been verified by visual studies [Glicksman, Lints and Katoh (1990); Rhodes, Mineo and Hirama (1991); Li et al.

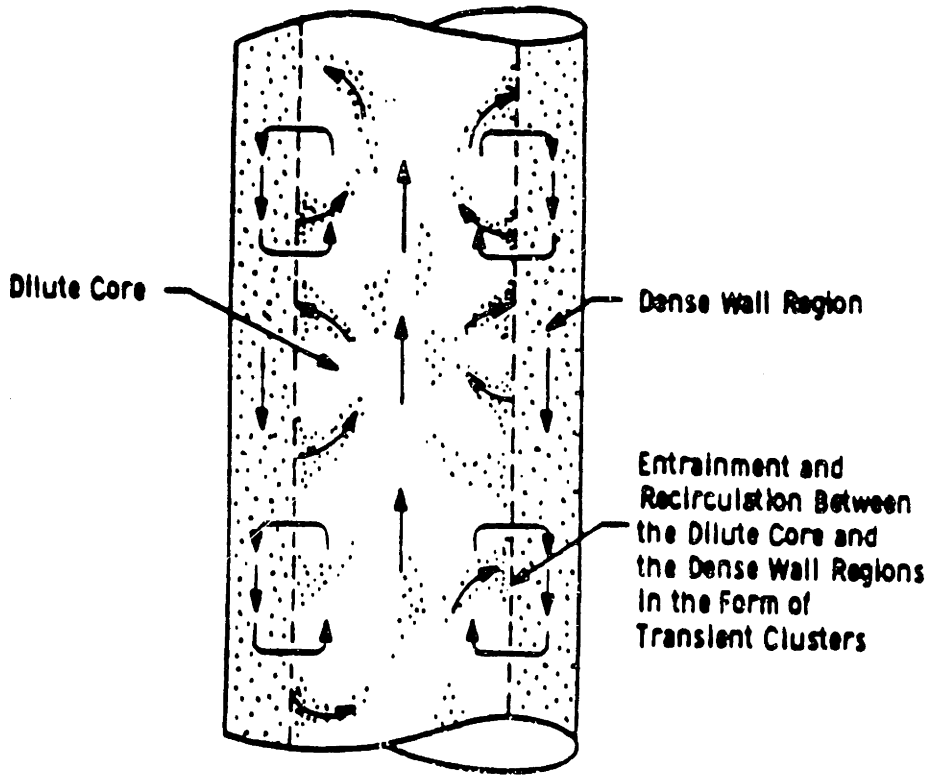

Figure 2.2 - Particle Motion in the Fast Fluidization Regime

(1991)], capacitance probes [Wu (1989); Dou (1990)] and optical probes [Horio et al. (1988); Hartge, Rensner and Werther (1988)]. However, in spite of the various studies which have been performed, the structure and motion of these clusters is not well known. The importance of the size, velocity, density and other attributes of the clusters to the heat transfer process at the wall is evident. These factors will be discussed in some detail after presenting the heat transfer model.

The fast fluidization regime has been reportedly observed over a wide range of local cross-section average solids fractions. The fluidization regime diagram by Li and Kwauk (1980) shows fast fluidization possible at solid fractions ranging from 15-20% down to values approaching 0%. This is in rough agreement with the values in Figure 2.1 from Kunii and Levenspiel (1991b), although their lower value is about 2%. Other researchers have seen characteristics of fast fluidization with solid fractions at or below 0.5% [Rhodes, Mineo and Hirama (1991)]. Boiler designers, in an effort to minimize pressure drops, tend to design the portion of the bed with heat transfer surfaces to operate in the low end of the range of solid fractions [Leckner (1991)]. Although there exists significant variations in CFB combustor design between various manufacturers, typical average solids fractions for the entire height of the bed are from 3% to less than 1% [Mack and Gould (1988)]. The solid fraction in the upper portion of the bed, which generally contains the heat transfer surfaces, will tend to be less than the average for the entire bed. A report on the recent test program at the 110 MWe Nucla CFB [Boyd and Friedman (1991)] cited solid suspension densities ranging from 0.1 to 0.6 lb/ft^3 (2 to 10 kg/m^3), corresponding to solids fractions well below 1%.

The heat transfer model and its parameters which will be examined here apply specifically to the fast fluidization regime, and more particularly to the lower density region (<~2% solids) of that regime. However, it is expected that some aspects of the model may find application in the other fluidization regimes.

2.2 Heat Transfer Model

2.2.1 Modes of Heat Transfer in a CFB

There are several modes of heat transfer occurring within a CFB combustor, including 1) convection between gas and particles, 2) conduction between particles, 3) both convection and conduction between the gas-solid suspension and the containing walls, and 4) radiation between the gas, suspended solids, and the walls. Both Grace (1986) and Leckner (1991) have shown that, due solely to convective heat transfer between the gas and the particles, the suspension of gas and solid particles should be at a uniform temperature almost throughout the bed. A theoretical model utilizing simultaneous convective and radiative heat transfer showed that the bed temperature deviates significantly only very near the heat transfer surface at the wall of the bed [Chen, Cimini and Dou (1988)]. These conclusions agree with experimental measurements made in a CFB combustor [Leckner (1991)]. Therefore, although various heat transfer processes take place within a CFB, the gas/solid mixing is sufficiently thorough that only the heat transfer between the gas-solids suspension as a whole and the bed wall must be considered.

As stated above, heat transfer between the suspension and the wall takes place by conduction, convection and radiation. Kobro and Brereton (1986) measured heat transfer coefficients in a 2.5 MW pilot CFB combustor at room temperature (25°C) and at a typical operating temperature (850°C). Since the primary effect of the increase in temperature is to increase the radiative heat transfer, the difference in heat transfer

between these two measurements gives a good indication of the relative importance on radiation to the total heat transfer coefficient. Their data show that radiation contributes roughly 50 W/m^2-K to the rate of heat transfer across a wide range of bed densities. The corresponding contribution to the total heat transfer coefficient varied from about 50% at a low bed density (10 kg/m^3) to 25% or less at a higher bed density (80 kg/m^3). Basu and Konuche (1988) made direct measurements of the radiation component of heat transfer in a CFB combustor using a radiometer probe. Although their data show an increase in the radiation heat transfer with increasing bed density, the results are in general agreement with those of Kobro and Brereton (1986).

It is apparent that the combined convection/conduction heat transfer from the gas-solid suspension to the wall is an important part of the total heat transfer coefficient in CFB combustors. An examination of the process is therefore essential to a better understanding of CFB heat transfer. Also, the majority of heat transfer measurements made in CFBs have been at or near room temperature. Under those conditions, the contribution of radiation to the total heat transfer coefficient is negligible, and a consideration of the heat transfer from the gas-solid suspension should be both necessary and sufficient to account for the experimental observations. The model which will be described in this work deals specifically with the combined convection/conduction heat transfer from the gas-solid suspension to the wall. The implications of this model with respect to radiation heat transfer will not be considered explicitly. However, if details regarding the motion and distribution of particles within the bed are known, it should be relatively straightforward

to predict the radiation heat transfer from the bed to the wall. This thesis will concentrate on examining those hydrodynamic parameters related to particle motion near the wall.

2.2.2 Wall Heat Transfer Mechanisms

The features of the mechanistic model of heat transfer described in this section have been previously reported in the literature. Therefore, only a brief review of this model is given here. Each of the parameters introduced in the model will then be discussed in greater detail in subsequent sections of this work.

As described in the Section 2.1, the bed contains two phases of material, dense and dilute. Heat transfer to the bed wall can be stated as an average of the heat transfer from these two phases [Subbarao and Basu (1986)]:

$$h = f h_c + (1-f) h_d \tag{2.1}$$

where h_c and h_d are the time-averaged heat transfer coefficients for clusters (dense phase) at the wall and dilute phase, respectively, and f is the fraction of the wall covered by clusters. Mickley and Fairbanks (1955) developed an expression for transient heat transfer between "packets" of particles which remain at the wall for time t then are periodically displaced from the heat transfer surface:

$$q = \Delta T \sqrt{\frac{k_c c_{p,c} \rho_c}{\pi t}} \tag{2.2}$$

This expression for heat flux can be used to define a heat transfer coefficient for transient conduction within the dense phase (or emulsion):

$$h_e = \sqrt{\frac{k_c c_{p,s} \rho_s (1-\epsilon_c)}{\pi t}} \tag{2.3}$$

Because the packing of the particles is disturbed near the heat transfer surface, Baskakov (1964) introduced an additional "contact" thermal resistance between the wall and the packet:

$$R_w = \frac{1}{h_w} = \frac{\delta d_p}{k_g} \tag{2.4}$$

where δ is of order unity. The exact expression for transient conduction from a semi-infinite body to a constant temperature surface with a series resistance is complicated. However, experimental measurements [Gloski, Glicksman and Decker (1984)] have shown that a close approximation to the actual heat transfer coefficient from a cluster is given by assuming that these two mechanisms, the contact resistance and the transient conduction to a homogeneous cluster of particles, act independently and in series with each other:

$$h_c = \left[\frac{1}{h_w} + \frac{1}{h_e}\right]^{-1} = \left[\frac{\delta d_p}{k_g} + \sqrt{\frac{\pi t}{k_c c_{p,s} \rho_s (1-\epsilon_c)}}\right]^{-1} \tag{2.5}$$

where the thermal conductivity of a cluster of particles is given by Gelperin and Einstein (1971) as:

$$k_c = k_g \left[1 + \frac{(1-\epsilon_c)\left(1-\frac{k_g}{k_s}\right)}{\frac{k_g}{k_s} + 0.28\epsilon_c^{0.63\,(k_s/k_g)^{0.18}}}\right] \tag{2.6}$$

Substituting Eq. 2.5 into Eq. 2.1 gives

$$h = f\left[\frac{\delta d_p}{k_g} + \sqrt{\frac{\pi t}{k_c c_{p,s} \rho_s (1-\epsilon_c)}}\right]^{-1} + (1-f)\, h_d \tag{2.7}$$

With k_c fixed by ε_c according to Eq. 2.6, Eq. 2.7 has five parameters which must be determined:

- f - fraction of wall covered by clusters
- δ - dimensionless effective gas layer thickness between wall and cluster
- t - time of contact between cluster and wall
- ε_c - void fraction of cluster
- h_d - dilute phase heat transfer coefficient

Each of these parameters will be considered in detail in Chapter 3.

Chapter 3

Heat Transfer Parameters

3.1 Wall Gas Layer Thickness

As described in section 2.1.2, the particle clusters adjoining the wall of a CFB are usually in motion with respect to the wall. In order for that to occur with any substantial particle velocity, the particles cannot be in contact with the wall, i.e. there must be a gas layer with few if any particles between the wall and the moving particle cluster. This gas layer introduces a resistance to the transfer of heat between the cluster and the wall which must be accounted for. This wall resistance is modelled as being due to steady-state conduction through the gas layer:

$$R_w = h_w^{-1} = \frac{\delta d_p}{k_g} \qquad (3.1)$$

A similar expression for the wall resistance was introduced by Baskakov (1964) in his model of transient heat transfer from clusters of particles in bubbling fluidized beds. However, Baskakov did not suppose a gas layer between the particles and the wall; his wall resistance accounted for the disturbance in the packing of particles near the wall, and the resulting increased porosity of the dense phase material. This viewpoint was supported by the experimental measurements of Gloski, Glicksman and Decker (1984). They found there were no significant differences between the heat transfer coefficients of packed and bubbling fluidized beds for very short measurement periods. This suggests

that there is no intervening gas layer between the heat transfer surface and the particles in a bubbling fluidized bed. Their results also showed that $\delta \approx 0.1$ due to the greater local voidage of the dense phase at the wall.

In a CFB, the void fraction must vary from zero at the wall to some non-zero value inside the clusters of particles. Accordingly, something like the packing disturbance found in the dense phase at the wall of packed and bubbling fluidized beds must also exist at the boundary of the clusters in a CFB, although this boundary may be at some distance from the wall of the bed. The value of δ found by Gloski, Glicksman and Decker (1984) for bubbling fluidized beds can therefore be considered as a minimum value for CFBs. If the heat flow between the wall and the cluster boundary is modeled as one-dimensional, then this minimum value of δ should be increased by an amount equal to x/d_p to account for the conduction resistance of a gas layer of thickness x between the wall and the cluster (see Figure 3.1).

There has been no accurate measure of the wall gas layer thickness in CFBs. Several recent studies [Dou (1990); Wu (1989); Acree Riley and Louge (1989)] have used capacitance probes to measure the local void fraction at the wall of a CFB. Dou (1990) used wall-mounted parallel plates which extended 3.2 mm into the bed; the needle capacitance probe of Wu (1989) had an active sensing region almost 10 mm long in the radial direction; and the flush-mounted wall probe of Acree Riley and Louge (1989) had a measurement volume which extended approximately 2 mm radially into the bed.

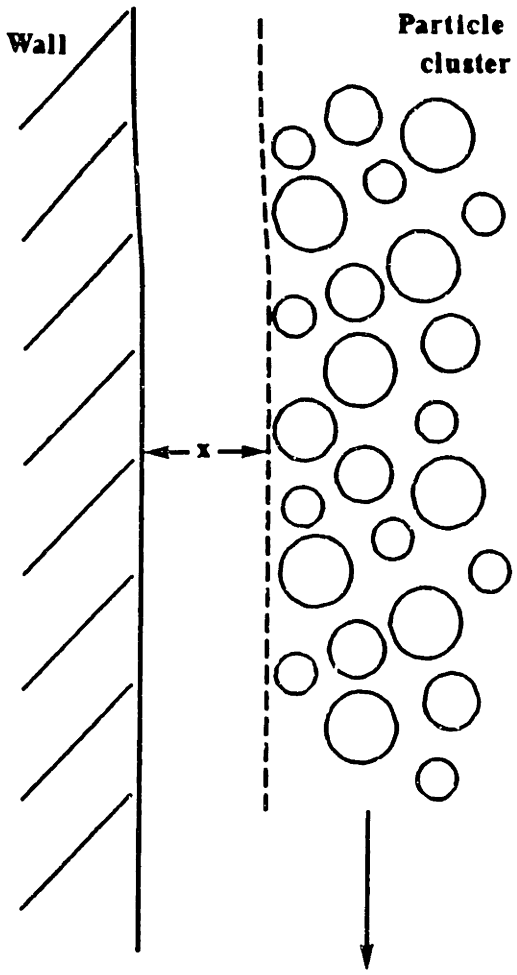

Figure 3.1 - Gas Layer Between Particle Cluster and Wall

In each case the measurement volume is too large to distinguish a wall gas layer within it which may be of order 100 μm in thickness.

Wirth and Seiter (1991) used a γ-ray absorption method to measure particle densities near the wall. They reported a particle-free gas layer almost 1 mm thick. However, if this value is applied to the heat transfer model it generates results which are inconsistent with available heat transfer data. Furthermore, micrographic video images taken on the 20 cm CFB at MIT [Glicksman, Lints and Katoh (1990)] showed that an obstruction of one particle diameter in thickness attached to the wall consistently disrupted the flow of

particle clusters. This strongly implies that the particles are often within one particle diameter of the wall. Wu (1989) found that the best fit of his heat transfer data to a model which included a contact resistance resulted from using a value of δ=0.4. A simplified cluster flow model based on the wall shear stress by Glicksman (1988) suggested that x could be as small as $d_p/24$.

If the gas layer thickness is small, then the resulting contact resistance will be small compared to the resistance to transient conduction within the cluster. In this case, it would not be necessary to know the exact value of δ in order to accurately estimate the overall heat transfer coefficient (see Eq. 2.5). However, for larger values of δ, the magnitude of the wall resistance will be comparable to the transient conduction resistance. Under those conditions, δ must be known in order to evaluate the heat transfer coefficient.

Knowledge of the thickness of the gas layer is also important to help understand the mechanism of particle motion down the wall of the bed. If δ is very small, then the shear stress between the wall and the down-flowing cluster may be the controlling force on the motion of the cluster, as suggested by Glicksman (1988). If δ is large, then the apparent independence of the cluster velocity on the superficial gas velocity (see Section 3.3) must be due to some other factor than the wall shear stress. Because of the general lack of knowledge regarding this potentially important heat transfer parameter, one of the primary goals of the experimental work was to measure the gas layer thickness.

3.2 Fractional Wall Coverage by Clusters

It has been observed [Glicksman, Lints and Katoh (1990); Li et al. (1991)] that the wall of a CFB is alternately covered by dense phase clusters and dilute phase regions. The relative abundance of each is of obvious importance to the heat transfer, and also indicative of the hydrodynamic behavior of the bed. A good deal of attention has been paid in recent studies to the local particle density in the wall region. Some of these studies have reported a value for the fraction of time during which the wall is covered by clusters. This temporal coverage fraction is assumed equal to the spatial coverage fraction in that part of the bed. Other studies may be interpreted to obtain a comparable value of wall coverage by clusters. All of these studies are summarized in Table 3.1; the wall coverage values which were either reported in them or generated from their data are shown in Figure 3.2, cross-plotted against the bed density.

To determine the fractional wall coverage by clusters, the micrographic video recording made by Glicksman, Lints and Katoh (1990) has been viewed frame-by-frame; the fraction of images which show a cluster of particles within about 1 mm of the wall is shown in Figure 3.2 (see Section 4.2 for additional details concerning that work). Rhodes, Mineo, and Hirama (1991) have also recorded video images near the wall. They report three flow conditions: dilute, dense, and swarm (cluster). The dense flow appears to have little by which to distinguish it from the dilute, except that a relatively greater number of individual particles are visible. However, the void fraction in their dense flow appears to be in excess of 0.9. Figure 3.2 shows their reported frequency of the swarm flow condition. Li et al. (1991) recorded micrographs near the wall of a CFB and have

Researcher(s)	Particles	Superficial Gas Velocity (m/s)	Solid Circulation Rate (kg/m^2-s)	Bed Diameter (cm)	Measurement Technique	Estimated Thickness of Measurement Region (mm)
Wu (1989)	Sand, 171 μm	7	N/A	15.2	Traversing capacitance probe	7
Dou (1990)	FCC, 87 μm	3	12.4 - 27.3	15.2	Wall-mounted capacitance probe	3.2
Glicksman et al. (1990)	Giass, 88 μm	1.24 - 2.49	0.08 - 2.44	20.3	Tangential magnified video	0.5
Louge et al. (1990)	FCC, 61 μm	2	17	19.7	Wall-mounted capacitance probe	2
Rhodes et al. (1991)	Alumina, 70 μm	2 - 5	8 - 80	30.5	External magnified video	?
Li et al. (1991)	FCC, 54 μm	2.62 - 3.49	17.5 - 64.7	9.0	Traversing micrographic video probe	~0 - 5

Table 3.1 - Summary of Experiments for Wall Coverage by Clusters

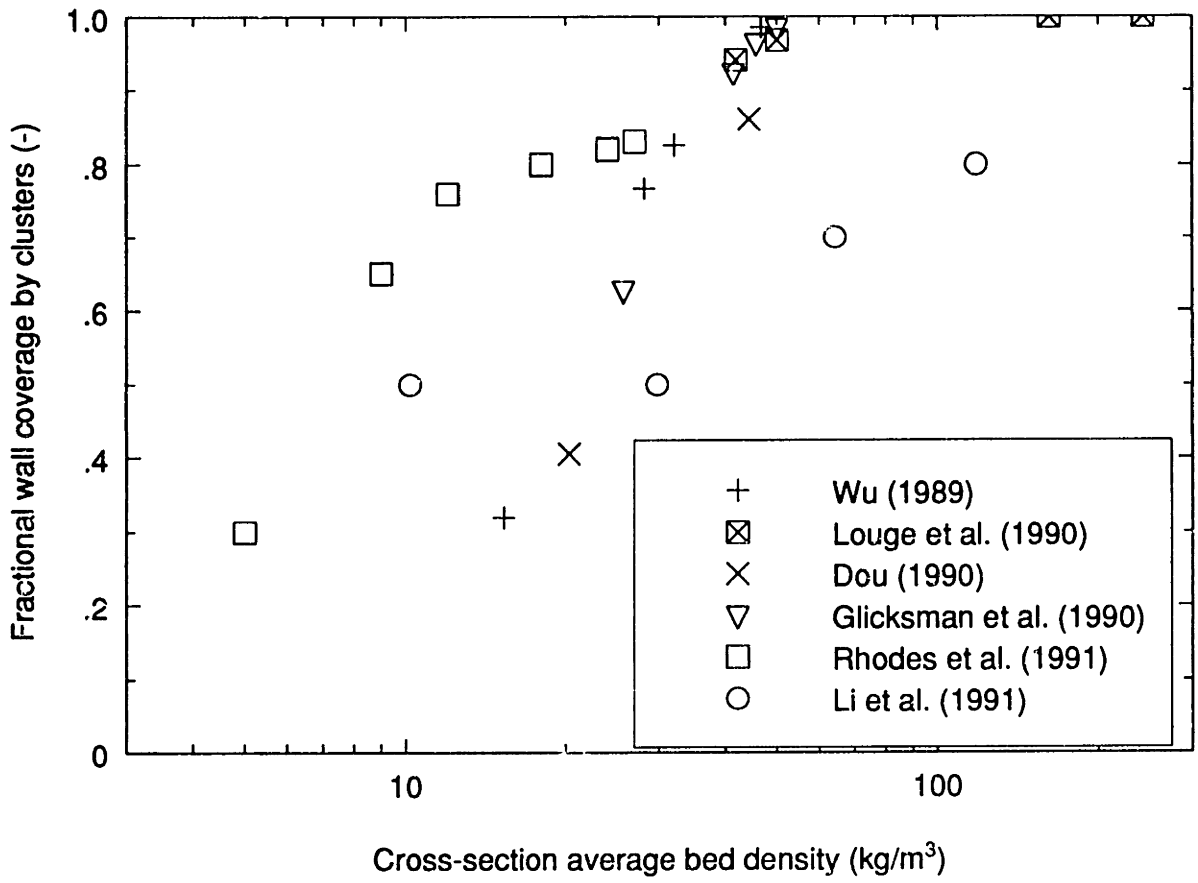

Figure 3.2 - Cluster Wall Coverage from Experimental Data of Various Researchers

tabulated the fraction of such images which showed "no clusters in the field of view". It may be surprising that their measurements of wall coverage by clusters are lower than the others - if they included images with even a portion covered by a cluster, one might expect their wall coverage fractions to be higher than those of the other researchers.

The process of obtaining values for the fractional wall coverage from the capacitance probe data is less straightforward than for the visual studies. Wu (1989) reported the cumulative time fraction of wall coverage by clusters of solid fractions between 0.0 and 0.6. Louge, Lischer and Chang (1990) give the probability density functions (PDF) of

the measured void fraction at several different bed heights, whereas Dou (1990) shows the PDF of the measured wall solid fraction. All three researchers show a fairly continuous spectrum of void fractions, without any apparent bimodality by which to characterize and differentiate the dense phase clusters. In order to obtain a value for f from any of their data, it is necessary to choose a value for the solid fraction which represents a boundary between the dense phase clusters and the dilute phase. Once this minimum value of the cluster solid concentration, $c_{c,min}$, has been selected, values for f can be read directly from the cumulative density functions of Wu (1989), or obtained by graphical integration of the PDFs of the other two researchers.

The values of f obtained in this manner will be dependent upon the assumed value of $c_{c,min}$. Figure 3.3 gives the resulting values of f using the data of these three researchers for three different values of $c_{c,min}$ between 0.02 and 0.10. The figure shows that f is rather sensitive to the value of $c_{c,min}$, especially at lower bed densities. Using a value of $c_{c,min}$ = 0.02 results in nearly complete coverage of the wall by clusters even at low values of the bed density. This is inconsistent with the visual observation that have been made and included in Figure 3.2. On the other hand, if $c_{c,min}$ is assumed to be 0.10, then f drops steeply with decreasing bed densities, resulting in very low values of f at low bed densities. Again, this is inconsistent with the visual observations, which show substantial, if less than complete, wall coverage by clusters at bed densities of 10-20 kg/m^3.

The only values of f in Figure 3.3 which are in reasonable agreement with the visual observations are for $c_{c,min}$ = 0.05, and that value was used in plotting the capacitance

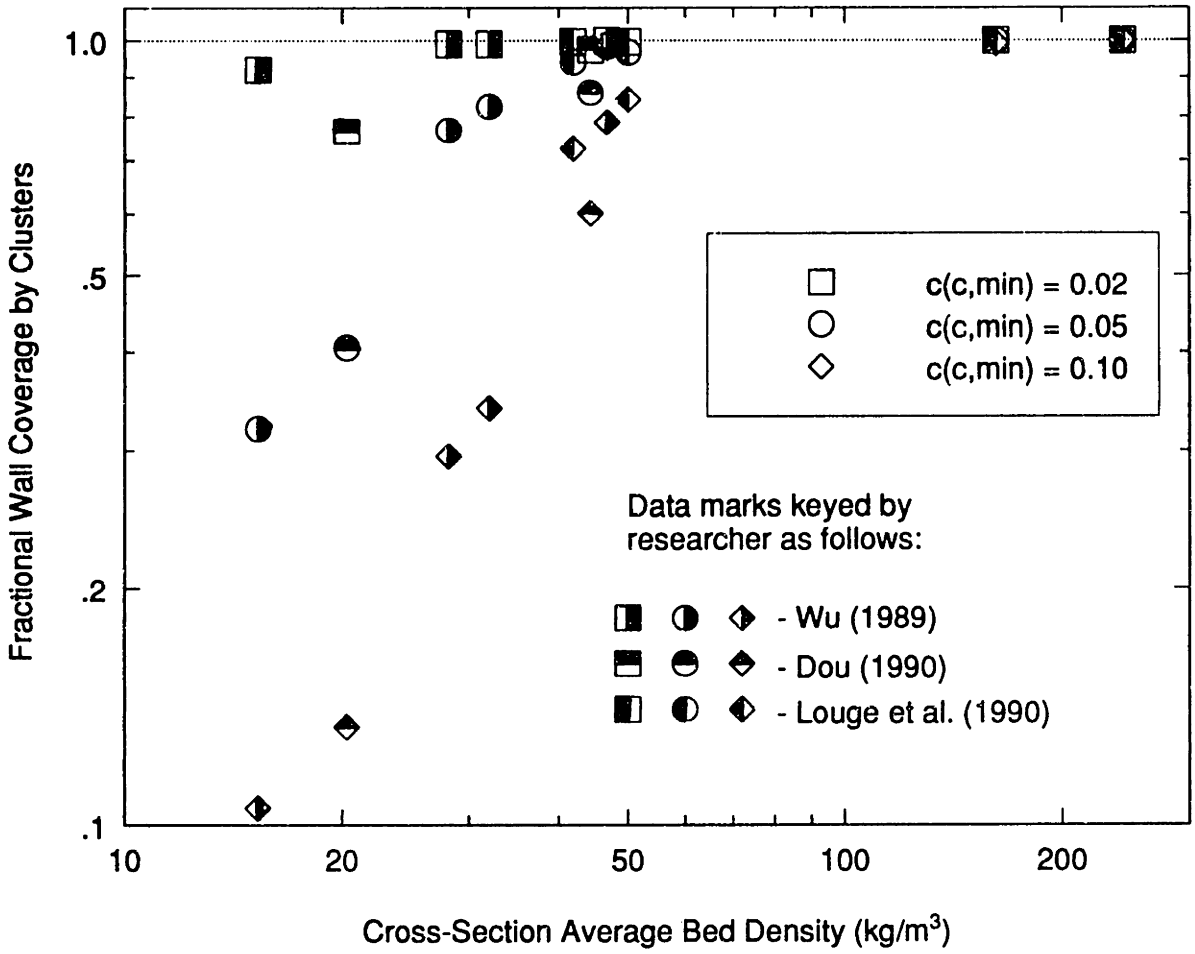

Figure 3.3 - Dependence of Cluster Wall Coverage on Minimum Cluster Solid Concentration

probe data on Figure 3.2. It is recognized that the choice is somewhat arbitrary; but given the continuous nature of the void fraction near the wall of CFBs as measured by the capacitance probes (see Section 3.4 for a more complete discussion), the division of the gas-solid suspension into dense and dilute phases is itself arbitrary, and warranted only by the visual observations of the phenomena which have been made. Therefore, the visual observations provide the only reasonable basis for determining if the differentiation between the two phases in the capacitance probe signal has been performed properly.

While it may be that 0.04 or 0.06 is a more appropriate choice for $c_{c,min}$ than 0.05, such a determination awaits a more detailed study of the matter than is presented here.

All the data in Figure 3.2 show a common tendency toward increased values of f with increasing cross-section average solids fractions. This trend may be expected, since higher bed densities are the result of greater particle hold-up, especially near the wall [Li et al. (1991)]. The greater amount of particle refluxing at the wall is likely to be accompanied by a larger fraction of wall coverage by clusters. There is also reasonable agreement between the different sets of data, considering the disparate ways by which they were obtained. There are obvious differences in the definition of a cluster, or in what constitutes coverage of the wall by a cluster, between the various studies. The lack of agreement between the data may also be due to the location of the measurement. For example, the tangential video images of Glicksman, Lints and Katoh (1990) only show clusters within 1 mm of the wall, whereas the measurement volume of the needle capacitance probe used by Wu (1989) extended nearly 10 mm away from the wall into the bed. The data of Li et al. (1991) is particularly difficult to understand. They made their nearest measurements to the wall at r/R = 0.9, which would correspond to a distance of about 5 mm from the wall. Perhaps because their bed was of a smaller diameter than those of the other researchers, the core region occupied most of the bed cross section at higher densities. In this case, the clusters may have often been displaced from the wall by the upward-flowing channels of gas which are normally seen in turbulent fluidization. For whatever reason, they documented less that complete coverage of their viewing area by clusters even at a cross-section average particle fraction as high as nearly 13%.

With the exception of the data of Li et al. (1991), it seems that complete wall coverage by clusters occurs at bed density of about 50 kg/m^3, or cross-section average solid fraction in the neighborhood of 2.5%. Increasing rates of heat transfer at higher bed densities must be due to other factors than an increasing value of f. However, the importance of the fractional wall coverage to the heat transfer at lower densities is apparent from the data of Wu (1989). Figure 3.4 shows a cross plot of Wu's measured fractional wall coverage for clusters of any density greater than about 5% solids at four different bed densities against the average heat transfer coefficient at those same densities taken from Figure 3.11 of Wu's thesis. Referring to the basic model of heat transfer, Eq. 2.1, the

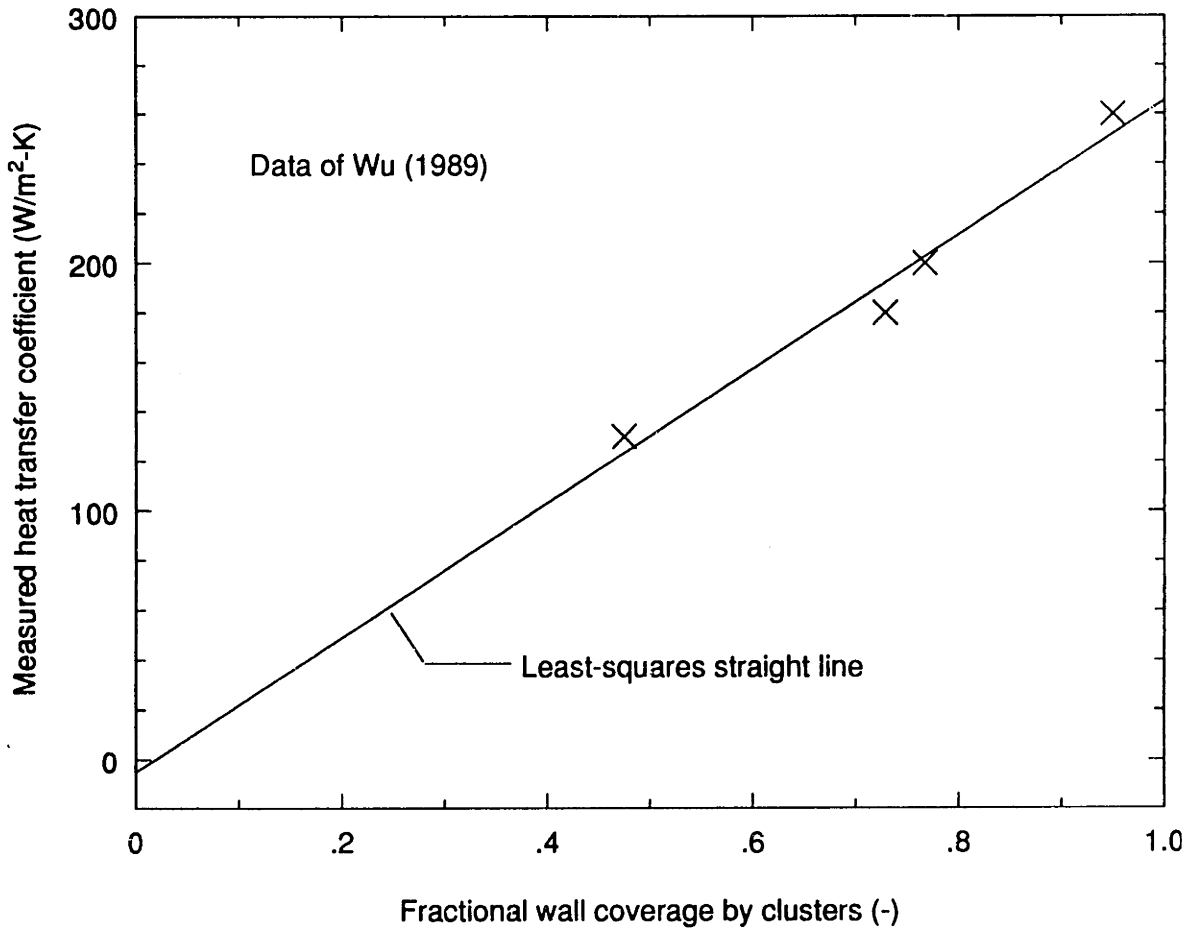

Figure 3.4 - Cluster Wall Coverage vs. Wall Heat Transfer Coefficient

strong linearity of the data in Figure 3.4 might imply that h_c and h_d are relatively constant within this density range, and that h is a function of f alone. Whether or not this is in fact the case, it is apparent that f is an important parameter to the rate of heat transfer. Further measurements of the fractional wall coverage by clusters was included in the experimental work described in the following chapters.

3.3 Time of Contact between Cluster and Wall

The time during which a cluster is in contact with the heat transfer surface is an important factor in the rate of heat transfer. According to Eq. 2.5, for very short contact times the contact resistance between the cluster and the wall will be the controlling factor in the dense phase heat transfer coefficient. For very long periods of contact, the resistance to conduction within the cluster will be the limiting factor. For intermediate contact periods, it is necessary to consider both resistances.

A determination of the cluster contact time must include a consideration of cluster motion. As described in Section 2.1.2, clusters are generally believed to migrate to the wall by some mechanism, such as turbulent eddies, and to remain near the wall for some period of time as they fall along it. Eventually the clusters are either swept from the wall and re-entrained into the high-velocity core region; or if the CFB is being operated so that the lower portions are under turbulent fluidization conditions, the clusters may instead fall out of the fast fluidization region of the bed into the turbulent fluidization region below.

The time which a cluster spends in contact with the wall may be expressed as follows:

$$t = \int \frac{dl}{U_c(l)} \tag{3.1}$$

where the limits of integration are the points at which the cluster comes into contact and breaks contact with the wall. While there have been several studies (which will be examined shortly) of the velocity of clusters in the wall layer, there have been no measurements made of the path which a cluster might typically follow within a CFB. Wu

(1989) looked at the cross-correlation between signals from two rapid-response heat transfer probes placed near each other along the axis of a CFB. His analysis found a characteristic residence length of clusters at the wall of order 10 cm, and varying directly with the bed density raised to the power 0.596. However, the evidence for such a relatively short contact length is not very strong. Wu correctly notes that the degree of cross-correlation is generally low, probably due to the presence of a wide spectrum of cluster velocities, rather than a single characteristic velocity. Furthermore, a short residence length is at odds with the experimental measurements made using long heat transfer surfaces. The data of Wu et al. (1989b) show a continual decrease in the local heat transfer coefficient moving downwards along a long heat transfer surface for a distance of at least 100 cm, which suggests that most of the particles remain in contact with the wall for at least that length.

Dou (1990) inferred thermal contact lengths from experimental heat transfer measurements using a model of transient conduction to the particle clusters. He reports contact lengths of between 2.5 cm and 12.5 cm which are directly proportional to the diameter of the particles. However, since his heat transfer surface was only about 3 cm long, his values for contact length and their dependence on particle diameter are likely due to the varying contact resistance, which was not included in his heat transfer model.

The present state of knowledge concerning CFB hydrodynamics is insufficient to estimate the actual contact length of clusters with the wall with any degree of certainty. Bader, Findlay and Knowlton (1988) measured residence times of salt tracer particles in a CFB

which exceeded 15 seconds. If the CFB is modeled as having perfect mixing of solids throughout the bed, then the concentration of a batch of tracer particles injected at time t=0 will vary according to:

$$C_{tr} = (C_{tr})_{t=0} e^{-\left(\frac{G_s A}{\rho_{bed} V_{bed}}\right) t} \qquad (3.2)$$

Because the average bed density during the solids residence time experiments of Bader, Findlay and Knowlton (1988) was so high ($\rho_{bed} \approx 250$ kg/m^3), the resulting characteristic solids residence time from Eq. 3.2 is also rather high, about 20 seconds. This is consistent with their experimental measurements, but such long residence times could be a result of either very good mixing between the core and the annulus, or fairly long contact lengths between the clusters within the annulus and the wall. Further data, such as the radial solid fluxes or solids residence time measurements taken at lower bed densities, would provide help in understanding cluster motion within CFBs. To date, no such measurements are known to have been made.

3.3.1 Contact Times for Short Probes and Cluster Velocity

In spite of the lack of knowledge concerning the contact length of clusters, it is possible to estimate the contact time for some heat transfer surfaces. If the active heat transfer surface is sufficiently short, then the clusters can be assumed to remain in contact with the surface for its entire length. If it is further assumed that the clusters have a velocity, U_c, which remains roughly constant for the duration of their passage across the heat transfer surface, then the contact time is given by:

$$t = \frac{L_h}{U_c} \tag{3.3}$$

A number of researchers have measured the velocity of clusters in the wall layer. Their results are summarized in Table 3.2. In view of the wide range of particles and operating conditions represented, the reported cluster velocities show greater uniformity than might be expected. With few exceptions, most of the data fall within a range from about -0.5 m/s to -3.0 m/s. The data that fall outside that range may have been taken under conditions outside the fast fluidization regime.

Figure 3.5 shows the cluster velocity plotted against the cross-section average solid concentration for those studies which reported the bed density. The vertical lines on some of the data points indicate the range of cluster velocities measured. As described in Section 2.1.2, the upper density limit for fast fluidization is 15%-20%. This is precisely the density above which Hartge, Rensner and Werther (1988) measured average cluster velocities greater than zero. As those particular measurements were made in the lower portions of the bed, it is quite possible that they were made in an area of turbulent fluidization. On the other hand, the data of Yang et al. (1990) was taken under very dilute conditions, as suggested by the title of their paper. Although they did not report the bed density, they fluidized small, light particles at a high velocity and low solids circulation rates. Furthermore, they measured average cluster velocities at the wall greater than or equal to zero for all their test conditions. By the definition of fast fluidization, this suggests that their bed was operating at the boundary of, if not actually within, the pneumatic transport regime. The most frequent particle velocities reported by Yang et

Researcher(s)	Particles	Superficial Gas Velocity (m/s)	Solid Circulation Rate (kg/m^2-s)	Bed Diam. (cm)	Velocity Measurement Technique	Cluster Velocity at Wall † (m/s)
Horio et al. (1988)	FCC, 60 μm	1.17 - 1.29	11.25 - 11.7	5.0	Intrusive light reflection probe	-0.65 → -0.45
Hartge et al. (1988)	FCC, 85 μm CFB ash, 120 μm	2.9 - 3.7	30 - 49	40	Intrusive light reflection probe	-2.8 → 0.9
Bader et al. (1988)	FCC, 76 μm	3.7	98	30.5	Pitot tube	-0.9 → -0.3
Gidaspow et al. (1989)	Glass, 520 μm	5	25	7.6	External visual	-1.1
Wu (1989)	Sand, 171 μm	7	N/A	15.2	External visual	-2.77 → -0.64
Yang et al. (1990)	FCC, 69 μm	6.5	10.6	18.6	Intrusive LDV probe	-1.2 → 3.1
Rhodes et al. (1991)	Alumina, 70 μm	3 - 4	20 - 40	30.5	External visual	-2.2 → -0.1
Wirth & Seiter (1991)	Phosphorescent ZnS, 50 μm	0.6 - 1.9	N/A	16.8	External visual	-3.0 → -1.0
Nowak et al. (1991)	FCC, 46 μm	4.0	55.7	20.5	Intrusive light reflection probe	-1.0 → -0.6

† Negative velocity denotes cluster motion down the wall of the bed

Table 3.2 - Summary of Cluster Velocity Measurements by Various Researchers

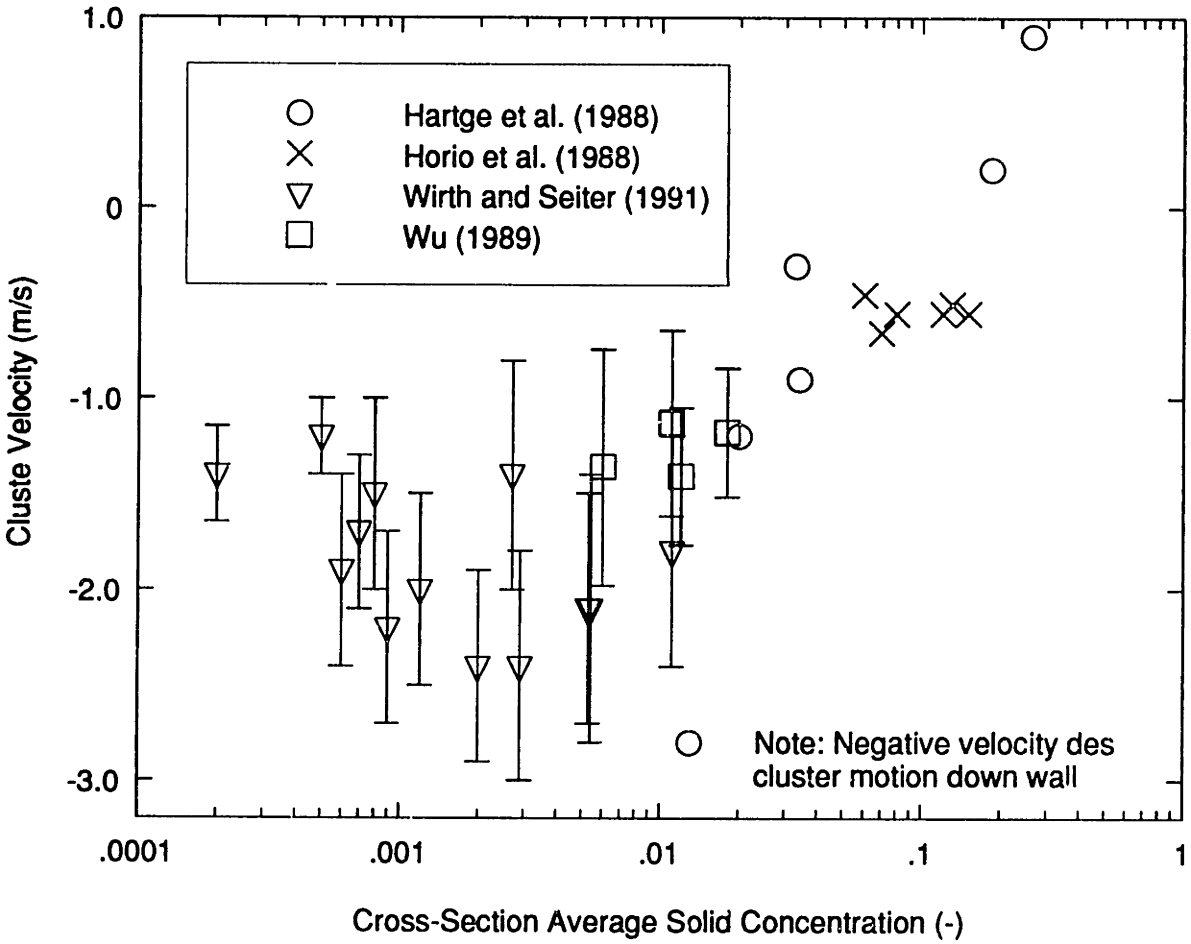

Figure 3.5 - Dependence of Cluster Velocity on Cross-Section Average Solid Concentration

al. (1990) at the wall appear to be in the range of -1 to 0 m/s; however, the average velocity is skewed by the less frequent occurrence of significantly greater positive particle velocities. For these reasons, the data of Yang et al. (1990) and the data of Hartge, Rensner and Werther (1988) taken at bed densities above 15% will not be considered further.

One interesting feature displayed by several of the data sets referenced in Table 3.2 is an apparent increase in the downward velocity of the clusters a small distance away from the wall. The three groups of researchers who used intrusive optic fiber probes utilizing light reflection to measure the velocity all indicate an increase in the downward cluster velocity of up to 50% at a distance of 0.05 D_b - 0.10 D_b. Similar behavior is also reported by Rhodes, Mineo and Hirama (1991), who used a high-speed video camera focused on the inner surface of their glass riser wall. They saw a range of cluster velocities from near zero to in excess of 2 m/s down the wall, with a value of about -0.3 m/s occurring most often. However, further away from the wall they saw "a steady bulk downflow of particles ... faster but more uniform and more dilute than the particle downflow in the form of swarms." They estimated the velocity of the bulk downflow to be around -1.0 m/s. Bader, Findlay and Knowlton (1988) note an even more striking effect, with the downward velocity increasing from about 1 m/s very near the wall to roughly 3 m/s at 3-5 cm away from the wall. However, they have calculated upward and downward velocities separately. If the upward velocities and particle fluxes which they measured in the wall region were included to obtain an average cluster velocity for particles moving in both directions, then the increase in the downward velocity a short distance away from the wall, while still present, would be less marked.

None of the other researchers who made velocity measurements externally noted the phenomenon described above; however, it seems quite possible that they unknowingly grouped together velocity measurements of clusters at varying distances from the bed wall. This may account at least in part for the fact that the velocity measurements made

by intrusive fiber optic probes tend to be somewhat lesser in magnitude than those made by external visual techniques. In any event, the greater ability of the intrusive probes to resolve the radial position of the falling clusters lends support to the data obtained by them, and suggests that the phenomenon described in the preceding paragraph is real.

The cluster velocity data exhibit no clear trend, except the lower cluster velocities tend to occur with the lower-density fluid cracking catalyst (FCC) material. A plot of the cluster velocities vs. the particle density is shown in Figure 3.6. It shows a weak trend towards cluster velocities of greater magnitude with increasing particle densities.

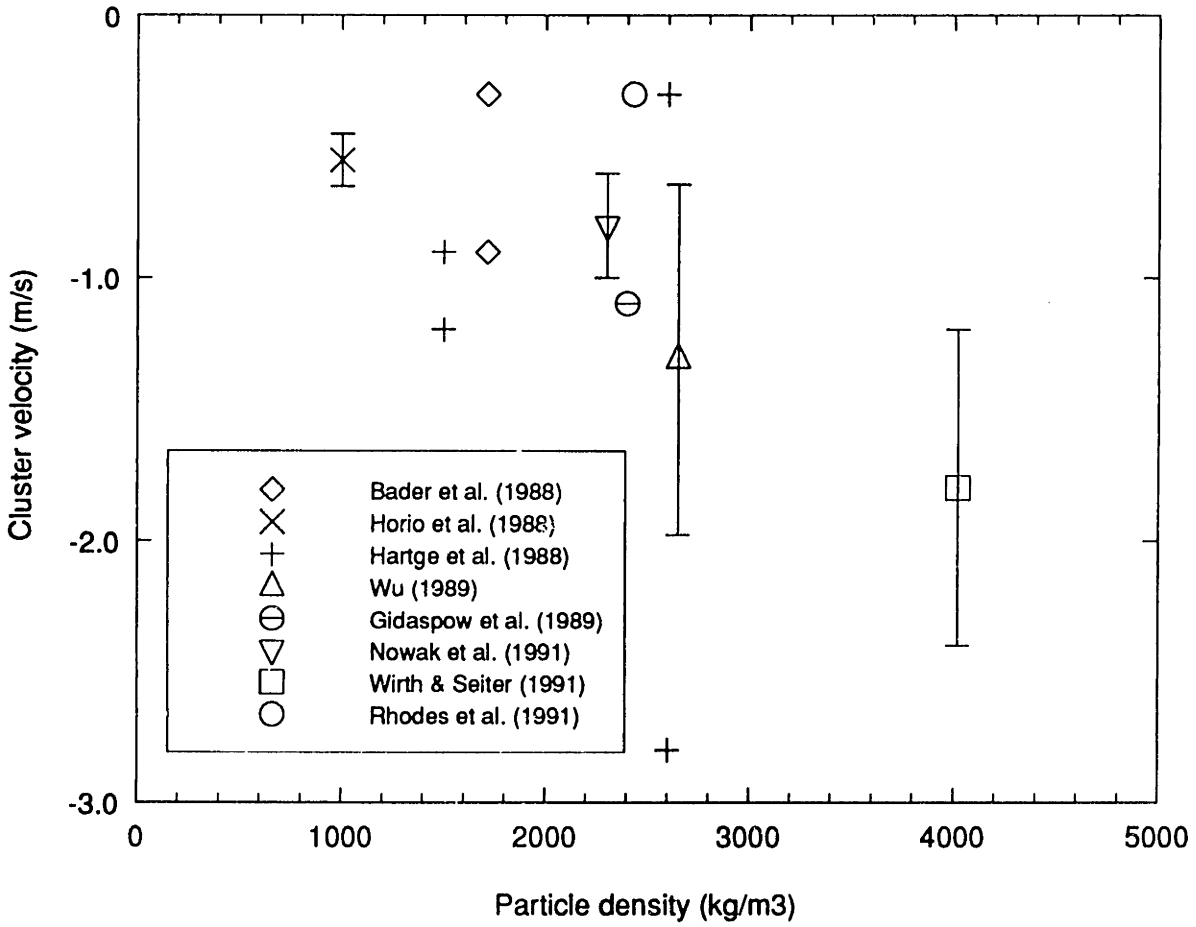

Figure 3.6 - Dependence of Cluster Velocity on Particle Density

However, since intrusive probes were used in all cases where the lighter FCC powders were being fluidized, the effect of particle density is likely to be confounded with the effect of the measurement technique. If only the data gathered by means sensitive to the radial position of the clusters is examined, as in Figure 3.7, there no longer appears to be any dependence of cluster velocity on particle density. Furthermore, except for an apparent outlier, all the data are in the range of -0.3 m/s to -1.2 m/s.

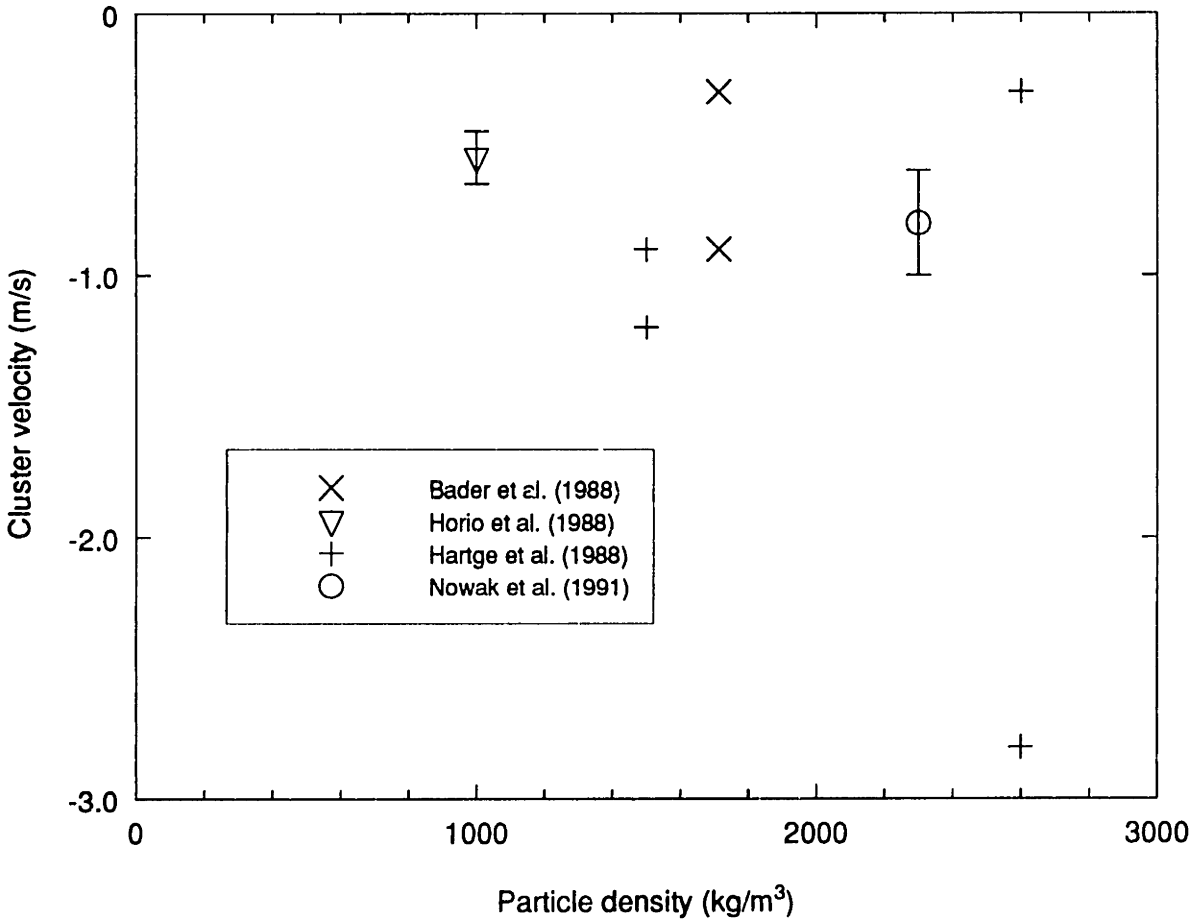

Figure 3.7 - Velocity Measurements of Clusters Made Within 5 mm of the Wall

The cluster velocity at the wall appears to be independent of the superficial gas velocity or particle properties. This fact has no easy explanation. It might be suggested,

following the analysis of Glicksman (1988), that the shear stress between the particle clusters and the wall is the governing effect on the motion of the clusters. However, measurements of the wall gas layer thickness (see Chapter 5) show that the clusters are too far from the wall for the shear stress between the two to be an important factor. A detailed explanation for the observed cluster motion at the wall is beyond the scope of this work. In view of the discussion above, a wall cluster velocity of -0.6 m/s will be used as a representative value to estimate the heat transfer coefficient for short heat transfer probes. This is within a factor of two of the range of reasonable values from Figure 3.7. Given the square root dependence of the emulsion heat transfer coefficient on the time of contact (Eq. 2.3), this should give an estimate for h_e within about 40% of the true value.

3.4 Cluster Void Fraction

For a given particle material, the cluster void fraction governs the thermal diffusivity of the particle cluster, which is in turn a controlling factor in the resistance to transient conduction within the cluster (Eq. 2.3). Many techniques have been used to measure the void fractions in CFBs . One of the first of these, and still the most common due to its simplicity, is to make differential pressure measurements axially along the bed. This technique is of questionable accuracy due to the presence of shear stresses on the wall of the bed [Van Swaaij, Buurman and Van Breugel (1970)], and the acceleration of particles, especially in regions of the bed with large voidage gradients [Louge and Chang (1990)]. However, even granted these limitations on accuracy, this method only gives the cross-section average bed density. It cannot be used to measure local densities within the bed, and so is unsuitable for measuring the cluster void fraction.

Other techniques have been used to determine the local solids distribution, including τ-ray absorption [Hartge and Werther (1986); Wirth and Seiter (1991)], X-ray absorption [Weinstein, Shao and Schnitzlein (1986)], light reflection [Hartge, Rensner and Werther (1988); Horio et al. (1988)] and capacitance probes [Wu et al.(1991); Dou (1990); Louge, Lischer and Chang (1990)]. All these techniques can provide the time-average local conditions; however, the cluster voidage is still unknown without also knowing the local time fraction during which clusters are present in the sampling volume. Time resolved measurements on a scale less than the typical cluster size are needed to ascertain the structure of the particle distribution within the bed. So far, this has been possible only with light reflection probes and capacitance probes.

Fiber optic probes which measure the intensity of light reflected from the interior of the bed back to the probe have been used by several researchers to determine local bed densities [Hartge, Rensner and Werther (1988); Horio et al. (1988); Rhodes, Mineo and Hirama (1991)]. However, such probes are not ideally suited to that purpose. Brereton (1987) notes the difficulty of obtaining local density variations on an instantaneous basis with such probes. Reh and Li (1991) raise a more fundamental concern related to the undefined measurement volume associated with the probes in which the optic fibers are arranged in a parallel fashion. This includes most, if not all, of the probes in the studies published in the literature to date. Even the crossed fiber probe developed by Reh and Li (1991) to correct the problem of an undefined measurement volume does not address all the problems of calibrating such a probe. Kudo et al. (1991) show that the reflectance of a cluster of spheres depends as much, if not more, upon the randomness or regularity of the packing than it does upon the density of the packing. Thus, while light reflection probes can give useful measurements of cluster velocity and qualitative behavior of the local solid concentration, at their present state of development they do not provide reliable quantitative measurements of the solid concentration. This leaves the data from capacitance probes with which to examine the void fraction of the dense phase clusters.

Early capacitance measurements in a CFB by Brereton and Stromberg (1986) give clear evidence of the cluster structure, but either the probe was not calibrated to give the solid fraction, or the solid fraction was not reported. Instantaneous capacitance traces by Brereton (1987) show variations in voidage indicative of two distinct phases near the bottom of the bed: a dense phase of voidage slightly greater than that for loose-packed

particles and a dilute phase with voidage $\varepsilon \approx 1$. Since the cross-section average bed density at that location was about 500 kg/m^3, corresponding to a void fraction of 75-80%, these measurements probably represent a turbulent fluidization condition. Higher up in the bed, within the region of fast fluidization ($\rho_{bed} \approx 80$ kg/m^3), the voidage values near the wall showed a more continuous distribution. Although the extreme values of voidage were roughly the same as those measured at the bottom of the bed, the capacitance probe more often sensed intermediate values of voidage between these two extrema.

Two possible explanations may be put forward for this apparent change in behavior. On the one hand, the size of the dense and dilute phase structures may have been reduced to less than the size of the sampling volume of the capacitance probe, in which case the intermediate void fractions which were measured might represent a volume-weighted average voidage of these two distinct phases. Only occasionally, when the entire sampling volume was occupied by one of the two phases, would an extreme value of voidage be indicated. Alternately, the range of voidage measurements may indicate a stochastic fluctuation in the void fraction of the dense phase between the two extreme values.

There is evidence to support the latter viewpoint. Using a reflected light probe to measure the velocity and time of passage of dense phase clusters within a CFB, Horio et al. (1988) calculated an average cluster length near the wall of 10-15 mm when operating at a bed density comparable to that of Brereton (1987). This is somewhat longer than the longest dimension of Brereton's capacitance probe. Additionally, given the cross-section

average bed density of 80 kg/m^3, the wall was likely to have been completely covered by dense phase clusters (see Section 3.2). Combined, these two factors suggest that the sampling volume was often substantially, if not completely, occupied by the dense phase. Nakajima et al.(1991) performed a study on the transition from bubbling to turbulent fluidization. They measured the bubble fraction in the bed using a light transmission probe, and the average bed density using differential pressure measurements. They found that "in the transition to turbulent fluidization, ... the emulsion phase expands more than that in the bubbling condition." This expansion of the dense phase with increasing gas velocity was also noted by Lanneau (1960), who measured the local capacitance in the center of a 3-inch diameter fluidized bed. Although he had no means to recirculate particles back into the bed, he found a drop in the density of the dense phase in going from the bubbling to the turbulent regime. The dense phase solid concentration decreased steeply as he approached gas velocities sufficiently high to cause rapid entrainment of solids from the bed. This trend of increasing voidage in the dense phase has also been noted in progressing from turbulent to the fast fluidization regime in CFBs, at least in the vicinity of the wall [Louge, Lischer and Chang (1990)].

Several researchers have made continuous time-resolved measurements of the void fraction at the wall of CFBs using capacitance probes of various designs. These studies are summarized in Table 3.3. The results of Brereton (1987) have already been discussed; those of the other researchers in Table 3.3 are shown in Figure 3.8. All of the results shown in Figure 3.8 were presented by the respective authors as probability density functions (PDFs), except for those of Wu (1989). He published cumulative density

Researcher(s)	Particles	Superficial Gas Velocity (m/s)	Solid Circulation Rate (kg/m^2-s)	Bed Diameter (cm)	Details of Capacitance Probe	Sampling Volume	Sample Rate (Hz)
Brereton (1987)	(Sand?)	6.5	62	15.2	Traversing, needle-type	Horizontal cylinder, ~9 mm long	100
Wu (1989)	Sand, 171 μm	7	N/A	15.2	Traversing, Needle-type	Horizontal cylinder, ~8 mm long	~80
Herb (1990)	FCC, 87 μm	2.4	20	15.2	Traversing, plate electrode with surrounding ground shield	250 mm^3, 15 mm long × 12 mm wide	100
Dou (1990)	FCC, 87 μm	3.0	12.4, 27.3	15.2	Wall-mounted, parallel plate	131 mm^3, 6.4 mm wide × 6.4 mm high, projecting 3.2 mm into bed	250
Louge et al. (1990)	FCC, 61 μm	2	17	19.7	Wall-mounted, flush concentric rings	Semi-toroidal, 11 mm outer diameter projecting 2.1 mm into bed	100

Table 3.3 - Summary of Experiments for Cluster Void Fraction Near the Wall

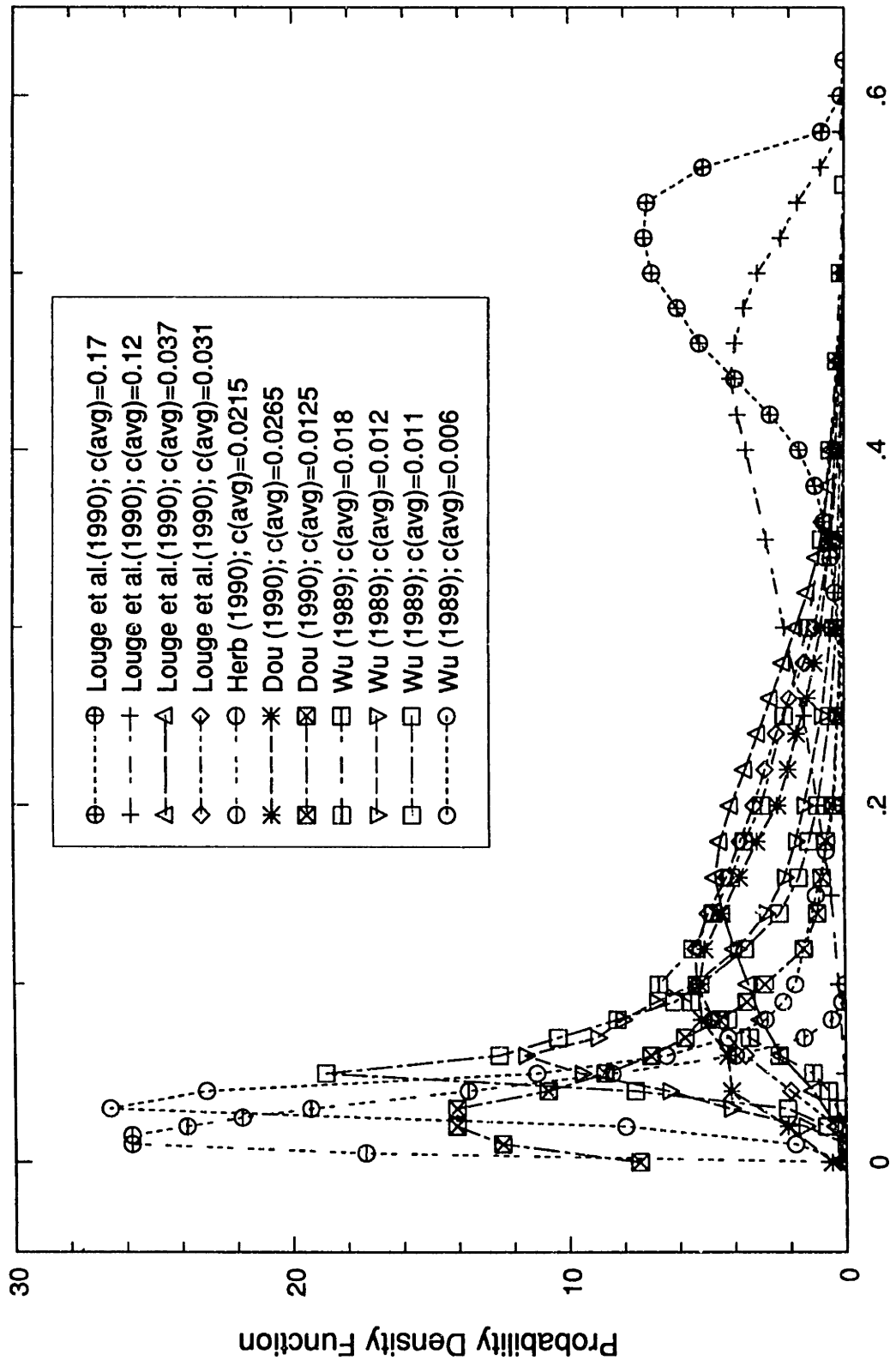

Figure 3.8 - Summary of Voidage Measurements by Capacitance Probes

functions, for which the derivatives have been taken graphically by the present author to obtain the PDFs. Each of the PDFs were normalized following Louge, Lischer and Chang (1990) by

$$\int_0^1 PDF(c)\,dc = 1 \qquad (3.4)$$

The general shape and location of the PDFs are fairly consistent from one study to the next. None of them show the bi-modal distribution indicative of two distinct phases which is typical of bubbling or slugging fluidized beds [Lanneau (1960); Lancia et al. (1988)] and of the central portion of the dense bed (turbulent) region of CFBs [Hartge, Rensner and Werther (1988); Herb (1990)]. They instead show a single peak of relatively low solid concentration at low values of the cross-section average bed density, with a tail extending to moderate values of solid concentration. The peak flattens and shifts to the right, and the range of voidages extends toward higher solid concentrations as the bed density increases. As the cross-section average solid concentration exceeds about 0.1, the peak again grows and approaches the bulk solid concentration of the particles. This is consistent with the near-wall measurements of both Hartge, Rensner and Werther (1988) and Herb (1990).

The PDF data presented in Figure 3.8 can be used to determine the average cluster void fraction. As in Section 3.2, a value of the solid concentration, $c_{c,min}$, which represents a boundary between the dense and dilute phases must be used. The average of all solid

concentrations above this value, weighted by the PDF, will give the average cluster solid concentration:

$$\overline{c}_c = \frac{\int_{c_{c,min}}^{1} PDF\, c\, dc}{\int_{c_{c,min}}^{1} PDF\, dc} \qquad (3.5)$$

The average cluster solid concentration so determined will depend upon the assumed value of $c_{c,min}$. Figure 3.9 shows the resulting values of $\overline{c}_c$ for three different values of $c_{c,min}$ using the PDFs from Figure 3.8 plotted against the cross-section average solid concentration. Figure 3.10 shows the same information, but plotted instead against the

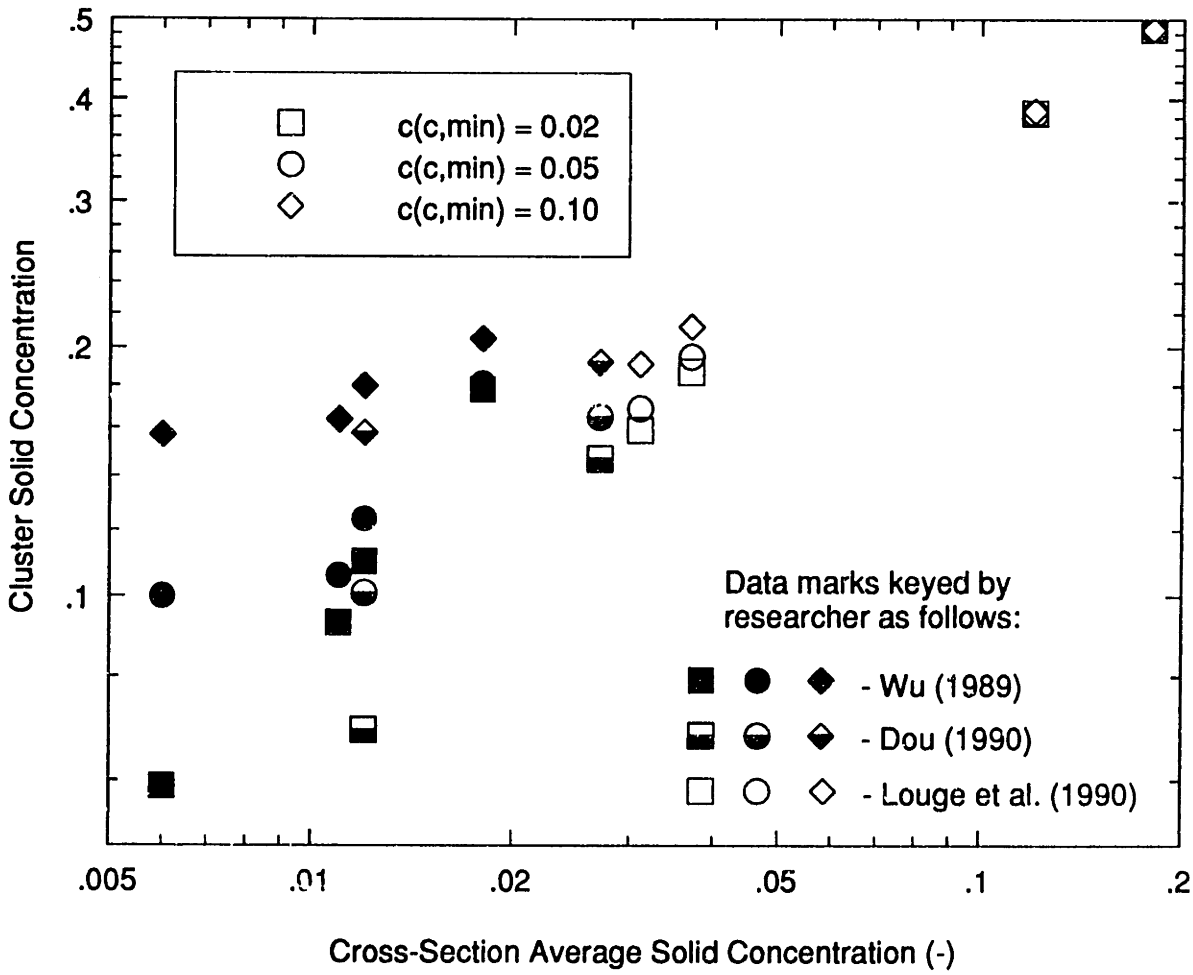

Figure 3.9 - Cluster Solid Concentrations from Capacitance Probe Measurements

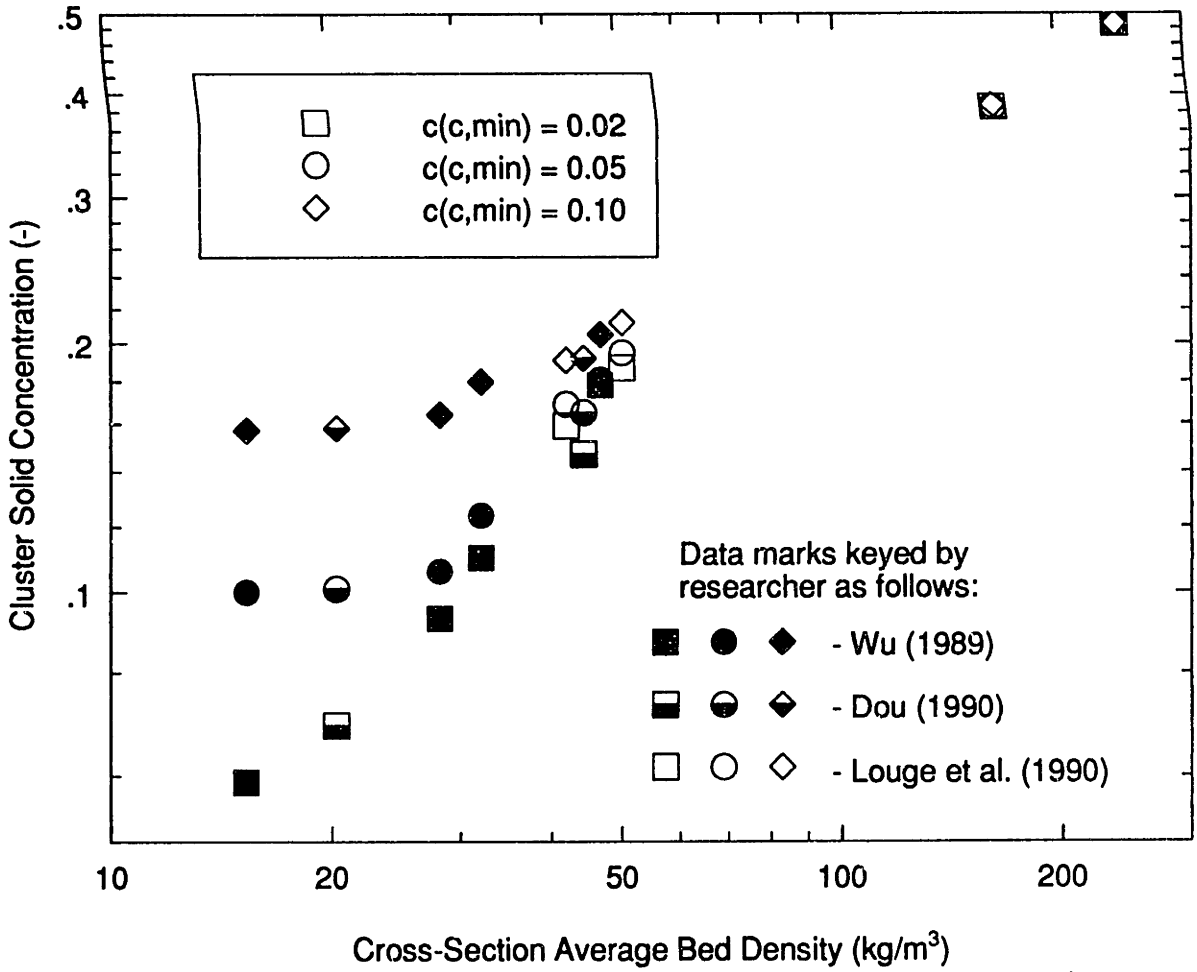

Figure 3.10 - Dependence of Cluster Solid Concentration on Bed Density

cross-section average bed density. It appears that the data correlates better with the bed density than with the solid concentration; it is not evident why this may be so. The differences in the capacitance probes and their sampling volumes between the different researchers may account for much of the scatter in Figure 3.9, and it may be happenstance that plotting $\overline{c}_c$ versus ρ_{bed} for these few data points reduces the scatter. In any event, the trends exhibited by the data are clear in both figures. At moderate to high solid loading, $\overline{c}_c$ is independent of $c_{c,min}$, and varies instead with the solid loading. However, at low to moderate solid fractions, the choice of $c_{c,min}$ is also a significant determinant of $\overline{c}_c$.

As discussed in Section 3.2, the choice of values for $c_{c,min}$ is somewhat arbitrary. To be consistent with the cluster wall coverage values developed there, a value of $c_{c,min} = 0.05$ will also be assumed here. The resulting values of $\overline{c}_c$ at the wall from the capacitance probe measurements of Table 3.3 are shown in Figure 3.11, along with the least-squares fit to the data. It should be noted that this least-squares fit also correlates rather well to the cluster solid concentration values resulting from using $c_{c,min} = 0.02$. Thus, $\overline{c}_c$ is not particularly sensitive to the choice of $c_{c,min}$, at least within the range $0.02 < c_{c,min} < 0.05$. The least-squares fit of Figure 3.11 is remarkably close to the elementary expression:

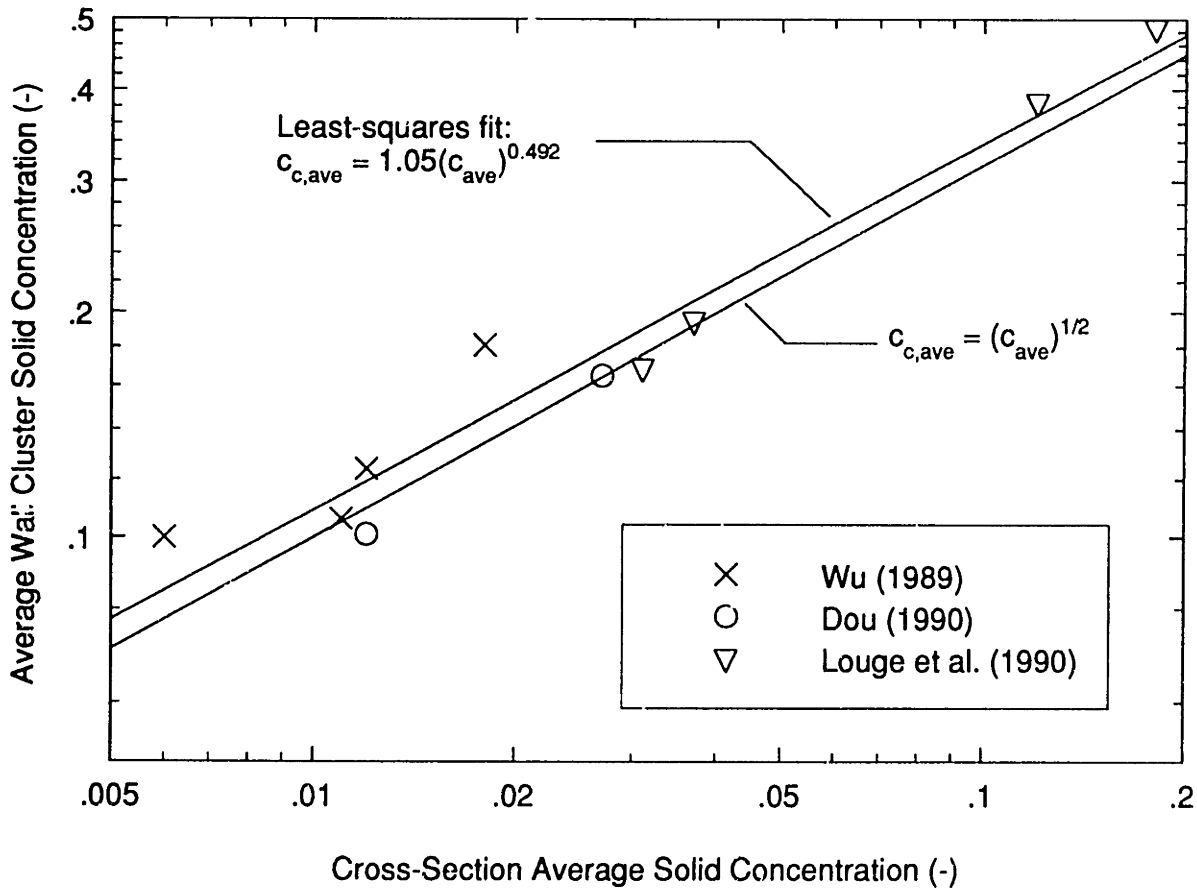

Figure 3.11 - Dependence of Cluster Solid Concentration on Cross-Section Average Solid Concentration

$$\overline{c}_c = \overline{c}^{1/2} \tag{3.6}$$

Because of its simplicity and ease of use, this latter expression will be assumed to adequately represent the functional dependence of the average cluster solid fraction at the wall on the cross-section average solid concentration.

3.5 Dilute Phase Heat Transfer Coefficient

There has been little attention paid to the heat transfer coefficient from the dilute phase of CFBs. Most models of CFB heat transfer either ignore heat transfer from the dilute phase through the explicit or implicit assumption that the entire surface is covered by particles [Sekthira, Lee and Genetti (1988); Mahalingam and Kolar (1991); Dou (1990)], or they use the single-phase correlation for flow of gas alone [Wu (1989); Kunii and Levenspiel (1991a)]. Since h_c is generally much greater than h_d [Grace (1986)], neither of these methods will cause significant error in estimating the heat transfer coefficient at moderate or greater bed densities with fractional wall coverages approaching unity (see Eq. 2.1). However, at lower bed densities, where f may be closer to 0 than to 1, a more accurate means of estimating h_d may be necessary.

Subbarao and Basu (1986) estimated the dilute phase heat transfer coefficient with an expression analogous to that for transient conduction in a particle cluster, with the dilute phase properties being those of the gas. But according to Basu and Nag (1987), this gives rather low values for h_d. They suggest that the Wen and Miller (1961) correlation be used instead, with c_d=0.001 taken from Kunii and Levenspiel (1969) for solids dispersed in the bubbles of bubbling fluidized beds. However, based on the capacitance probe measurements, the solid concentration at the wall of CFBs rarely if ever approaches a value this low, even in the dilute phase.

An estimate of the dilute phase heat transfer coefficient may be obtained by looking at experimental heat transfer measurements. The wall heat transfer measurements in CFBs

which are available in the literature are summarized in Table 3.4. The heat transfer data are plotted against the cross-section average bed density in Figures C.1 through C.7 of Appendix C. Looking at these figures, it can be seen that within the range $0 \leq \rho_{bed} \leq 50$ kg/m^3, the wall heat transfer coefficient measured by most researchers increases approximately linearly with the cross-section average bed density. Referring to Eq. 2.7, the reason for a linear increase in h with ρ_{bed} is not clear, and is probably due to a combination of several factors. However, from the discussion in Section 3.2, it is clear that f decreases with decreasing ρ_{bed}; and in the limit as $\rho_{bed} \rightarrow 0$, f will also approaches zero and $h \rightarrow h_d$. Since this is the case, then the heat transfer data taken at low bed densities can be extrapolated to zero bed density to obtain an estimate of h_d. Strictly speaking, if it is assumed that h_d also varies with ρ_{bed}, then the heat transfer coefficient extrapolated at zero bed density (h_0) will be an estimate of the value of h_d only at (or near) zero bed density. But if h_d does not depend strongly on ρ_{bed}, then h_0 may be a good estimate of h_d over a reasonable range of solid concentrations. Furthermore, a better understanding of h_d at very low bed densities may provide some knowledge regarding the nature of any influence which the bed density may have on h_d.

Figure 3.12 shows the least-squares linear curve fits to the wall heat transfer data of various researchers presented in detail in Appendix C. Only data with $\rho_{bed} \leq 50$ kg/m^3 have been used in generating the curves in Figure 3.12 in order to restrict the data to the region in which $f<1$ and varies with the bed density. Furthermore, only data with $T_{bed} \leq$ 400°C have been used to minimize the effect of any radiation heat transfer. The solid portions of the lines in Figure 3.12 represent the range of the actual data taken by the

Curve No. (Fig 3.12)	Researcher(s)	Particles	Superficial Gas Velocity (m/s)	Length of Heat Transfer Surface (cm)	Estimated Single-Phase h_g (W/m^2-K)	Zero-Density Heat Transfer Coefficient (W/m^2-K)
1	Basu et al. (1987)	Sand, 87 μm	3.7 - 5.0	2.5	56	56 ± 151
2	Dou (1990)	FCC, 87 μm	2.4 - 3.5	3.2	38	63 ± 22
3	Wu et al. (1989a)	Sand, 171 μm	7	1	52	69 ± 10
4	Subbarao & Basu (1986)	Sand, 130 μm	>1.7	2.5	56	88 ± 98
5	Feugier et al. (1987)	Sand, 95 μm	10	~95	19	19 ± 23
6	Dou (1990)	Sand, 125 μm	4.25 - 7.5	3.2	49	23 ± 12
7	Basu et al. (1987)	Sand, 227 μm	3.0 - 5.0	2.5	56	98 ± 39
8	Furchi et al. (1988)	Glass, 109 μm	5.8 - 8.9	100	22.5	50 ± 16
9	Kobro & Brereton (1986)	Sand, 170 μm	8 - 10	10	42	25.5 ± 52
10	Subbarao & Basu (1986)	Sand, 260 μm	>2.4	2.5	56	97 ± 40
11	Dou (1990)	Sand, 268 μm	5.1 - 7.1	3.2	54	24 ± 19

Table 3.4 - Summary of Heat Transfer Measurements by Various Researchers

Curve No. (Fig 3.12)	Researcher(s)	Particles	Superficial Gas Velocity (m/s)	Length of Heat Transfer Surface (cm)	Estimated Single-Phase h_g (W/m^2-K)	Zero-Density Heat Transfer Coefficient (W/m^2-K)
12	Feugier et al. (1987)	Sand, 215 μm	10	~95	19	25.5 ± 17
13	Basu et al. (1991)	Sand, 310 μm	5.6 - 11.4	30	39	59 ± 7
14	Wu et al. (1987)	Sand, 188 μm	4 - 7	30	4.5	38 ± 17
15	Basu (1990)	Sand, 250 μm	~5?	10.1	31	36 ± 53
16	Wu et al. (1989b)	Sand, 241 μm	7.5	159	8	48 ± 6
17	Kobro & Brereton (1986)	Sand, 250 μm	8 - 10	10	42	50 ± 51
18	Wu et al. (1987)	Sand, 356 μm	4 - 7	30	4.5	28 ± 16
19	Sekthira et al. (1988)	Sand, 300 μm	4.9 - 7.3	10	28	29 ± 15
20	Furchi et al. (1988)	Glass, 196 μm	5.8 - 8.9	100	22.5	25 ± 7
21	Furchi et al. (1988)	Glass, 269 μm	5.8 - 8.9	100	22.5	27 ± 3
22	Feugier et al. (1987)	Sand, 625 μm	10	~95	19	24 ± 5

Table 3.4 (cont.) - Summary of Heat Transfer Measurements by Various Researchers

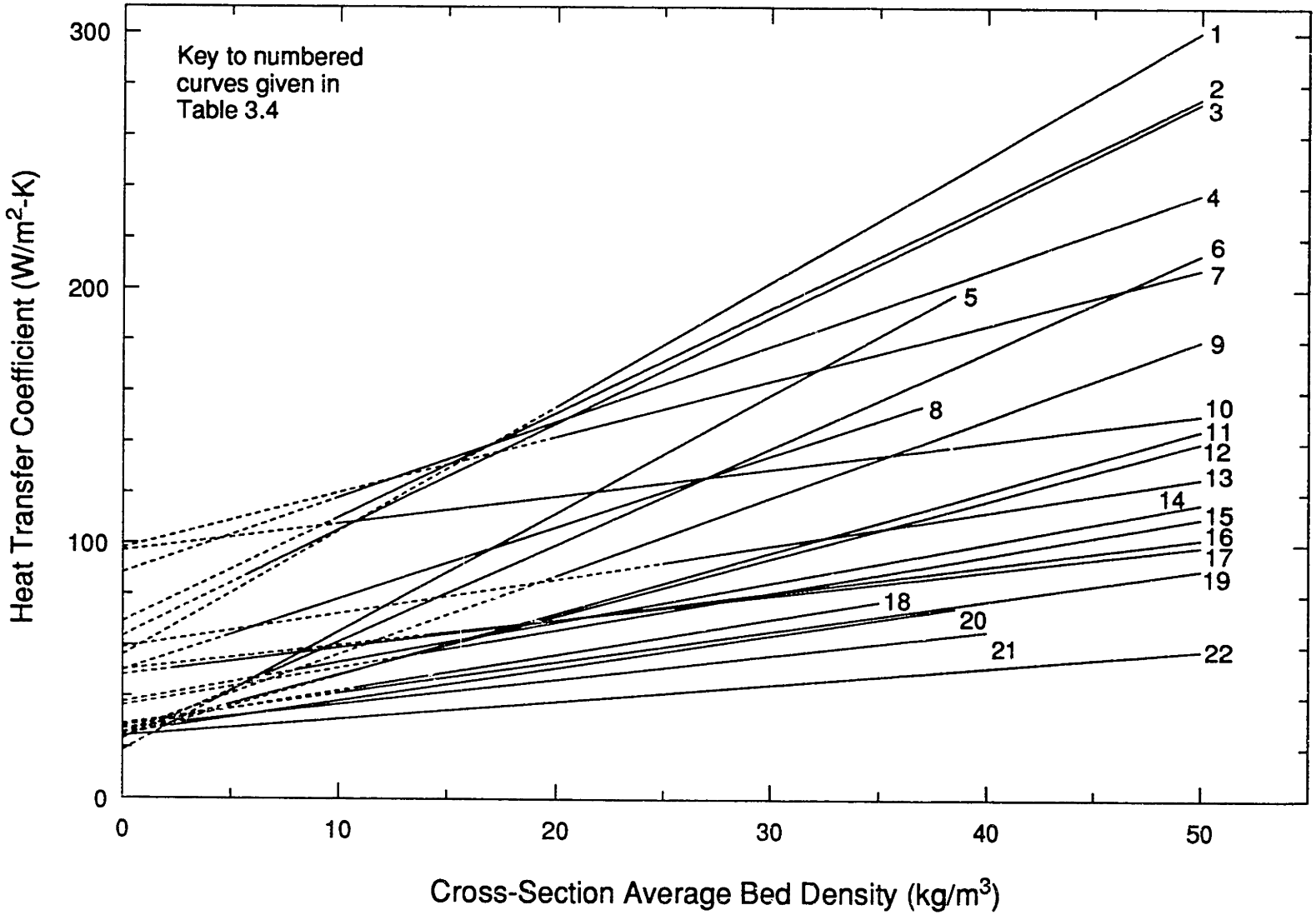

Figure 3.12 - Summary of CFB Heat Transfer Measurements at Low Density

various researchers; the dashed portions are the linear extrapolations to zero density. These zero-density heat transfer coefficients are listed in Table 3.4, along with their 95% confidence intervals determined according to standard linear regression techniques [Chatterjee and Price (1977)]. The zero-density heat transfer coefficients, h_0, range from 19 to 98 W/m^2-K, with the greatest concentration of values clustered at the low end of that range.

In an effort to explain the variations in h_0, these data were cross-plotted against the particle diameter, the length of the heat transfer surface (L_h), and the midpoint of the reported range of superficial gas velocities. These plots are shown in Figures 3.13, 3.14,

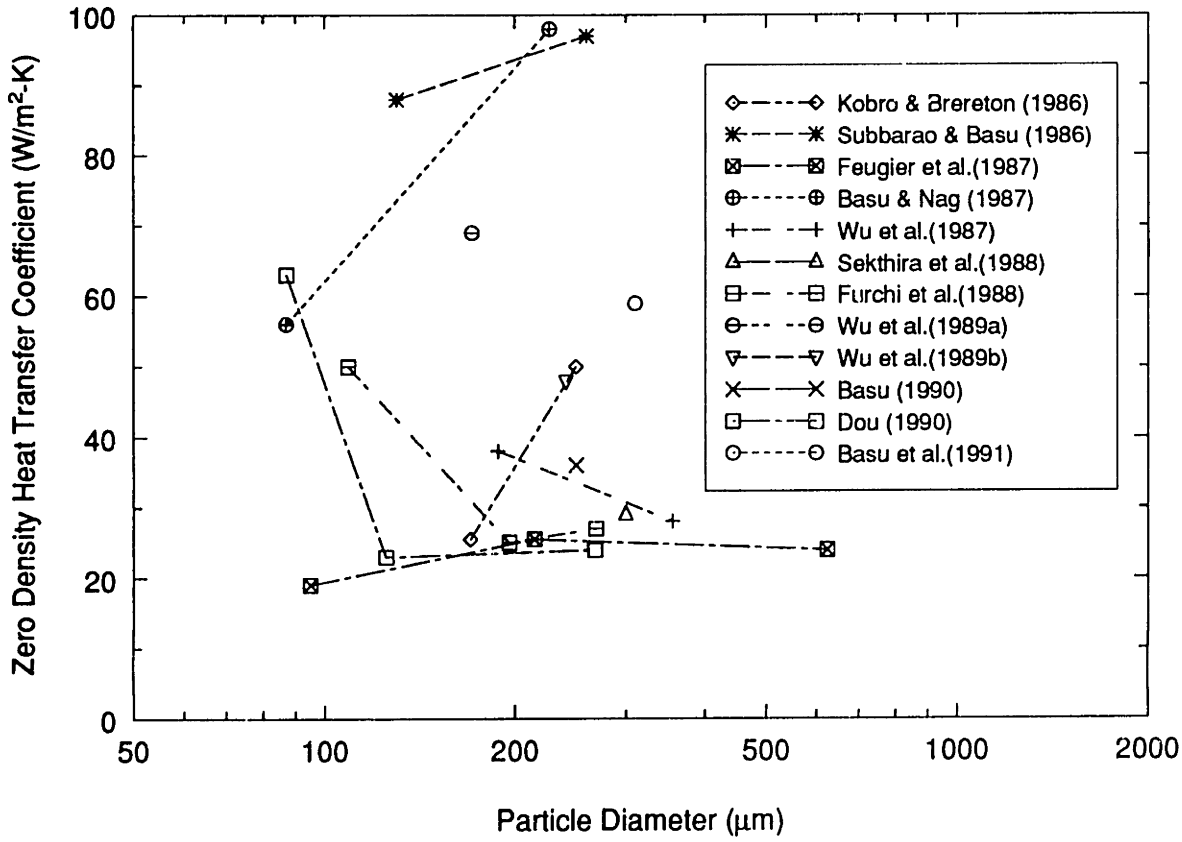

Figure 3.13 - Dependence of h_0 on Particle Diameter

and 3.15, respectively. None of these figures exhibit any strong dependencies of h_0, although there are weak trends towards decreasing h_0 with increasing L_h or U_g. The apparent tendency to decreasing h_0 with increasing U_g has no obvious explanation, and

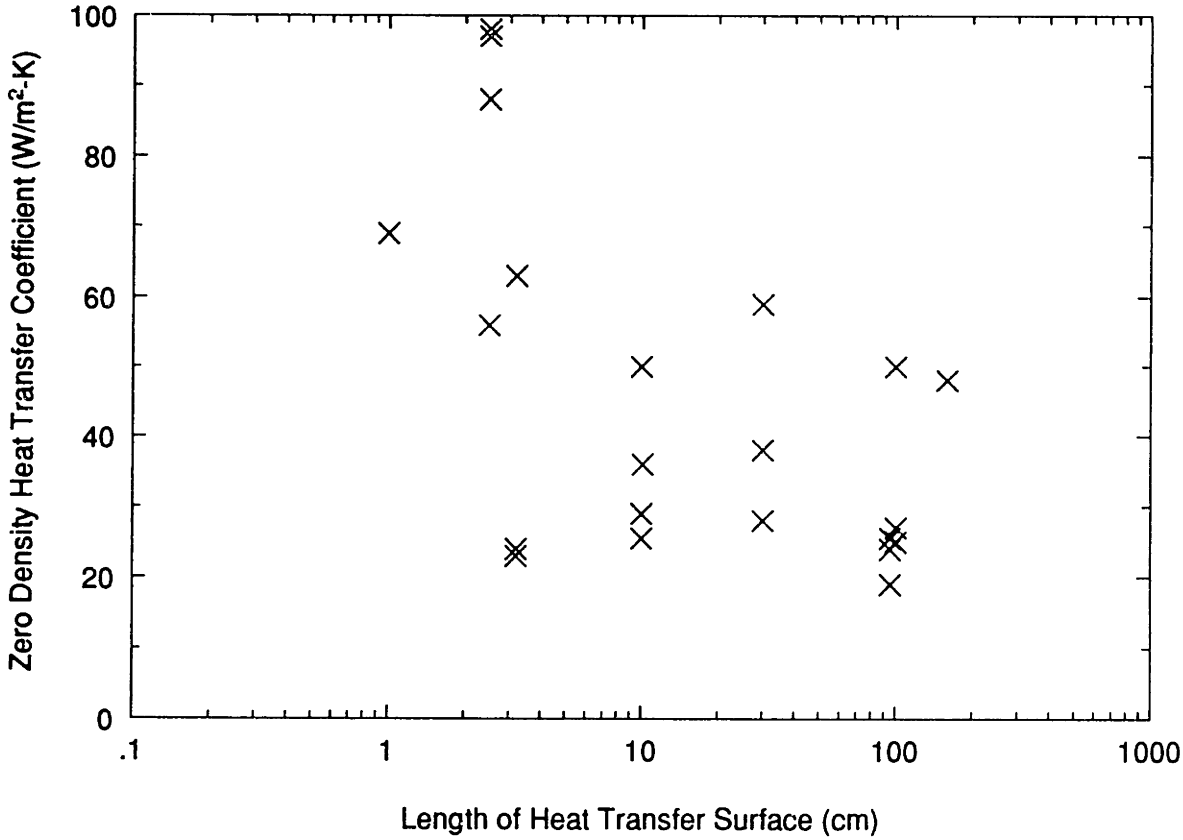

Figure 3.14 - Dependence of h_0 on Length of Heat Transfer Surface

may be coincidental. However, the tendency for longer heat transfer surfaces to give lower values of the zero-density heat transfer coefficient is consistent with the idea of the equivalence of h_d and the single-phase gas heat transfer coefficient, h_g.

In order to compare these two quantities for the different sets of data, the experimental set-up of each researcher in Table 3.4 was examined and an estimate was made of the

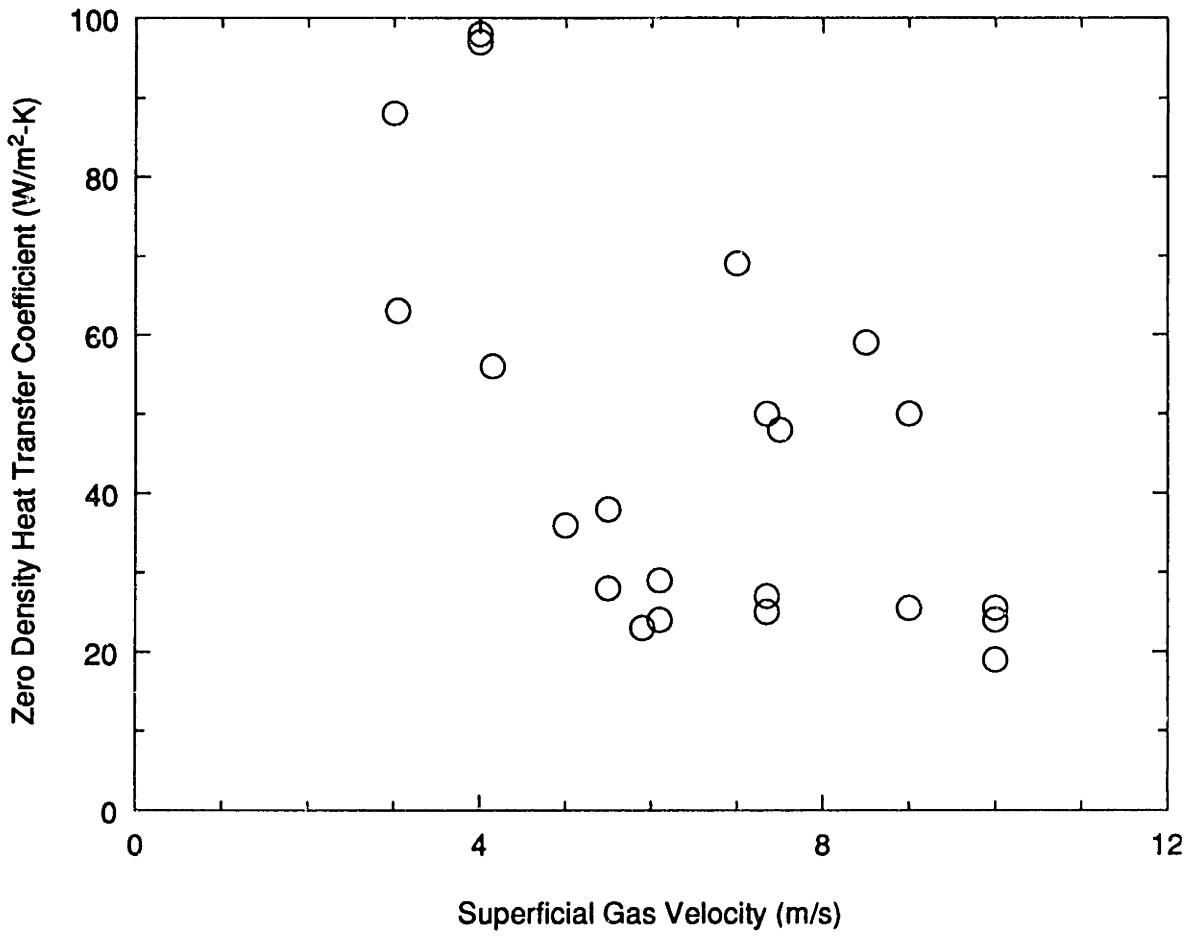

Figure 3.15 - Dependence of h_0 on Superficial Gas Velocity

forced convection heat transfer coefficient corresponding to the flow of air through the apparatus at the average superficial gas velocity and bed temperature. These results are included in the sixth column of Table 3.4, and are cross-plotted with h_0 in Figure 3.16. The data points in Figure 3.16 are differentiated according to the configuration of the heat transfer surface on which the measurement was taken. Tubular heat exchangers are those which completely enclose the circular bed for some axial length; flat plate heat exchangers are either small, circular surfaces set in the wall of the bed, or, in the case of Wu et al. (1987, 1989b), a long membrane water-wall comprising part of the enclosing walls of the bed. The lowest Reynolds number calculated for the experiments with

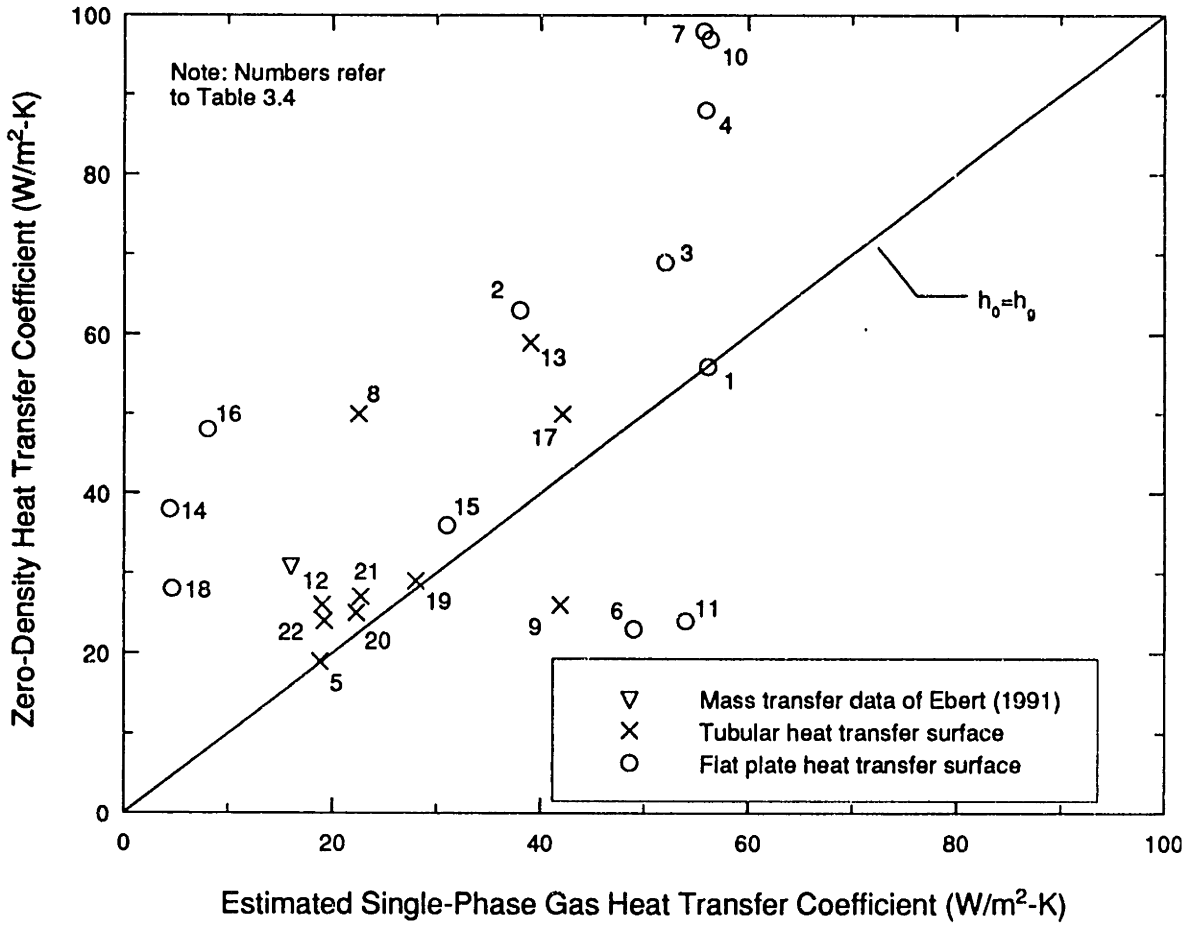

Figure 3.16 - Comparison of Single-Phase Gas Heat Transfer Coefficient to h_0

tubular heat exchangers was about 15,000; therefore, turbulent flow was assumed in all cases, and the correlation of Petukhov (1970) was used to calculate the rate of heat transfer:

$$Nu = \frac{(f/8)\,RePr}{1.07+12.7\sqrt{f/8}\,(Pr^{2/3}-1)} \tag{3.7}$$

where f is the friction factor, given by:

$$f = [1.82\log_{10}(Re) - 1.64]^{-2} \tag{3.8}$$

For those cases where L/D < 6, the Nusselt number was obtained from the figure presented by Kays and Perkins (1973) for combined thermal and hydrodynamic entry length with constant surface temperature by a graphical integration. For the flat plate heat exchangers, the highest Reynolds number is less than 2×10^5, so the analytical expression for the Nusselt number in laminar flow was used [Karlekar and Desmond (1982)]:

$$Nu = 0.664 Re^{1/2} Pr^{1/3} \tag{3.9}$$

Figure 3.16 also contains a point which represents the mass transfer data of Ebert (1991). The ordinate of the point is the average mass transfer coefficient measured by Ebert at a low bed density (12.8 kg/m^3), transformed to an equivalent heat transfer coefficient by the Colburn analogy; the abscissa is the estimated single-phase gas heat transfer coefficient for a heat transfer surface of the same configuration as his mass transfer surface. Because of the nature of his experiment, Ebert's (1991) results are not an exact measure of the dilute phase heat transfer coefficient, but should represent an upper bound of h_d.

Figure 3.16 shows reasonably good agreement between h_g and h_0, with a tendency for h_g to underpredict h_0. Some of the discrepancy between the two may be attributed to the uncertainty in h_0. Figure 3.17 shows the same data as Figure 3.16, but with the 95% confidence interval on h_0 included. Another possible source of error is in the estimate of the single-phase gas heat transfer coefficient. The literature does not always contain a sufficiently detailed description of the experimental apparatus and operating conditions

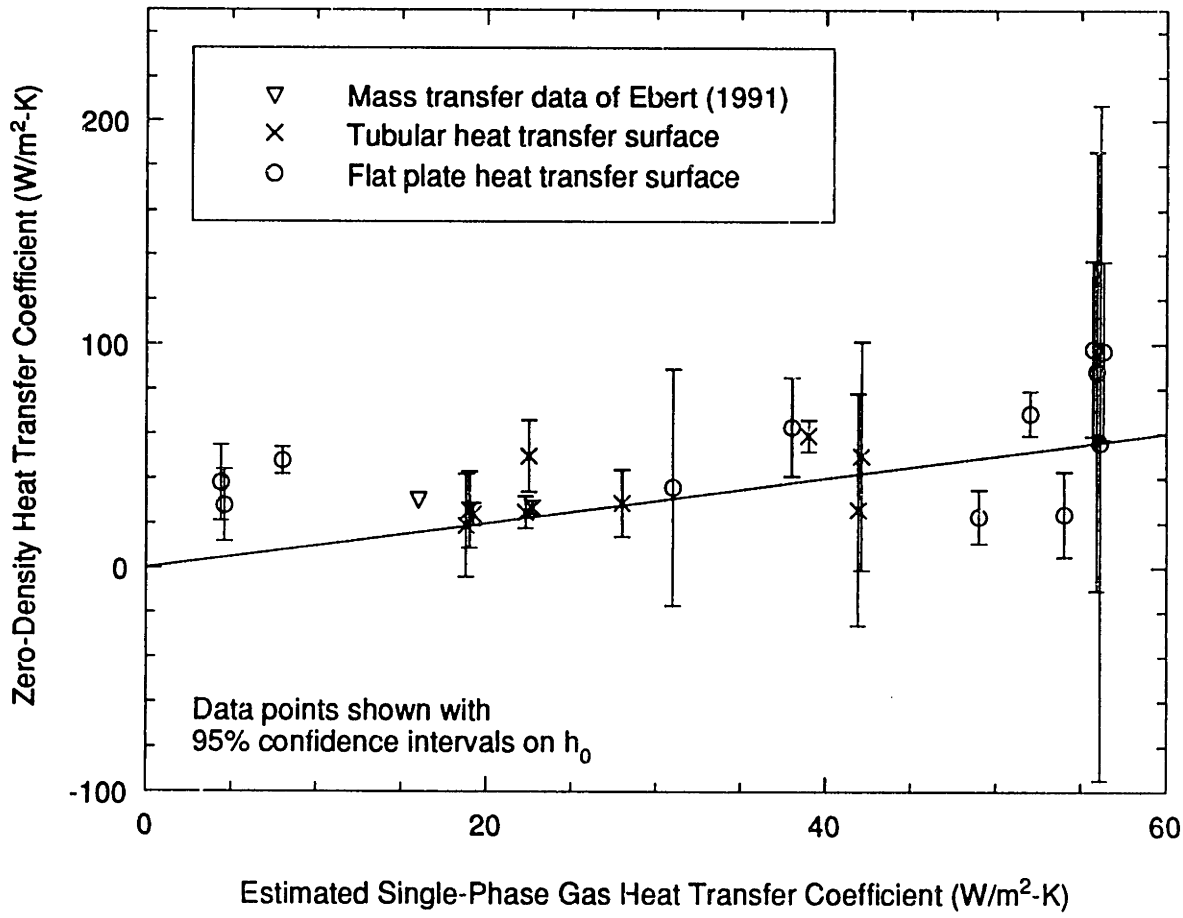

Figure 3.17 - Single-Phase Gas Heat Transfer Coefficients vs. h_0 with Uncertainties

to allow an accurate estimation of h_g to be made. For example, it has been generally assumed that the profile of the wall surface where it meets the heat transfer surface is sufficiently rough to disturb the boundary layer, such that a combined thermal and hydrodynamic entry length correlation is appropriate. The effect of considering only the thermal entry length for the heat transfer surface and assuming either a fully developed velocity profile or some unheated starting length would be to reduce the estimated single-phase heat transfer coefficient to some degree (as much as 50% for the shortest surfaces). However, although some of the differences between h_g and h_0 are undoubtedly due to

inaccuracies and random errors, variations are also the result of actual differences which exist in the phenomena characterized by these two factors.

The first of these differences is that the dilute phase at the wall of CFBs is not made up of gas alone, but also of some low concentration of particles. In fact, if the definition of a cluster suggested in Section 3.4 is used ($c_{c,min}$=0.05), then the concentration of particles in the dilute phase will range from 0 to 5%. Furthermore, considering the shape of the PDFs from the capacitance probe measurements also presented in that section (Figure 3.8), the average particle concentration in the dilute phase will be tend toward the upper end of that range. Since the particles typically have a higher thermal conductivity than the gas, the effective thermal conductivity of this dilute gas-solid mixture will be somewhat higher than that of the gas alone. According to the Gelperin and Einstein (1971) model, Eq. 2.6, this increase in the thermal conductivity, and so the heat transfer coefficient, will be nearly 10% for a dilute phase solids concentration of 3%. If the dilute phase conductivity is instead estimated by Maxwell's (1892) expression for the conductivity of disperse spheres in a continuous medium, the increase due to 3% solids is about 8.5%. Therefore, it is expected that the thermal conductivity of the dilute phase will be roughly 10% higher than that of the gas alone.

In addition to the increase in thermal conductivity, the addition of a small fraction of particles will also cause a substantial increase in the thermal capacity of the dilute phase relative to the single-phase gas. If the thermal time constant of the particles is not significantly greater than the time scale for diffusion through the thermal boundary layer,

then the thermal capacity of the particles will effectively reduce the thermal diffusivity of the dilute phase and thereby increase the Prandtl number. A more detailed analysis is required to determine the exact extent to which this effect may contribute to any enhancement of h_d over h_g. However, it is clear that both a higher Prandtl number and a greater thermal conductivity will tend to increase the convective heat transfer coefficient, such that h_d will be at least 10% higher than h_g. The exact degree of the enhancement will be dependent upon the actual concentration of particles in the dilute phase and the change that it produces in the effective thermal transport properties relative to the gas phase alone.

A second difference between the phenomena characterized by h_g and h_d is pointed out by the data of Wu et al. (1987, 1989b) in Table 3.4. All of these data were taken using a long (>1.5 m) water wall heat exchanger; in the case of Wu et al. (1987), h was measured on only the topmost 30 cm of a longer heat transfer surface. The very low estimates of h_g corresponding to these data shown in Table 3.4 are a result of a thick thermal boundary layer developing along this long heat transfer surface. However, even at very low solid concentrations, some clusters will occasionally sweep the wall of a CFB. This will disturb the boundary layer, thereby increasing the heat transfer coefficient. Although this disturbance of the boundary layer will also occur for short heat transfer surfaces, its effect will be less noticeable. If the length of the heat transfer surface is much less than the distance along the wall between clusters, then the boundary layer will only occasionally be disturbed by the passage of clusters, and the heat transfer coefficient will not be greatly affected. It is in the case of long heat transfer surfaces that the effect of the

boundary layer disturbance will be most noticeable. Figure 3.18 shows the effect of the regular passage of particle clusters on the boundary layer development of a long heat transfer surface. When particles are present, the long heat transfer surface may appear hydrodynamically similar to a series of shorter heat transfer surfaces. In this case, it is more appropriate to use the undisturbed boundary layer length (l_d) than the total length of the heat transfer surface.

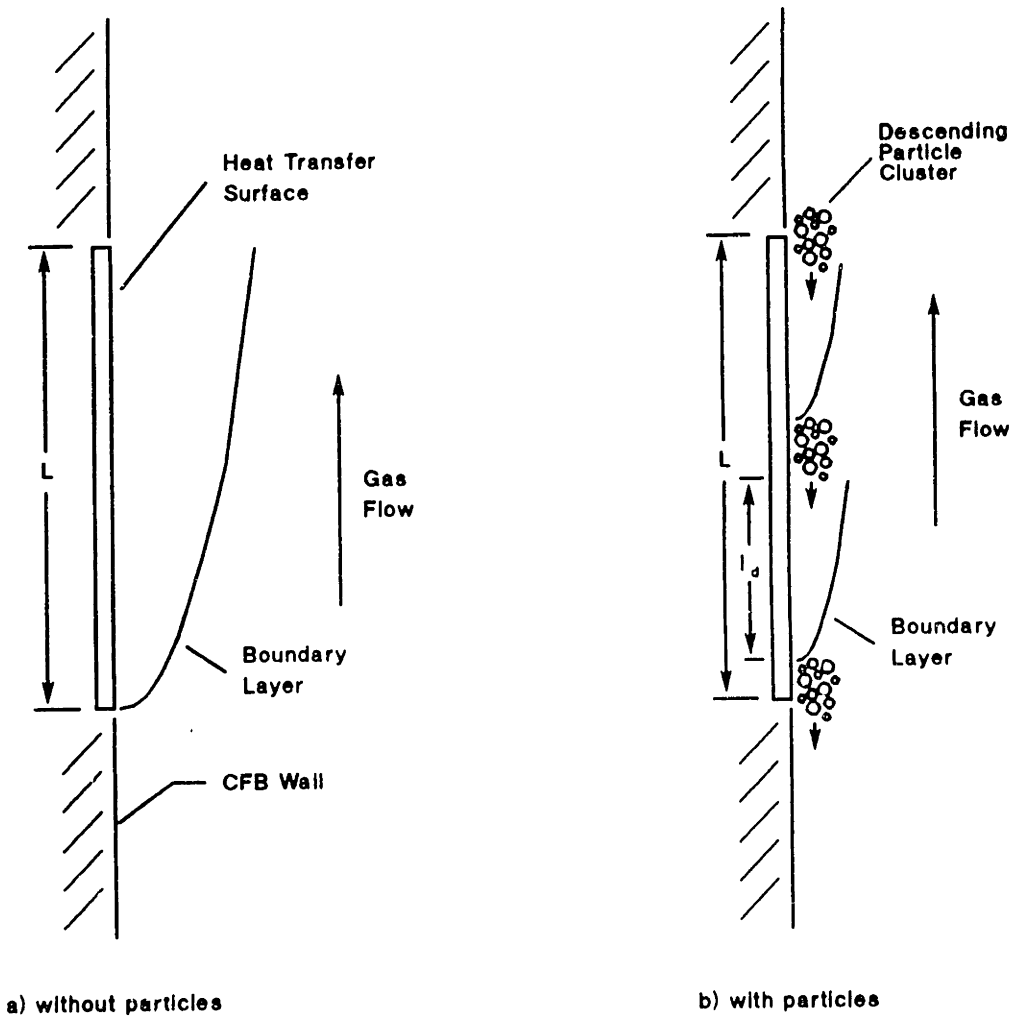

Figure 3.18 - Disruption of Boundary Layer Development by Passage of Clusters

Although this undisturbed length, or the distance between clusters, is not known, the data of Basu (1990) in Table 3.4 shows good agreement between h_g and h_0 with a flat plate heat exchanger of length ~10 cm, whereas Wu et al. (1987, 1989b) show poor agreement with a length of ~1.5 m. If a value of l_d= 10 cm is used to calculate h_g for the data of Wu et al. (1987, 1989b), then the resulting values show much better agreement with the corresponding values of h_0.

The use of a similar value for the undisturbed length of flow along the wall is suggested by the mass transfer measurements of Ebert (1991). He measured the sublimation rate from a naphthalene panel 14 cm long in a CFB without particles and at three different particle densities. He found that the presence of particles in the bed increased the mass transfer rates by an average of about 30%. This same increase in mass transfer would result from a reduction in the undisturbed flow length from 14 cm to 8.3 cm. Since the glass beads used in the experiment were inert to naphthalene, the enhanced mass transfer must be due to some change in the hydrodynamic conditions at the surface caused by the particles.

Disturbance of the boundary layer by clusters is only one of the possible explanations for the enhancement in the rate of mass transfer in Ebert's experiments. At the highest bed density tested, it was visually observed that the wall of the bed was completely covered by particle clusters [Ebert, Glicksman and Lints (1990)]. An increased rate of mass transfer was still recorded, but there was essentially no dilute phase at the wall in which to develop a boundary layer which could then be disturbed by the passage of a cluster.

Clearly, some other transport mechanism is dominant in this situation. In spite of this, disturbance of the boundary layer is still postulated as an important factor in accurately describing the dilute phase heat transfer at lower densities; and lacking any better indications, 10 cm still appears to be a reasonable estimate of the undisturbed flow length for these conditions.

Based on the foregoing, h_d may be estimated by using the correlations in the published literature for h_g, with the following adjustments:

1) assume that the length of flow along the heat transfer surface is no greater than 10 cm, and

2) assume that $k_d = 1.1\ k_g$.

Figure 3.19 shows the values of h_d estimated in this fashion for the experiments in Table 3.4 plotted against the corresponding values of h_0. There is still a fair degree of scatter about the line of equality, but the fit is generally better than that of Figure 3.16. If h_0 is accepted as a reliable indicator of the actual value of h_d, then it appears that h_d can be predicted at least to within a factor of 2 by the present method. It is also clear that further study in this area is needed before h_d can be predicted with greater confidence.

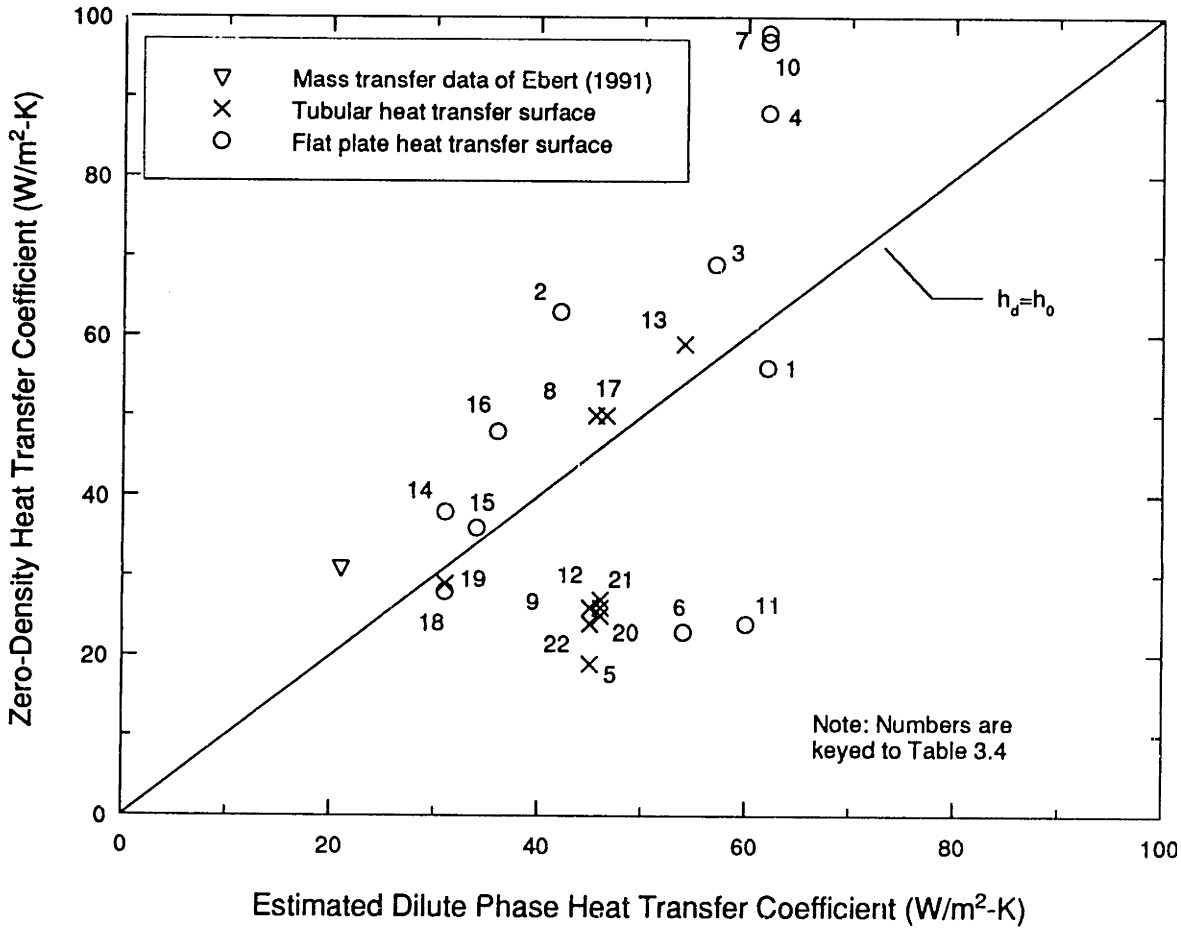

Figure 3.19 - Comparison of Estimated Dilute Phase Heat Transfer Coefficient to h_0

Chapter 4

Experimental Program

The experimental work of this thesis was performed in two successive stages. First, it was desired to obtain a greater understanding of the general behavior of particle clusters near the wall of a CFB. To this end, visual observations and recordings of clusters under several different controlled conditions were made. Based upon the results of that work, a second set of experiments was carried out to quantify some of the parameters important to the heat transfer process. A detailed description of the experimental work is given below.

4.1 Studies of Macroscopic Cluster Behavior

As discussed in Section 3.3, the time of contact between a cluster and the wall is one of the determining factors of the rate of transient heat conduction within the cluster. When this experimental work was begun, the Mickley and Fairbanks (1955) model for transient conduction within a cluster of particles had been applied to heat transfer in a CFB by Subbarao and Basu (1986). However, there were no published data on the motion of particles near the wall by which the time of contact, or any of the other important heat transfer parameters which might be demonstrated by the macroscopic cluster behavior, could be estimated. Although the situation has improved since then (see Section 3.3.1), there has still been no systematic study of the influence of various operating parameters

on the motion of clusters within a CFB. A study of the behavior of particle clusters was undertaken in order to gain some of this information.

4.1.1 Particle Cluster Injection Tube

Although greater knowledge of particle behavior in CFBs was desired, the initial experiments were performed in a much simpler device. This allowed testing with a wider range of gas velocities than would have been possible in a CFB. It also simplified problems associated with testing of different particles and obtaining ideal viewing conditions.

4.1.1.1 Experimental Apparatus and Procedure

A schematic of the experimental apparatus is shown in Figure 4.1. The device consists of a vertical transparent acrylic tube 10 cm in diameter with air flowing through it from bottom to top. Near the top of this tube, a smaller, horizontal tube was fitted out as a pneumatic cannon. To simulate a particle cluster arriving at the wall of a circulating bed, a small volume of particles was injected by the pneumatic cannon horizontally against the inside wall of the vertical tube. A video camera attached to a standard VHS VCR was positioned so that its field of view extended approximately half a meter along the height of the 10 cm viewing tube, with the pneumatic cannon near the top of its field of view. The apparatus was placed in a darkened area and illuminated by a stroboscope which was synchronized to the framing speed of the video system (30 Hz).

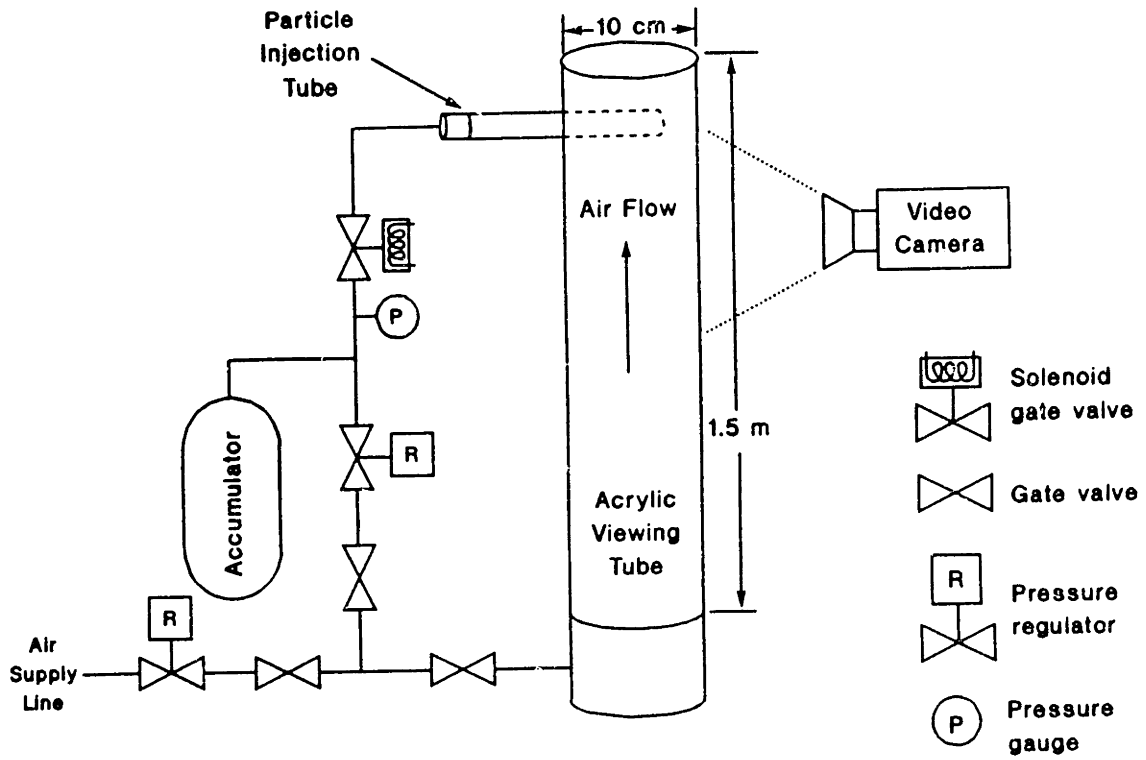

Figure 4.1 - Particle Injection Tube Experimental Apparatus

Two different particles were used in the tests, 80 μm silica particles and 600 μm aluminum particles. The characteristics of these particles is given in Appendix A. Before each test, the rate of air flow in the viewing tube was adjusted by a globe valve in the air supply line going to the base of the tube, and measured by an orifice plate meter further upstream. The accumulator was then charged by opening the gate valve just upstream of its regulator. A small amount of particles, roughly 10 cm^3, was then placed in the base of the cannon. The particles were then fired against the wall of the tube by manually activating the solenoid gate valve downstream of the accumulator. Video pictures of the process were taken and the velocity of the falling sheet of particles was determined from

the change in position of its leading edge or some other identifiable feature observed over successive frames.

4.1.1.2 Results and Discussion

At each test condition, the velocity histories of between four and twelve clusters were recorded. These results are shown in full in Appendix B. Figures 4.2 and 4.3 give the cluster velocities averaged at each location along the tube and at each gas velocity for the 80μm silica and the 600μm aluminum particles, respectively.

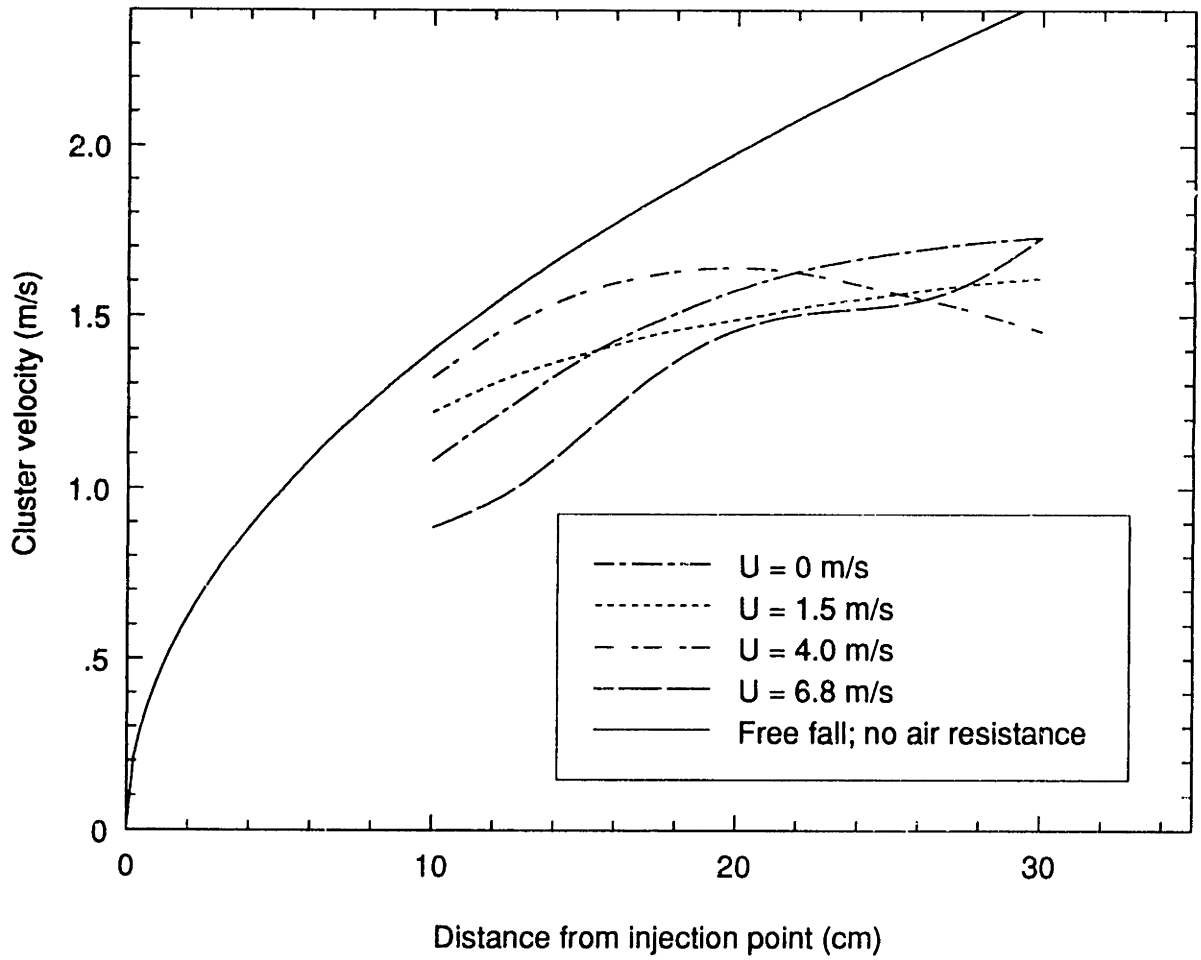

Figure 4.2 - Cluster Velocities in Particle Injection Tube for Small Particles

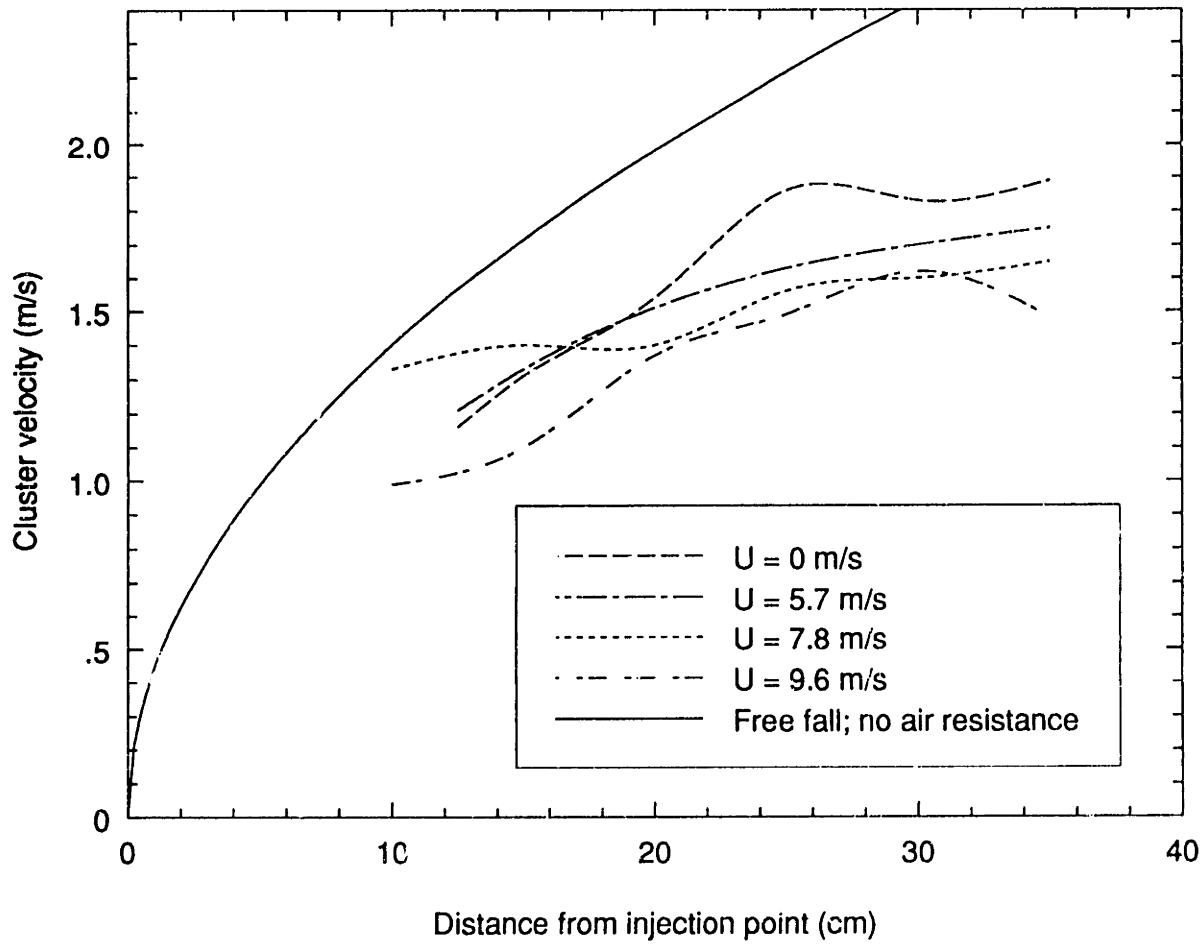

Figure 4.3 - Cluster Velocities in Particle Injection Tube for Large Particles

It can be seen from either the individual velocity histories or from the averages shown in Figures 4.2 and 4.3 that, in the first fifteen centimeters below the injection point the velocities are approximately the same as that for a body freely falling in a vacuum. The velocities then tend to level off, and within 15 to 25 centimeters of the injection point the clusters approach a constant velocity. Individual clusters exhibited similar trends. However, after reaching a constant (maximum) velocity, they tend to then decelerate before breaking apart and being swept up in the gas stream.

For the range of conditions tested, the average maximum falling velocity reached by the clusters was found to be between 1.2 and 2 m/sec. The maximum falling velocity observed for individual clusters was about 3 m/sec. The main effect of higher air velocities was to reduce the percent of material moving downward in the tube and to reduce the distance the cluster fell before breaking up, but it had little effect on the maximum falling velocity of the cluster. It can also be observed that the two different particles exhibited remarkably similar behavior. This is particularly notable in view of the fact that the aluminum particles are so much larger then the silica, and have a mass more than 2 orders of magnitude greater than that of the silica particles.

Of course, these results are not directly applicable to circulating fluidized beds. Because the particle clusters were injected by the pneumatic cannon at speeds on the order of 5 m/s, they would sometimes rebound downward with initial velocities approaching 3 m/s. Although a lower initial velocity, closer to that expected for particles in free fall with no air resistance, was more common, the method of injection of the particle clusters could have influenced their subsequent motion in ways which might not be representative of cluster behavior in a CFB. To verify the relevance of these findings to CFB heat transfer, similar tests were performed using a circulating fluidized bed.

4.1.2 Macroscopic Cluster Motion in a CFB

For the purpose of measuring the cluster velocity and other important hydrodynamic parameters, a 20 cm circulating fluidized bed with transparent walls was constructed. For practical reasons, the range of conditions tested in the CFB was narrower than in the particle cluster injection tube. However, as described below, the results show no substantial differences in the cluster behavior between the two different experiments.

4.1.2.1 Experimental Apparatus and Procedure

Figure 4.4 shows a schematic of the 20 cm circulating fluidized bed. Air is admitted at the bottom of the riser by four large bubble caps. Low pressure steam may be injected into the air supply line for humidification, if necessary. Particles also enter near the bottom of the riser via the 15 cm horizontal leg of the L-valve. The riser is about 7 m high, but due to lack of space at its upper end, it makes a 180-degree bend down to the cyclonic particle separators, which are located about 4 m above the bottom of the riser. A bag filter downstream of the cyclones prevents any particles from being exhausted. The outlets of the two cyclones both feed into the top of a 15 cm downcomer, whose bottom end makes up the vertical leg of the L-valve. A butterfly valve is located near the top of the downcomer for measuring the particle circulation rate, with a small bypass line in place to maintain the pressure balance in the bed when the butterfly valve is closed.

The main air supply was controlled by a gate valve and measured by an orifice plate flow meter in the supply line. The accuracy of the gas flow measurement depended on the

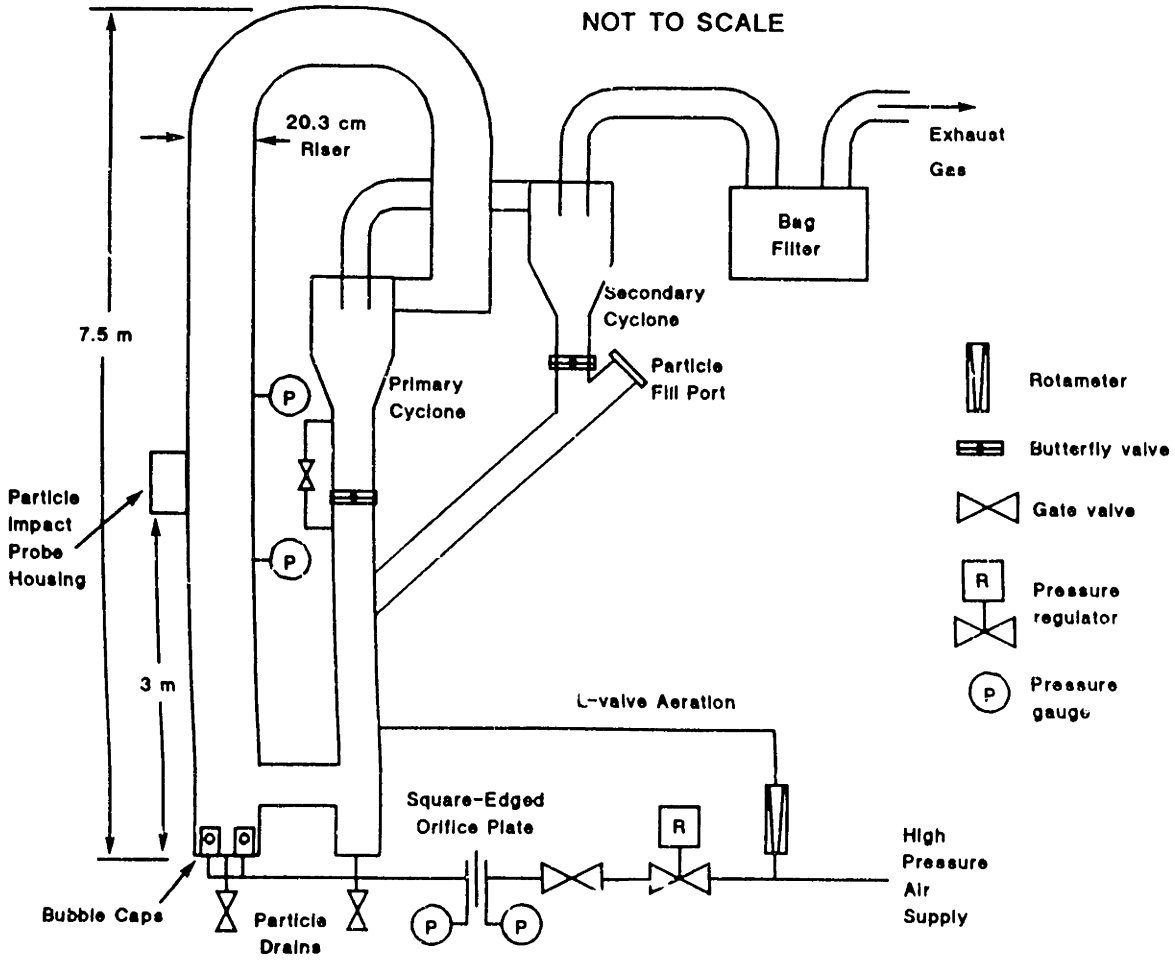

Figure 4.4 - 20 cm Circulating Fluidized Bed Facility

operating condition; at high particle circulation rates and low gas velocities, conditions similar to slugging in the bottom of the bed led to unsteady gas flow rates. However, at normal, steady operating conditions, the uncertainty of the superficial gas velocity was no greater than 0.1 m/s. The rate of aeration to the L-valve was both controlled and metered by a rotameter. Since the L-valve aeration was always less than 1% of the main air flow rate, it was ignored in calculating the superficial gas velocity. The particle circulation rate was measured by timing the rate at which solids collect above the butterfly valve in the semi-transparent downcomer with the butterfly valve closed. Pressure taps are located at approximately 1 m intervals along the riser for measuring the

bed pressure gradient. The cross-section average bed density was assumed equal to the bed pressure gradient. As with the superficial gas velocity, the accuracy of the measurement of the pressure gradient depended upon the operating conditions. The accuracy of the reported values for bed density are generally about ±10%.

The particles used in the CFB for these tests were glass beads with a surface mean diameter of 88μm. The particle characteristics are detailed in Appendix A. A video camera and VCR were used to record the motion of clusters within the CFB, which was illuminated from the opposite side of the bed. The velocity of clusters was determined by a frame-by-frame analysis of the video record, similar to that performed for the particle cluster injection tube tests. The bed was operated at superficial gas velocities between 2.9 and 4.3 m/s, and at bed densities ranging from 4.5 to 14.8 kg/m_3. At higher densities, it became difficult to obtain adequate lighting conditions so that particular features of a cluster could be identified in sequential frames.

4.1.2.2 Results and Discussion

Figures B.10 through B.13 in Appendix B shows the plots of velocity vs. location for each of the particle clusters which was examined. Since the clusters did not arrive at the wall and start to move downwards at any particular or discernible position, the location of the clusters as plotted is a relative measure, referenced only to the field of view of the video camera. As shown in the figures, the cluster move down the wall at velocities ranging from about 0.3 to nearly 4 m/s. For each cluster, an average velocity was determined from the total distance which it was tracked within the video record. The

mean velocities are in the range of 1 to 2 m/s, similar to the cluster velocity measurements which other researchers have made.

As discussed in Section 3.3.1, it is possible to estimate the time of contact between the cluster and the heat transfer surface if the velocity of the cluster is known. Furthermore, since the order of magnitude of ε_c is also known (see Section 3.4), one can estimate the emulsion heat transfer coefficient, h_e, using Eq. 2.3. Table 4.1 shows the resulting estimates of h_e using the representative values for ε_c of 0.9 and 0.5, respectively, for heat transfer surfaces of various lengths.

Length of heat transfer surface (cm)	Time of contact (s)	Emulsion heat transfer coefficient (W/m^2-K)		Measured wall heat transfer coefficient (W/m^2-K)
		ε_c=0.5	ε_c=0.9	
1	0.01	1836	1022	200-400[1]
10	0.1	580	323	100-200[2]
100	1.0	184	102	50-150[3]

Table 4.1 - Comparison of h_e to h

In constructing Table 4.1, the cluster velocity was assumed to be 1 m/s, and particle properties typical of sand were used. Also shown in the table is the range of heat transfer

[1] Wu, Lim and Grace (1989a)

[2] Kobro and Brereton (1986)

[3] Furchi et al. (1988)

coefficients measured using heat transfer surfaces of the given length. The values shown were those measured at relatively high bed densities, so that the corresponding fractional wall coverage (f) is expected to be very nearly equal to unity (see Section 3.2). Therefore, according to Eq. 2.1, the measured heat transfer coefficients should be a good estimate of the heat transfer coefficient from the cluster, h_c.

According to Eq. 2.5, repeated below, the cluster heat transfer coefficient comprises a wall resistance, represented by h_w, in series with the emulsion heat transfer coefficient.

$$h_c = \left[\frac{1}{h_w} + \frac{1}{h_e}\right]^{-1} = \left[\frac{\delta d_p}{k_g} + \sqrt{\frac{\pi t}{k_c c_{p,s} \rho_s (1-\epsilon_c)}}\right]^{-1} \qquad (2.5)$$

Referring to Table 4.1, it is apparent that the wall resistance is an important factor in the overall heat transfer at short to moderate contact times. Even for relatively long contact times, the data of Furchi et al. (1988) shows a strong dependence of the heat transfer coefficient on the particle diameter. This implies that the wall resistance can be an important component of h_c for relatively long heat transfer surfaces.

In order to accurately estimate the wall resistance, it is necessary to know how far the particle clusters are from the wall (see Section 3.1). The next stage of the experimental work was undertaken to examine this parameter in detail.

4.2 Microscopic Cluster Motion in a CFB

The specific goal of this phase of the experimental work was to accurately measure the distance, δ, between the particle clusters and the wall of a CFB, so that the wall resistance could be estimated with some degree of confidence. It was also hoped that a greater general knowledge of the characteristics and behavior of particle clusters near the wall would be gained.

An indication of δ was determined in the experimental work of Glicksman, Lints and Katoh (1990). This experiment consisted of micrographic video recordings taken from the interior of a CFB next to and perpendicular to the wall. A schematic of the apparatus used is shown in Figure 4.5. Images were recorded in the 20 cm CFB while operating at densities between about 25 and 60 kg/m^3 using 88 μm glass beads. The clusters appear as bright, hazy bands which vary in both their intensity and their prevalence. The clusters tended to appear brighter and more frequent as the bed density increased. These trends are consistent with the discussions in Sections 3.2, which describes an increase in the fractional wall coverage at higher bed densities; and in Section 3.4, which shows evidence of increased cluster solids concentrations at the wall at higher bed densities.

Figures 4.6 and 4.7 show sample images taken from the micrographic video recording. Figure 4.6 shows a cluster of particles near the wall, which is the dark region occupying the right side of the frame. The scale of the image is such that the total vertical height depicted is about 12 mm. It appears that the thickness of the cluster in Figure 4.6 is

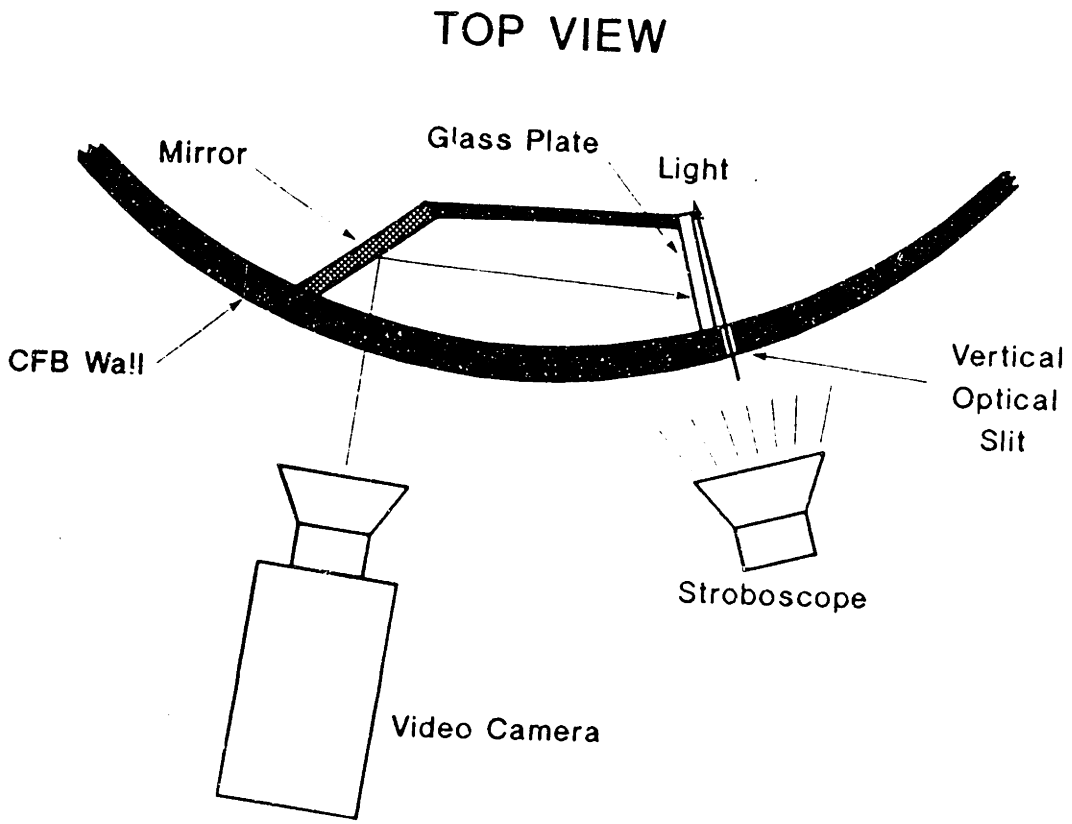

Figure 4.5 - Micrographic Video Experimental Apparatus

approximately 2 mm. The image resolution is not sufficient to allow direct measurement of the distance between the clusters and the wall from the video recording.

Figure 4.7 shows a similar view, but with a small, square-edged step 100 μm in thickness applied to the wall. The step, which is in about the middle of the frame, does not show clearly, but its effect on the particle clusters is very evident. As shown in Figure 4.7, the clusters were often deflected away from the wall by the step. This is seen in the figure as a displacement of the bright band (cluster) to the left, away from the wall. The deflection of clusters seemed to be more common and more pronounced as the bed density increased. Based on this behavior, the following observations may be made:

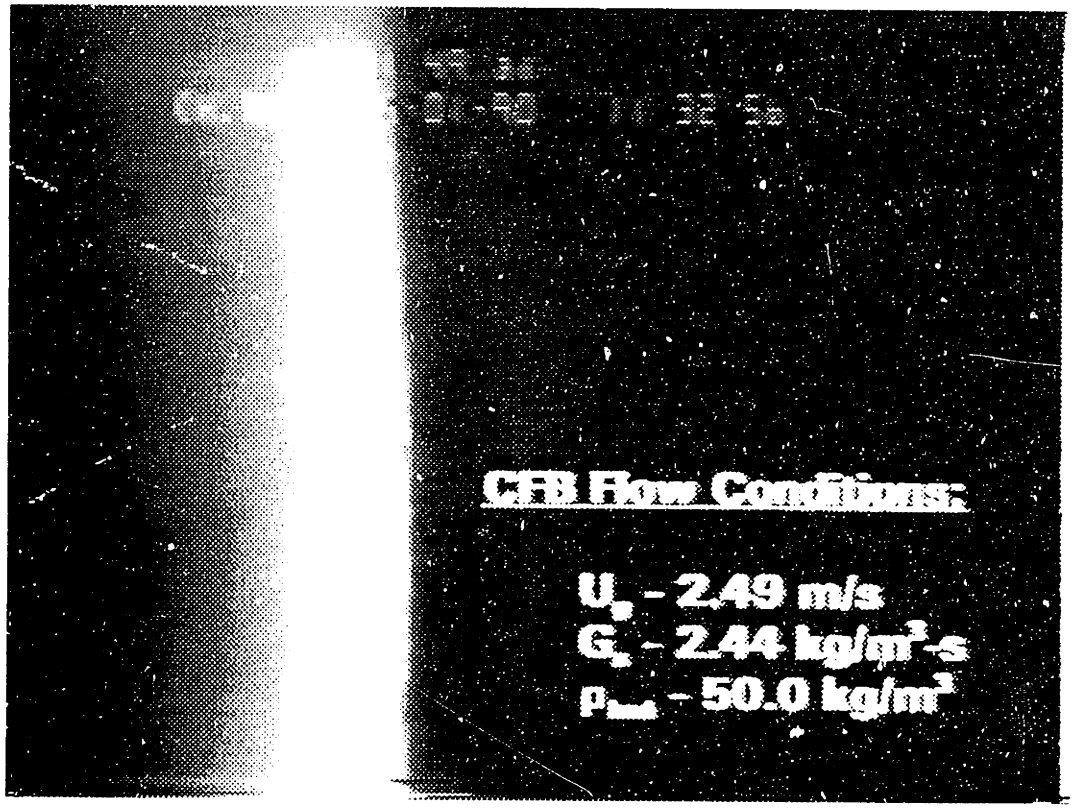

Figure 4.6 - Micrographic Video Image of Cluster at Wall

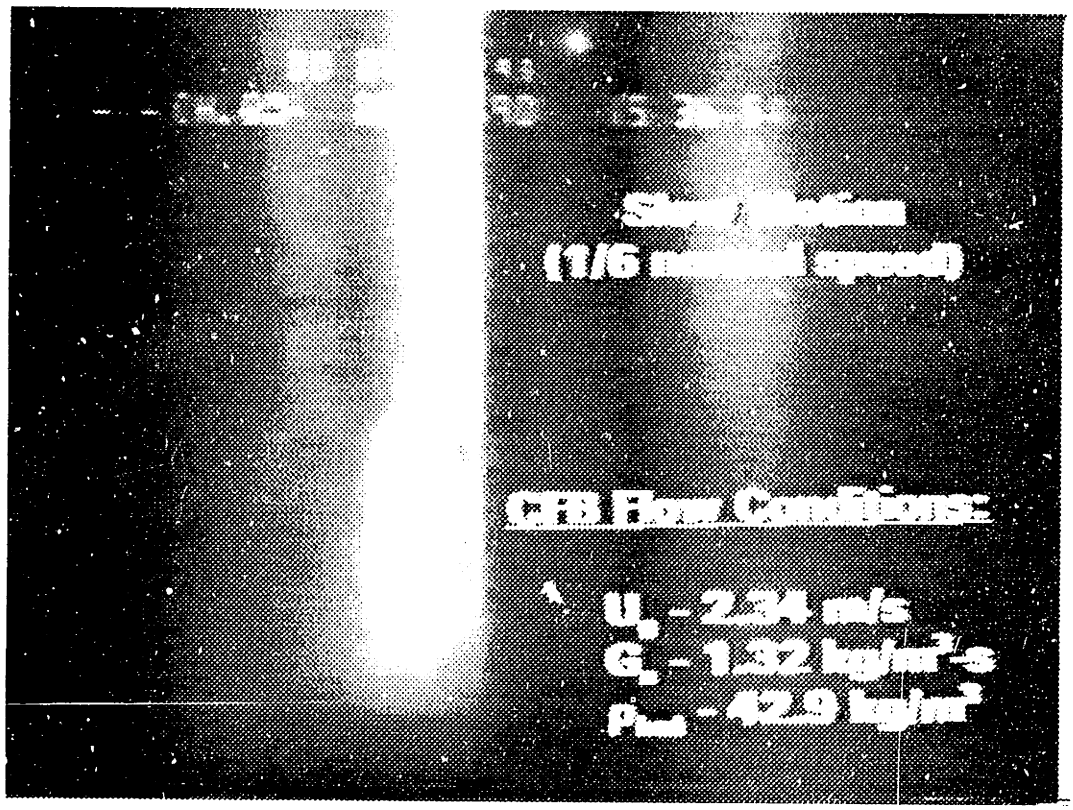

Figure 4.7 - Micrographic Video Image of Cluster at Wall with Step

1) the minimum value of δ is less than or equal to one, and 2) δ exhibits some variability both for a given bed operating condition and between different operating conditions. A more precise means of measuring δ was developed in order to quantify these somewhat general observations.

4.2.1 Experimental Apparatus

The method which was developed to sense the particles within the CFB and to measure the distance between the particles and the wall is a particle impact probe. The probe consists of a phonograph needle attached to a magnetic cartridge which enters the bed through a small hole in the wall. When particles strike the needle, a signal is generated by the cartridge which is then amplified and recorded. The probe is mounted on a linear translation stage in order to control precisely its location relative to the wall of the bed. A schematic of the apparatus is shown in Figure 4.8; a more detailed description of it follows.

The phono cartridge used for the impact sensor was a Digitrac 300 SE, a moving magnet-type cartridge with a frequency response of 20 Hz - 20 kHz. The needle and cartridge as supplied have a dynamic lateral compliance of 35 μm/Mn and an output voltage at 1 kHz of 4mV @ 5 cm/s. However, the needle was modified for use in the sensor by grinding off the stylus and polishing the end of the needle to obtain a square-edged cylindrical tube 0.6 mm in diameter. The original distance from the pivot point of the needle to the stylus was about 5 mm; the modified needle is roughly 3.5 mm long measured from the pivot point. The compliance and output specifications of the modified

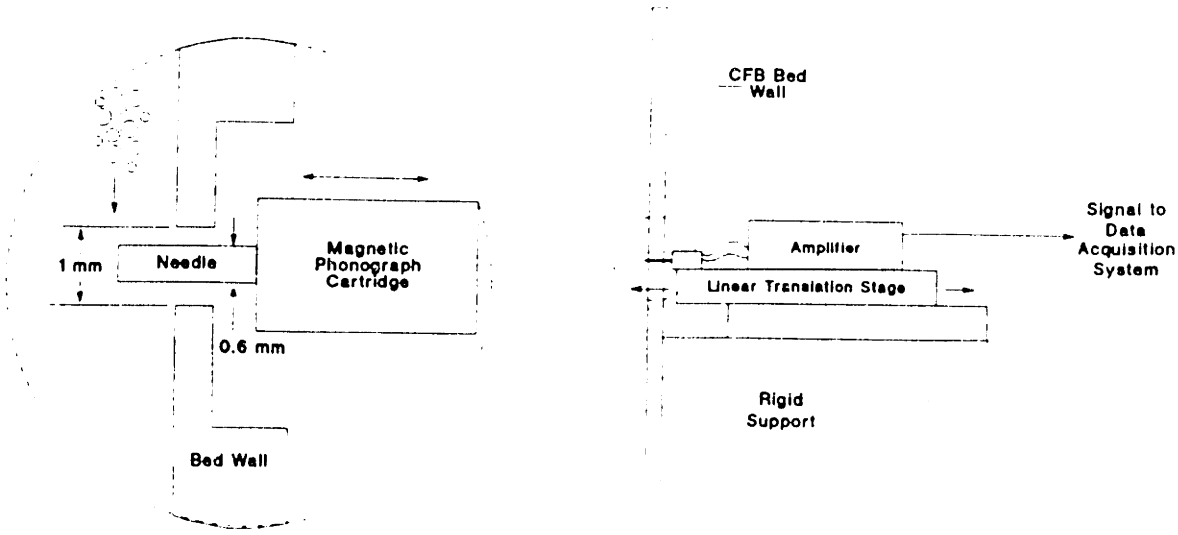

Figure 4.8 - Particle Impact Probe Experimental Apparatus

needle will vary accordingly.

Quartz sand particles of 182 μm mean diameter were used for the impact probe testing (particle characteristics given in Appendix A). Particles striking the needle generate a very low signal level, typically 0.2 to 1.0 mV, depending upon the size and velocity of the particle. To minimize the noise level in the signal, the amplifier was mounted as close to the cartridge as possible. The amplifier was constructed from op amps (LF353N) configured as an AC voltage follower and two subsequent amplification stages with a total gain of 1000, followed by an RC high-pass filter. Both the amplifier and the

needle/cartridge assembly were mounted on a single-axis linear translation stage (Newport #420-05) with a resolution of 1 μm.

The signal from the amplifier was connected to an oscilloscope for real-time monitoring of data. It was also connected to a data acquisition system (DAS) to record the signal for later analysis. The DAS consisted of an IBM AT with a MetraByte DASH-16 12-bit A/D board. Data was collected using the STREAMER software operating on one channel at 100 kHz.

4.2.2 Calibration of Particle Impact Probe

The amplifier was calibrated by providing a small sinusoidal signal of varying frequency at the input and measuring the resulting output. It demonstrated a flat gain of 60 dB up to a frequency of about 20 kHz. Since 20 kHz is the highest specified frequency response of the needle and cartridge, this was considered adequate performance.

The position of the needle relative to the wall was calibrated by two methods: brushing the interior wall of the bed with a stiff piece of cardboard as the needle is slowly advanced through the opening in the wall; and holding a flat, polished metal disk 3 mm in diameter over the opening, such that the axis of the disk was aligned with the axis of the opening, again as the needle is advanced. In each case, the location at which the needle first generates a signal is taken as being flush with the wall. Since the acrylic wall of the bed is stiffer than the cardboard, the cardboard could flex into the opening in the bed wall to some extent, and contact the needle before it was flush with the wall. On the

other hand, the flat metal disk was too stiff to bend, and must have bridged the cylindrical surface of the bed wall to a certain degree. Considering the geometry of the arrangement, with the inside wall of the bed assumed to be perfectly cylindrical, the center of the 3 mm disk would remain 5 μm away in the radial direction from the edge of the 1 mm opening in the bed wall, so that the needle would have to emerge about 5 μm from being flush with the bed wall in order to contact the metal disk. Therefore, these two tests should give the upper and lower limits of the actual zero point, where the tip of the needle is precisely flush with the inside surface of the bed wall. The minimum difference expected between the two measurements was 5 μm, and it should be greater than 5 μm by an amount equal to the distance which the cardboard would flex below the surface of the wall opening.

The calibration of the position of the needle was performed before and after each set of tests. It was found that the difference in the zero points measured by these two methods varied from 5 to 15 μm, and was usually very close to 10 μm. This was consistent with the expected value, and the average value was taken to be the actual zero point. The resulting uncertainty in the location of the tip of the needle relative to the inside surface of the bed wall is roughly 5 μm.

4.2.2.1 Probe Sensitivity to Particle Collisions

A test was then conducted to determine the sensitivity of the probe to particle collisions. A semi-circular channel was attached to the wall of the bed, centered over the opening for the impact probe. About 10 cm above the probe, a funnel feeding into the top of the

channel was also attached to the wall. When particles were poured into the funnel, they would flow down through the channel in a dense stream. If the impact probe was then advanced into the flow stream, collisions with the particles could be recorded. Figure 4.9 shows a schematic of the experimental apparatus; Figure 4.10 shows a sample trace of the resulting probe signal which contains several particle collisions. Two of the particle strikes, denoted by the letter "A", are easily distinguishable by their peak amplitudes, which are much higher than the background noise level. However, there are three other particle strikes shown by the letter "B" in Figure 4.10 which are evidenced more by the periodicity of the signal than by the amplitude.

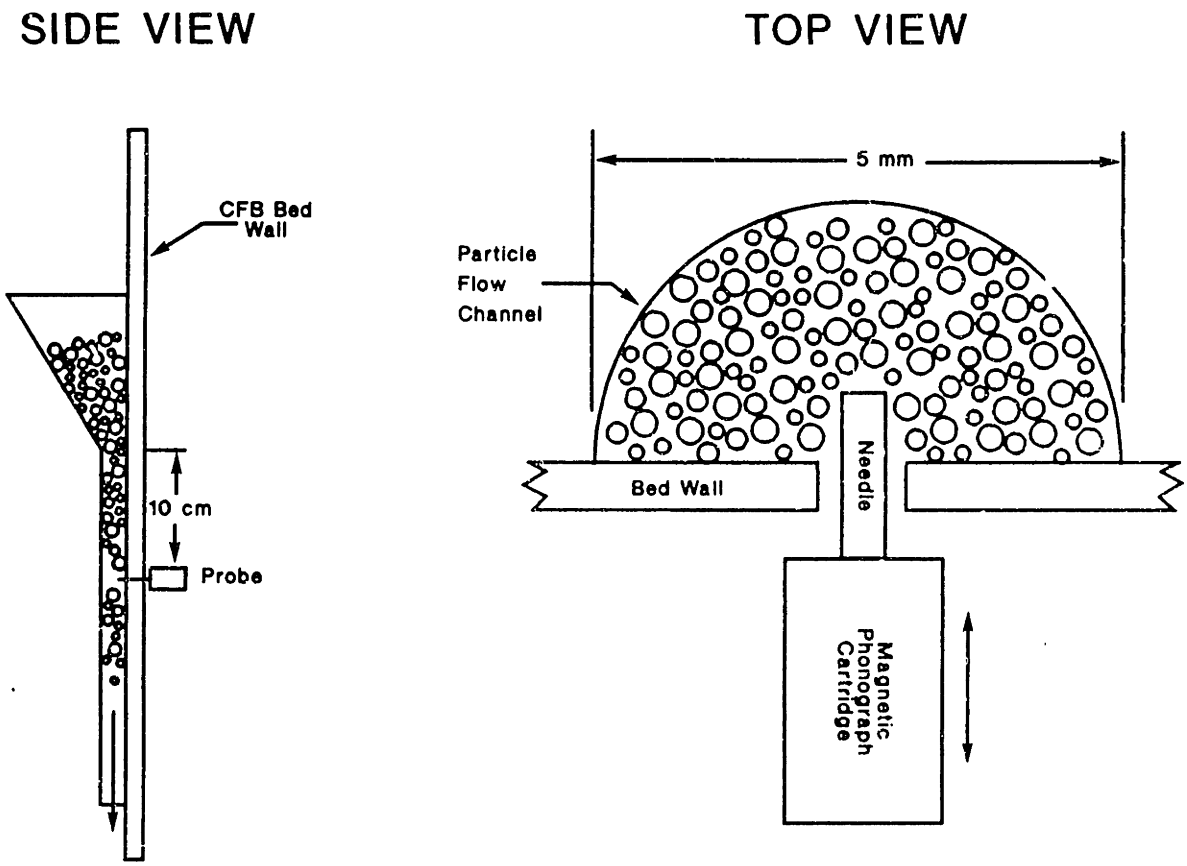

Figure 4.9 - Calibration Set-Up for Particle Impact Probe

In order to distinguish such low-amplitude strikes from the background noise, the signal was analyzed using a sliding 16-point FFT window. In other words, a discrete FFT was performed on the first 16 data points of the signal. Then, the first data point was dropped from the set of 16 and the next data point (the seventeenth) was added to the set. An FFT was then made for those 16 points. The process continued, such that each sequential set of 16 points had an FFT performed on it; and each data point, except those near the beginning or end, was a part of 16 such sequential sets of points. The computer program to perform this analysis is given in the appendix. Since the sample period for the signal was $(100 \text{ kHz})^{-1} = 10^{-5}$ seconds, the frequency step for the discrete transform was (16 ×

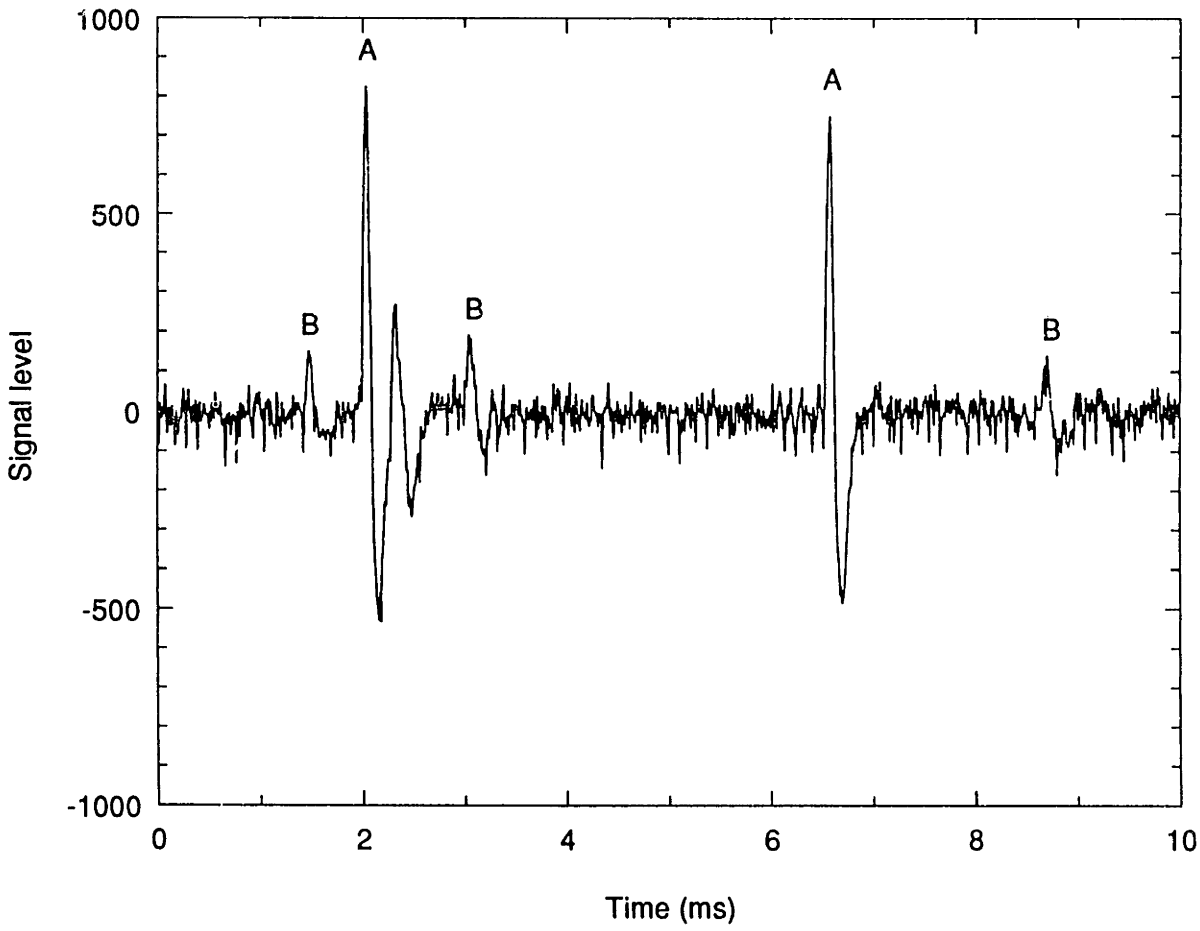

Figure 4.10 - Sample Signal Output of Particle Collisions on Impact Probe

10^{-5} s)$^{-1}$ = 6.25 kHz [Press et al. (1989)]. This is very close to the observed frequency of the signal due to a particle strike, so the amplitude of the lowest discrete frequency of the FFT's was examined to locate particle strikes.

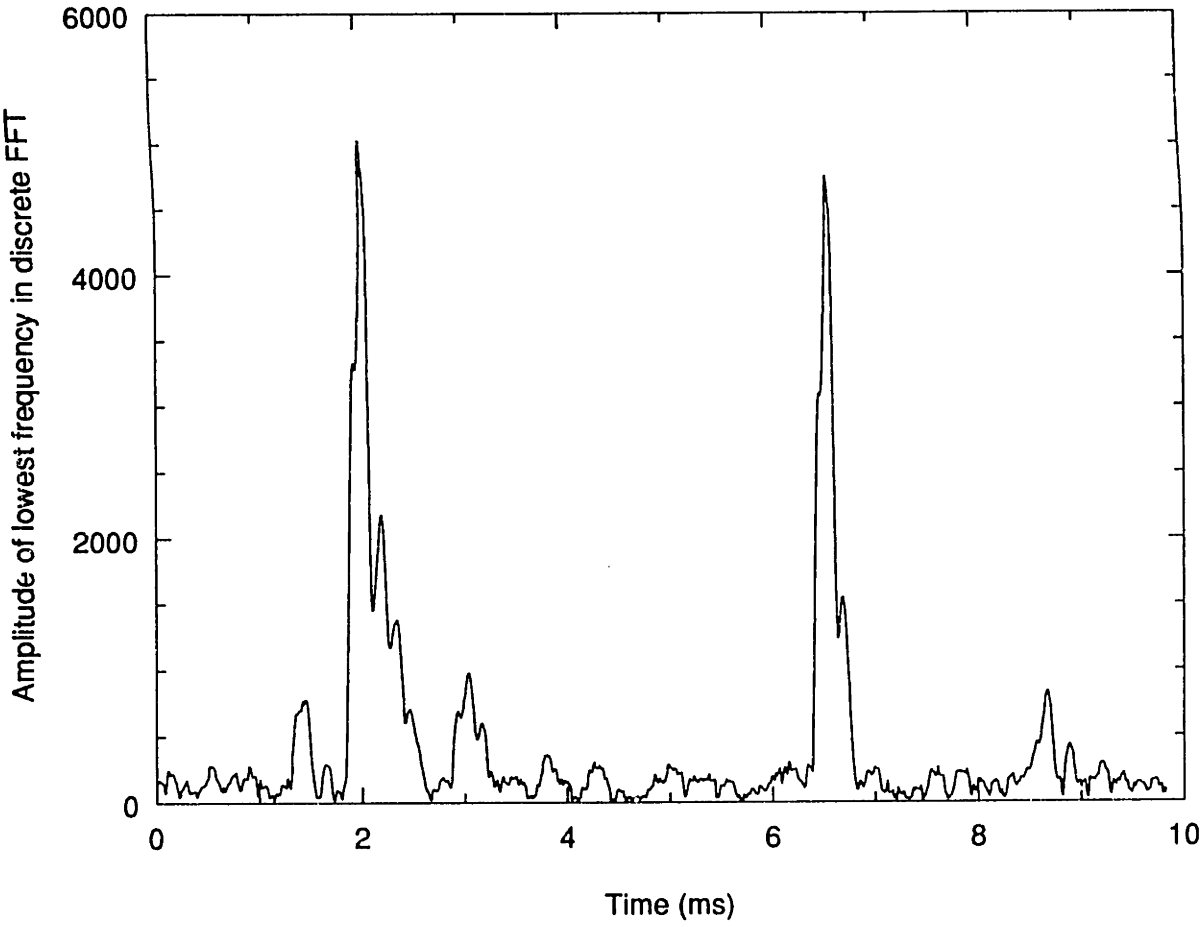

Figure 4.11 - Discrete FFT Analysis of Sample Signal Output

Figure 4.11 shows the FFT output corresponding to the sample signal of Figure 4.10. The two large-amplitude strikes show very clearly, but it is also possible to locate the three low-amplitude particle strikes which might otherwise escape detection by a data analysis

program. However, even with the use of the FFT algorithm to maximize the sensitivity to particle strikes, the possibility still remained that either small or slow particles striking the needle could not be counted.

To examine this possibility, a series of tests was performed, starting with the needle nearly flush with the wall and advancing it into the flow stream by a small amount (20 μm) for each subsequent test. The signal was recorded during each test, and the number of particle strikes on the needle was counted. Figure 4.12 shows the results of one such test series.

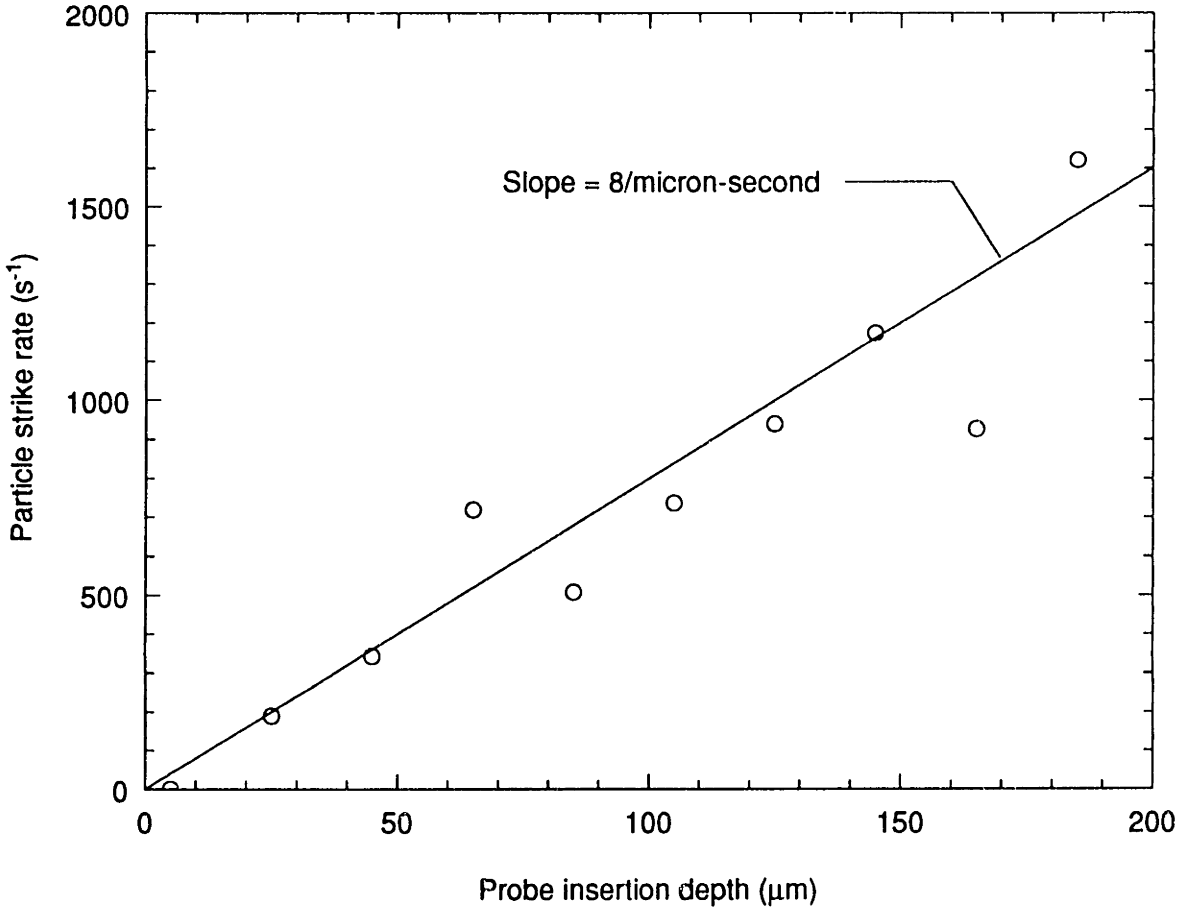

Figure 4.12 - Particle Strike Rate in Calibration Flow Channel

Two important features are evident in the figure:

1) the frequency of particle strikes is greater than zero at the smallest insertion distance greater than zero, indicating that the particles in the flow stream are very close to the wall, and

2) although there is scatter in the data, the particle strike rate increases roughly linearly with the probe insertion depth, implying that the particles are uniformly distributed in the flow stream near the wall.

The mass flow rate of particles through the channel during these tests was measured at 3.6 g/s; the corresponding specific mass flow rate is roughly 360 kg/m^2-s. From the particle sieve analysis, the particle number density is found to be 2.8×10^8 kg^{-1}. Since the flow area swept by the probe is equal to its diameter (0.6 mm) times its insertion depth, the rate of particle strikes/unit insertion depth is given by:

$$(360\,kg/m^2\text{-}s)\,(2.8\times10^8/kg)\,(0.6\,mm) \approx 60/\mu m\text{-}s \qquad (4.3)$$

This result is nearly an order of magnitude greater than the slope of the data in Figure 4.12. A further set of tests was performed to examine this discrepancy.

The same type of test as described above was performed using samples of the same sand particles which were size-classified by sieving. Particle strike rates were measured for each size of sand particle at two insertion depths, 50 μm and 100 μm, and the mass flow rate through the channel was also measured for each particle size. The differences in the particle strike rates at the two insertion depths was then compared to the value predicted

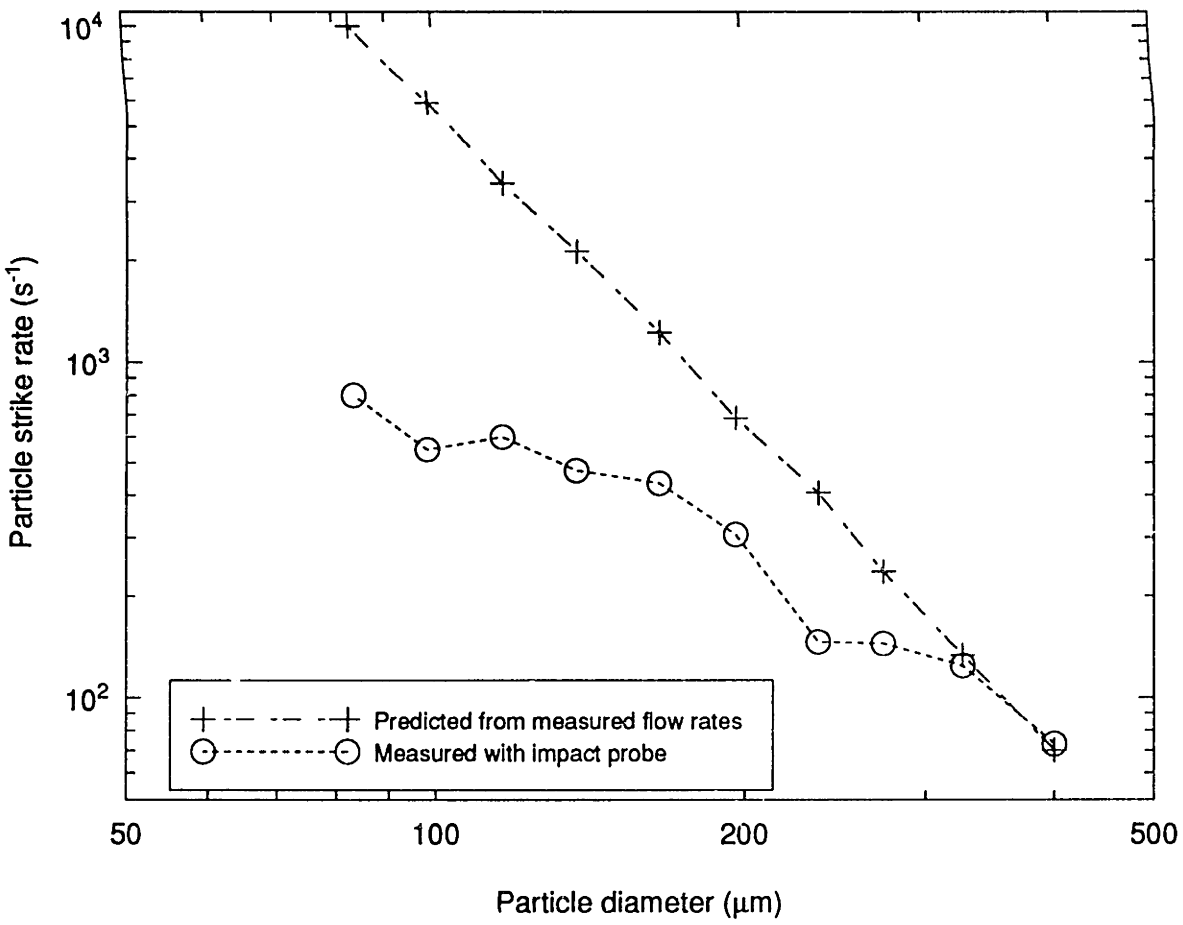

Figure 4.13 - Comparison of Measured and Predicted Particle Strike Rates

by a calculation similar to Eq. 4.3. The results are shown in Figure 4.13.

This technique of taking the difference between two insertion depths was followed in order to minimize any variations in the measurement due to non-uniformity of the particle flow stream near the wall. The technique appeared to work well, judging by the close agreement between the measured and predicted strike rates for the largest size particles evident in Figure 4.13. However, as the particle size decreases, the impact probe measures a decreasing fraction of predicted particle flow rate. There seems to be at least two reasons for this trend. The first is obvious, that smaller particles have less mass and

therefore less kinetic energy at a fixed velocity to impart to the needle. The resulting signals are more difficult to differentiate from the background noise level of the sensor, so that only the largest and fastest particles which impact the most directly can be counted.

A second reason for undercounting the smaller particles is that there is a bias toward such undercounting at higher strike rates inherent in the measurement technique. For example, looking at Figure 4.10, the second large-amplitude particle strike (in addition to many others which were recorded) shows that the needle has a rather high damping ratio, and that a single particle strike will drive the signal through a single up-down cycle before returning to the level of the background noise. However, the first large-amplitude strike in that figure shows a second oscillation. This is most probably another particle strike, following closely behind the first, but it is difficult to distinguish as such with the FFT analysis (see Figure 4.11). As particles strike the needle at increasing rates, it becomes more difficult to distinguish each individual particle strike.

A close examination of the output from the probe shows that the frequency of oscillation of the needle due to a particle strike is about 5 kHz (see Figure 5.10 and accompanying discussion). Theoretically, this is the maximum rate at which particle strikes could be detected. However, since the impacts are not evenly spaced, the signals from sequential strikes begin to overlap one another, and thus cause undercounting of the total number of particle strikes, at average strike rates which are well below the theoretical maximum.

For whatever reason, it appears from the results shown in Figure 4.13 that a large fraction of the particles pass by the probe undetected, and that it is either not quick or not sensitive enough to count all the particle collisions with the needle. Even so, most of the larger particles are counted, and roughly half of the flow stream is sensed on a mass-weighted basis. If no significant amount of size-ordering occurs within the clusters in a CFB, then the probe is sufficiently sensitive to detect the passage of such clusters and thereby obtain a good deal of information regarding their motion.

4.2.2.2 Sensitivity of Probe to Purge Pressure

The last step in preparing the probe for use under CFB conditions was to enclose it within an airtight housing attached to the exterior wall of the bed. This addressed the concern that any difference in pressure existing across the opening for the probe in the bed wall might induce a flow through that opening which could disturb the normal motion of particle clusters in the vicinity. This was not a problem in the channel flow tests described in the previous section, which were conducted at ambient pressure. However, the internal bed pressure under CFB operating conditions is substantially greater than ambient. The probe enclosure was provided with a high-pressure air feed with a needle valve for flow rate control. A pressure gauge was attached to monitor the differential pressure between the enclosure and the bed interior.

Due to the fluctuating nature of the interior bed pressure, it would have been very difficult to maintain the enclosure at exactly the same fluctuating pressure. If the bed pressure was higher than the enclosure pressure, there was a tendency for particles to

lodge in the annular space between the needle and the opening in the bed wall, thus restricting the free movement of the needle in response to particle collisions. To counteract this tendency, the pressure in the enclosure was maintained somewhat higher than the pressure in the bed. It was recognized that this differential "purge pressure" would induce a flow across the opening, but it was hoped that this would have a minimal effect on the particle motion in the vicinity of the opening.

A series of tests were performed to determine whether or not the particles near the opening were affected by the flow of purge air. While operating the bed as a CFB, the probe was inserted a small distance into the bed and the particle strike rate was measured using different purge pressures. The local bed density during testing was 10 kg/m^3, and two different insertion depths were used, 20 μm and 50 μm. Figure 4.14 show the results of the testing. Although their is a large degree of variability in the data, the least-squares fits show that there is little if any dependence of the strike rate on the purge pressure within the range tested.

The variability displayed by the data is due to the random fluctuations typical of particle behavior in CFBs. The data plotted in Figure 4.14 are for sample periods of one second. Presumably, if one were to sample for a long enough period of time at given conditions and location, the variability would gradually disappear. However, because of the high sampling rates, this would also generate a great deal of data. In this work, the choice was instead made to sample at a large number of locations for a limited length of time, and to use the expected functional relationship between the probe location and the particle

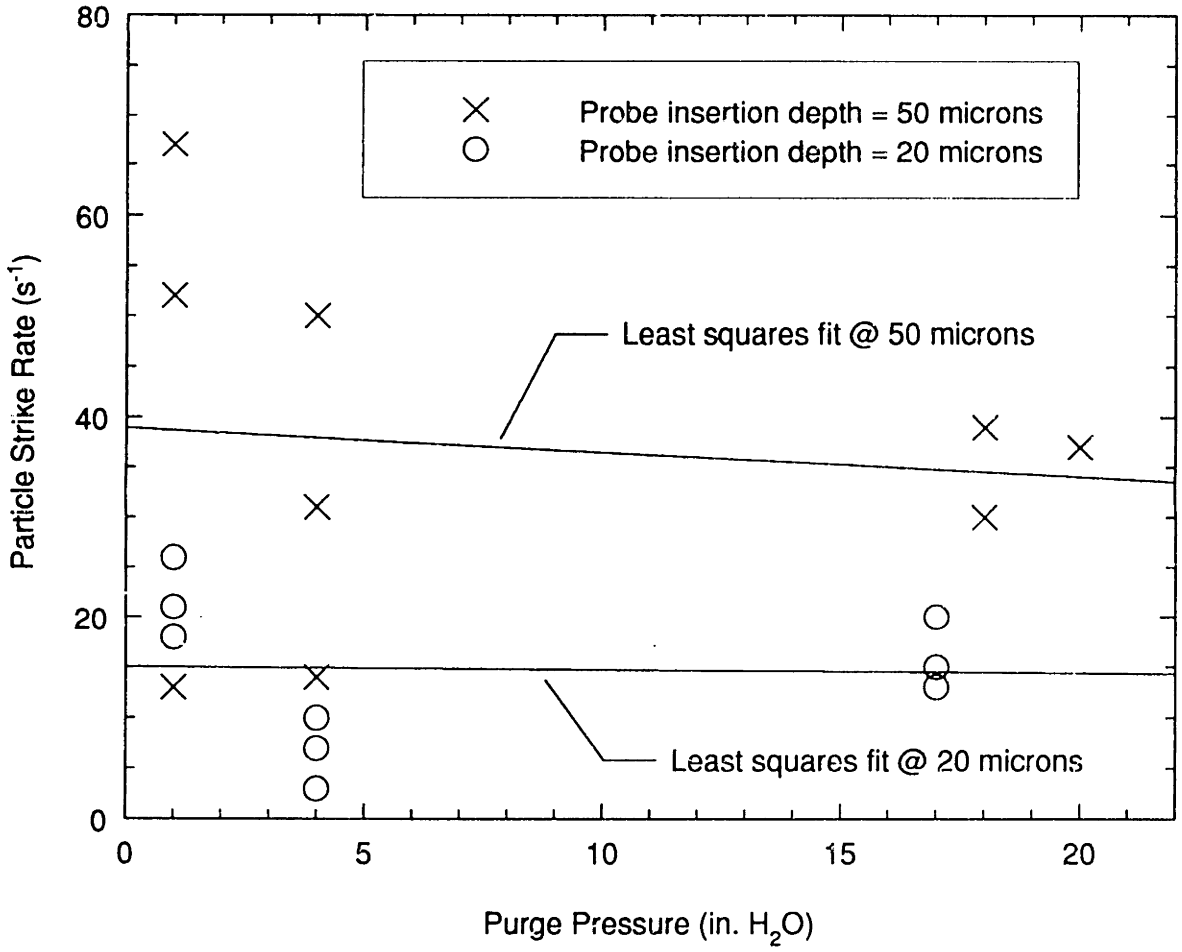

Figure 4.14 - Sensitivity of Particle Strike Rate to Purge Pressure

behavior as the basis for a statistical treatment of the resulting data. This is described further in Chapter 5.

4.2.3 Experimental Procedure

As stated previously, the primary goal of the experimental work was to determine the gas layer thickness between the falling particle clusters and the wall. Although secondary objectives were considered, the experimental procedure was developed with the primary goal in mind.

To begin the experiment, the zero position of the needle relative to the inside wall surface was found in the manner already described in Section 4.2.2. The bed was then sealed, and the desired rate of air flow was established by opening the gate valve in the air supply line. The signal from the impact probe was then recorded for use as a control to compare with signals measured later. Aeration was then provided to the L-valve and particles began to circulate into the bed. After making the necessary adjustments to obtain the desired local bed density and superficial gas velocity, the signal from the impact probe was again recorded. The probe was then advanced into the bed in small steps, with its output signal being recorded by the DAS at each step.

After the probe had been advanced a certain distance into the bed, which varied from one test to another, its motion was reversed. As the probe was withdrawn from the bed in small steps, the output signal was again recorded at each step. Finally, when the probe was back to its zero location, the particle flow was stopped by shutting off the L-valve aeration, and a control signal was again recorded. Occasionally, the particle flow was stopped and the signal recorded with the probe fully advanced into the bed. On none of these occasions was there any evidence that the needle was affected by turbulence in the air stream. Finally, the gate valve was closed, stopping the air flow in the bed.

After shutting down the bed, the access panel was removed and the zero location of the probe was re-checked. When operating at low bed densities (<20 kg/m^3), the zero position was usually changed little, if any. However, at higher bed densities, the zero position would often move, sometimes by as much as 20 μm, and always in the direction

which advanced the needle further into the bed. A visual examination of the needle under a microscope confirmed that erosion of the needle was taking place, and that such erosion was more severe when operating at higher bed densities. Also, the most severe wear was on the upper surface of the needle, that is, the leading edge with respect to particles flowing down the wall. But in spite of the erosion, the cross-sectional profile of the probe with respect to the particle flow was little changed, except for the shift in the zero position. Since this was recalibrated regularly, the net effect was to change the estimate of uncertainty in the position of the needle somewhat, increasing it from about 5 μm to 10 or 20 μm, depending on the degree of erosion (and its resultant zero shift) for the each particular experiment.

4.2.4 Data Analysis

With the DAS operating at 100 kHz, a great deal of data was generated in a relatively short amount of time. The question which then arises is how best to analyze the data in order to gain the desired information about the particle behavior. This section describes the approach which was developed in answer to that question.

Figure 4.15 shows a one-second sample of the signal from the impact probe. The horizontal axis represents time, as noted on the figure. The vertical axis represents the magnitude of the output signal from the impact probe. While it would have been possible to perform a calibration of the signal strength due to a particle collision to the kinetic energy of the particle, the wide range in size and mass of individual particles in the bed would render such information of little value. The signal strength was viewed in a binary

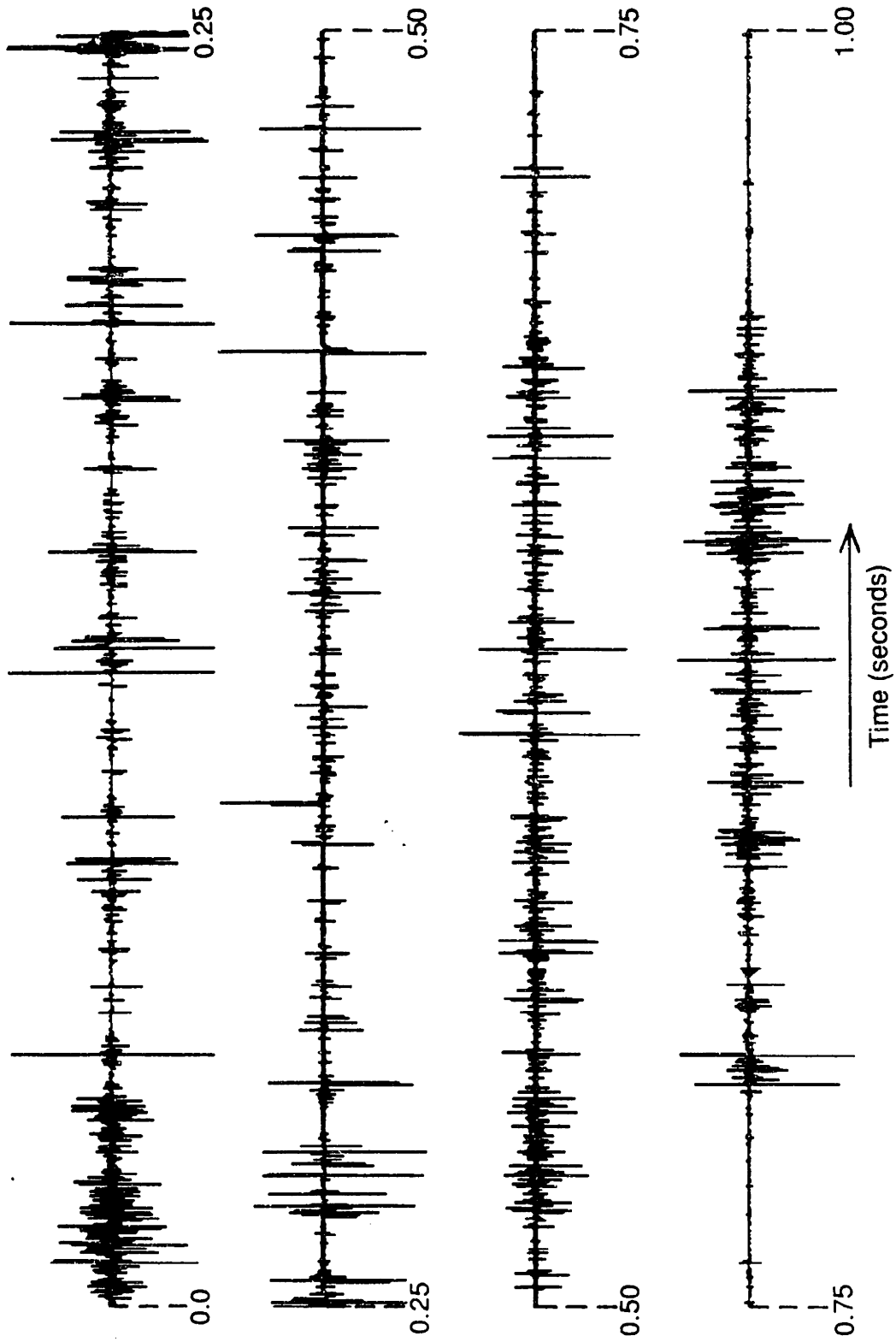

Figure 4.15 - One-Second Sample Output Signal from CFB Operation

fashion: either it was greater than the level of the background noise, indicating a particle collision; or it was not, indicating no collision at that moment. The specific criteria by which this decision was made is described in the next section.

Looking at Figure 4.14, it can be seen that the particle strike rate near the wall is small, in no case more than 70/s for the conditions in that figure. An examination of the signal traces for the tests of Figure 4.14 show individual, widely dispersed particle strikes. On the other hand, Figure 4.15, taken about 1½ particle diameters from the wall, shows hundreds of collisions in a second, often clustered together in a dense pattern of sequential strikes.

The widely dispersed individual strikes are indicative of the dilute phase flowing past the probe needle. As discussed in Sec. 3.5, the presence of particles in low concentrations within the dilute phase has important implications to the dilute phase heat transfer coefficient. However, it is the dense phase clusters which are the primary contributors to the high heat transfer rates typical of CFBs, and it is the distance between these clusters and the wall which were of primary interest in these experiments. Therefore, a means of analyzing the data to determine the prevalence of clusters was needed.

4.2.4.1 Cluster Analysis of Impact Probe Data

A software program was written to examine the data from the impact probe and calculate the temporal fraction of wall coverage by clusters, where a cluster was defined as some

minimum number of sequential particle strikes. Inherent in this definition are three parameters which must be determined:

1) the minimum signal level which represents a strike, as opposed to the background noise level,

2) the maximum time allowed between sequential strikes in order for them to be considered within the same cluster, and

3) the minimum number of such closely-spaced strikes required in order for them to be considered as a cluster.

The first of these parameters is addressed by examining both the control samples taken with gas flow but no particles in the bed (as described in Section 4.2.3), and the background noise level within the samples being studied. For example, Figure 4.16 shows the measured particle strike rate plotted against the minimum strike signal level, where a particle strike is defined as one excursion of the output signal above and then back below the minimum strike signal level. The control sample shows no strikes above a signal level of 30, with a steep increase in the apparent strike rate at lower levels. It is clear that these apparent strikes are the result of using too low a value for the minimum strike signal level, and that these spurious "strikes" represent random small spikes in the background noise and not actual particle collisions (see, for example, Figure 4.10). Similarly, the other samples plotted in the figure show a gradual increase in the strike rate with decreasing minimum strike signal levels, representing the inclusion of an increasing number of strikes of smaller magnitude, until the same signal level of 30 is reached. Below that level, the strike rate increases dramatically due to the inclusion of the spurious

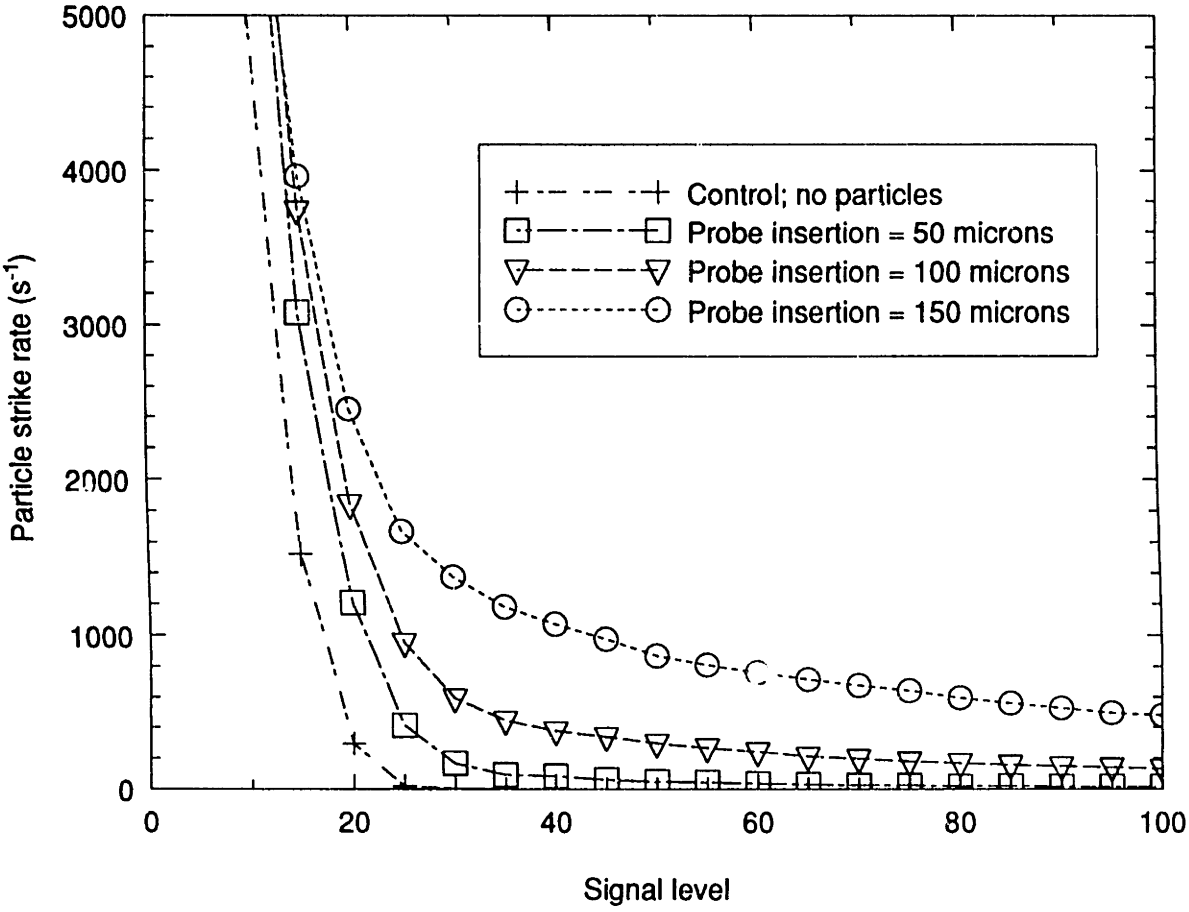

Figure 4.16 - Dependence of Particle Strike Rate on Signal Level

strikes within the background noise. In order to maximize the number of actual particle collisions sensed while minimizing the chance of counting spikes in the background noise as collisions, a value of 30 was used as the minimum strike level for this set of data. A minimum strike level was selected for each set of experiments by examining plots similar to Figure 4.16. Not surprisingly, the same value of 30 for the minimum strike level was chosen as appropriate for all of the experiments.

The second parameter in the cluster definition is the maximum time between particle strikes. This is a difficult parameter to quantify, because it depends on so many different

variables, including the particle density within the cluster, the fraction of such particles sensed by the impact probe, the velocity of the cluster, and the varying cross-sectional area of the cluster swept by the impact probe as it is moved into and out of the flow stream.

An order-of-magnitude estimate of this parameter can be obtained by referring back to the channel-flow experiments used to calibrate the impact probe (Sec. 4.2.2.1). The distance from the entry of the channel to the probe location was ~10 cm. Assuming the particle stream to be in free fall from the entry, the velocity at the probe was about 1.4 m/s. For the measured solid flux in the channel, this corresponds to a density of about 260 kg/m^3 for the particle stream, or about 10% solids. Figure 4.12 shows that the rate of change in the frequency of particle strikes with varying depth of probe insertion into the cluster is about 8/μm-s. Therefore, if the probe were to be inserted 10 μm into a cluster with the same voidage and velocity as the particle stream in the channel-flow experiments, the expected time between strikes would be (10 μm × 8/μm-s)$^{-1}$ = 12.5 ms.

The third parameter, the minimum number of strikes in a cluster, will display a similar variability. For a given cluster size, changes in the velocity or particle density of the cluster or in the probe insertion depth into the cluster will all change the number of particle strikes expected for that cluster. Horio et al. (1988) calculated an average cluster length near the wall of 10-15 mm. If this size is applied to the hypothetical cluster of the previous paragraph, it would pass by the probe in about 10 ms, and therefore at the same

solids density and velocity as the channel flow experiments, the cluster would be expected to generate no more than a single particle collision.

It is unrealistic to use a single collision as evidence of the passage of a cluster of particles, and indeed, clusters of greater density or with a deeper probe insertion depth should generate more than a single strike. Since the parameters of the cluster analysis depend upon so many variables, a sensitivity analysis to those parameters was considered essential. As a starting point, suppose that the minimum cluster length is 6 mm in the flow direction, and that they move at 0.6 m/s; then the time for the passage of the cluster past the probe is 10 ms. Suppose further that the signal from the cluster is required to have at least 5 strikes, then the average time between strikes within the cluster will be 2 ms. This set of assumptions leads to an operational definition of a cluster as follows: any group of five or more sequential strikes which are separated one from another by no more than 2 ms. It is recognized that this definition may have shortcomings; however, it provides a reasonable reference point for the sensitivity analysis.

Figure 4.17 shows the results of variations in the minimum number of particle strikes in a cluster using a maximum time between strikes of 2 ms. The data of Figure 4.17 was taken at a bed density of 30 kg/m^3 and with a superficial gas velocity of 3.6 m/s, with the probe insertion depth varying between 0 and 300 μm. It shows that the effect on the calculated wall coverage by clusters due to changing the minimum number of particle strikes is not large, at least within the range of three to ten particle strikes per cluster. This implies that when the wall is covered by clusters, it is usually covered by clusters

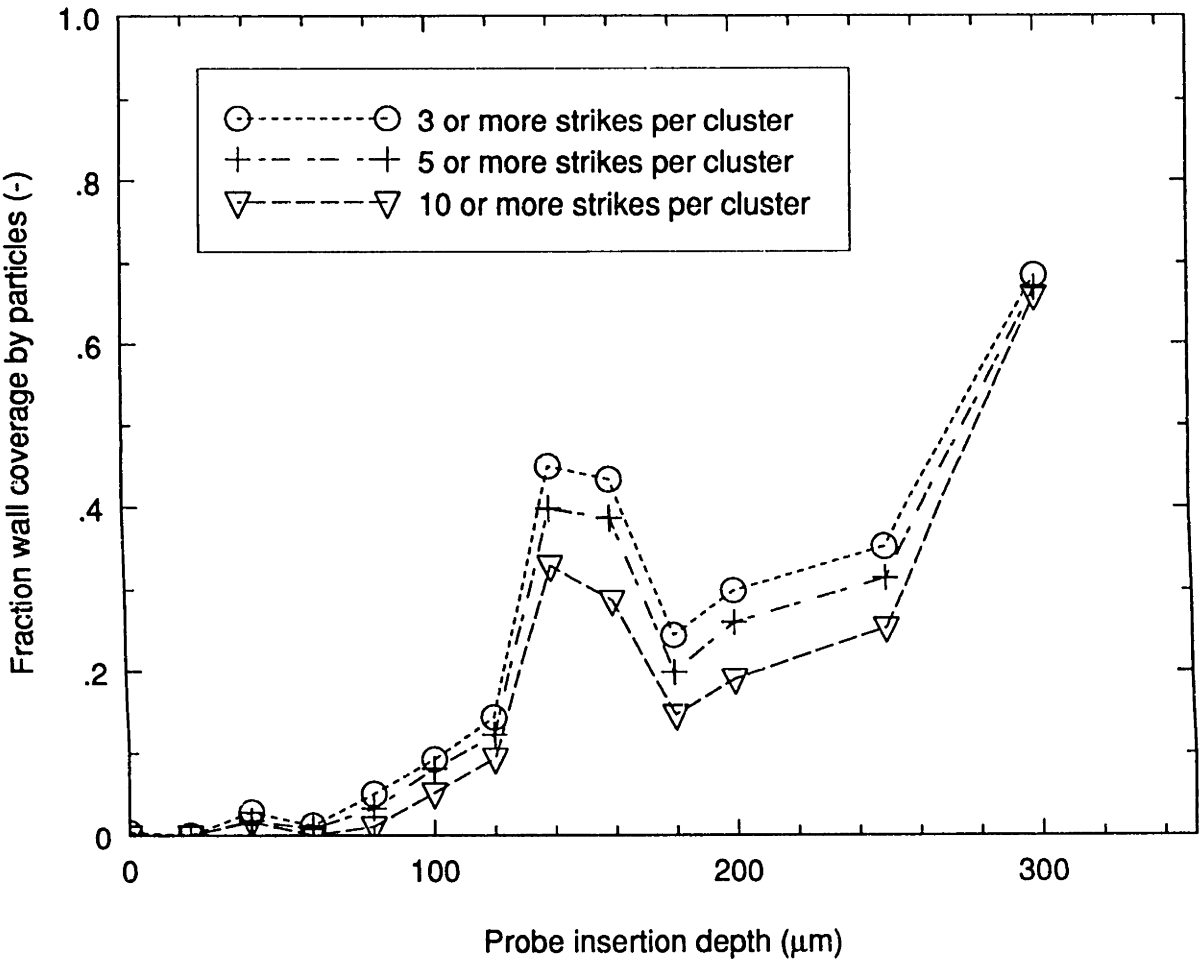

Figure 4.17 - Dependence of Fractional Wall Coverage by Cluster on Minimum Number of Strikes per Cluster

which contain at least ten particle strikes. Since the cluster analysis appears relatively insensitive to the minimum number of particle strikes, a value for this parameter of five will be assumed for use in the rest of the work related to cluster coverage.

It is more difficult to select an appropriate value for the maximum time between strikes within a cluster. Figure 4.18, which uses the same sample data as Figure 4.17, shows that the calculated fraction of time that the wall is covered by clusters is rather sensitive to the value of this parameter. In this case, the value selected requires careful justification.

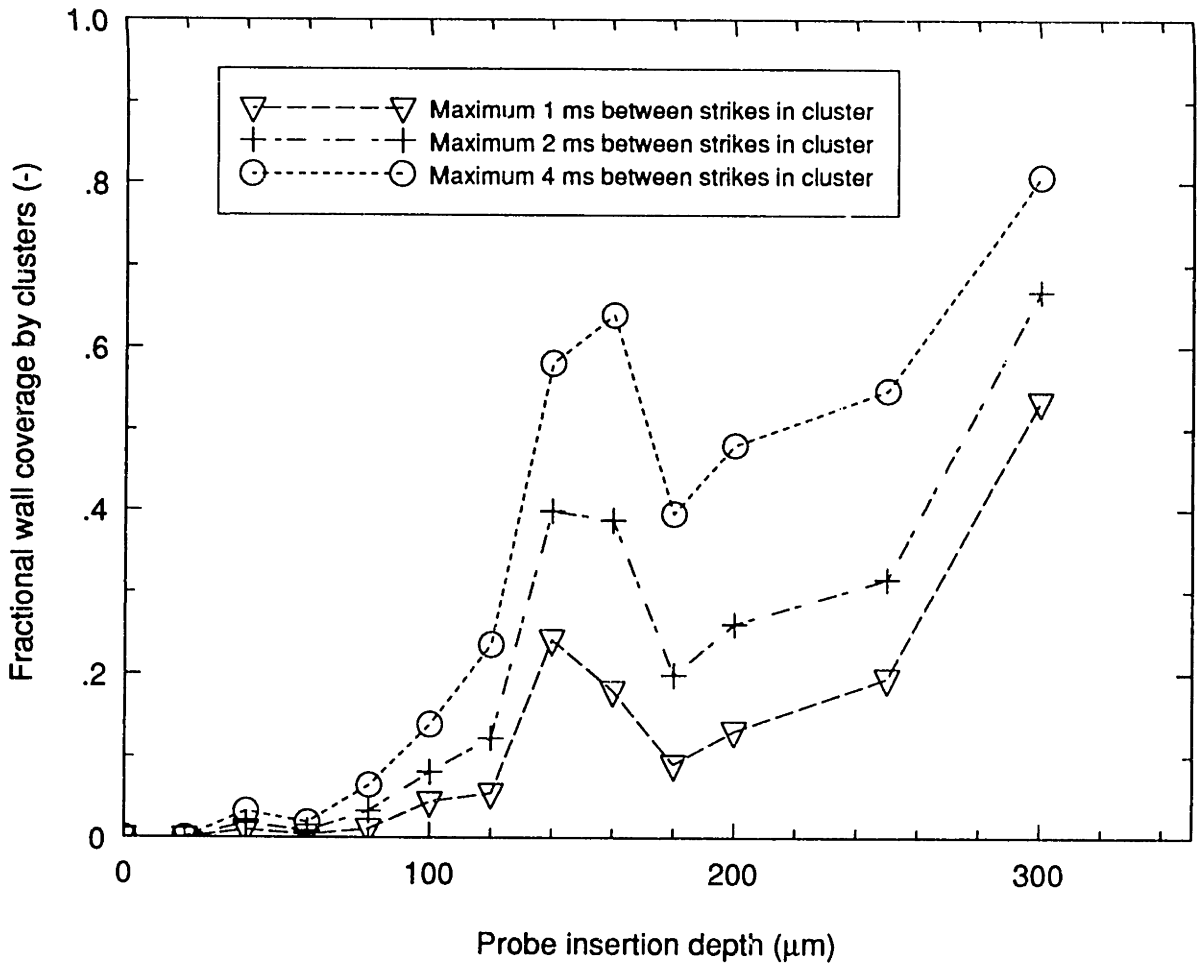

Figure 4.18 - Dependence of Fractional Wall Coverage by Clusters on Maximum Time Between Strikes in Cluster

There are several reasons for considering the lower value of 1 ms as too restrictive, and for opting instead to use one of the higher values for the maximum time between strikes.

In Chapter 5, these data are fit to a model which provides estimates of the wall gas layer thickness, δ, and the cluster wall coverage, f. If a value of 1 ms is used for the maximum time between particle strikes in a cluster, then the resulting values of f are lower than those previously reported in the literature (see Sec. 3.2). Also, the resulting values of f appear too low based upon a visual examination of the sample signal traces.

Finally, the initial order-of-magnitude estimate for this parameter was 12.5 ms. As discussed previously, this value will be inversely proportional to the insertion depth of the probe into the flow path of the cluster. In order to maximize the sensitivity of the measurement to the location of the edge of the clusters near the wall, one must minimize the depth into the cluster which the probe must penetrate before sensing the cluster. In terms of the data analysis proposed here, this means using the largest reasonable value for the maximum time between strikes in the cluster.

For these reasons, a value of 1 ms is too low to be used for the maximum time between strikes within a cluster. A value of 4 ms for this parameter is expected to provide the best data for subsequent determination of the gas wall layer thickness. However, this choice will also have important implications for the estimate of the fractional wall coverage by clusters derived from the data, as well as the cluster void fraction. As these heat transfer parameters are developed from the experimental data in Chapter 5, their sensitivity to the value used for the maximum time between strikes will be considered.

Chapter 5

Results and Discussion

The data gathered by the experimental program described in the previous chapter contains a great deal of very detailed information regarding the behavior of particles near the wall of a CFB. These results have important implications for each of the parameters in the heat transfer model. These parameters will be re-examined, and the significance of the experimental results to each of them will be discussed. However, due to the random fluctuations exhibited by the experimental data, it is first necessary to develop a statistically-based model to describe the coverage of the wall by particle clusters.

5.1 Model of Cluster Wall Coverage

The pattern of cluster wall coverage displayed in Figure 4.18 is typical of those for all the experimental operating conditions. In each case, there are essentially no clusters very close to the wall. As the probe is advanced into the flow stream, it begins to sense clusters striking it. The proportion of time during which the probe senses clusters increases as it is advances further into the flow stream. If the probe goes far enough away from the wall, the fractional wall coverage by clusters appears to reach a maximum value, and further penetration by the probe results in no further increase in this value.

This description is consistent with a physical model which assumes a layer of gas near the wall which is free of clusters. Clusters exist outside this layer with a prevalence

which increases with the distance from the wall. Most of the clusters near the wall are within some maximum distance from it, such that their prevalence increases slowly, or not at all, beyond that distance.

These tendencies are shown in Figure 5.1. The samples for Figure 5.1 were taken at a bed density of 40 kg/m^3 and a superficial gas velocity of 4.0 m/s. Since the probe was inserted further into the flow stream than was the case in Figure 4.18, the tendency of the

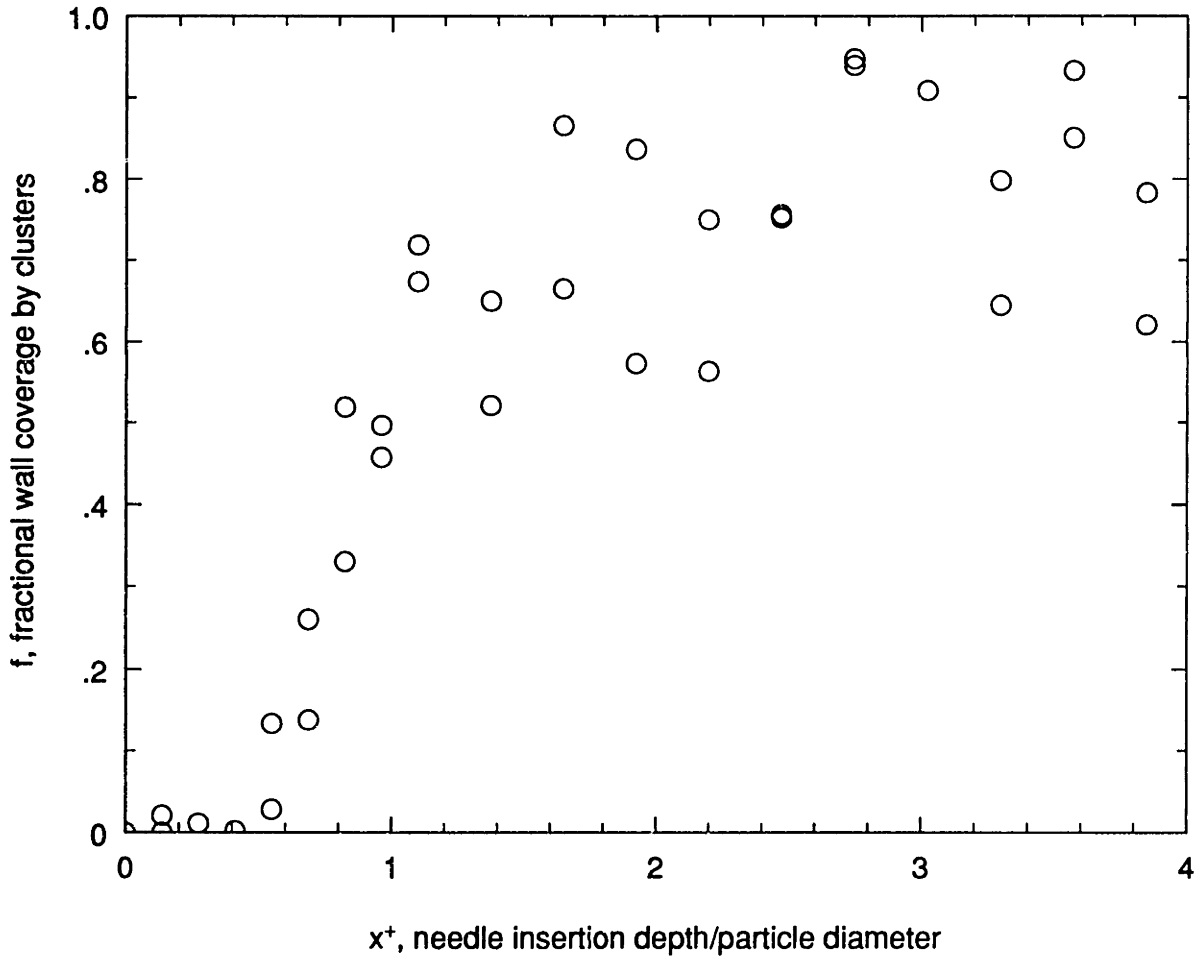

Figure 5.1 - Variation in Cluster Wall Coverage with Probe Insertion Depth

coverage to level off at a maximum value is more clearly displayed. It is also clear from both of these figures that the cluster coverage data does not follow these trends smoothly. The stochastic nature of CFB hydrodynamics is evident from the fluctuations in the data about their mean trend line. Because of this, no single data point can be considered as an accurate indicator of the mean coverage at that location. Rather, it is appropriate to fit the data to a model of the variation in cluster coverage with position by statistical techniques.

The model that was chosen to represent the variation in cluster coverage is shown in Figure 5.2. It is made up of three line segments, and has the same general characteristics which were previously described for the cluster coverage data. It is fixed by the values of the three parameters shown: δ, the non-dimensional probe insertion depth at which clusters are first sensed; df/dx^+, the slope of the increase in the wall cluster coverage with probe insertion depth; and f_0, the maximum value for the fractional wall coverage by clusters. Also shown in the figure is δ', the value of the probe insertion depth at which $f=f_0$.

The present model assumes a linear increase in the cluster wall coverage between δ and δ'. Two other models were examined in the course of this work, one which used a parabolic profile for the increasing cluster coverage, and another with an exponential increase which approached f_0 asymptotically as x^+ increased. These models all fit the data about equally well, and are equally defensible from a mechanistic consideration of the possible structure of clusters near the wall. They also give comparable results for the heat

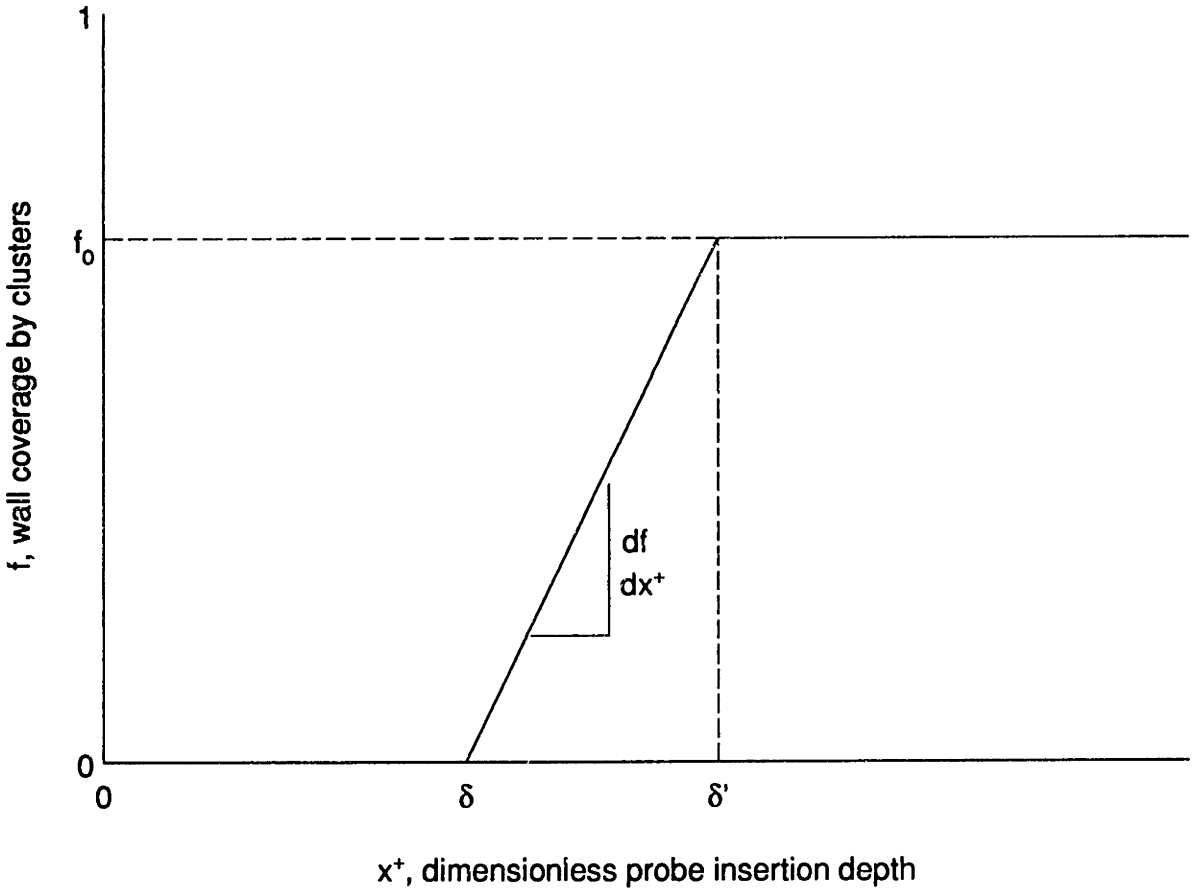

Figure 5.2 - Model of Cluster Wall Coverage

transfer parameters. The linear model is used here for its simplicity in conception, and the fact that the statistical analysis showed that it fit the data somewhat better than the other two models in many instances. It also consistently gave reasonable values for f_0. This was not always the case for the other two models, particularly if the wall cluster coverage was still increasing at the greatest probe insertion depth tested.

The statistical analysis that was used to fit the data was a multiple regression using weighted least squares. It was necessary to use a weighted least squares estimator because the data points have unequal variances. For example, if the actual fractional wall

coverage at a point is equal to zero, then a sample taken at that point will be likely to show a fractional wall coverage which is very close to zero. However, if f=0.5 at a different point, then a sample from that point might vary from between 0.3 to 0.7, or perhaps an even wider range. The data point which is known more precisely should be weighted more heavily by a maximum likelihood estimator. In fact, the maximum likelihood estimate of the cluster coverage model parameters is obtained by minimizing the quantity [Press et al. (1989)]:

$$\chi^2 = \sum_{i=1}^{N} \left(\frac{f_i - f(x_i^+; \delta, df/dx^+, f_0)}{\sigma_i} \right)^2 \qquad (5.1)$$

called the "chi-square," where σ_i is the standard deviation for the data point (x_i^+, f_i).

As described in the section on experimental procedure, two samples were recorded at each location of the probe. Using these two samples, an average value for f and a sample standard deviation, s, can be calculated at each location. The standard deviations of all the data are plotted against the corresponding values for the average fractional wall coverage in Figure 5.3. It shows that the standard deviation is very small at f=0, increases with f to a maximum at about f=0.5, and then decreases back to small values as f approaches 1. If the sample variance, s^2, is assumed to give an unbiased estimate of the population variance, σ^2, then this suggests a functional dependence for σ on f of the form:

$$\sigma(f) = \sigma_{max} - (\sigma_{max} - \sigma_{min}) |2f - 1| \qquad (5.2)$$

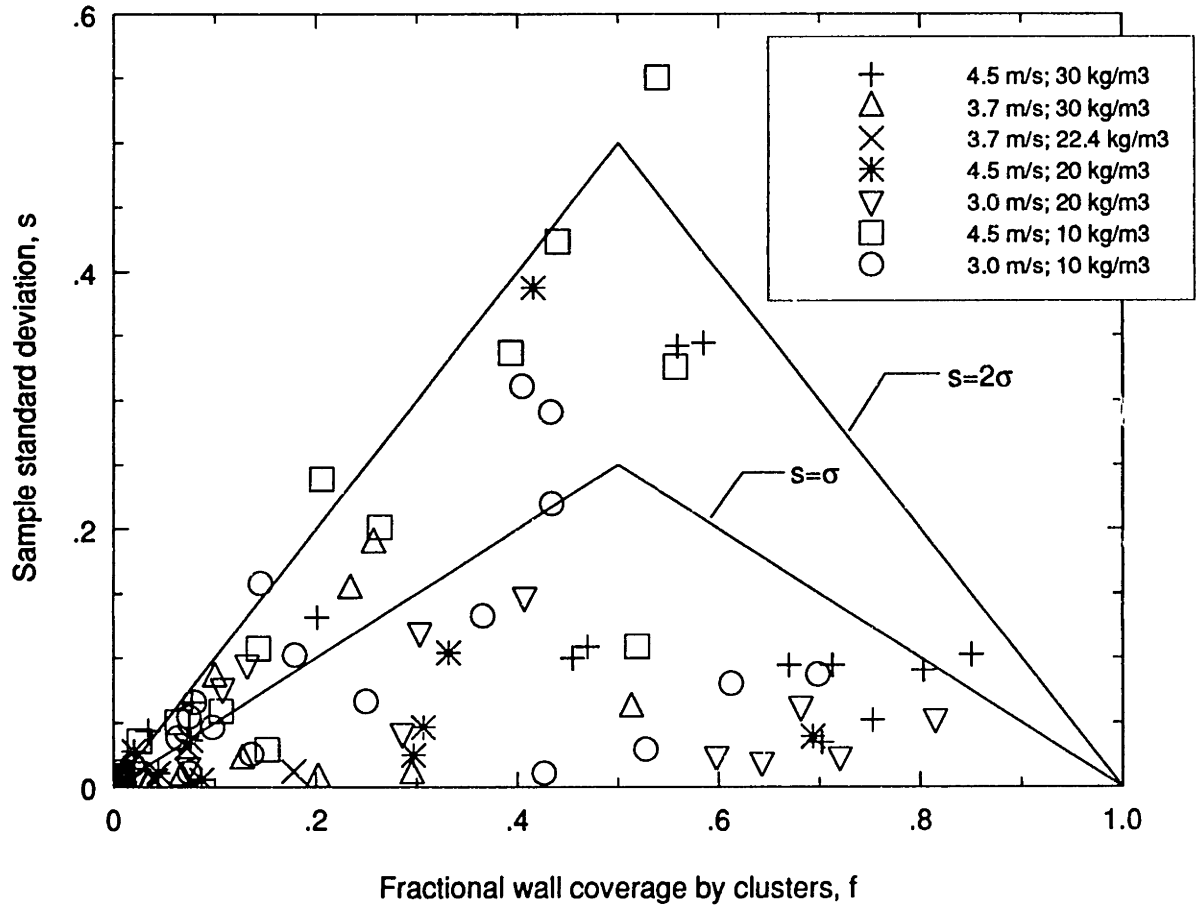

Figure 5.3 - Variation in Sample Standard Deviation of Wall Coverage

Figure 5.3 contains plots of σ and 2σ using $\sigma_{max}=0.25$ and $\sigma_{min}=0$. It shows that this choice of σ is a good descriptor of the variability of s with f. However, it can't be used in Eq. 5.1 because the value within the summation would go to infinity at $\sigma=0$. Instead, a small, non-zero value must be used for σ_{min}. Figure 5.4 shows the normalized sample standard deviations, $s^*=s/\sigma$, using $\sigma_{min}=0.1\sigma_{max}$. There is still a tendency for s^* to increase with f in the neighborhood of f=0, but is much less marked than in Figure 5.3. Lower values of σ_{min} equalize the variances even further; however, they also increase the weight of those data points near f=0 and f=1 in the χ^2 statistic. The proper value for σ_{min} requires a balance between equalizing the sample variances and giving too much weight

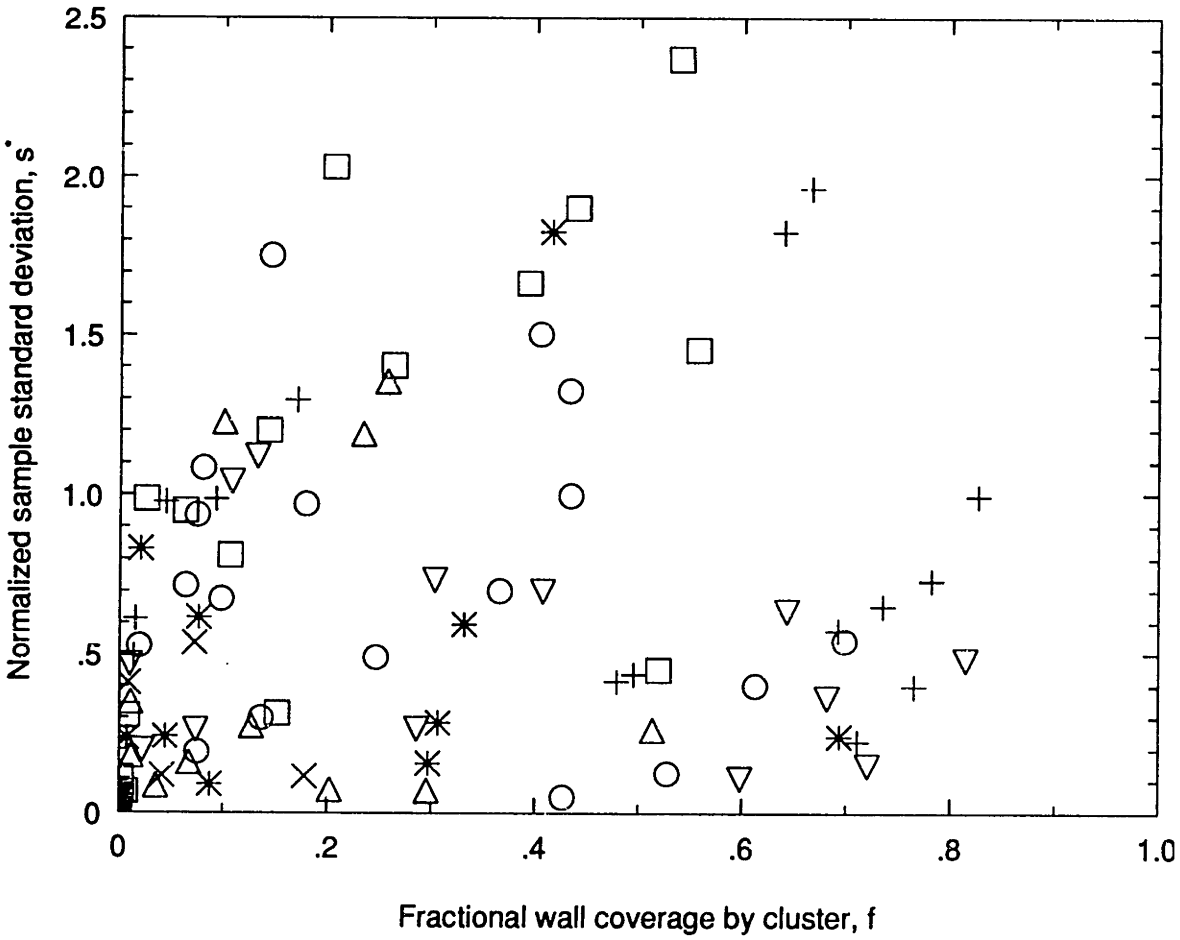

Figure 5.4 - Normalized Standard Deviation of Wall Coverage

to some of the data points [Huber (1991)]. For these studies, a value of $\sigma_{min} = 0.1\sigma_{max}$ was used to provide that balance.

A model of the cluster wall coverage was calculated in this manner for each of the experimental operating conditions. A sample plot of the experimental data and the resulting model is shown in Figure 5.5. Appendix D contains a full set of such plots for all of the operating conditions which were tested.

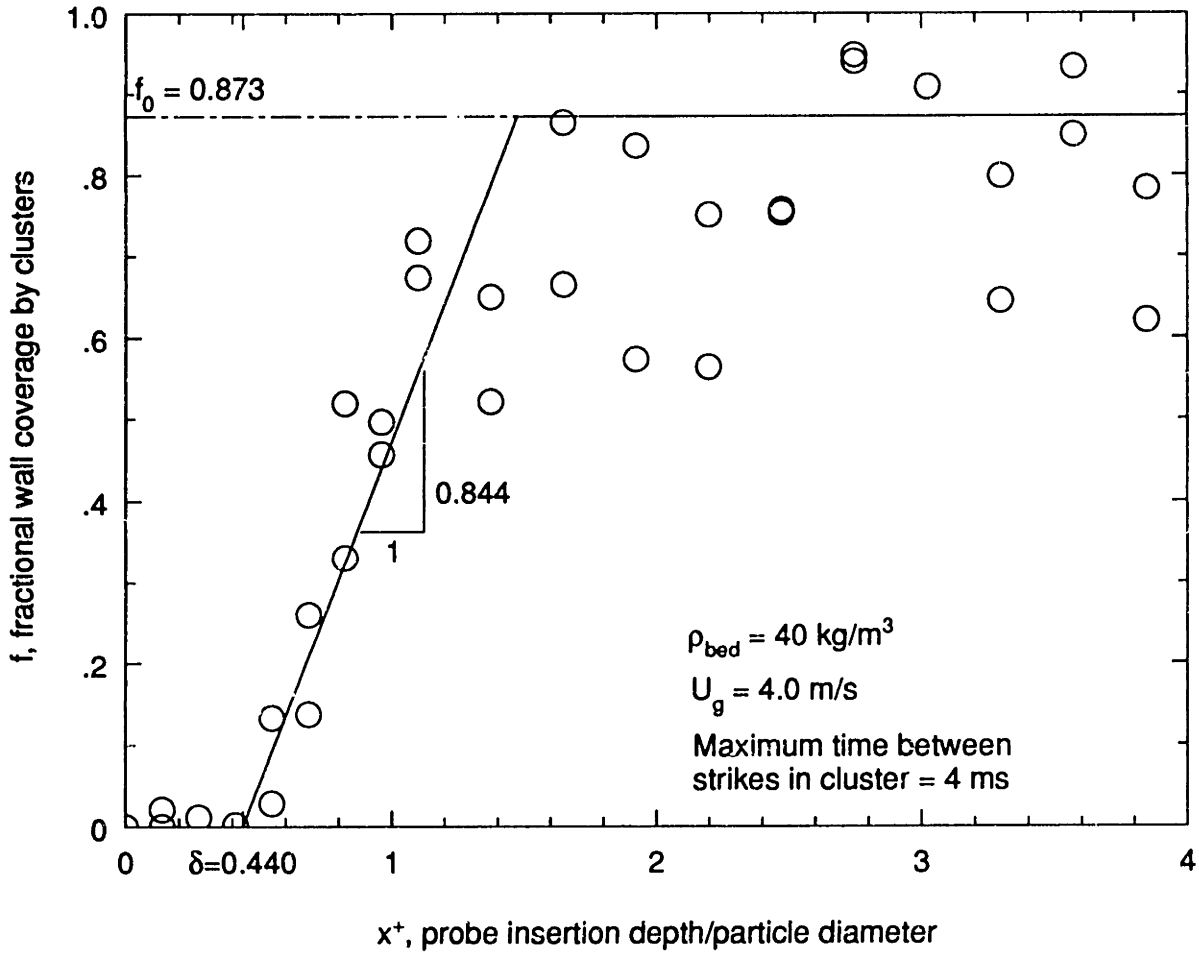

Figure 5.5 - Fit of Wall Coverage Model to Sample CFB Impact Probe Data

5.2 Recommended Values for Heat Transfer Parameters

Each of the heat transfer parameters introduced in Chapter 2 is re-examined below in light of the experimental results, particularly the cluster analysis of the impact probe data.

5.2.1 Wall Gas Layer Thickness

It is clear from Figure 5.5 and the similar plots in Appendix D that there is a gas layer at the wall which contains few, if any, particle clusters. Referring to Figure 5.2, the thickness of that gas layer is represented by δ. Figure 5.6 shows a plot of the δ value

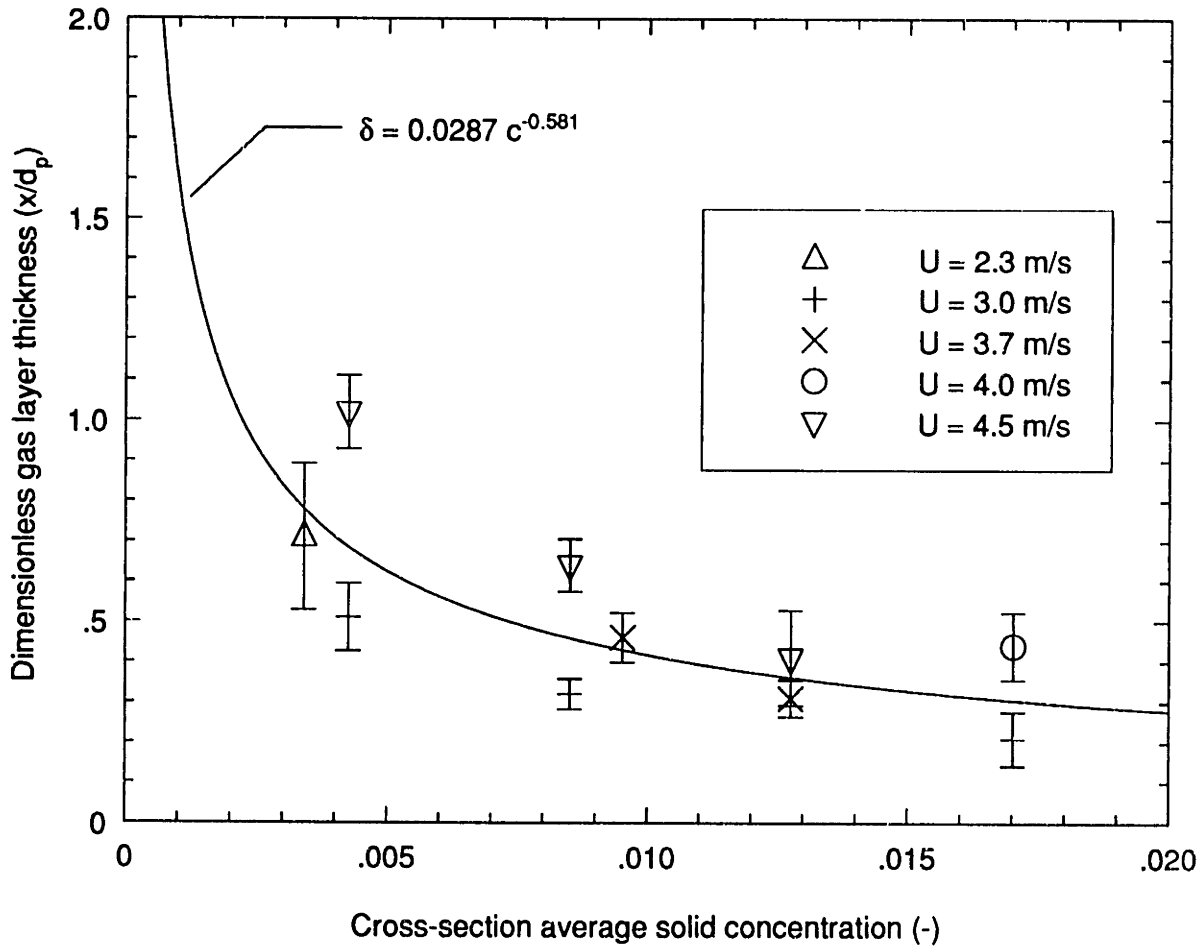

Figure 5.6 - Thickness of Gas Layer Between Cluster and Wall

and its standard error, derived in the χ^2 analysis of the previous section, for each of the experimental operating conditions, using a maximum time between strikes in the cluster analysis of 4 ms. Two trends are displayed by these data.

The first of these trends is a decrease in the gas layer thickness as the density of the bed increases. This variation in δ exceeds any which could be easily explained by random fluctuations, since the standard deviations of δ are smaller than the changes in δ between different bed densities. This variability was not expected, but it is also not surprising. A decrease in the wall gas layer thickness would reduce the resistance to heat transfer through the gas layer and, along with the increased coverage of the wall by clusters, help to increase the overall heat transfer coefficient as the bed density increases. This is consistent with experimental observations (see Figure 3.12).

A second trend in the data is an apparent increase in the thickness of the gas layer as the superficial gas velocity is increased. Although this observation is based upon relatively few data, it is displayed unambiguously (except for the one point at the lowest bed density). This tendency is less easily accepted than the previous one, especially since there has been no documented evidence of a dependency between the superficial gas velocity and the overall heat transfer coefficient. An increase in the gas layer thickness at higher values of U_g would tend to reduce the rate of heat transfer. Based on the discussion of Section 3.5, this tendency might be offset somewhat by a resulting increase in the dilute phase heat transfer coefficient due to higher U_g; but at greater bed densities,

with their higher values of f, this effect would become negligible (see Eq. 2.1). For the present, this apparent trend cannot be explained, but only noted.

It is also worth noting that although the values in Figure 5.6 were calculated using 4 ms as the maximum time between strikes in the cluster analysis, they are not particularly sensitive to that choice. As the figures in Appendix B show, the main effect of reducing the maximum time between strikes to 2 ms is to reduce the rate at which the cluster coverage increases with increasing x^+, and to reduce the value f_0 which the cluster coverage eventually reaches. However, the value δ is little affected by the choice of the maximum time between strikes. Again, the one exception to this observation is at the lowest bed density tested, 8 kg/m_3. In this case, the difference in δ between using a value of 2 ms or 4 ms for the maximum time between strikes within a cluster is significant. As discussed in Sec. 4.2.4.1, the larger value for this cluster parameter should give a more sensitive measure of δ, particularly for the lower density clusters which are expected to accompany lower bed densities. Because of this, the lower value of δ given by the maximum time between strikes of 4 ms is probably more accurate.

Figure 5.6 shows the least-squares power curve fit to the experimental data. It is suggested that this expression,

$$\delta = 0.0287\,\overline{C}^{-0.581} \qquad (5.3)$$

be used to estimate the thickness of the gas layer between the particle cluster and wall for the range of bed densities represented by the experimental data. Within that range, the values of δ vary from about 1.0 to 0.2.

5.2.2 Fractional Wall Coverage by Clusters

The previous measurements reported in the literature which were reviewed in Section 3.2 could resolve the location of near-wall clusters no better than within 1-2 mm, whereas the present measurements extended no further than 0.7 mm from the wall. However, within that 0.7 mm distance, the wall coverage by clusters appeared to reach a maximum value, at least for bed densities greater than 10 kg/m^3. This maximum value of the cluster wall coverage, f_0, should provide a measure of the parameter which is comparable to those previously examined.

Figure 5.7 shows the values of f_0 obtained from the statistical model of the cluster wall coverage plotted on the same graph as the data reviewed in Section 3.2. The present values fall generally within the range of those previously measured. The values corresponding to a maximum time between strikes of 4 ms tend to be at the high end of that range, while those calculated using 2 ms are more centrally located with respect to the previous data. Both the present and the previous data display a large amount of scatter. Although there is a clear tendency for the wall coverage to increase with the bed density, the exact relationship is not clear. However, the general trend of the data seems to be described fairly well by the central curve shown on Figure 5.7:

$$f = 7\,\overline{c}^{1/2} \tag{5.4}$$

Except for the data of Li et al. (1991) at high solids fractions, which is somewhat questionable, the data generally fit within a band of values centered about Eq. 5.4. The scatter in the data of Figure 5.7 shows that either better measurements of this parameter

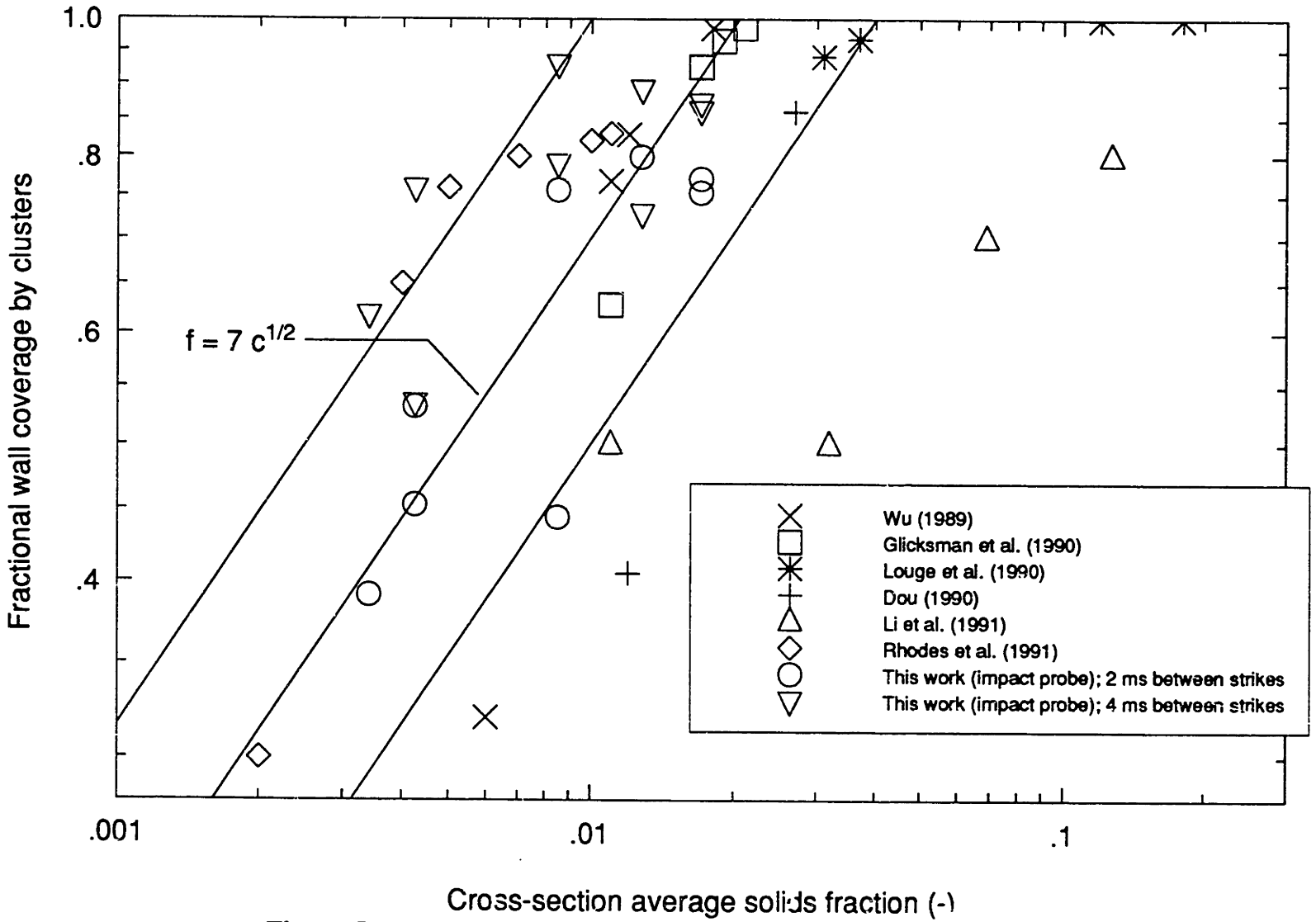

Figure 5.7 - Measurements of Fractional Wall Coverage by Clusters

need to be made, or it is dependent on other variables than just the average cross-section solid concentration. For the present, Eq. 5.4 will be used to predict the value of f for the purpose of estimating the heat transfer coefficient.

5.2.3 Time of Contact between Cluster and Wall

Of the experimental work of the previous chapter, the one best suited to following the motion of particle clusters was the visual observations in the particle cluster injection tube (Section 4.1.1). It showed that particles stayed at the wall for a longer distance at low gas velocities, and tended to get swept up into the gas stream within a shorter distance as the gas velocity was increased. However, this was not a CFB, and there were no particles in the core during the test. Therefore, there was no continuous radial flux of particles to the wall, which may be an important mechanism in tending to keep particles at the wall. For that reason, among others, the results of the injection tube tests cannot be applied directly to cluster motion in CFBs.

Visual observations and recordings were also made in the 20 cm CFB. The results of those tests show that at least some clusters remain near the wall and identifiable for distances ranging from 10 to nearly 50 cm; most of them were tracked for at least 20 cm. It should be noted that the upper limit is that of the field of view of the video system, and does not necessarily represent a maximum distance for the cluster to remain at the wall. It should also be noted that the clusters which were tracked through sequential frames are a biased sample of the clusters which were present at the wall. The emphasis in that work was to measure the cluster velocities. Those clusters selected for closer study were

chosen because they could be identified and followed for an appreciable distance, thereby yielding velocity measurements. Although the results of these experiments are at least representative of some clusters in CFBs, they cannot necessarily be said to be typical. However, taken together with the data of Wu et al. (1989b) which shows a continual decrease in the rate of heat transfer moving downwards along a long (>1 m) heat transfer surface, the evidence suggests that clusters do tend to remain near the wall for at least 20 cm, and probably longer distances, if the wall is smooth.

External visual measurements of the cluster velocity were made in both the particle injection tube and the 20 cm CFB. These measurements are plotted with those of other researchers in Figure 5.8. The present cluster velocities are within the range that others have measured, especially those who have used similar techniques. The present velocity measurements suffer from the same shortcoming as the other external visual measurements, namely that there is no method to differentiate clusters which are very close to the wall from those which may be significantly further away.

Calculation of the cluster velocity from the impact probe data was not possible with the particles which were used. Although the response of the impact probe is proportional to the kinetic energy of the particle striking it, the range of masses of individual particles was too great to derive any meaningful particle velocity data from the present experiments. It is suggested that future work might include the use of closely-sized particles with the impact probe in order to measure the velocity of particles near the wall.

In the meantime, a cluster velocity at the wall of 0.6 m/s will continue to be used as an estimated value, based on the discussion in Section 3.3.1.

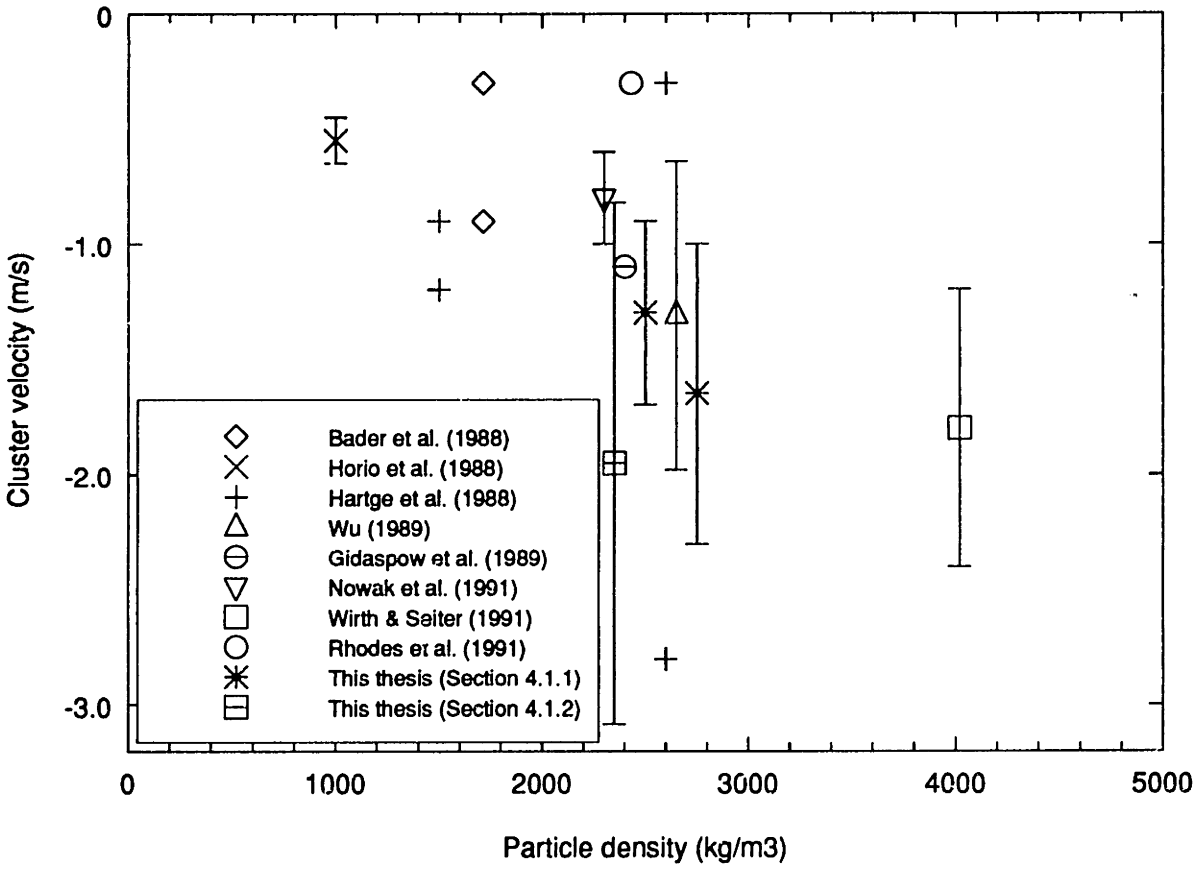

Figure 5.8 - Cluster Velocity Measurements at the Wall

5.2.4 Cluster Void Fraction

Based on the calibration of the impact probe, it is clear that not all of the particles which passed by the probe would be counted. But the frequency of particle strikes on the impact probe can yield information on the relative void fraction of clusters at different bed operating conditions. If the total time during which the probe senses clusters is divided by the number of particle strikes sensed during that same time, a value for the

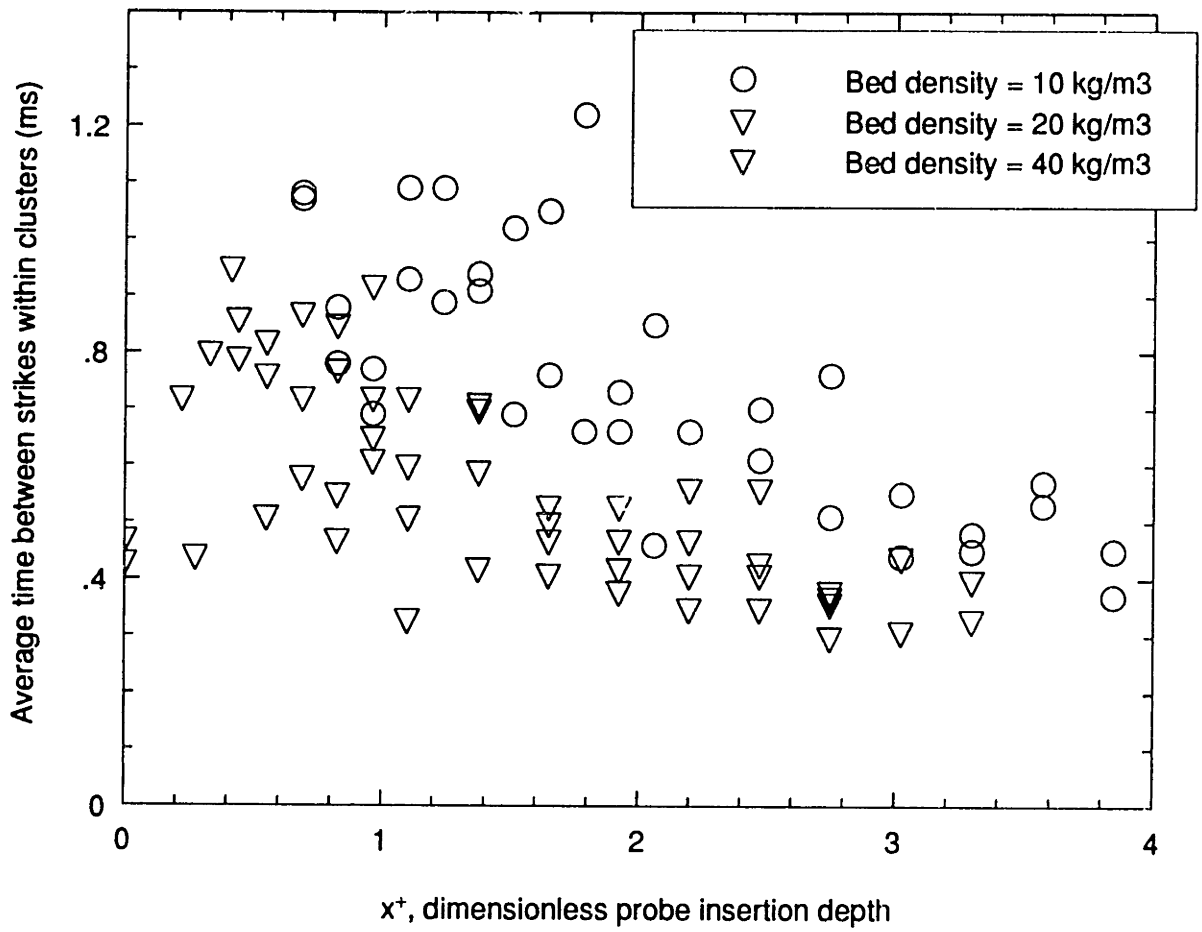

Figure 5.9 - Cluster Void Fraction Data from Impact Probe Measurements

average time between strikes within the clusters is obtained. Figure 5.9 shows that value plotted against the dimensionless probe insertion depth for three different bed densities, all at a superficial gas velocity of 3 m/s.

One feature to be noted in Figure 5.9 is that the average time between strikes is less than 1 ms for nearly all the data. This might seem unusual, since the maximum time between strikes used to define these clusters was 4 ms. Apparently, even when clusters are defined as all groups of strikes within 4 ms of one another, most of the strikes within the clusters fall much closer together than that.

Figure 5.9 shows that the particle strikes tend to be closer together in clusters at a higher bed density. This tendency is particularly noticeable at lower values of x^*. As the probe is inserted further into the flow stream, a larger cross-section of the needle is struck by particles. This will reduce the average time between strikes even if the clusters maintain the same fraction of solids. This effect is displayed clearly by the data taken at $\rho_{bed} = 10$ kg/m^3.

However, this trend cannot continue indefinitely. The probe has a maximum frequency response to particle strikes, which corresponds to a minimum average time between strikes which can be measured. Figure 5.10 contains a typical sample of the probe output signal, but one which has been selected as representative of the maximum frequency response of the probe to particle strikes. It shows roughly 20 particle strikes (21 as counted by the cluster analysis) in a time of 5 ms, giving a strike frequency of about 4 kHz, or a time of 0.25 ms between strikes. The dynamics of the needle probe are such as to prevent the measurement of particle collisions at a higher rate. Furthermore, occasional spans of time within a cluster of 1 ms or greater duration without strikes will increase the average time between strikes for the cluster. In actuality, the average time

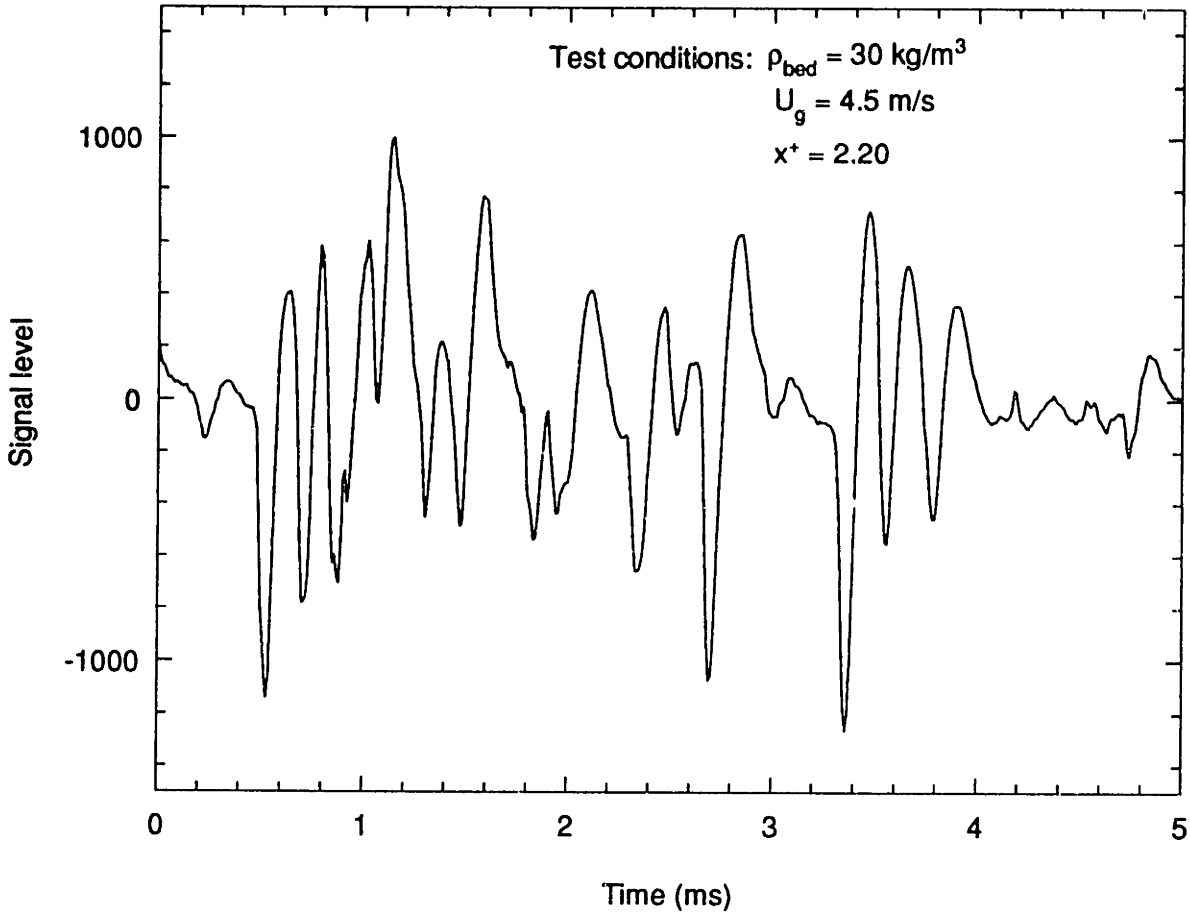

Figure 5.10 - Sample Output Signal of Maximum Strike Frequency for Impact Probe

between strikes was never less than 0.3 ms for the clusters defined by a maximum time between strikes of 4 ms. For practical purposes, this may be considered the saturation limit of the probe.

Referring back to Figure 5.9, it can be seen that the data at each bed density approach an average time between strikes of about 0.3 ms as the insertion depth is increased. Of greater interest is the average time between strikes at the lesser insertion depths, at about one-half to one particle diameter from the wall, where the clusters are first detected. There is some variability in the values, but the average is about 1.0 ms for ρ_{bed}=10 kg/m^3;

at a bed density of 40 kg/m^3, the average is about 0.5 ms. If the average time between strikes varies inversely with the cluster solid fraction, then this data exhibits precisely the square root dependence between cluster solid fraction and bed density which is predicted by Eq. 3.6.

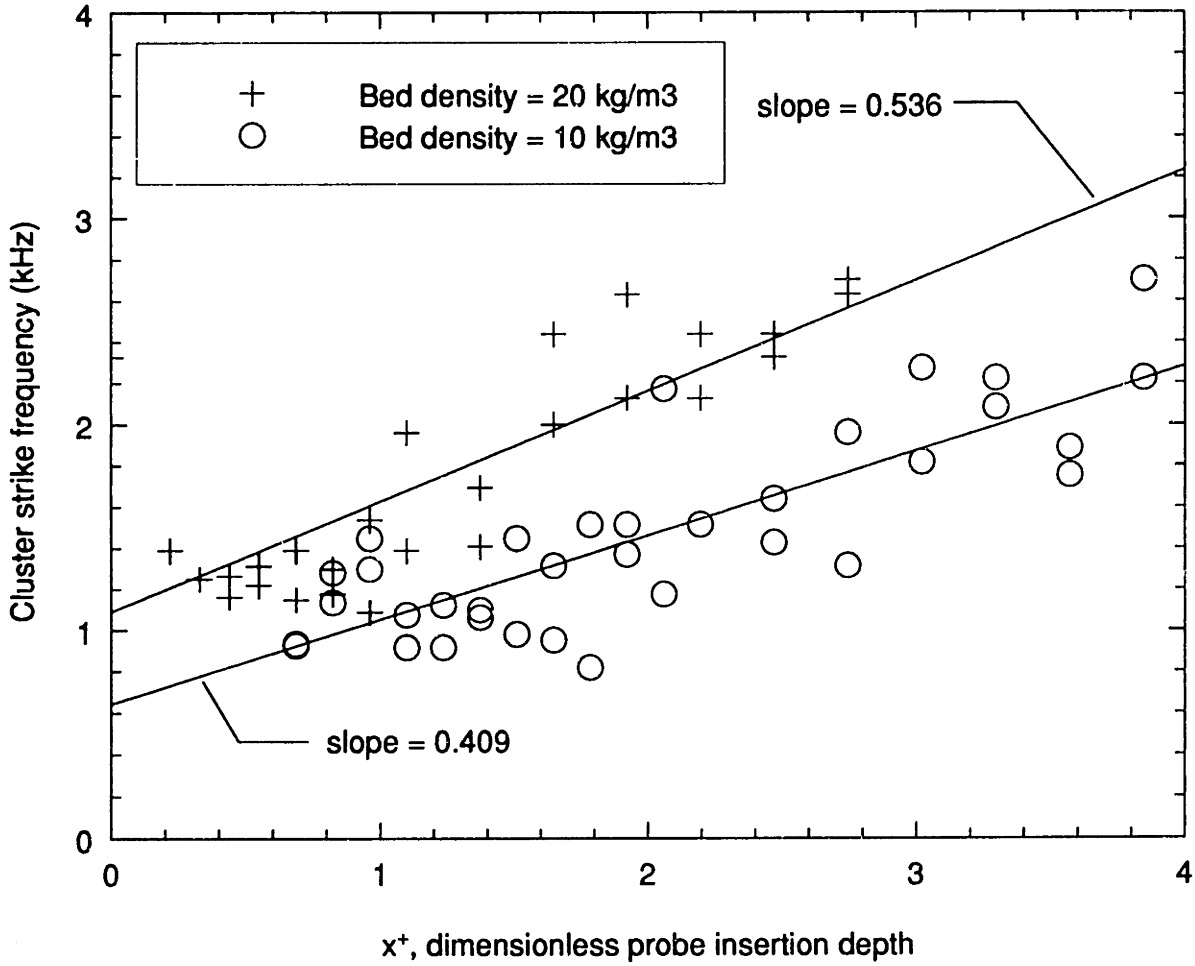

Figure 5.11 - Variation of Cluster Strike Frequency with Probe Insertion Depth

A numerical value for the cluster solid fraction can be estimated by a closer examination of the particle strike rate within the clusters. Figure 5.11 plots the cluster strike frequency against the probe insertion depth for the two lower bed densities. The data exhibits a clear tendency towards increasing cluster strike frequency at greater insertion depths. Below the saturation strike frequency of the probe, the cluster strike frequency should be

directly proportional to the cluster solid fraction and the depth of insertion of the probe into the cluster. If the cluster is assumed homogeneous, then the slope of the least-squares linear fits to the data shown in Figure 5.11 give the cluster strike frequency per unit insertion depth of the probe. For the bed density of 10 kg/m^3, the value is 0.409 kHz/182 μm = 2.25/μm-s; at 20 kg/m^3, the value is 2.95/μm-s.

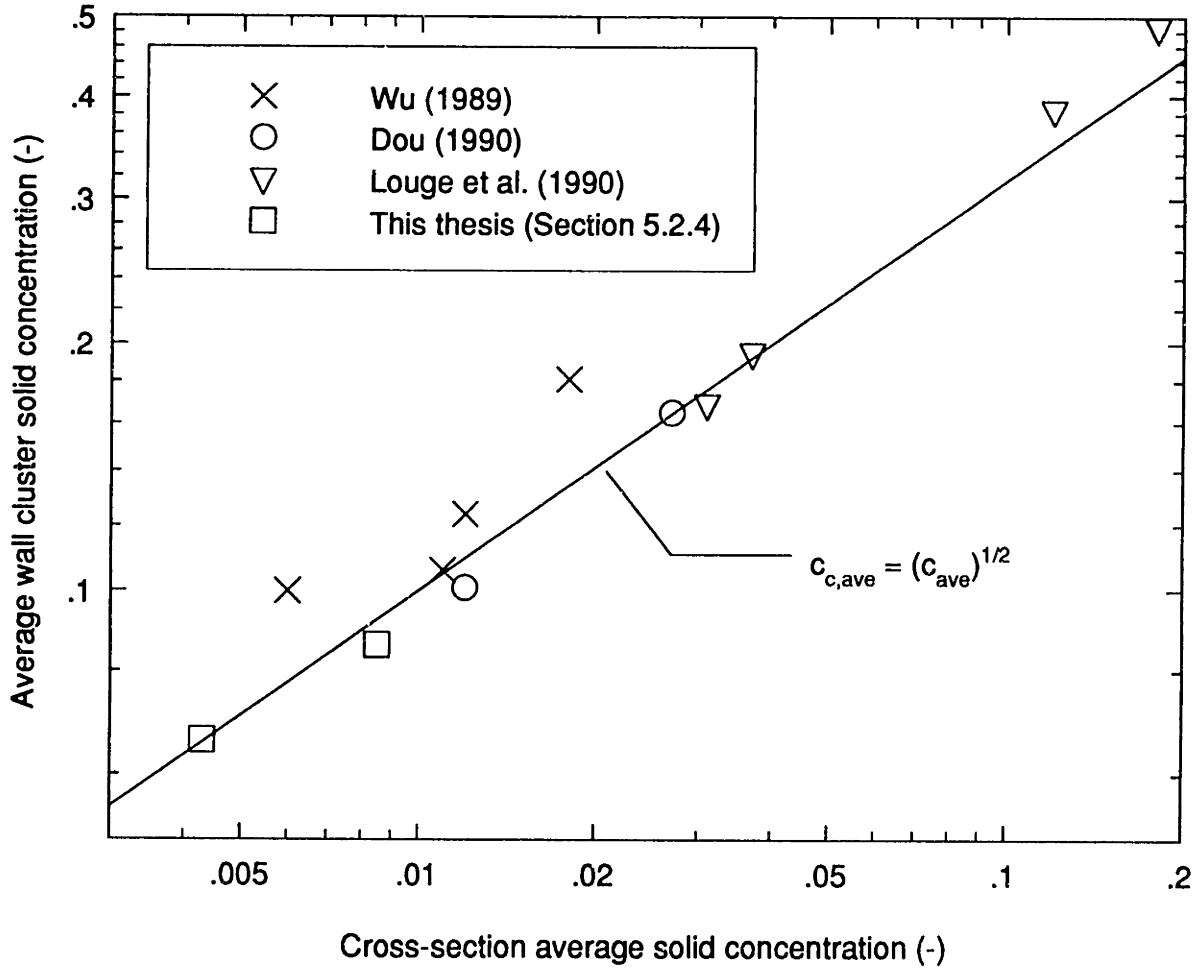

Figure 5.12 - Variation in Wall Cluster Solid Concentration with $\bar{c}$

The cluster solid concentration can be estimated by scaling these values using the results of the calibration channel flow. As shown in Figure 4.12, a flow of 10% solids at 1.4 m/s gave a strike rate per insertion depth of 8/μm-s. Using an assumed velocity of 0.6 m/s for the clusters in Figure 5.11, the resulting solid fractions are 6.6% at 10 kg/m^3, and

8.6% at 20 kg/m^3. These data are plotted in Figure 5.12 with the previous results of Section 3.4. As can be seen, they follow the proposed relationship between cluster solid fraction and cross-section average solid fraction almost exactly. This provides further evidence that the average cluster solid fraction varies with the bed density, and that Eq. 3.6 accurately describes that variation.

5.2.5 Dilute Phase Heat Transfer Coefficient

In Section 3.5, it was suggested that the presence of particles in a CFB acted in two ways to enhance the dilute phase heat transfer coefficient relative to the single-phase gas heat transfer coefficient:

1) individual particles which are present in low concentration in the dilute phase change its effective thermal properties, and

2) clusters regularly sweeping along the wall of the bed disturb the gas flow, thereby limiting the effective length of the heat transfer surface with respect to the boundary layer development.

The results of the cluster analysis of the data from the impact probe can be used to examine both of these effects.

The length of time between clusters in the output signal from the probe represents the duration of the dilute phase at the probe for that instance. Since the spacing between clusters may be expected to fluctuate, the distribution of such spacings should be examined. Figure 5.13 gives the distribution of the length of time between clusters at several different bed densities, for a superficial gas velocity of 3 m/s. Figure 5.13

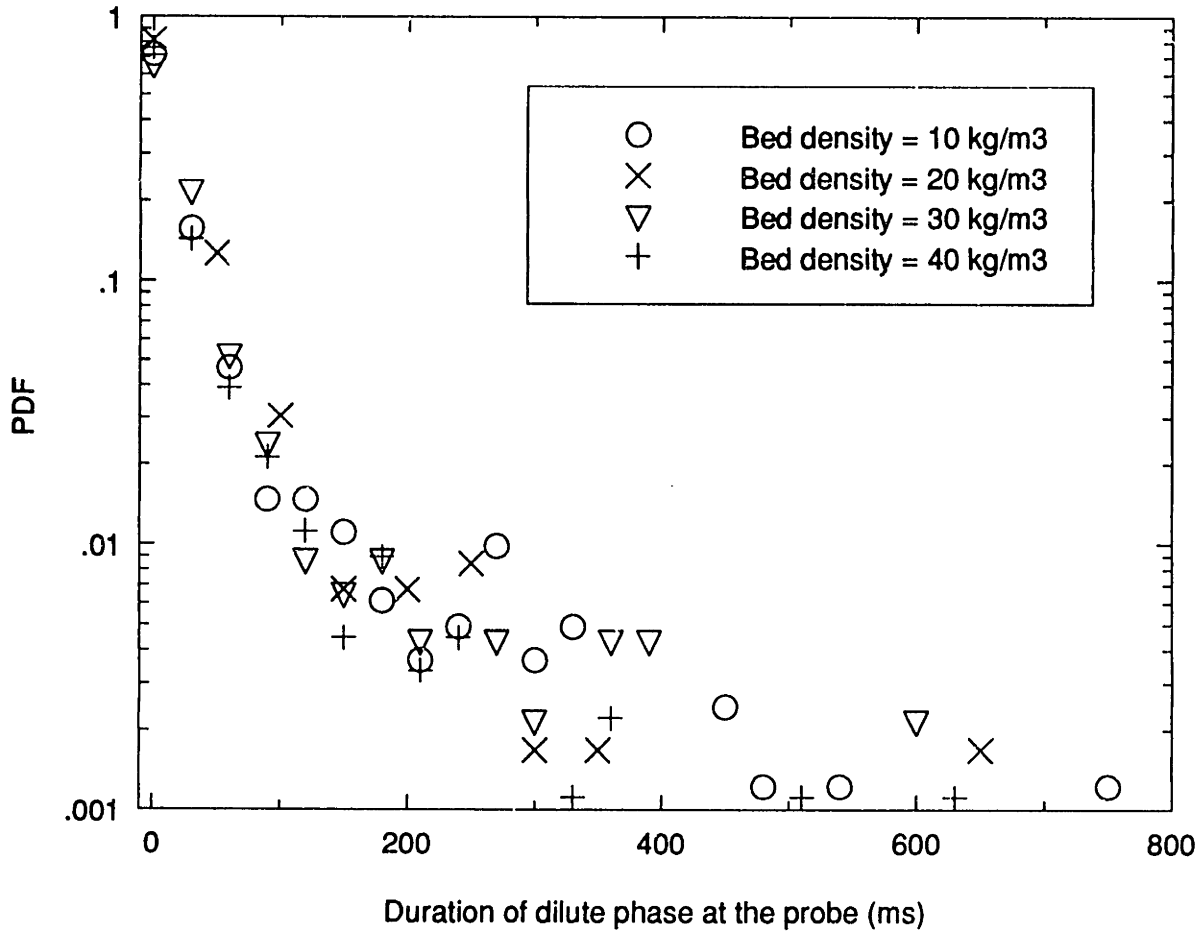

Figure 5.13 - Distribution of Dilute Phase Duration at the Probe

includes only the durations from samples in which at least two cluster were detected; the range of insertion depths represented by the data of Figure 5.13 is from just over zero to about four particle diameters. The figure shows that only rarely does the time between clusters exceed 100 ms. If the clusters are assumed to move down the wall with a velocity of 0.6 m/s, then 100 ms would correspond to a spacing between clusters of 6 cm. This is somewhat less than the suggested value for the undisturbed flow length (cluster spacing) in Section 3.5.

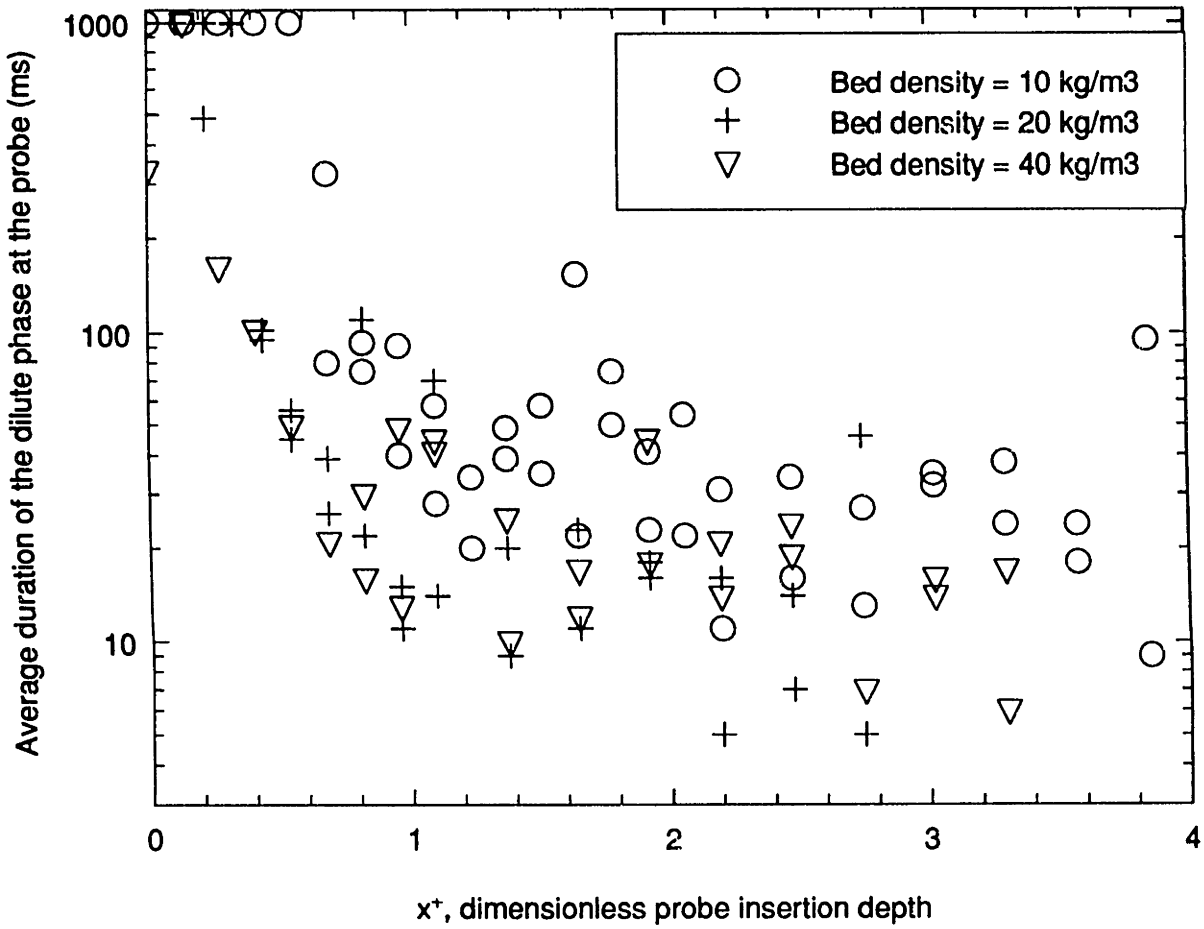

Figure 5.14 - Dependence of Dilute Phase Duration on Probe Insertion Depth

A better idea of the actual structure of the cluster spacing is obtained by looking at the dependence of that spacing on the probe insertion depth. Figure 5.14 shows the average duration of the dilute phase for each sample plotted against the probe insertion depth. In this case, the maximum duration is equal to the sample period, 1000 ms, for those samples near the wall in which no clusters were detected. However, the mechanism of dilute phase heat transfer supposes exposure of the heat transfer surface to the gas flow in the core of the bed. Therefore, it is more relevant to look at the duration of the dilute phase further from the wall, such that no clusters are present within at least a few particle diameters of the wall. Figure 5.14 shows that for $x^+>1$, there does not appear to be a

strong dependence of cluster spacing on the bed density. The average time between clusters is typically between 10 and 100 ms, which at a cluster velocity of 0.6 m/s corresponds to a cluster spacing of 0.6 to 6 cm. This suggests that the value of 10 cm assumed in Section 3.5 for the undisturbed flow length may be too high, and that a lower value may give a better estimate of h_d in at least some circumstances.

The other means by which particles may increase the dilute phase heat transfer coefficient is by increasing the thermal conductivity and Prandtl number of the gas. The extent of this increase will depend upon the concentration of particles in the dilute phase. An estimate of that concentration was made in Section 3.5 using capacitance probe data from the literature. The frequency of particle strikes on the impact probe in the dilute phase offers another estimate of that parameter.

Figure 5.15 gives the frequency of particle strikes within the portion of the output signals corresponding to the dilute phase for the same operating conditions as Figure 5.13. It shows that the frequency is roughly zero at the wall and increases as the probe is advanced into the flow stream. The frequency reaches a plateau at about $x^+=1$ and fluctuates within the range of 50 to 200 Hz for larger values of x^+. This leveling off is due to the upper limit on the dilute phase strike frequency inherent in the definition of a cluster. For the data of Figure 5.15, a maximum time between strikes within the clusters of 4 ms was used, equivalent to a minimum strike frequency of 250 Hz. Since by definition, any strikes of greater frequency were within clusters, the dilute phase strike frequency must be somewhat less than that, with an expected average of about 125 Hz.

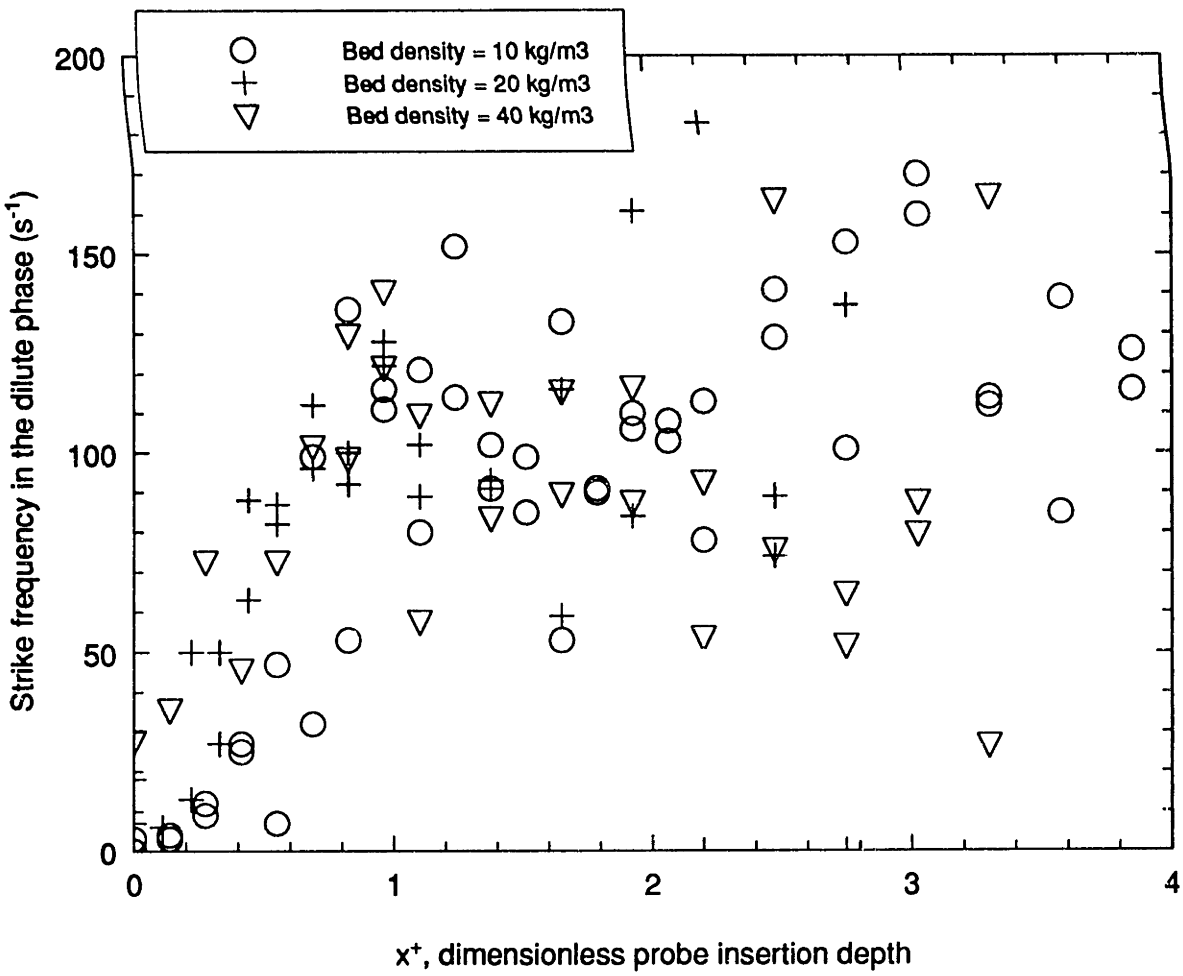

Figure 5.15 - Frequency of Particle Strikes in the Dilute Phase

However, with respect to both the probe signal and the heat transfer process, the interesting area is near the wall, at $x^+<1$. Figure 5.16 shows an expansion of that region. Also, the range of the dilute phase strike frequency has been extended to 500 Hz by using the results of the cluster analysis with a maximum time between strikes of 2 ms. If a constant velocity is assumed for the particles passing the probe, then the rate of increase in the average dilute phase strike frequency with increasing x^+ is proportional to the solid fraction of the dilute phase. The slope of the data for ρ_{bed} = 20 kg/m^3 and 40 kg/m^3 are roughly the same, about 300 Hz, whereas the slope for ρ_{bed} = 10 kg/m^3 is less than half of that value. Based on this data, it appears that the dilute phase solid fraction increases

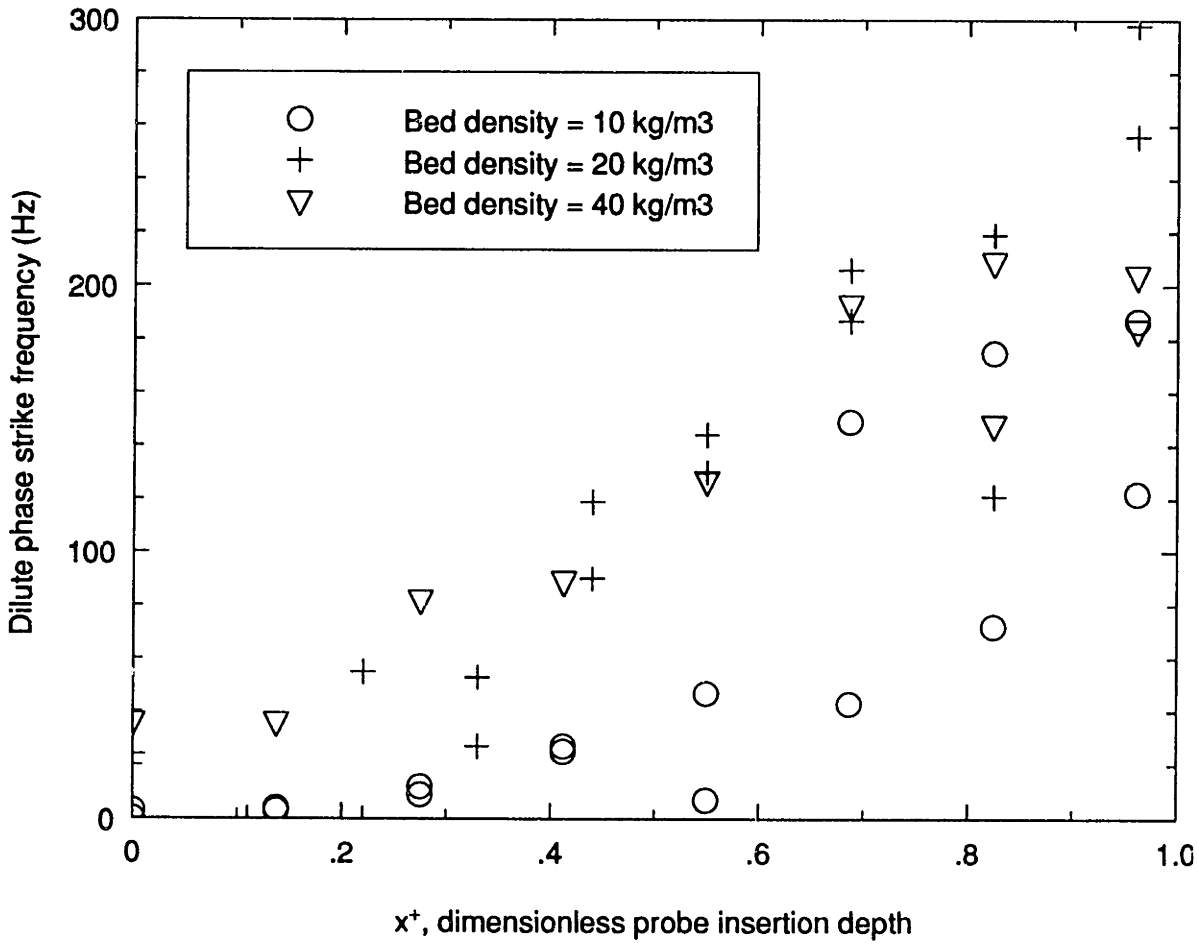

Figure 5.16 - Dilute Phase Strike Frequency Near the Wall

with the cross-section average bed density up to a value of about 20 kg/m^3, but not beyond that.

In order to estimate the value of the dilute phase solid fraction, the slopes of Figure 5.16 can be compared to that of the calibration channel flow. In Section 4.2.4.1 the strike rate per unit insertion depth into a flow stream of 10% solids was found to be 8/μm-s (see Figure 4.12). Using the dimensional probe insertion depth, x, the steeper slope in Figure 5.16 is about 1.6/μm-s. This implies a dilute phase solid fraction of about 2% at the higher bed densities, assuming equal velocities for the dilute phase and the calibration

channel flows. Given the uncertainty in the velocity estimates, this is consistent with the approximation of 3% derived in Section 3.5.

The dilute phase solid fraction estimated from the slope of the data in Figure 5.16 will vary directly with the assumed value of the dilute phase velocity past the probe. However, there is little information available regarding this parameter. The only measurements of particle velocity in the dilute phase known to this author may be those of Yang et al. (1990). Using laser doppler velocimetry, they measured the velocity of particles at the wall of a dilute CFB. Their reported velocities range from about -1 to 5 m/s, with a large number of measurements bunched between -1 and 0 m/s. These velocities represent both the dilute phase and any clusters which may have been present, since they did not differentiate between the two. One may speculate that the more frequent velocities grouped between about -1 and 0 m/s represent clusters, while the more disperse measurements between 0 and 5 m/s represent the velocities of particles in the dilute phase. Whether or not this is so, it is clear that the dilute phase particle velocity remains largely unknown at the present time. The main point being made here is that the assumed velocity for clusters at the wall, -0.6 m/s, is not necessarily the appropriate value to use for the dilute phase velocity.

5.3 Heat Transfer Estimated by Model

The experimental results verify the basic features of the heat transfer model proposed in Chapter 2, i.e. alternate coverage of the wall by dilute phase and dense phase clusters, the latter of which is separated from the wall by a gas (or dilute phase) layer. However, some question still remains as to the structure of the clusters at the wall. The statistical model which was developed to provide estimates of the gas layer thickness and cluster wall coverage contains a gradual increase in the cluster coverage with distance from the wall. The fact that the impact probe data fit such a model could be the result of several different particle structures, including: homogeneous clusters of uniform density which are at varying distances from the wall; clusters at a fixed distance from the wall with solid concentrations which increase with distance from the wall; or, clusters with solids concentrations which vary randomly (within limits) at either a fixed or variable distance from the wall.

The selection from among these different possibilities will have important implications for the heat transfer process. If homogeneous clusters are at varying distances from the wall, then the average thickness of the gas layer may be much greater than the minimum thickness shown in Figure 5.6, and the corresponding wall resistance may be large. On the other hand, the transient conduction through clusters of varying porosity at a fixed distance from the wall may not be estimated accurately by the Mickley and Fairbanks (1955) expression (Eq. 2.3).

The sensitivity of the heat transfer coefficient to the structure of the near-wall clusters can be determined by looking at two different possible flow structures: uniform clusters at a fixed distance from the wall, equal to the minimum distance from the statistical model; and uniform clusters at a varying distance from the wall, assuming the linear variation in cluster wall coverage with distance from the wall given by the statistical model. These two different cases may be considered as the upper and lower limits, respectively, to the actual rate of heat transfer.

For the first case, the heat transfer will be given by Eq. 2.7, slightly modified:

$$h = f\left[\frac{\delta d_p}{k_g} + \sqrt{\frac{\pi t}{4 k_c c_{p,s} \rho_s (1-\epsilon_c)}}\right]^{-1} + (1-f)\, h_d \qquad (5.5)$$

The factor of four has been included in the term for transient conduction in the cluster in order to predict the time-averaged, as opposed to the instantaneous, rate of heat transfer. The various parameters of Eq. 5.5 are estimated by:

$$f = 7\,\overline{c}^{1/2} \qquad (5.4)$$

$$\delta = 0.0287\,\overline{c}^{-0.581} \qquad (5.3)$$

$$t = \frac{L_h}{U_c} \qquad (3.3)$$

with U_c = 0.6 m/s;

$$\epsilon_c = 1 - c_c = 1 - \overline{c}^{1/2} \qquad (5.6)$$

and h_d estimated according to the method proposed in Section 3.5.

For the second case, the analytical expression for the heat transfer coefficient is developed in Appendix E, and is given by:

$$h = f\left(\frac{df}{dx^+}\frac{k_g}{d_p}\ln\left|\frac{\delta d_p}{k_g}+\sqrt{\frac{\pi t}{4k_c\rho_s c_s(1-\varepsilon_c)}}\right|_{\delta}^{\delta'}\right)+(1-f)\,h_d \qquad (5.5)$$

Figures 5.17 through 5.19 give the comparison of the heat transfer coefficient estimated by these two methods with experimental measurements made by other researchers for heat transfer surfaces of three different lengths. Figures 5.17 and 5.19 each contain the results

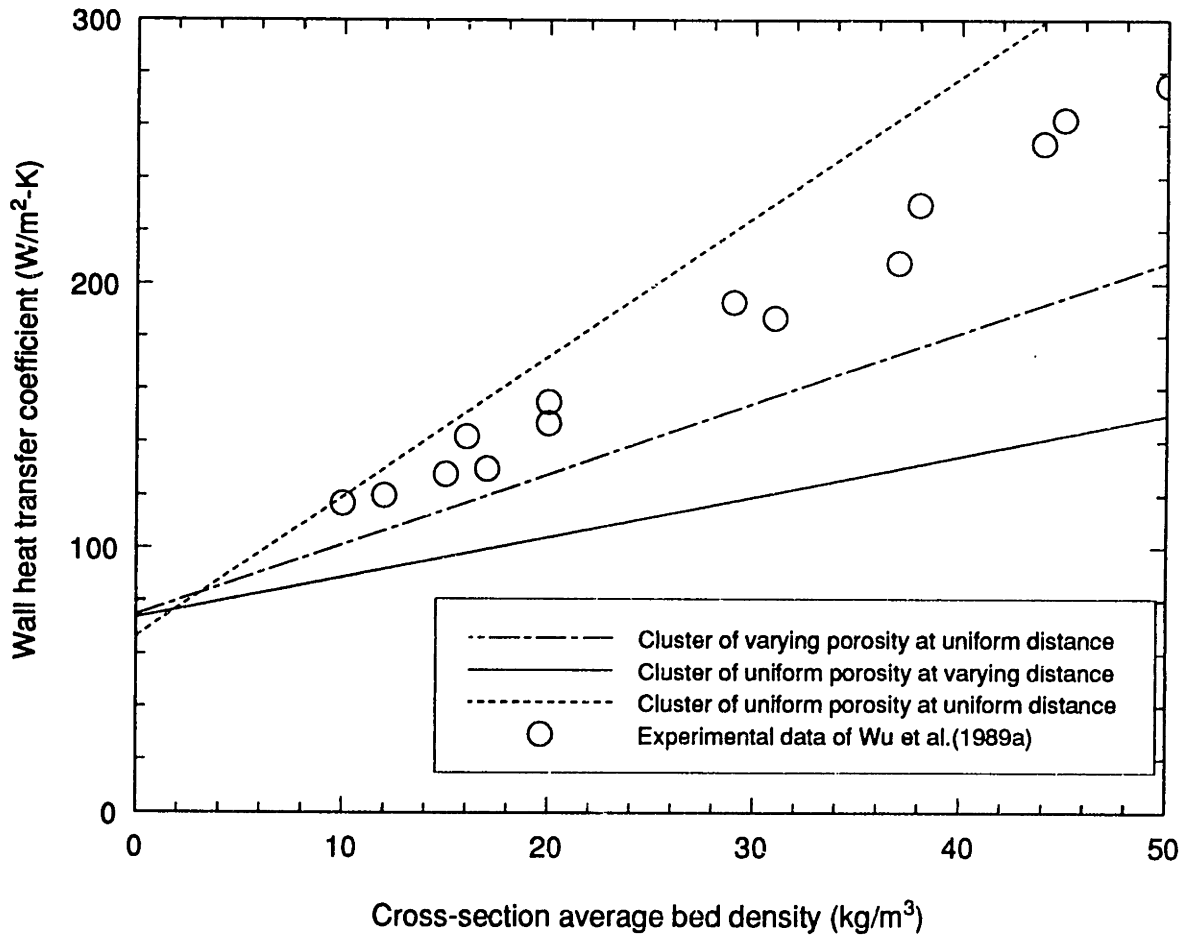

Figure 5.17 - Comparison of Model Predictions of Heat Transfer to Experimental Measurements for Heat Transfer Surface Length of 1 cm

of an additional model of the heat transfer process. The additional curve in Figure 5.17 is based on clusters of varying porosity, which will be discussed shortly. Figure 5.19 contains a prediction of the rate of heat transfer based on a heat transfer surface length of 1 m. Its significance will be mentioned in Chapter 6.

The difference between the results of the two basic models is greatest for the shortest heat transfer surface length. Figure 5.17 shows predicted heat transfer coefficients which vary by a factor of two at 50 kg/m^3. Figures 5.18 and 5.19 show that the difference between

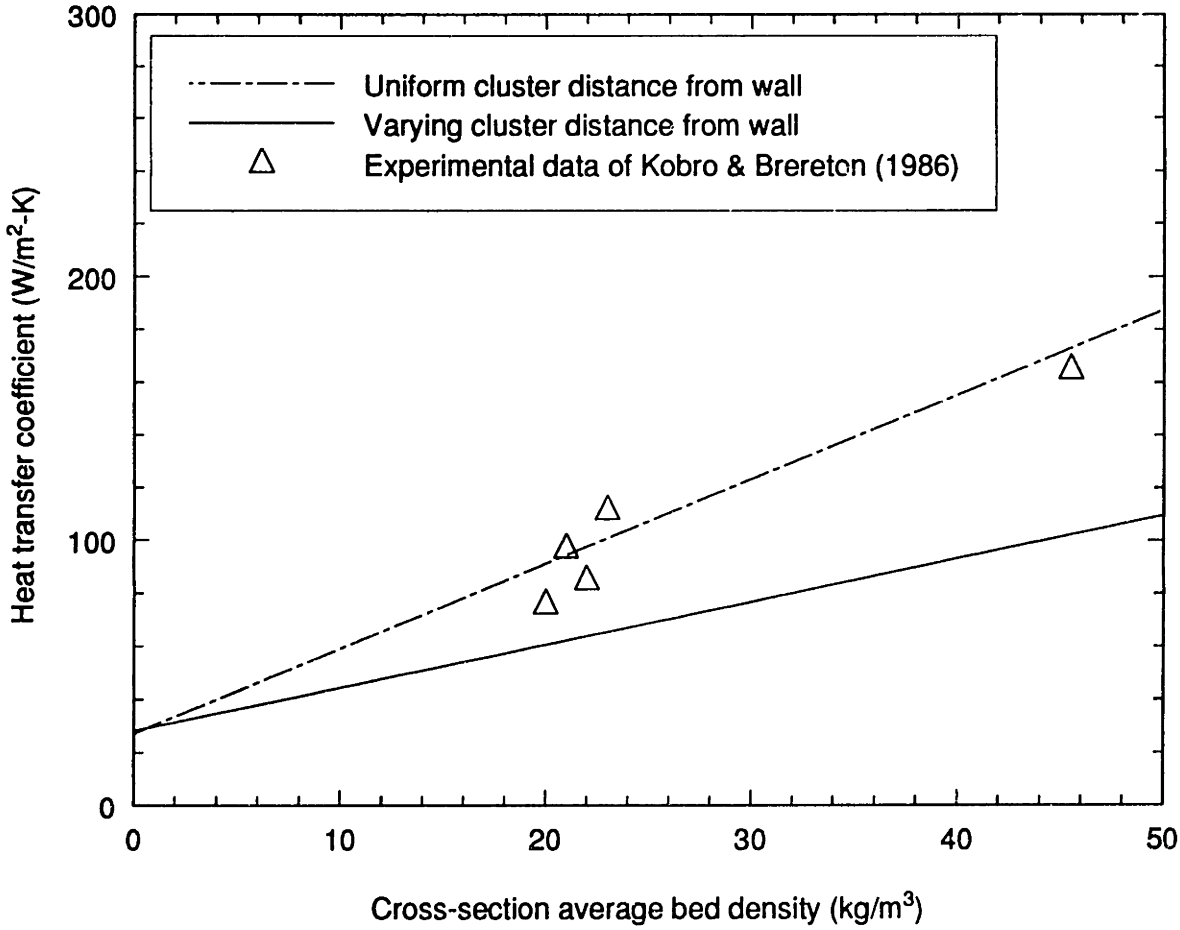

Figure 5.18 - Comparison of Model Predictions of Heat Transfer to Experimental Measurements for Heat Transfer Surface Length of 10 cm

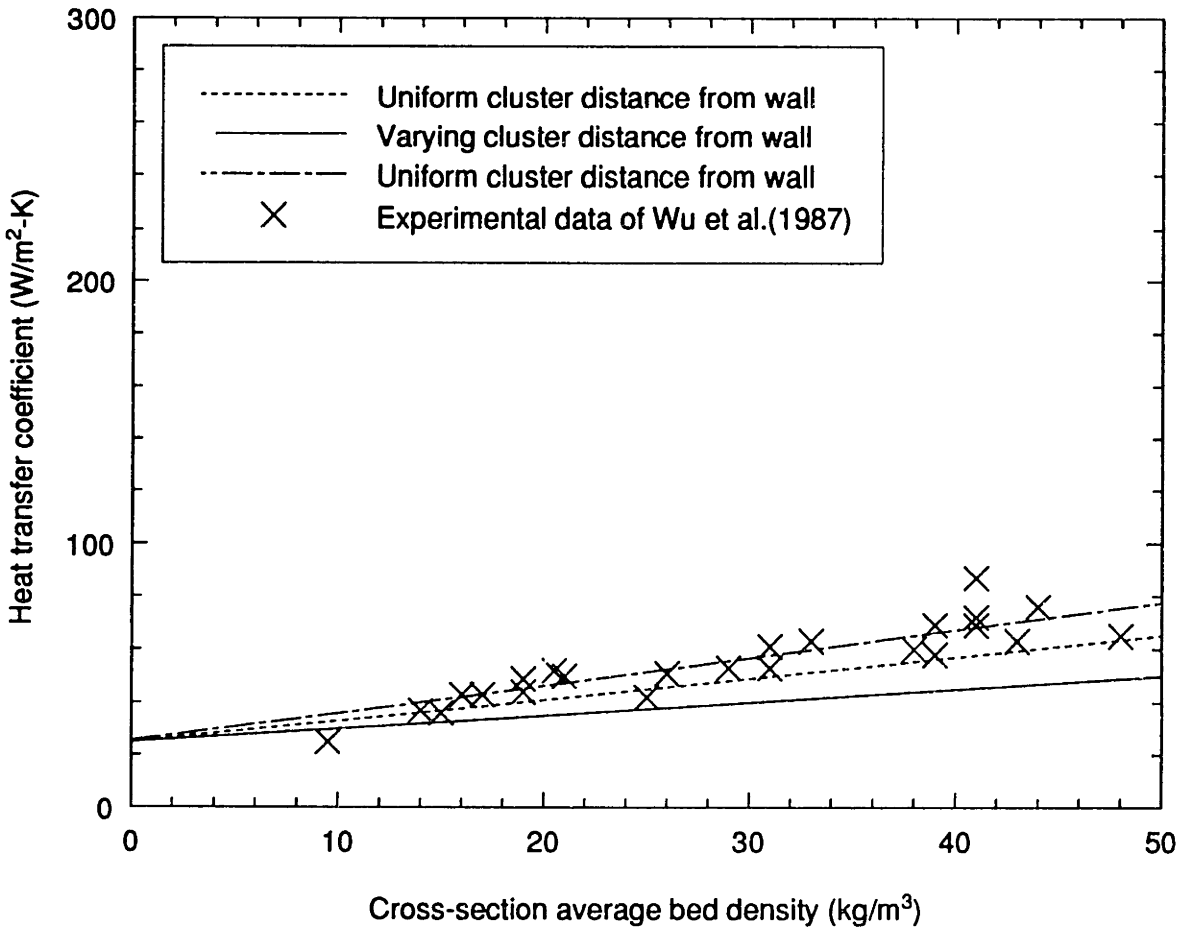

Figure 5.19 - Comparison of Model Predictions of Heat Transfer to Experimental Measurements for Heat Transfer Surface Length of 1.5 m

the predictions of the two models decreases as the length of the heat transfer surface increases. This is to be expected, since the thermal resistance in the gas layer is constant, whereas the resistance to conduction in the cluster increases with time. For long heat transfer surfaces, the clusters remain at the wall long enough for the cluster resistance to dominate the heat transfer process, and the difference in the gas conduction distances between the two models becomes relatively unimportant. This is shown graphically by Figure 5.20, wherein the two different heat transfer coefficients which combine in series (see Eq. 2.5) to form the cluster heat transfer coefficient, h_c, are plotted for three different

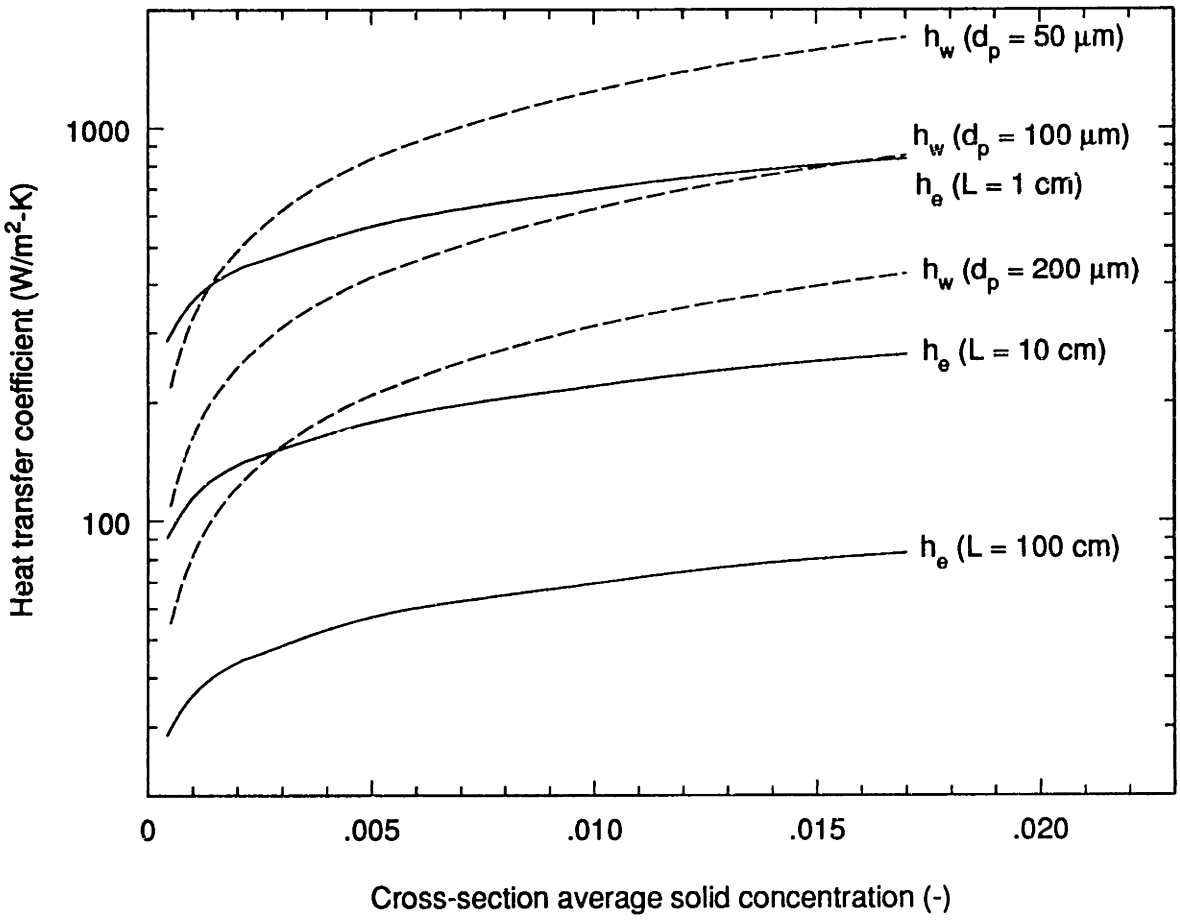

Figure 5.20 - Comparison of Terms in the Cluster Heat Transfer Coefficient

flow lengths and three different particle diameters.

The solid lines in Figure 5.20 show the variation with bed density of the heat transfer due to transient conduction within the cluster, with the cluster velocity assumed constant at 0.6 m/s and the thermophysical particle properties typical of sand. The dashed lines show the change in the wall heat transfer coefficient with bed density, using the value given by Eq. 5.3 for the gas layer thickness. Figure 5.20 shows that for heat transfer surfaces of either 10 cm or 100 cm, transient conduction in the cluster is the dominant resistance to heat transfer (the resistance being the reciprocal of the heat transfer coefficients plotted

in the figure) for particle sizes up to 200 μm in diameter. It appears that the wall heat transfer coefficient drops more steeply with decreasing solid concentration than the cluster heat transfer coefficient, so that the wall resistance becomes increasingly important at the lower bed densities. However, it should be remembered that the lowest solid concentration of the data on which the figure is based was $\bar{c} \approx 0.0035$. Furthermore, at a value of $\bar{c} = 0.0025$, the corresponding average cluster solid fraction given by Eq. 3.6 is 5%, which was proposed in Chapter 3 as the point of division between the dense phase and the dilute phase. Therefore, the proposed heat transfer model may not be applicable at cross-section average solid concentrations below this value, and the low density region of Figure 5.20 should be regarded with suspicion.

For both the 10 cm heat transfer surface and the 1.5 m surface, the higher predictions given by the model of homogeneous clusters at a uniform distance match the experimental data fairly closely. This suggests that the proposed flow structure of homogeneous clusters with a gas layer of constant thickness can provide a good estimate of the heat transfer coefficient. It does appear to overpredict the heat transfer coefficient for short heat transfer surfaces (or equivalently, for short contact times between clusters and the wall). This apparent inaccuracy could be the result of varying porosity in the clusters. For very short times, the portion of the cluster nearest the wall is most affected by the heat transfer. If that part of the cluster has a lower solid concentration than the bulk of the cluster, then according to Eq. 2.3 the transient conduction in the cluster would be less than would otherwise be expected in a strictly homogeneous cluster.

In packed beds, it has been shown that the solid fraction increases from zero at the wall to its uniform core value in about 0.5 d_p [Yagi and Kunii (1961); Pillai (1977)]. The transition in the solid fraction for clusters at the wall of a CFB will certainly be no more abrupt, and may be less so. If the thermal penetration depth into the cluster is approximated by $3.66\sqrt{\alpha t}$, then a cluster of 200 μm particles at 10% solids concentration would reach a thermal penetration of 1/2 d_p in roughly 5 ms. This compares to a total time for transient conduction within the cluster of about 17 ms for a 1 cm heat transfer surface. The average conduction heat transfer coefficient in such a case could be noticeably affected by a reduction in conduction for the first 5 ms; furthermore, if the packing disturbance within the cluster extends as far as one particle diameter, the thermal penetration depth may not reach the homogeneous portion of the cluster at all.

One way to model this effect is to suppose a cluster structure in which clusters are at a stance, δ, from the wall, and their solid fraction varies linearly from 0 to $\bar{c}_c$ as x^+ goes from δ to δ′. The numerical solution to the rate of heat transfer in such a situation is presented in Figure 5.17. As expected, the predicted heat transfer is less than that for uniform clusters at a fixed distance from the wall. The experimental data lies between the rates of heat transfer predicted by these two models, suggesting that the actual cluster structure may be intermediate to them.

It would be possible to refine the model in other ways to improve the agreement with the experimental data for the short surface, but there is little reason to do so. Heat transfer

surfaces in actual CFB combustors are sufficiently long that the thermal penetration depth into the cluster goes well beyond one particle diameter. The good agreement between the experimental data and the uniform cluster model predictions for the longer heat transfer surfaces indicate that the model is sufficiently accurate for those cases. There are other factors than the precise nature of the cluster structure which are important and the further study of which may provide greater benefit to understanding heat transfer at the wall in CFBs. These are the subject of Chapter 6.

Chapter 6

Conclusions and Recommendations

A heat transfer model of particle convection in CFBs which was previously published in the literature has been examined closely by this thesis. The model contains five parameters which are either unknown, or known uncertainly. Each of those parameters has been considered individually, through interpretation of experimental results in the literature and original experimental work. A "design rule" has been suggested for each of these parameters. These rules have been correlated to the extent possible with the cross-section average bed density, usually as indicated by the bed pressure gradient. This is an easily measured operating parameter, and, based on the results on numerous researchers, of primary importance to the rate of heat transfer.

The use of these design rules, along with the heat transfer model on which they are based, provides good estimates of the heat transfer coefficient for heat transfer surfaces longer than a few centimeters. However, there is further work which should be performed before these results can be of general use in the design of CFB combustors.

First of all, it is necessary to include the radiation component of the heat transfer. At the elevated temperatures present inside combustors, radiation contributes substantially to the rate of heat transfer. As discussed in Chapter 2, this is particularly true at the low bed densities commonly found in commercial CFB combustors. Due to the coupling between

the radiative and convective modes of heat transfer, it is necessary to know the distribution of particles within the bed and, especially, near the wall in order to calculate the radiation component of the heat transfer. If the particle distribution is sufficiently well known, then it should be relatively straightforward to predict the radiation heat transfer in the bed. It is hoped that this thesis provides a good foundation for such work.

Another area which should be examined further is the pattern of particle circulation within the bed. It has been assumed in this work that particles arrive at the wall and move down along it in well-defined clusters, which remain at the wall and maintain their identity for at least the length of the heat transfer surface. This may well be the case, or at least a close approximation, for relatively short heat transfer surfaces. However, for the long surfaces typically found in commercial CFB combustors, this model of cluster motion may not strictly apply. Particles from the core may be deposited on and mixed with clusters already at the wall; or, clusters may get swept from the wall and re-entrained in the core flow after some residence time or length at the wall.

If such re-entrainment occurs frequently, then it may be appropriate to consider a characteristic length of contact between the wall and the cluster which is substantially less than the overall length of the heat transfer surface. Such a characteristic length was a feature in the heat transfer models of both Wu (1989) and Dou (1990). Dou suggests that the length of contact is of order 10 cm, and varies linearly with the particle diameter, whereas Wu's model gave the best agreement with experimental data at "very large" residence length (>1.7 m). It may be that the slight tendency for the present model to

underpredict the experimental data for the long (1.5 m) heat transfer surface evidenced in Figure 5.19 is due to this effect. Figure 5.19 contains an additional curve which shows the predicted heat transfer coefficient calculated for a heat transfer surface one meter in length; it appears to give somewhat better agreement with the experimental data. This suggests that a characteristic residence length for clusters at the wall of order 1 m may be appropriate. This is also indicated by the local heat transfer measurements of Wu et al. (1989b) on a 1.59-m long heat transfer surface. They show an initial decrease in heat transfer along the length of the surface which reaches a roughly constant value at a length of about 1 m. This issue is of obvious importance in the design of commercial CFB equipment, and should be examined further.

The most important limitation in the applicability of this work to the design of CFB combustors may be the problem of scaling the results. The important hydrodynamic parameters which govern the heat transfer process exist within a relatively thin layer at the wall, but they have been correlated against the cross-section average solid concentration. The data on which those correlations are based were generally from small laboratory-scale CFBs with bed diameters from 5 to 20 cm. Although the same basic model of heat transfer should still apply and the same hydrodynamic parameters should govern the process in larger beds, the relation of those parameters within the wall layer to the average conditions across the entire area of the bed can be expected to change substantially between beds of greatly different size. The issue of scaling the hydrodynamics of CFBs for beds of different size remains as one of the most critical areas for further study.

References

Acree Riley, C. and M. Louge, "Quantitative Capacitive Measurements of Voidage in Gas-Solid Flows," Particulate Sci. & Technol., 7, 51, 1989.

Andersson, B.-A., F. Johnsson and B. Leckner, "Heat Flow Measurements in Fluidized Bed Boilers," Proc. 9th Int. Conf. Fluidized Bed Combustion, 592-598, Boston, Mass., May, 1987.

Arena, U., A. Commarota, L. Massimilla and D. Pirozzi, "The Hydrodynamic Behavior of Two Circulating Fluidized Bed Units of Different Sizes," in Circulating Fluidized Bed Technology II, P. Basu and J.F. Large, eds., Pergammon Press, 1988.

Bader, R., J. Findlay and T.M. Knowlton, "Gas/Solid Flow Patterns in a 30.5-cm-Diameter Circulating Fluidized Bed," in Circulating Fluidized Bed Technology II, P. Basu and J.F. Large, eds., Pergammon Press, 1988.

Baskakov, A.P., "The Mechanism of Heat Transfer between a Fluidized Bed and a Surface," Int. Chem. Eng., 4, 320-324, April, 1964.

Basu, P. and P.K. Nag, "An Investigation into Heat Transfer in Circulating Fluidized Beds," Int. J. Heat Mass Transfer, 30, 2399-2409, 1987.

Basu, P., P.K. Nag, B.H. Chen and M. Shao, "Effect of Operating Variables on Bed to Wall Heat Transfer in a Circulating Fluidized Bed," Chem. Eng. Comm., 61, 227-237, 1987.

Basu, P. and F. Konuche, "Radiative Heat Transfer from a Fast Fluidized Bed," in Circulating Fluidized Bed Technology II, P. Basu and J.F. Large, eds., Pergammon Press, 1988.

Basu, P., "Heat Transfer in High Temperature Fast Beds," Chem. Eng. Sci., 45, 3123-3136, 1990.

Basu, P., D. Lawrence, M.N. Ali Moral and P.K. Nag, "An Experimental Investigation into the Effect of Fins on Heat Transfer in Circulating Fluidized Beds," Int. J. Heat Mass Transfer, 34, 2317-2326, 1991.

Brereton, C. and L.Stromberg, "Some Aspects of the Fluid Dynamic Behavior of Fast Fluidized Bed," in Circulating Fluidized Bed Technology, P. Basu, ed., Pergamon Press, 1986.

Brereton, C., "Fluid Mechanics of High Velocity Fluidised Beds," Doctoral Thesis, University of British Columbia, 1987.

Boyd, T.J. and M.A. Friedman, "Operations and Test Program summary at the 110 MWe Nucla CFB," in Circulating Fluidized Bed Technology III, P. Basu, M. Horio and M. Hasatani, eds., Pergamon Press, 1991.

Chatterjee, S. and B. Price, Regression Analysis by Example, pp. 2-5, Wiley, 1977.

Chen, J.C., R.J. Cimini and S.-S. Dou, " A Theoretical Model for Simultaneous Convective and Radiative Heat Transfer in Circulating Fluidized Beds," in Circulating Fluidized Bed Technology II, P. Basu and J.F. Large, eds., Pergamon Press, 1988.

Dou, S., "Experimental Study of Heat Transfer in Circulating Fluidized Beds," Doctoral Thesis, Lehigh University, 1990.

Ebert, T., L.R. Glicksman and M. Lints, "Heat Transfer in Circulating Fluidized Beds, Determination of Particle Convective and Gas Convective Components," presented at 1990 AIChE Annual Meeting, Chicago, Ill., November, 1990.

Ebert, T., "An Experimental Investigation of Particle and Gas Convection Heat Transfer in a Circulating Fluidized Bed," Masters Thesis, Mass. Inst. of Tech., 1991.

Feugier, A., C. Gaulier and G. Martin, "Some Aspects of Hydrodynamics, Heat Transfer and Gas Combustion in Circulating Fluidized Beds," Proc. 9th Int. Conf. Fluidized Bed Combustion, 613-618, Boston, Mass., May, 1987.

Furchi, J.C.L., L. Goldstein Jr., G. Lombardi and M. Mohseni, "Experimental Local Heat Transfer in a Circulating Fluidized Bed," in Circulating Fluidized Bed Technology II, P. Basu and J.F. Large, eds., Pergamon Press, 1986.

Geldart, D., "Types of Gas Fluidization," Powder Technology, 7, 285-292, 1973.

Gelperin, N.I. and V.G. Einstein, "Heat Transfer in Fluidized Beds," in Fluidization, J.F. Davidson and D. Harrison, eds., Academic Press, 1971.

Gidaspow, D., Y.P. Tsuo and K.M. Luo, "Computed and Experimental Cluster Formation and Velocity Profiles in Circulating Fluidized Beds," in Fluidization VI, J.R. Grace, L.W. Shemilt and M.A. Bergougnou, eds., Engineering Foundation, 1989.

Glicksman, L.R., "Circulating Fluidized Bed Heat Transfer," in Circulating Fluidized Bed Technology II, P. Basu and J.F. Large, eds., Pergammon Press, 1988.

Glicksman, L.R., M. Lints and Y. Katoh, "Visualization of the Particle Behavior Near the Wall of a Circulating Fluidized Bed," Video Presentation at the 2nd ASME-JSME Fluid-Engineering Joint Conference, Nagoya, Japan, October, 1990.

Gloski, D., L. Glicksman and N. Decker, "Thermal Resistance at a Surface in Contact with Fluidized Bed Particles," Int. J. Heat Mass Transfer, 27, 599-610, 1984.

Grace, J.R., "Heat Transfer in Circulating Fluidized Beds", in Circulating Fluidized Bed Technology, P. Basu, ed., Pergamon Press, 1986.

Hartge, E.-U., Y. Li and J. Werther, "Analysis of the Local Structure of the Two-Phase Flow in a Fast Fluidized Bed," in Circulating Fluidized Bed Technology, P. Basu, ed., Pergamon Press, 1986.

Hartge, E.-U. and J. Werther, "Strömungsstrukturen in zirkulierenden Wirbelschichten," Chem.-Ing.-Tech., 58, 688-689, 1986.

Hartge, E.-U., D. Rensner and J. Werther, "Solids Concentration and Velocity Patterns in Circulating Fluidized Beds," in Circulating Fluidized Bed Technology II, P. Basu and J.F. Large, eds., Pergamon Press, 1988.

Herb, B.E., "A Study of Solid Particle Distribution in Circulating Fluidized Beds," Doctoral Thesis, Lehigh University, 1990.

Horio, M., K. Morishita, O. Tachibana and N. Murata, "Solid Distribution and Movement in Circulating Fluidized Beds," in Circulating Fluidized Bed Technology II, P. Basu and J.F. Large, eds., Pergamon Press, 1988.

Hovmand, S. and J.F. Davidson, "Pilot Plant and Laboratory Scale Fluidized Reactors at High Gas Velocities; the Relevance of Slug Flow," in Fluidization, J.F. Davidson and D. Harrison, eds., Academic Press, 1971.

Huber, Peter J., Professor of Applied Mathematics, MIT, personal communication, September, 1991.

Jahnig, C.E., D.L. Campbell and H.Z. Martin, "History of Fluidized Solids Development at Exxon," in Fluidization, J.R. Grace and J.M. Matsen, eds., Plenum Press, 1980.

Karlekar, B.V. and R.M. Desmond, Heat Transfer, 2nd ed., p. 531, West Publishing Co., 1982.

Kato, K., T. Takarada, T. Tamura and K. Nishino, "Particle Hold-up Distribution in a Circulating Fluidized Bed,", in Circulating Fluidized Bed Technology III, P. Basu, M. Horio and M. Hasatani, eds., Pergamon Press, 1991.

Kays, W.M. and H.C. Perkins, "Forced Convection, Internal Flow in Ducts," in Handbook of Heat Transfer, W.M. Rohsenow and J.P. Hartnett, eds., McGraw-Hill, 1973.

Kehoe, P.W.K. and J.F. Davidson, "Continuously Slugging Fluidized Beds," Inst. Chem. Eng. (London) Symp. Ser., 33, 97, 1971.

Kobro H. and C. Brereton, "Control and Fuel Flexibility of Circulating Fluidized Beds," in Circulating Fluidized Bed Technology, P. Basu, ed., Pergamon Press, 1986.

Kudo, K., H. Taniguchi, Y.-M. Kim and W.-J. Yang, "Transmittance of Radiative Energy through Three-Dimensional Packed Spheres," presented at ASME-JSME Thermal Engineering Conference, Reno, Nevada, March, 1991.

Kunii, D. and O. Levenspiel, Fluidization Engineering, p. 202, Wiley, 1969.

Kunii, D. and O. Levenspiel, "A General Equation for the Heat-Transfer Coefficient at Wall Surfaces of Gas/Solid Contactors," Ind. Eng. Chem. Res., 30, 136-141, 1991a.

Kunii, D. and O. Levenspiel, "Flow Modeling of Fast Fluidized Beds," in Circulating Fluidized Bed Technology III, P. Basu, M. Horio and M. Hasatani, eds., Pergamon Press, 1991b.

Lancia, A., R. Migro, G. Volpicelli and L. Santoro, "Transition from Slugging to Turbulent Flow Regimes in Fluidized Beds Detected by Means of Capacitance Probes," Powder Technology, 56, 49-56, 1988.

Lanneau, M.A., "Gas-Solids Contacting in Fluidized Beds," Trans. Instn. Chem. Engrs., 38, 125-137, 1960.

Leckner, B., "Heat Transfer in Circulating Fluidized Beds," in Circulating Fluidized Bed Technology III, P. Basu, M. Horio and M. Hasatani, eds., Pergamon Press, 1991.

Leva, M., M. Grummer, M. Weintraub and M. Pollchik, "Introduction to Fluidization," Chem. Eng. Prog., 44, 511-520, 1948.

Li, Y. and M. Kwauk, "The Dynamics of Fast Fluidization," in Fluidization, J.R. Grace and J.M. Matsen, eds., Plenum Press, 1980.

Li, J., Y. Xia, Y. Tung and M. Kwauk, "Micro-Visualization of Two-Phase Structure in a Fast Fluidized Bed," in Circulating Fluidized Bed Technology III, P. Basu, M. Horio and M. Hasatani, eds., Pergamon Press, 1991.

Louge, M. and H. Chang, "Pressure and Voidage Gradients in Vertical Gas-Solid Risers," Powder Technology, 60, 197-201, 1990.

Louge, M., J. Lischer and H. Chang, "Measurements of Voidage Near the Wall of a Circulating Fluidized Bed Riser," Powder Technology, 62, 269-276, 1990.

Mack, G. and G. Gould, "CFB Boiler Designs Address Project-Specific Requirements," Power, 29-31, January, 1988.

Mahalingam, M. and A.J. Kolar, "Emulsion Layer Model for Wall Heat Transfer in a Circulating Fluidized Bed," AIChE Journal, 37, 1139-1150, 1991.

Martin, H., "Heat Transfer between Gas Fluidized Beds of Solid Particles and the Surfaces of Immersed Heat Exchanger Elements, Parts I and II," Chem. Eng. Proc., 18, 157, 1984.

Maxwell, J.C., A Treatise on Electricity and Magnetism, 3rd ed., Vol I, p. 440, Oxford, 1892.

Mickley, H.S. and D.F. Fairbanks, "Mechanisms of Heat Transfer to Fluidized Beds," AIChE Journal, 1, 374-384, 1955.

Nakajima, M., M. Harada, M. Asai, R. Yamazaki and G. Jimbo, "Bubble Fraction and Voidage in an Emulsion Phase in the Transition to a Turbulent Fluidized Bed," in Circulating Fluidized Bed Technology III, P. Basu, M. Horio and M. Hasatani, eds., Pergamon Press, 1991.

Nowak, W., H. Mineo, R. Yamazaki and K. Yoshida, "Behavior of Particles in a Circulating Fluidized Bed of a Mixture of Two Different Sized Particles," in Circulating Fluidized Bed Technology III, P. Basu, M. Horio and M. Hasatani, eds., Pergamon Press, 1991.

Petukhov, B.S., "Heat Transfer and Friction in Turbulent Pipe Flow with Variable Physical Properties," in Advances in Heat Transfer, T.F. Irvine, Jr. and J.P. Hartnett, eds., Academic Press, 1970.

Pillai, K.K., "Voidage Variation at the Wall of a Packed Bed of Spheres," Chem Eng Sci, 32, 59-61, 1977.

Press, W.H., B.P. Flannery, S.A. Teukolsky and W.T. Vetterling, Numerical Recipes, the Art of Scientific Computing (FORTRAN version), Cambridge University Press, 1989.

Reh, L. and J. Li, "Measurement of Voidage in Fluidized Beds by Optical Probes," in Circulating Fluidized Bed Technology III, P. Basu, M. Horio and M. Hasatani, eds., Pergamon Press, 1991.

Rhodes, M.J., H. Mineo and T. Hirama, "Particle Motion at the Wall of the 305 mm Diameter Riser of a Cold Model Circulating Fluidized Bed," in Circulating Fluidized Bed Technology III, P. Basu, M. Horio and M. Hasatani, eds., Pergamon Press, 1991.

Rowe, P.N., B.A. Partridge and E. Lyall, "Bubbles in Fluidized Beds," Nature, 195, 278-279, July 21, 1962.

Sekthira, A., Y.Y. Lee and W.E. Genetti, "Heat Transfer in a Circulating Fluidized Bed," presented at 25th National Heat Transfer Conference, Houston, Texas, July, 1988.

Subbarao, D. and P. Basu, "A Model for Heat Transfer in Circulating Fluidized Beds," Int. J. Heat Mass Transfer, 29, 487-489, 1986.

Van Swaaij, W.P.M., C. Buurman and J.W. Van Breugel, "Shear Stresses on the Wall of a Dense Gas-Solids Riser," Chem Eng Sci, 25, 1818-1820, 1970.

Wen, C.-Y. and E.N. Miller, "Heat Transfer in Solids-Gas Transport Lines," Ind. Eng. Chem., 53, 51-53, 1961.

Weinstein, H., M. Shao and M. Schnitzlein, "Radial Variation in Solid Density in High Velocity Fluidization," in Circulating Fluidized Bed Technology, P. Basu, ed., Pergamon Press, 1986.

Wirth, K.E. and M. Seiter, "Solids Concentration and Solids Velocity in the Wall Region of Circulating Fluidized Beds," Proc. 1991 Int. Conf. on Fluidized Bed Combustion, Vol. 1, 311-316, Montreal, Quebec, April, 1991.

Wu, R.L., C.J. Lim, J. Chaouki and J.R. Grace, "Heat Transfer from a Circulating Fluidized Bed to Membrane Waterwall Surfaces," AIChE Journal, 33, 1888-1893, 1987.

Wu, R.L., "Heat Transfer in Circulating Fluidized Beds," Doctoral Thesis, University of British Columbia, 1989.

Wu, R.L., C.J. Lim and J.R. Grace, "The Measurement of Instantaneous Local Heat Transfer Coefficients in a Circulating Fluidized Bed," Can. J. Chem. Eng., 67, 301-307, 1989a.

Wu, R.L., J.R. Grace, C.J. Lim and C.M.H. Brereton, "Suspension-to-Surface Heat Transfer in a Circulating-Fluidized-Bed Combustor," AIChE Journal, 35, 1685-1691, 1989b.

Wu, R.L., C.J. Lim, J.R. Grace and C.M.H. Brereton, "Instantaneous Local Heat Transfer and Hydrodynamics in a Circulating Fluidized Bed," Int. J. Heat Mass Transfer, 34, 2019-2027, 1991.

Yagi, S. and D.Kunii, "Studies on Heat Transfer in Packed Beds," Int. Heat Transfer Dev., 4, 750-757, 1961.

Yang, W.C., "A Model for the Dynamics of a Circulating Fluidized Bed Loop," in Circulating Fluidized Bed Technology II, P. Basu and J.F. Large, eds., Pergamon Press, 1988.

Yang, Y.-L., Y. Jin, Z.-Q. Yu, Z.-W. Wang and D.-R. Bai, "The Radial Distribution of Local Particle Velocity in a Dilute Circulating Fluidized Bed," presented at 3rd International Conference of Circulating Fluidized Beds, Nagoya, Japan, October, 1990.

Yerushalmi, J., D.H. Turner and A.M. Squires, "The Fast Fluidized Bed," Ind. Eng. Chem., Proc. Des. Dev., 15, 47-53, 1976.

Yerushalmi, J. and N.T. Cankurt, "Further Studies of the Regimes of Fluidization", Powder Technology, 24, 187-205, 1979.

Zhang, H., Y. Xie, Y. Chen and M. Hasatani, "Mathematical Modeling for Longitudinal Voidage Distribution of Fast Fluidized Beds," in Circulating Fluidized Bed Technology III, P. Basu, M. Horio and M. Hasatani, eds., Pergamon Press, 1991.

Appendix A

Particle Characteristics

80 μm Silica Particles

Bulk density = 1550 kg/m^3

Particle density = 2660 kg/m^3

Mean diameter = 80 μm

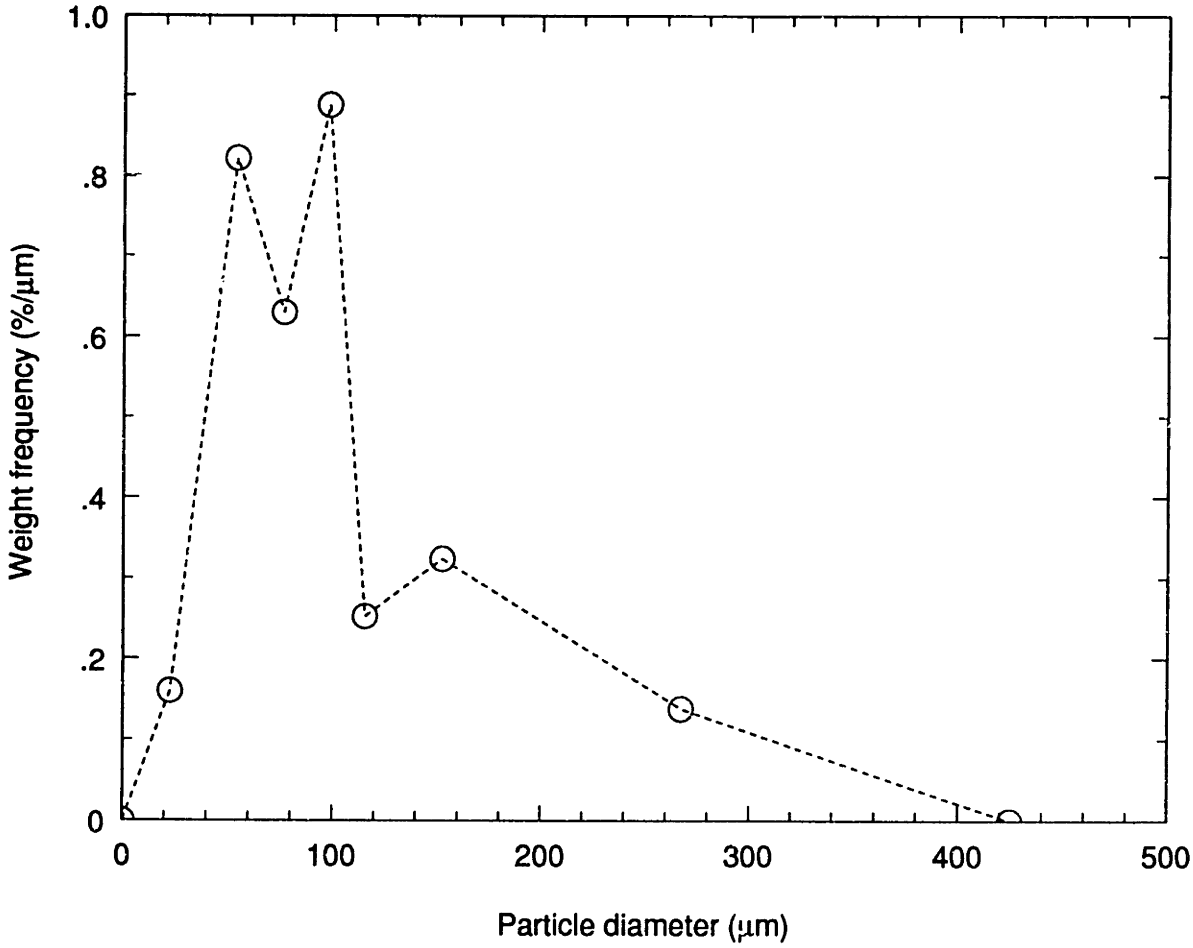

Figure A.1 - Results of sieve analysis for 80 μm silica

88 μm Glass Particles

Bulk density = 1420 kg/m^3

Particle density = 2400 kg/m^3

Mean diameter = 88 μm

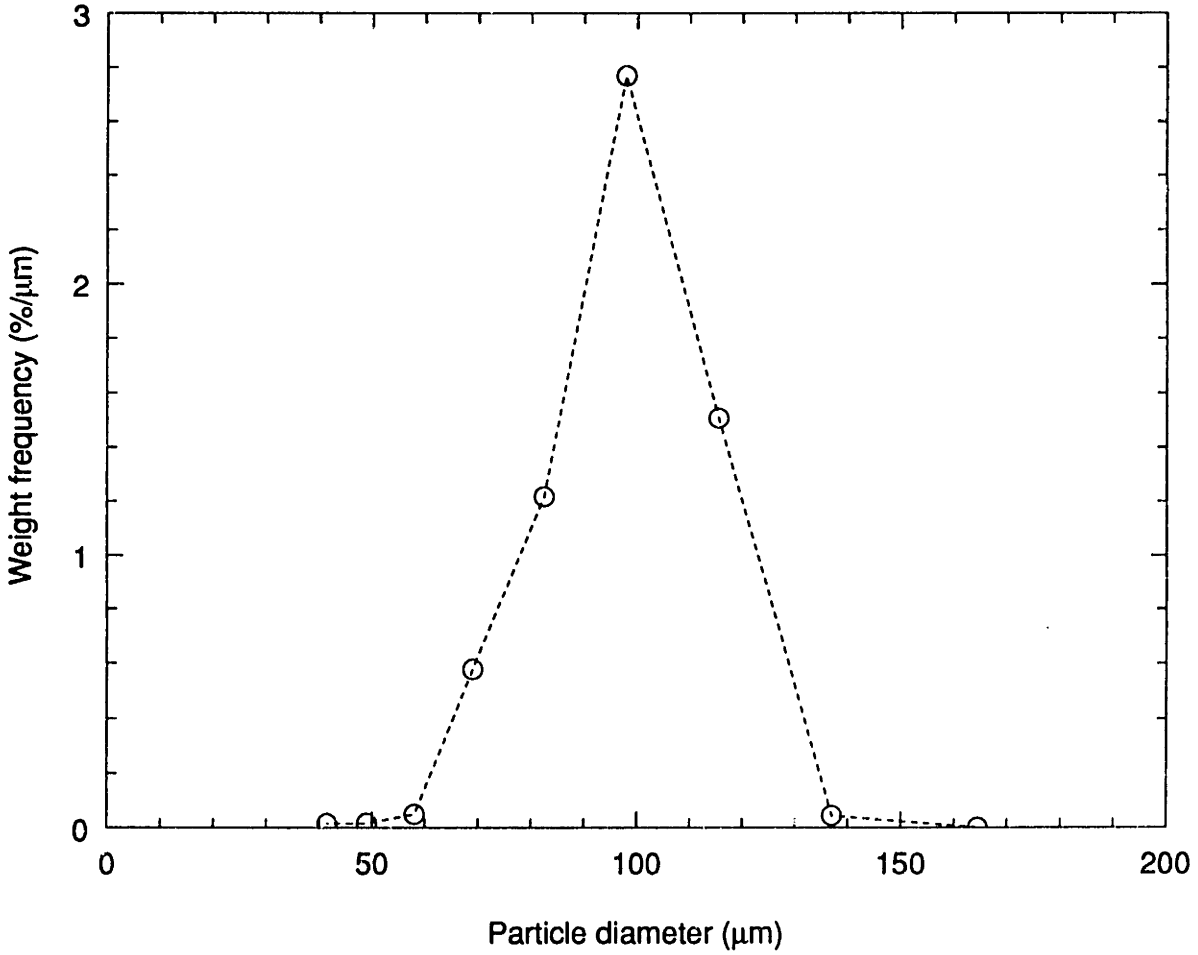

Figure A.2 - Results of sieve analysis of 88 μm glass beads

182 μm Quartz Sand Particles

Bulk density = 1400 kg/m^3

Particle density = 2350 kg/m^3

Mean diameter = 182 μm

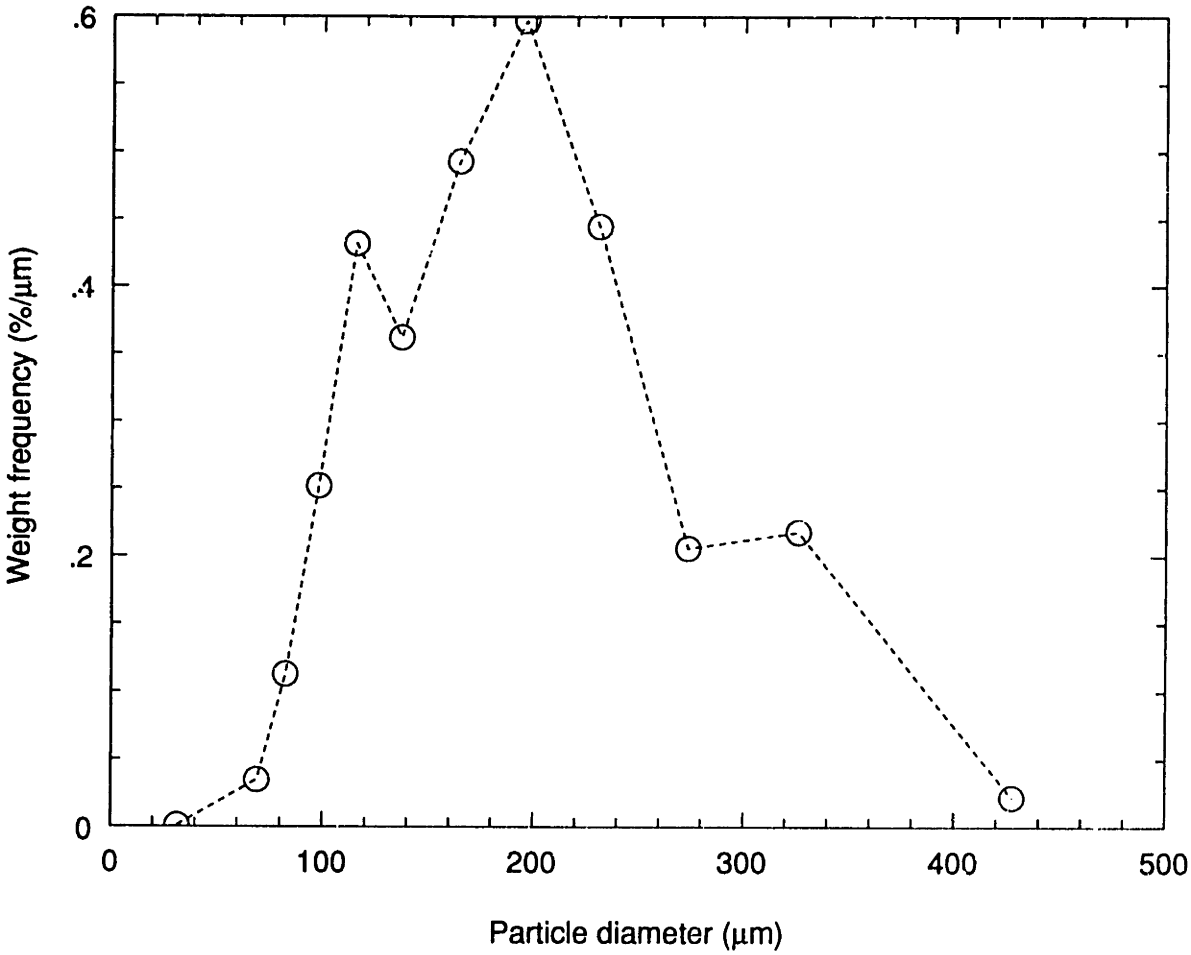

Figure A.3 - Results of sieve analysis of 182 μm quartz sand

600 μm Aluminum Particles

Bulk density = 1650 kg/m^3

Particle density = 2750 kg/m^3

Size range = 25 - 40 mesh

Mean diameter = ~600 μm

Blank page

Appendix B

Cluster Velocity Measurements

Figures B.1 - B.4:
Cluster velocity measurements in particle injection tube; 80 μm silica

Figures B.5 - B.8:
Cluster velocity measurements in particle injection tube; 600 μm aluminum

Figures B.9 - B.12:
Cluster velocity measurements in CFB; 88 μm glass beads

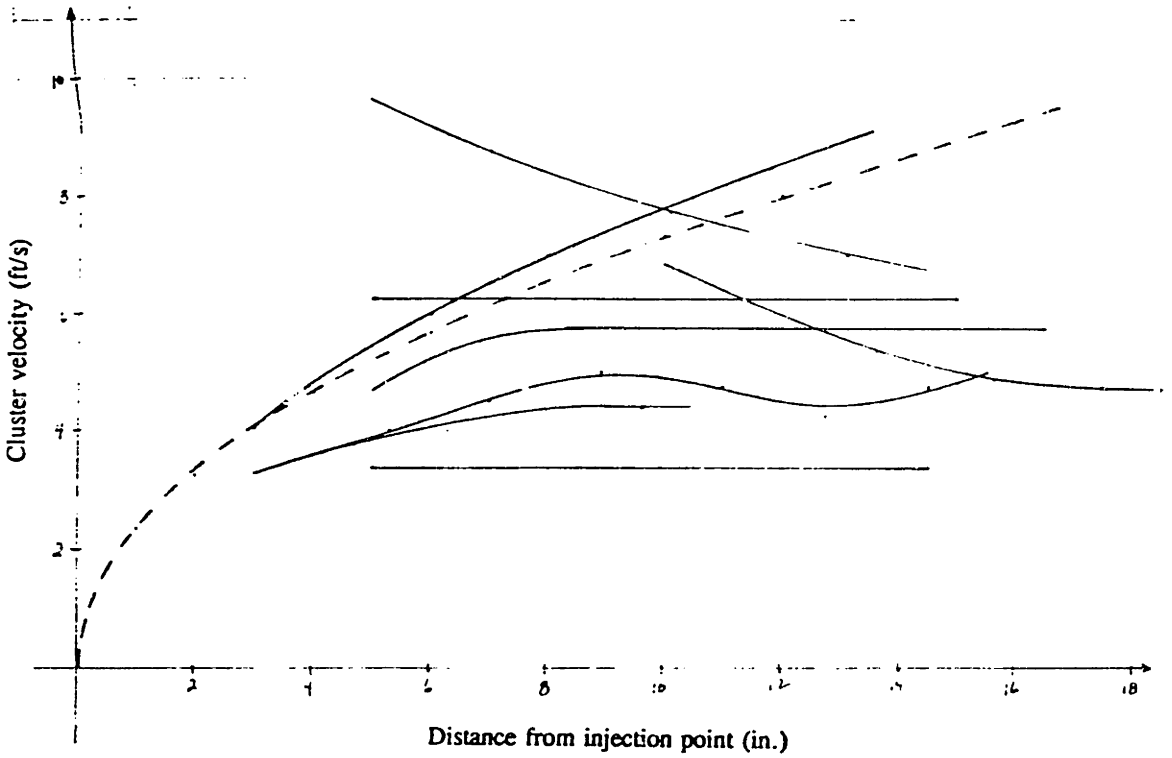

Figure B.1 - Cluster velocities for 80 μm silica; U = 0 m/s

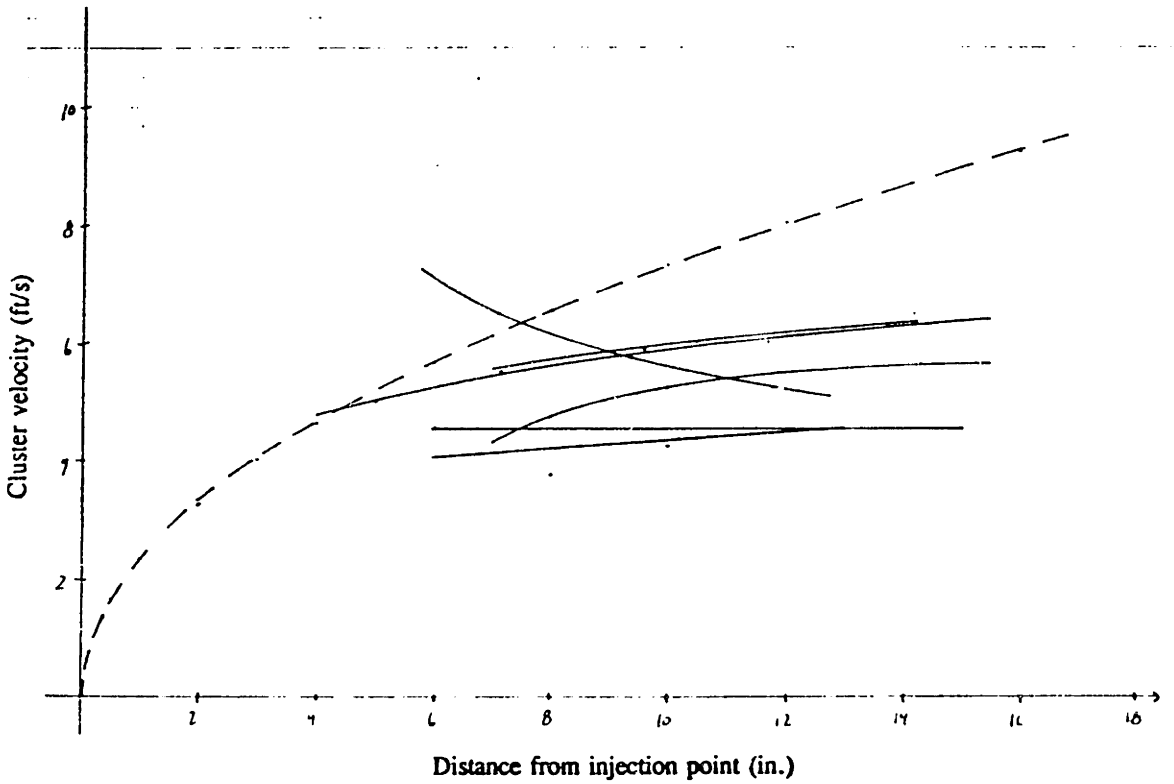

Figure B.2 - Cluster velocities for 80 μm silica; U_g = 1.5 m/s

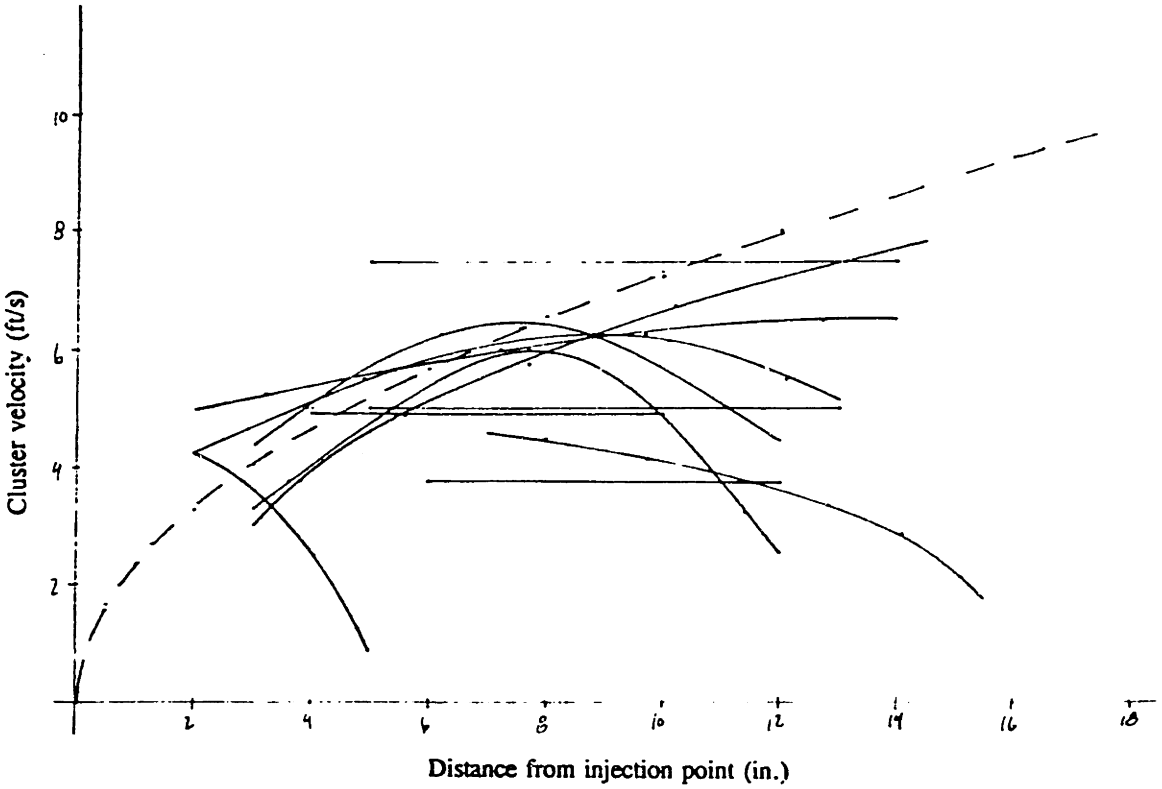

Figure B.3 - Cluster velocities for 80 μm silica; U = 4.0 m/s

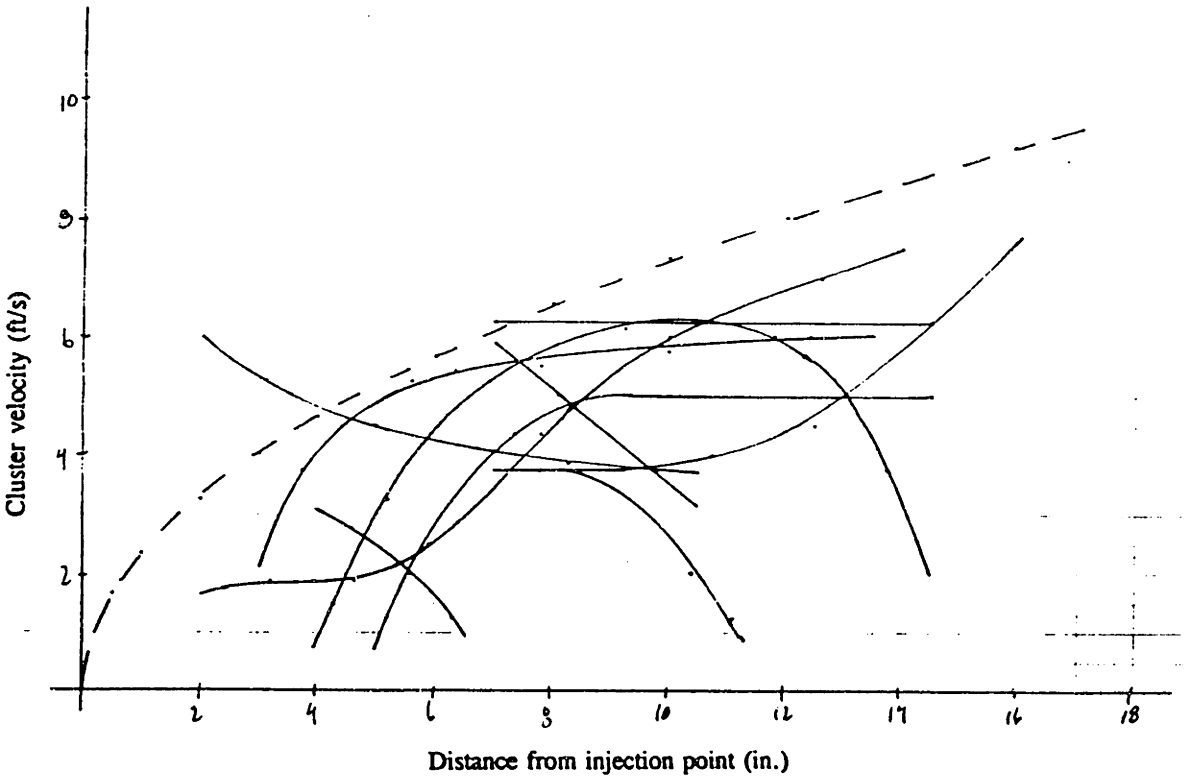

Figure B.4 - Cluster velocities for 80 μm silica; U_g = 6.8 m/s

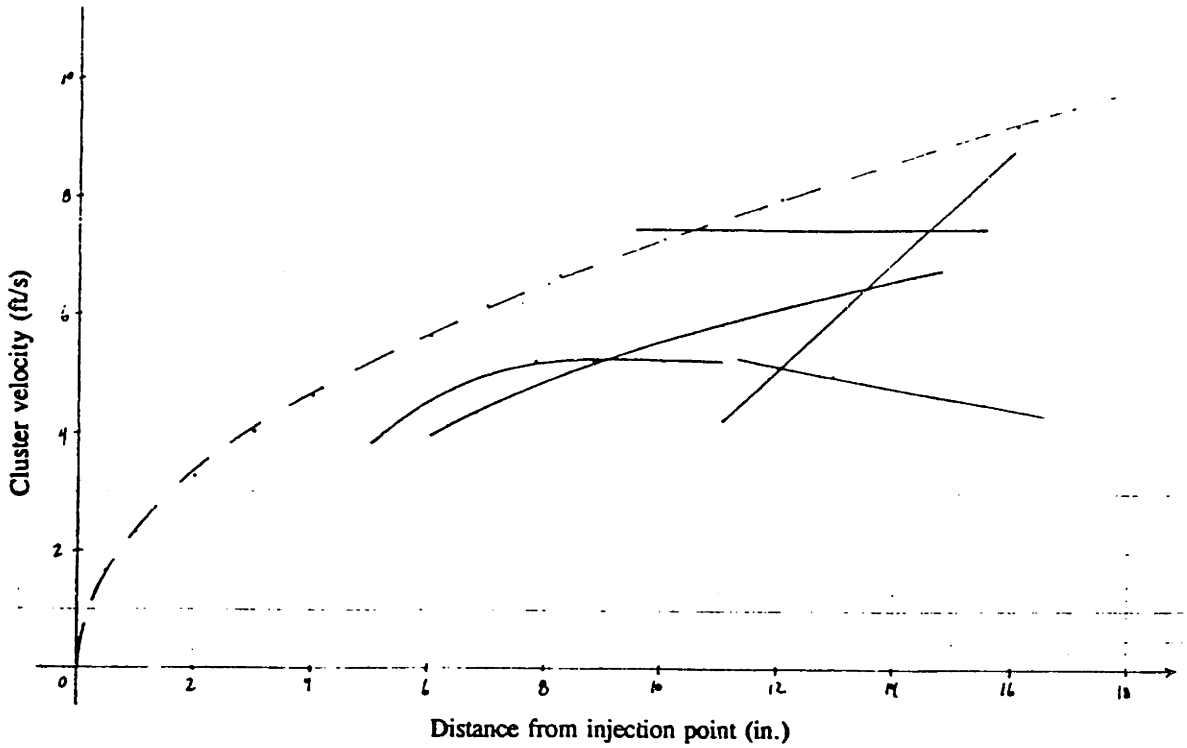

Figure B.5 - Cluster velocities for 600 μm aluminum; U = 0 m/s

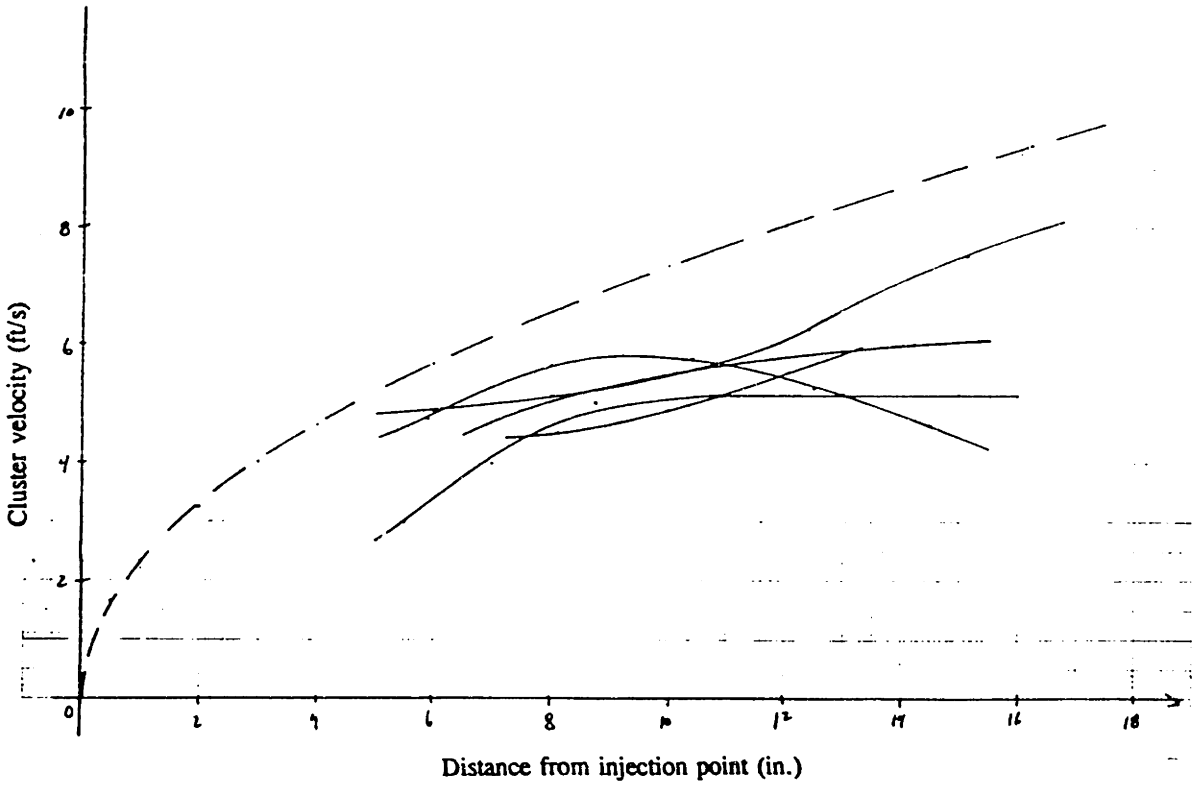

Figure B.6 - Cluster velocities for 600 μm aluminum; U = 5.7 m/s

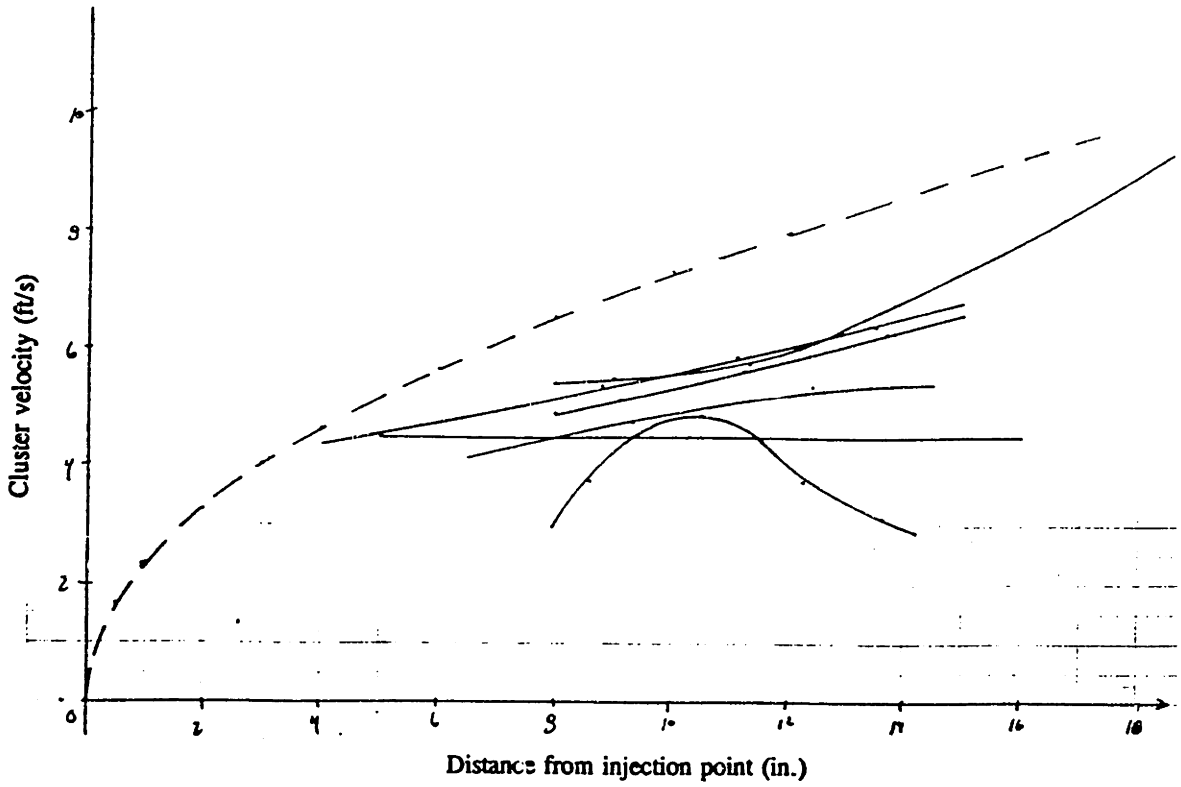

Figure B.7 - Cluster velocities for 600 μm aluminum; U_g = 7.8 m/s

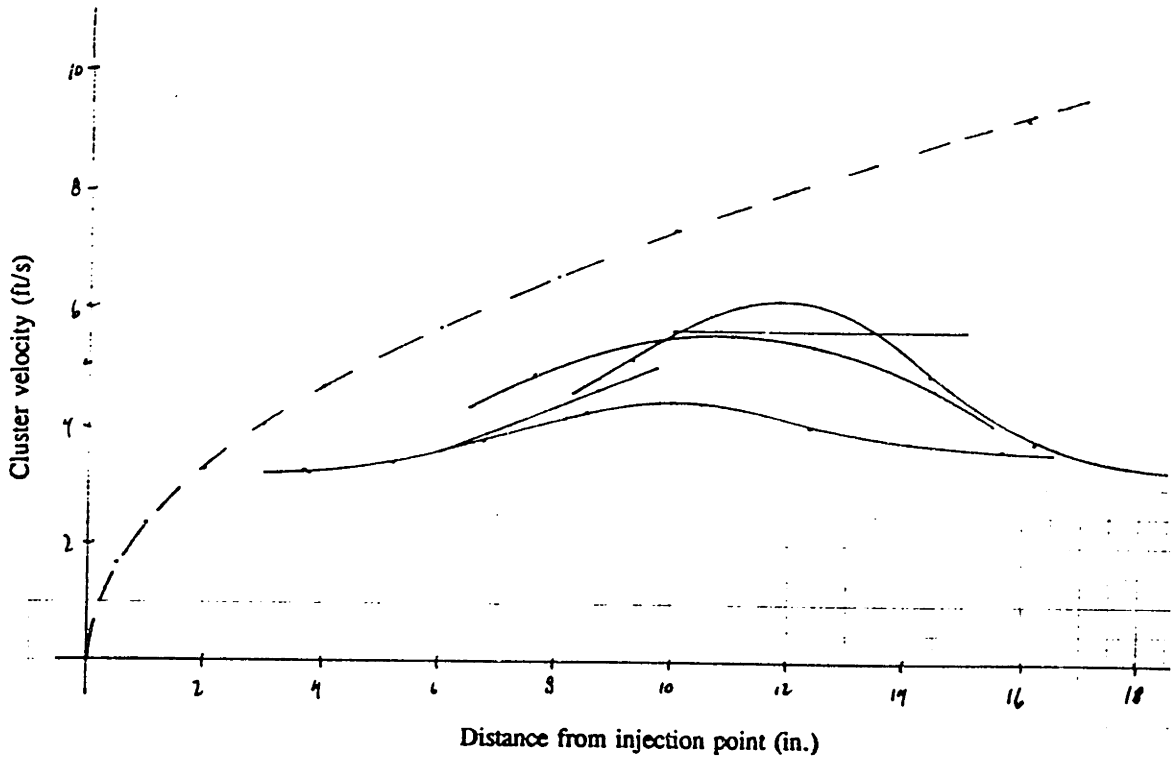

Figure B.8 - Cluster velocities for 600 μm aluminum; U = 9.6 m/s

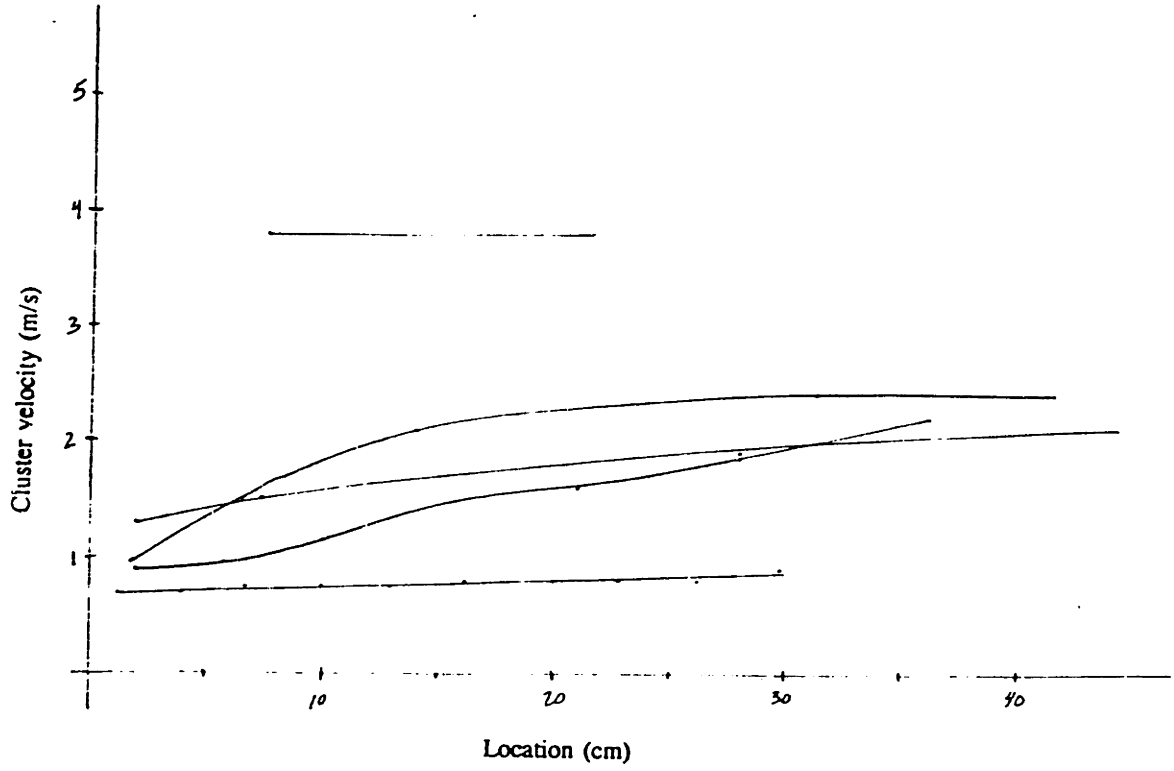

Figure B.9 - Cluster velocities for 88 μm glass beads; ρ_{bed} = 4.5 kg/m^3, U_g = 4.3 m/s

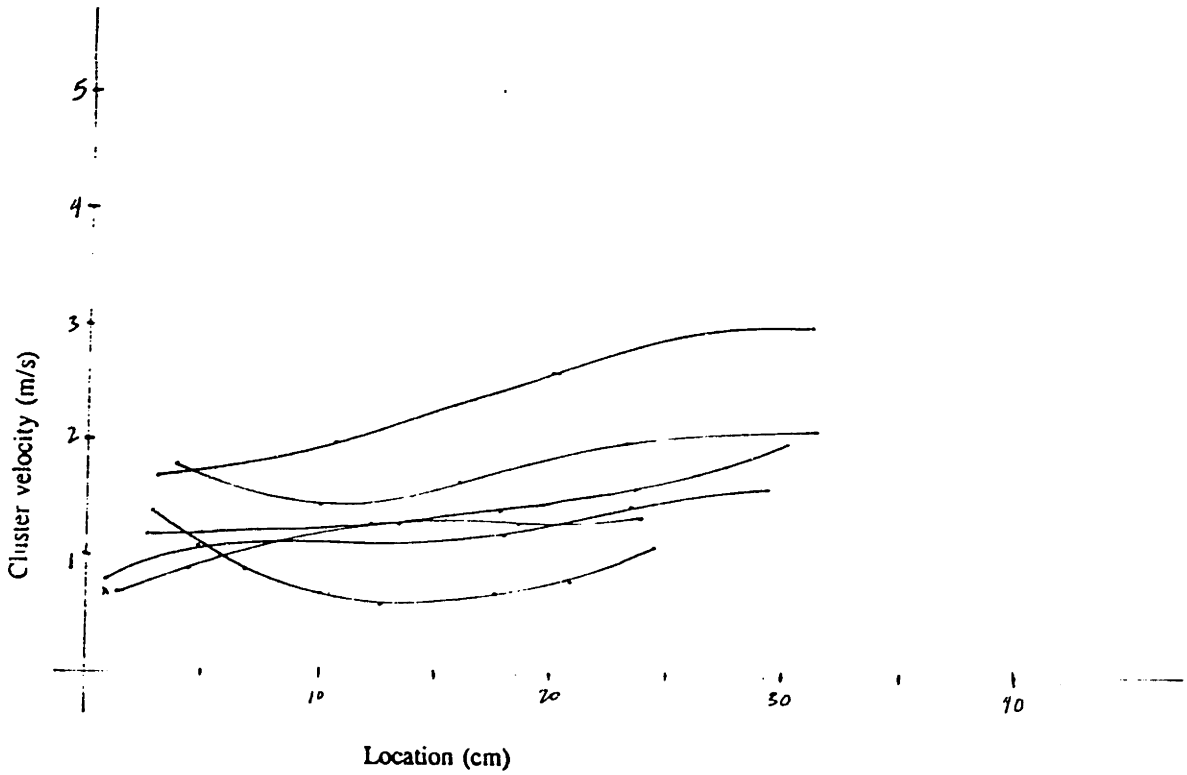

Figure B.10 - Cluster velocities for 88 μm glass beads; ρ_{bed} = 6.8 kg/m^3, U_g = 2.9 m/s

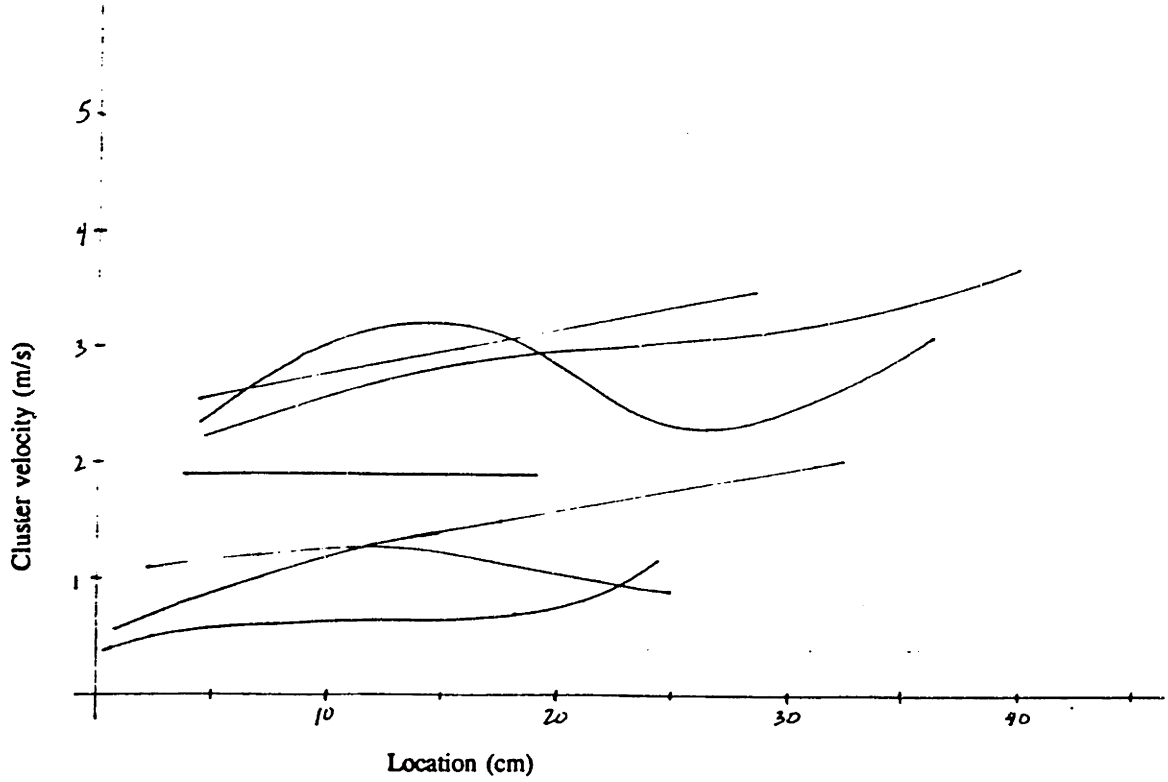

Figure B.11 - Cluster velocities for 88 μm glass beads; ρ_{bed} = 10.2 kg/m^3, U_g = 3.3 m/s

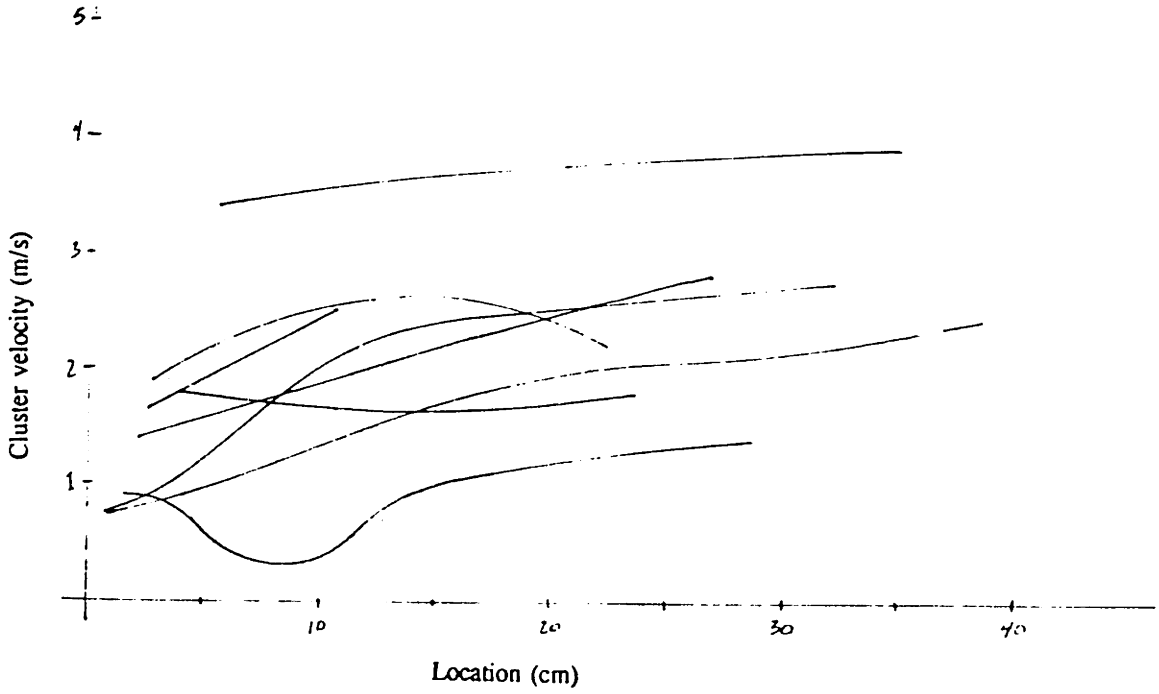

Figure B.12 - Cluster velocities for 88 μm glass beads; ρ_{bed} = 14.8 kg/m^3, U_g = 4.2 m/s

Blank page

Appendix C

Heat Transfer Measurements by Other Researchers at Low Density

Each figure also shows the least-squares linear curve fit to each set of data. Refer to Table 3.4 in the text for further details of the experimental conditions for these measurements.

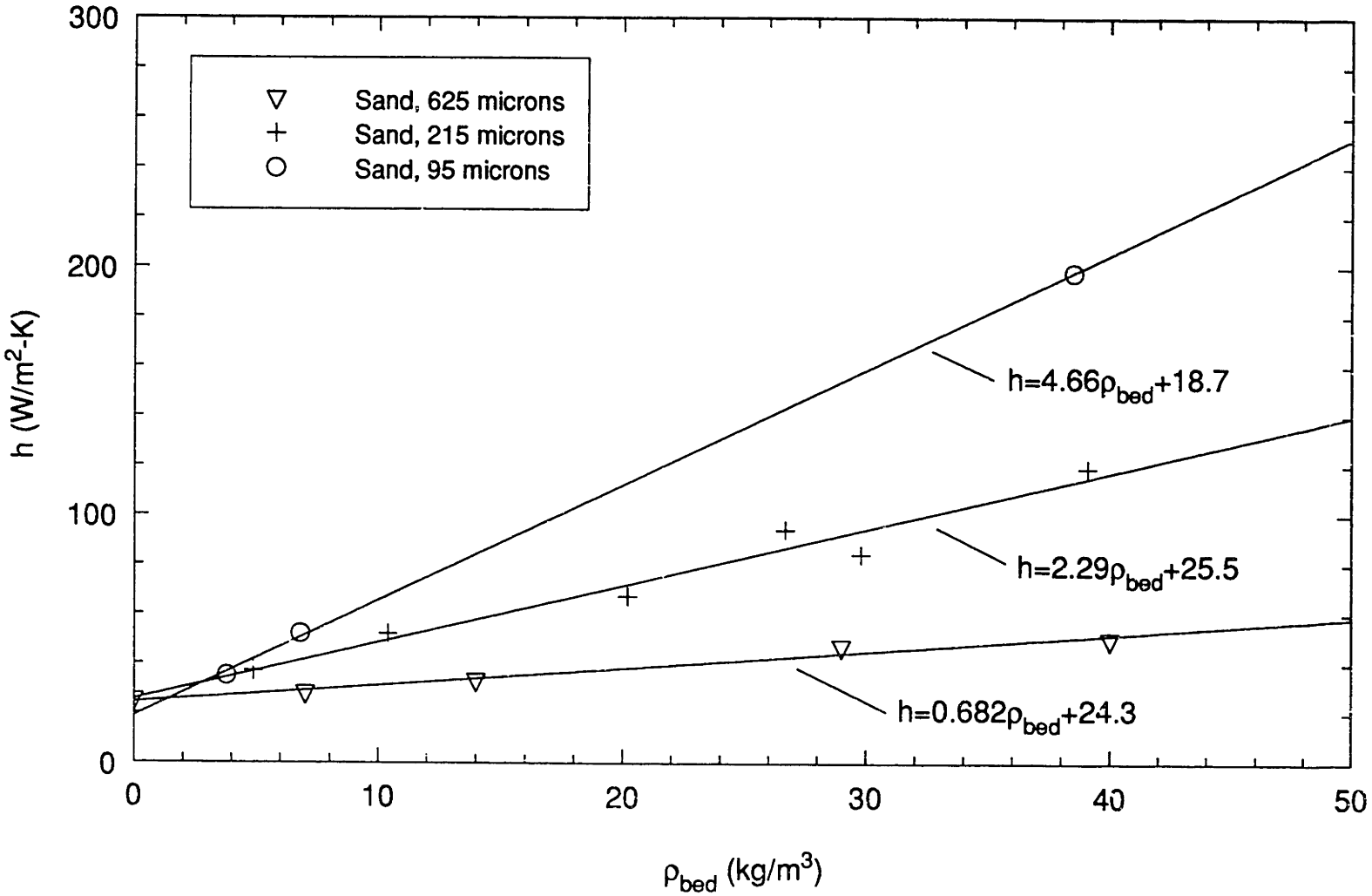

Figure C.1 - Heat transfer data of Feugier et al.(1987)

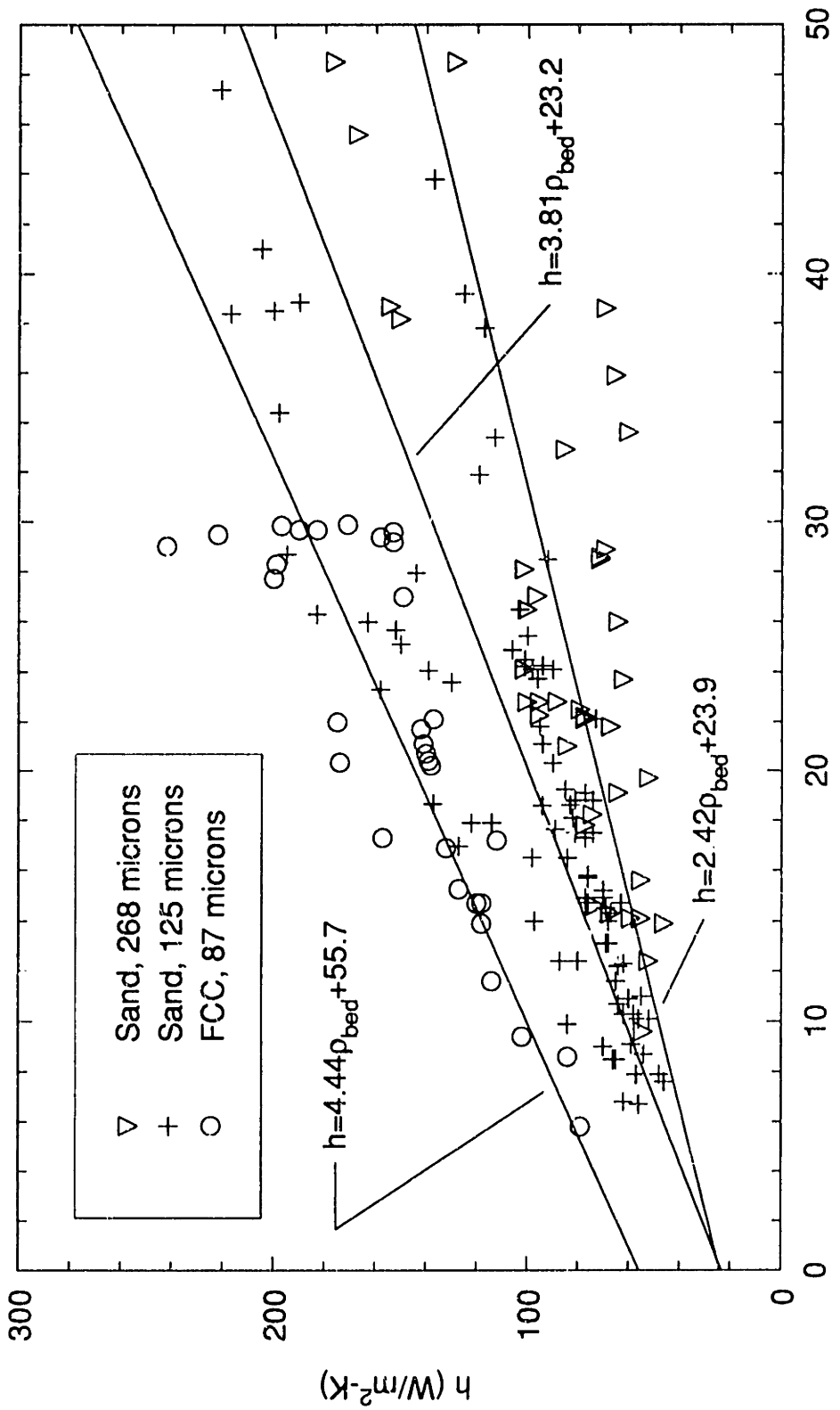

Figure C.2 - Heat transfer data of Dou (1990)

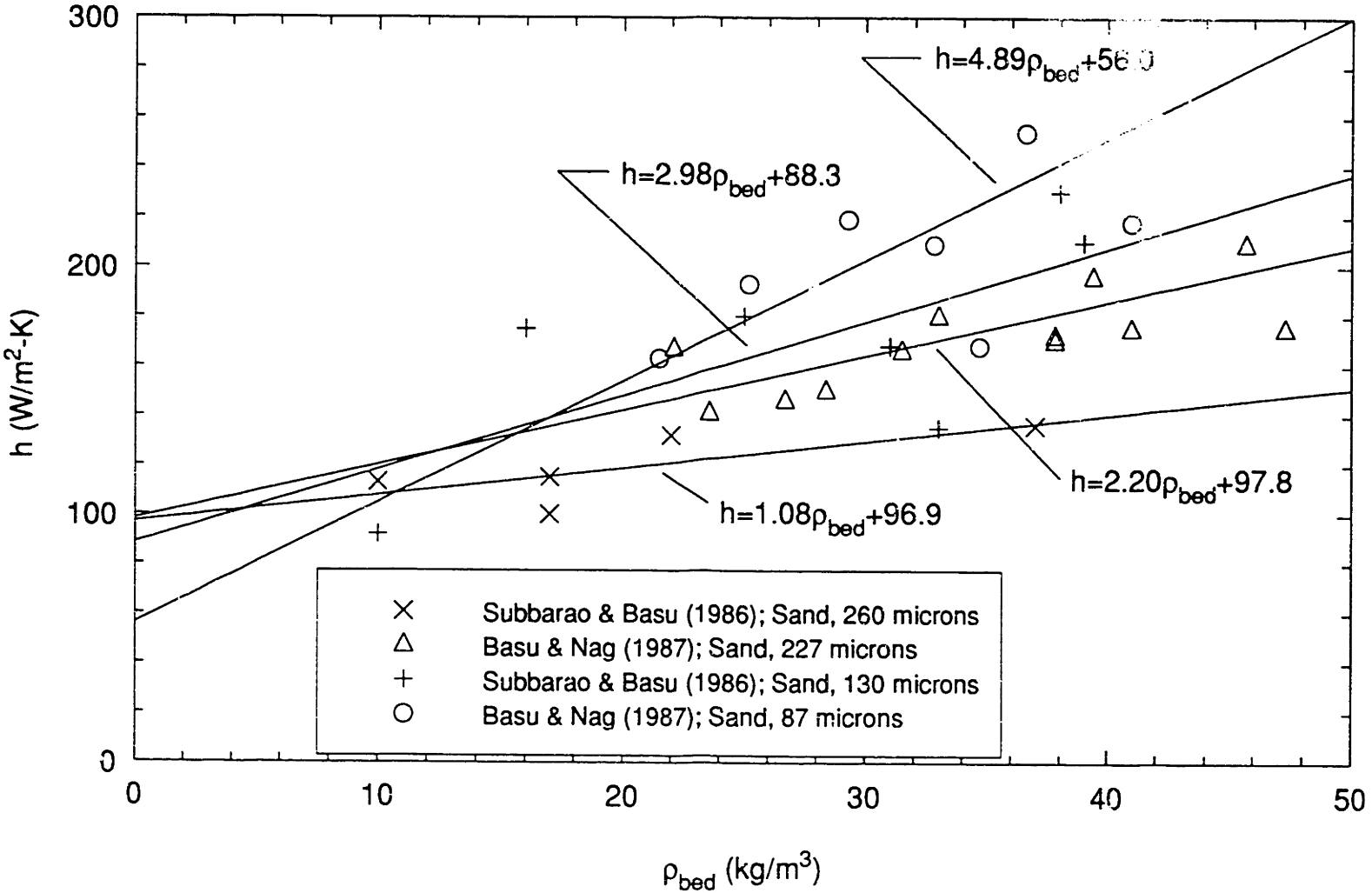

Figure C.3 - Heat transfer data of Subbarao & Basu (1986), and Basu & Nag (1987)

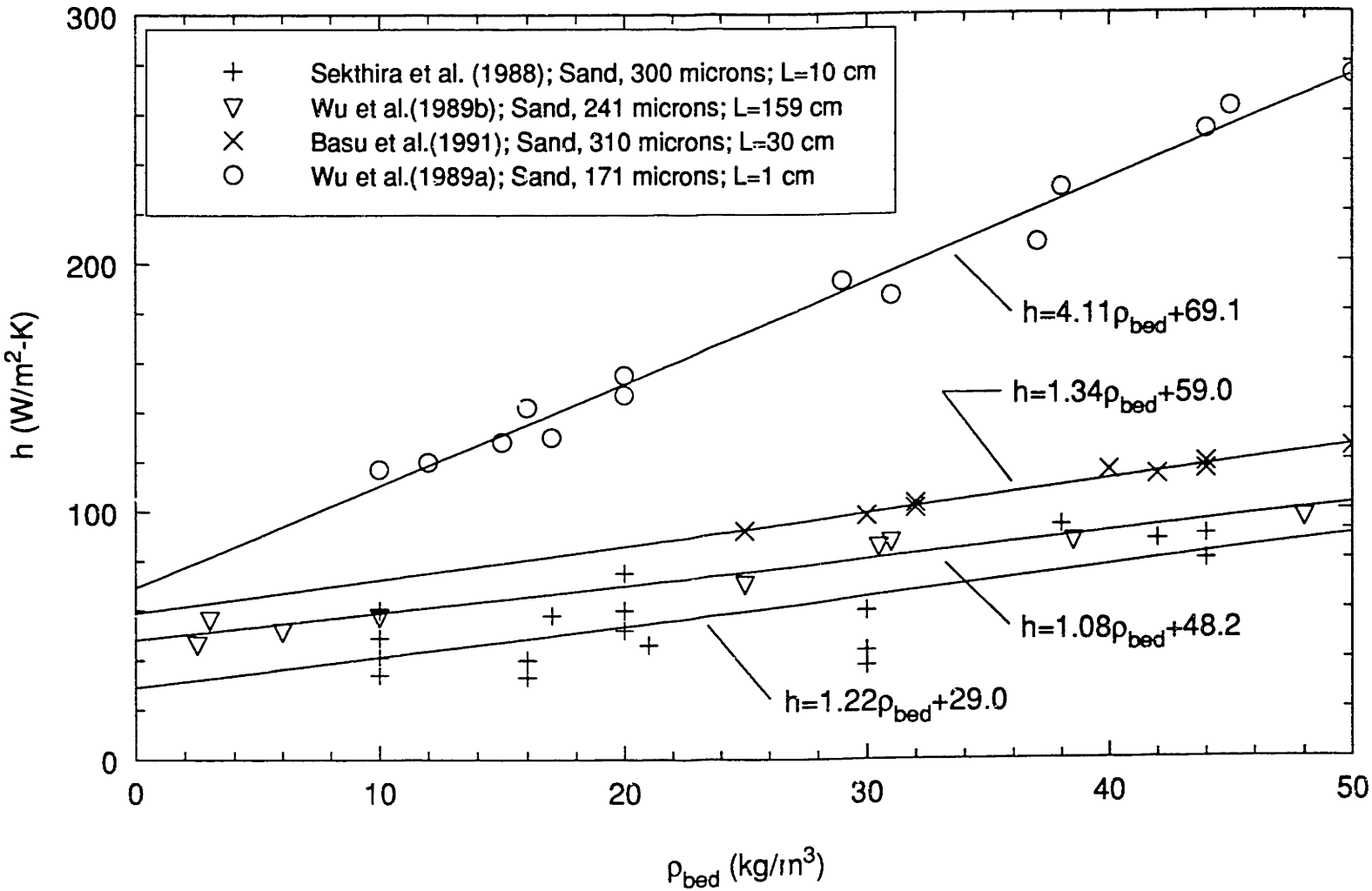

Figure C.4 - Heat transfer data as noted

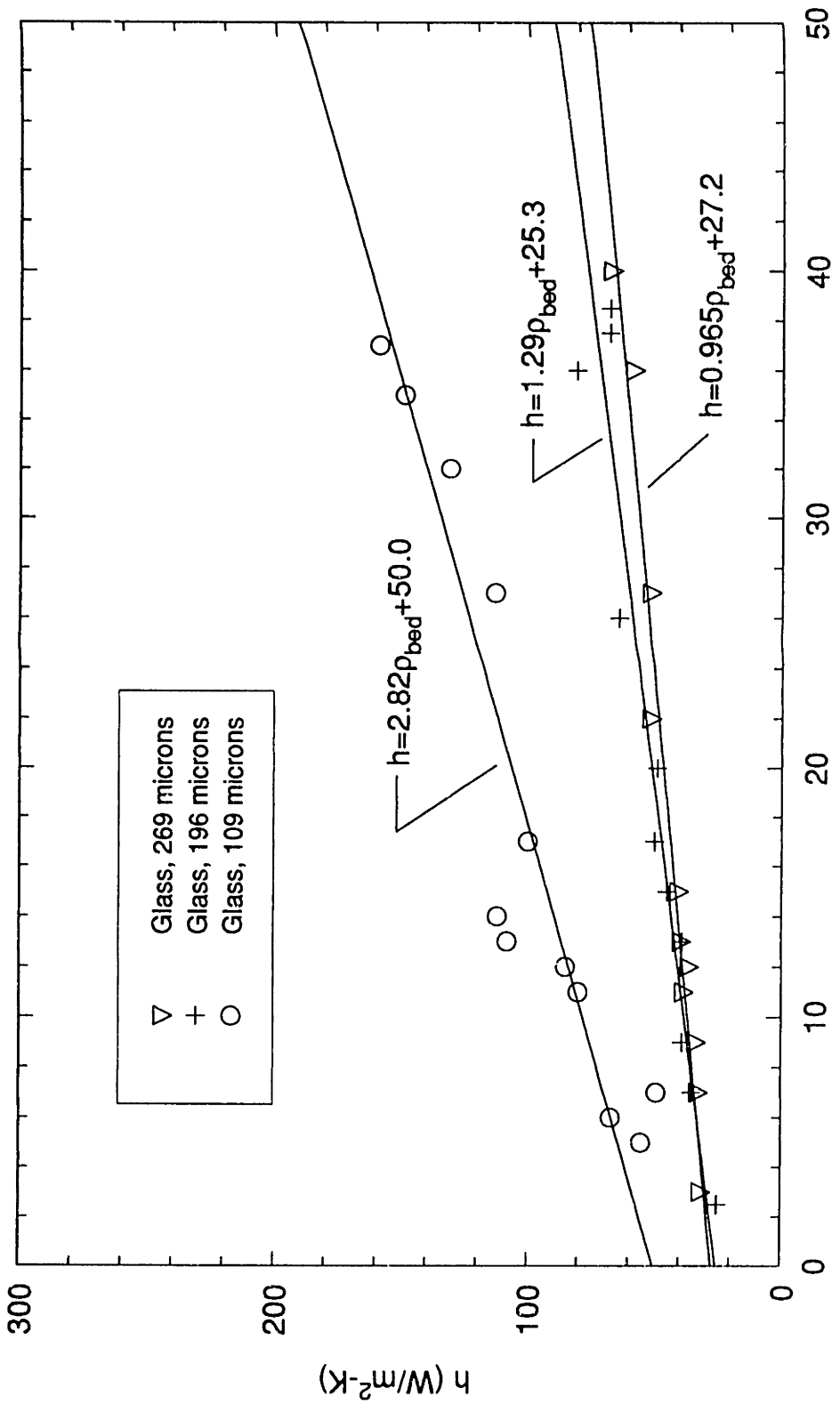

Figure C.5 - Heat transfer data of Furchi et al. (1988)

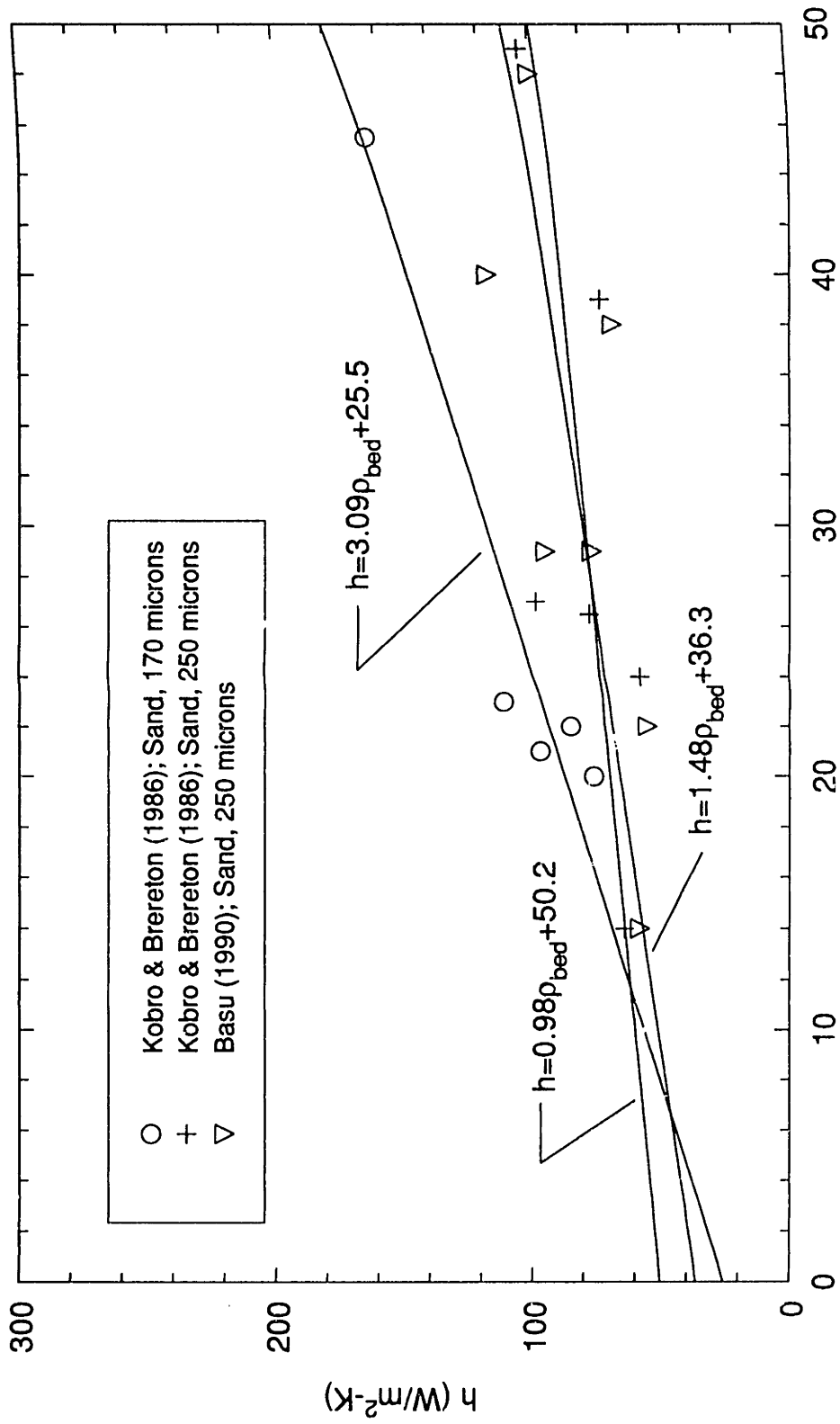

Figure C.6 - Heat transfer data of Kobro & Brereton (1986), and Basu (1990)

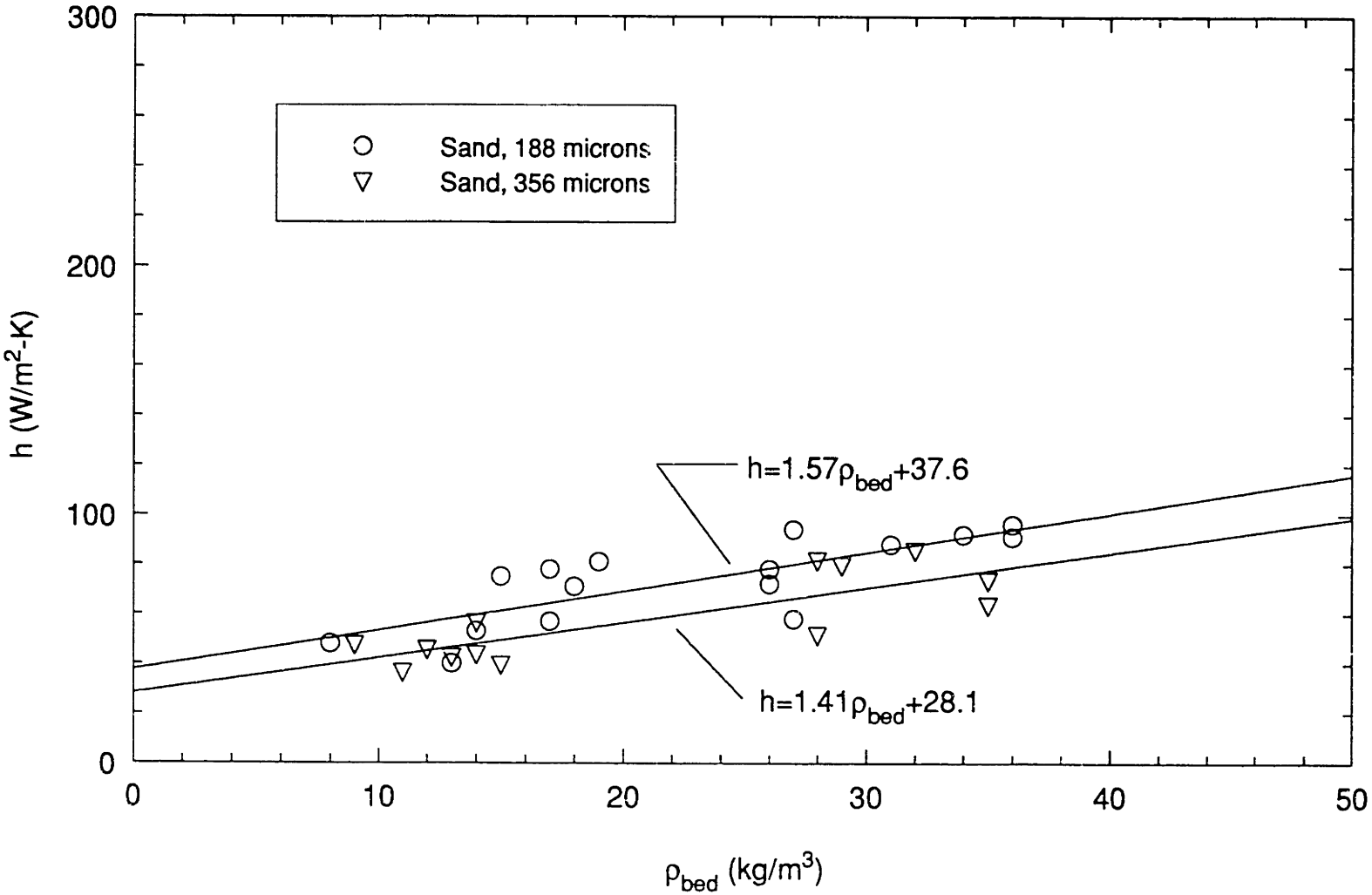

Figure C.7 - Heat transfer data of Wu et al. (1987)

Appendix D

Results of Statistical Analysis

of Wall Coverage by Particle Clusters

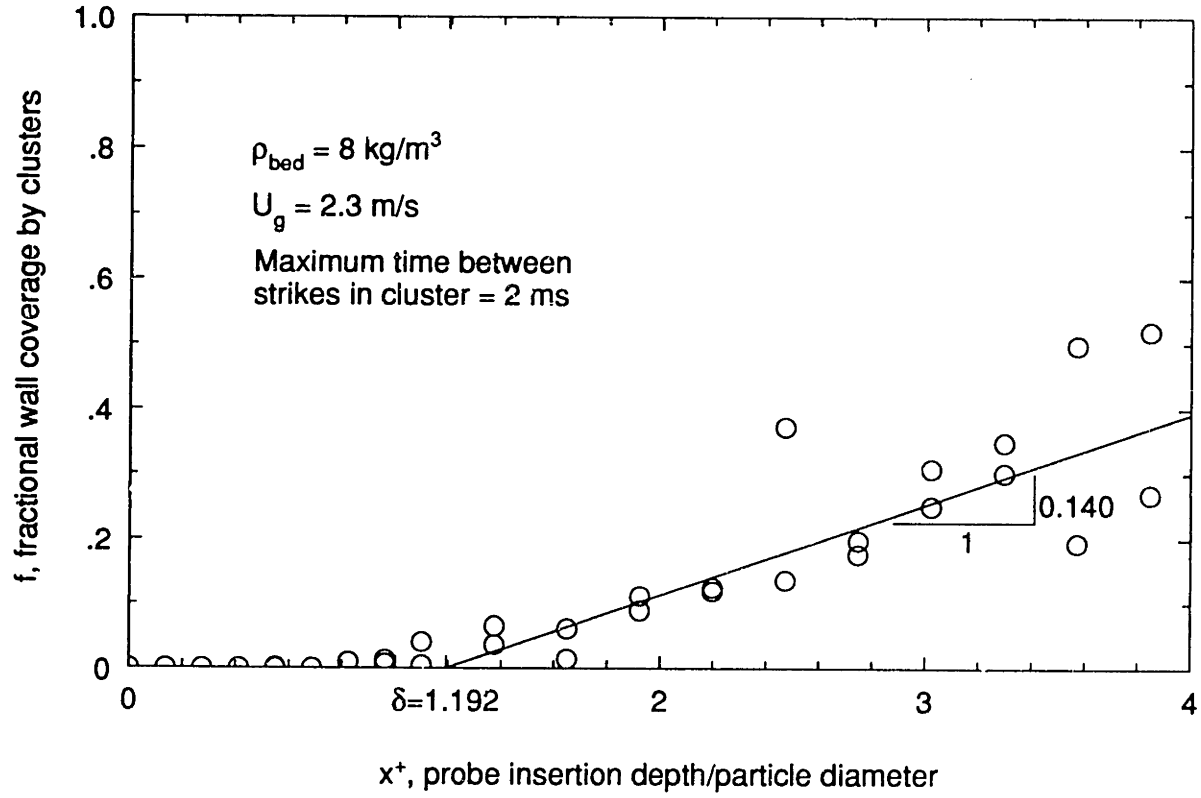

Figure D.1

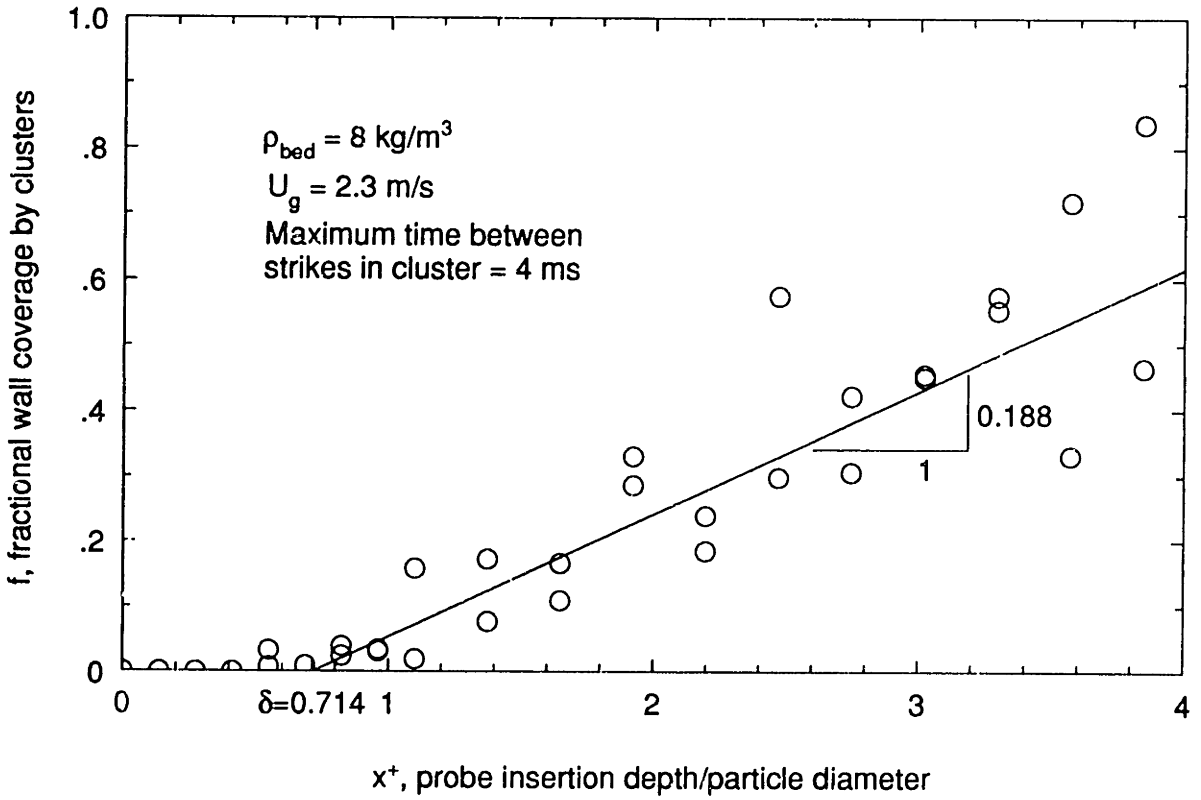

Figure D.2

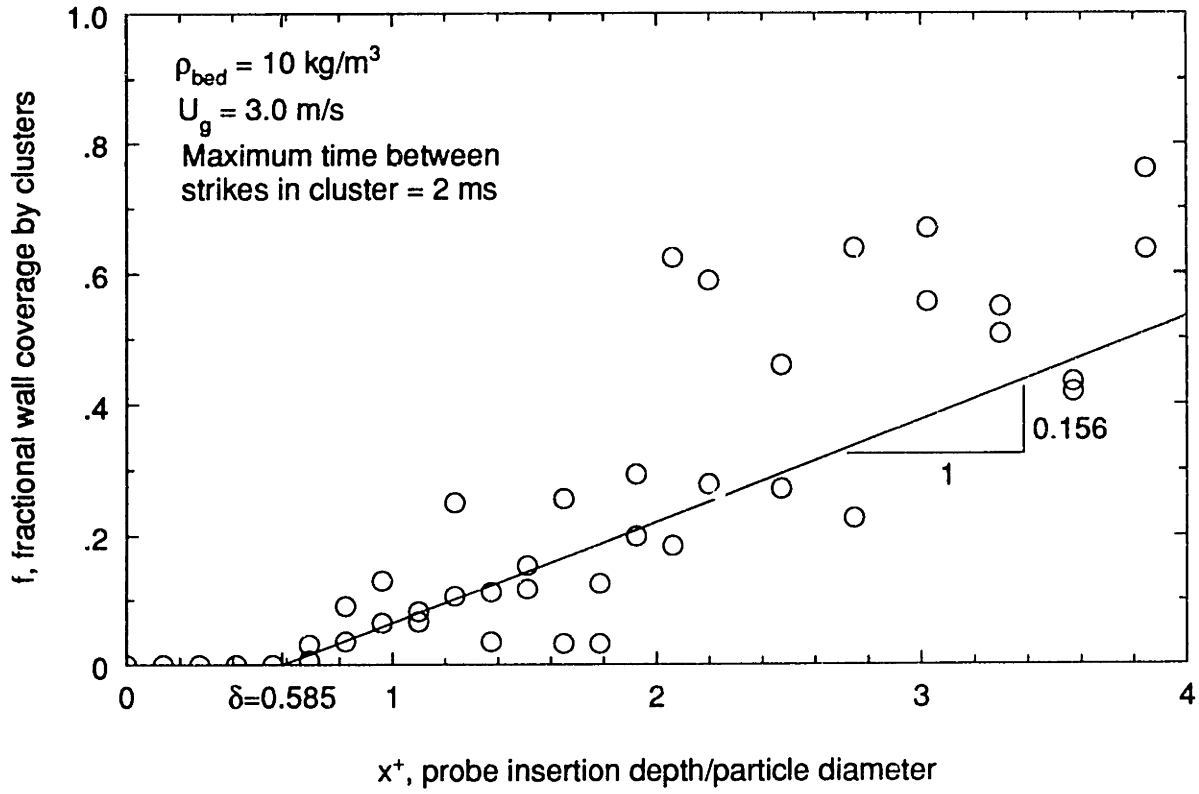

Figure D.3

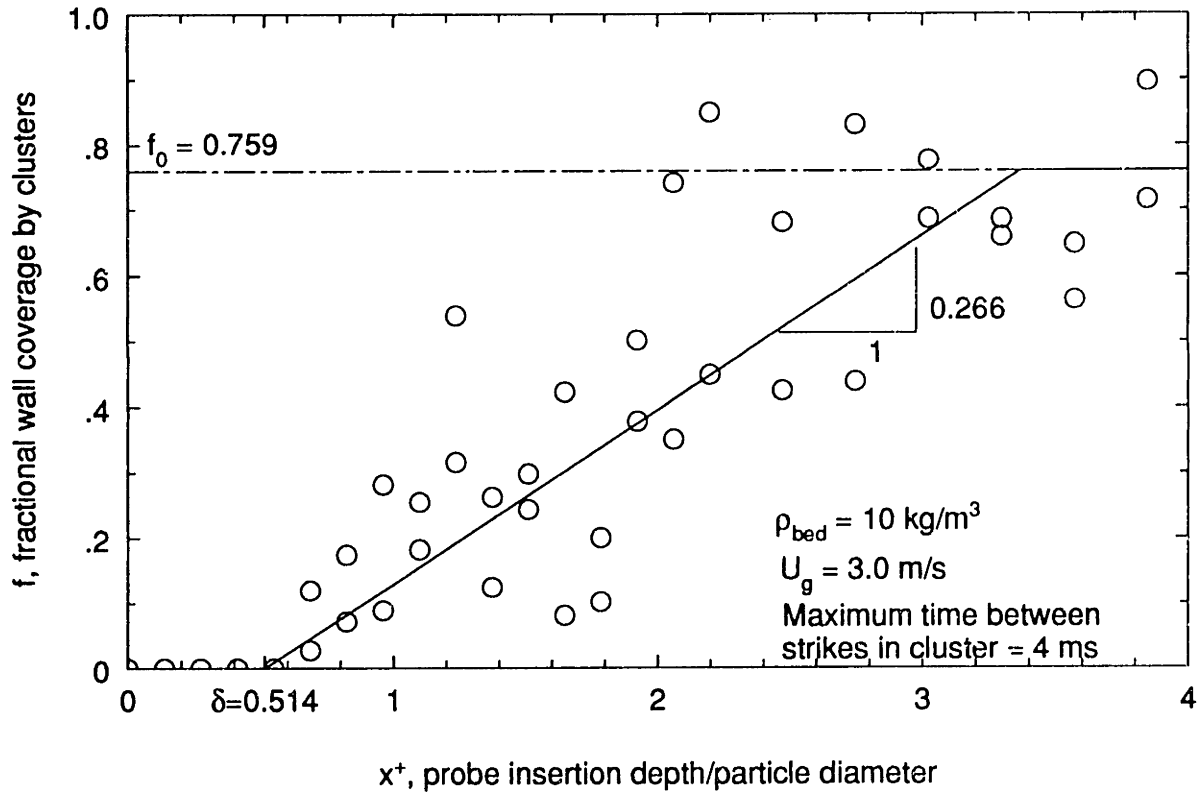

Figure D.4

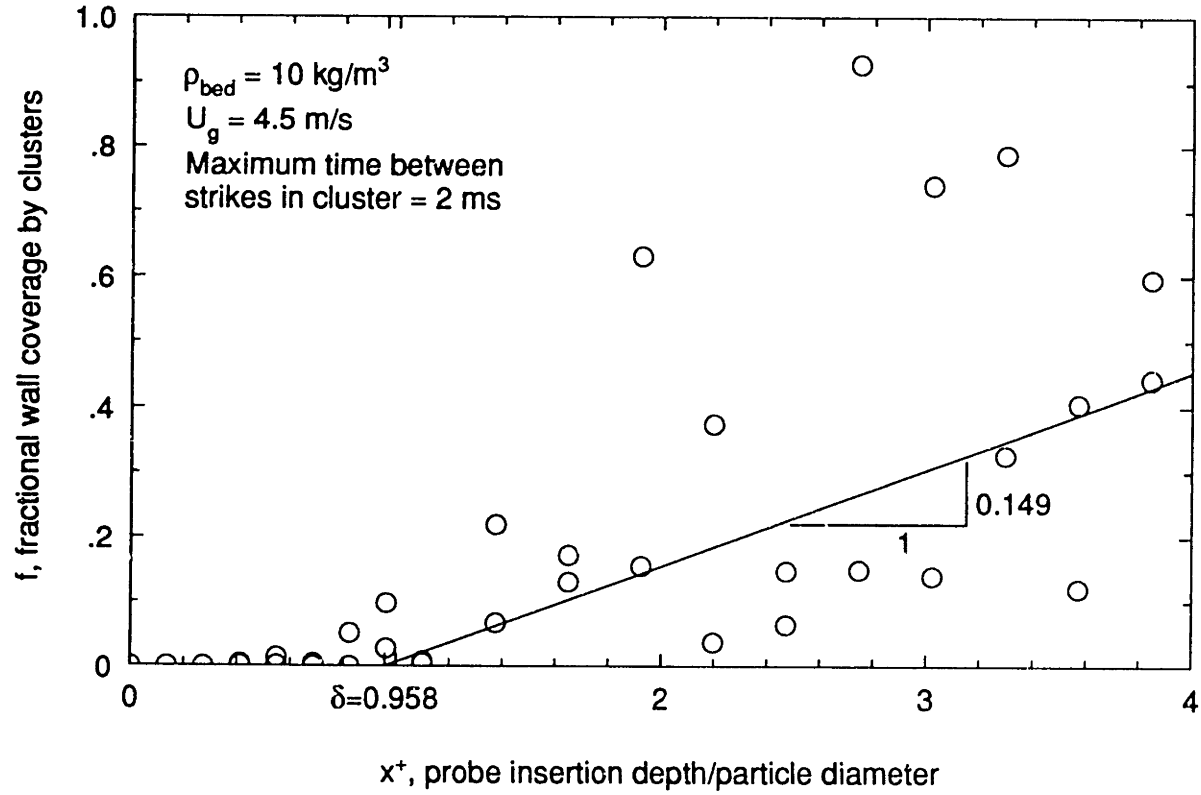

Figure D.5

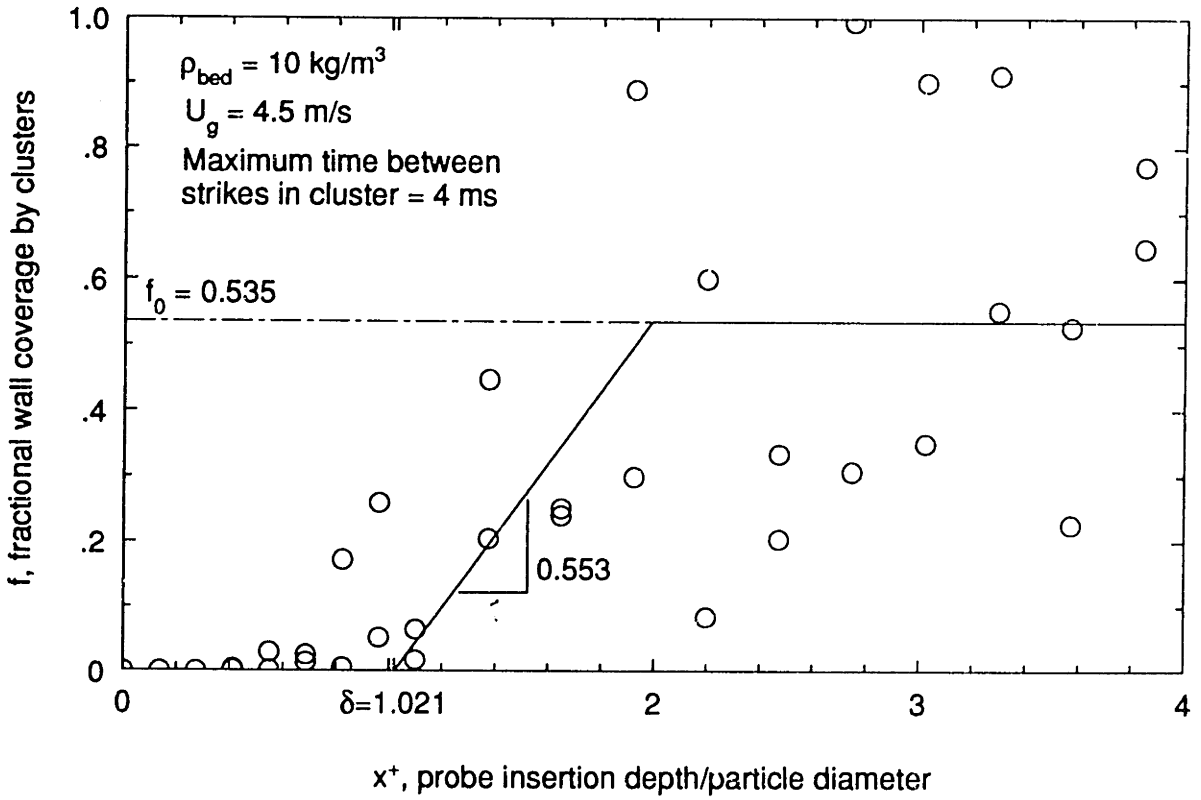

Figure D.6

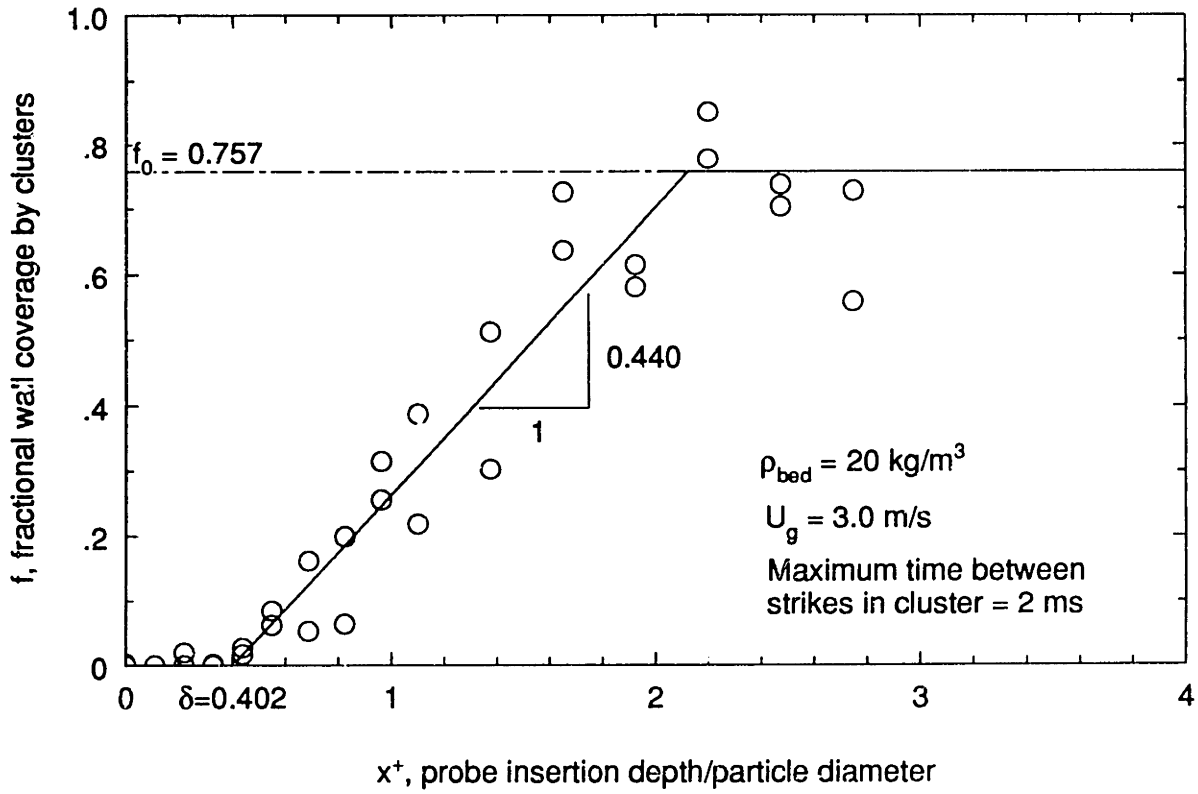

Figure D.7

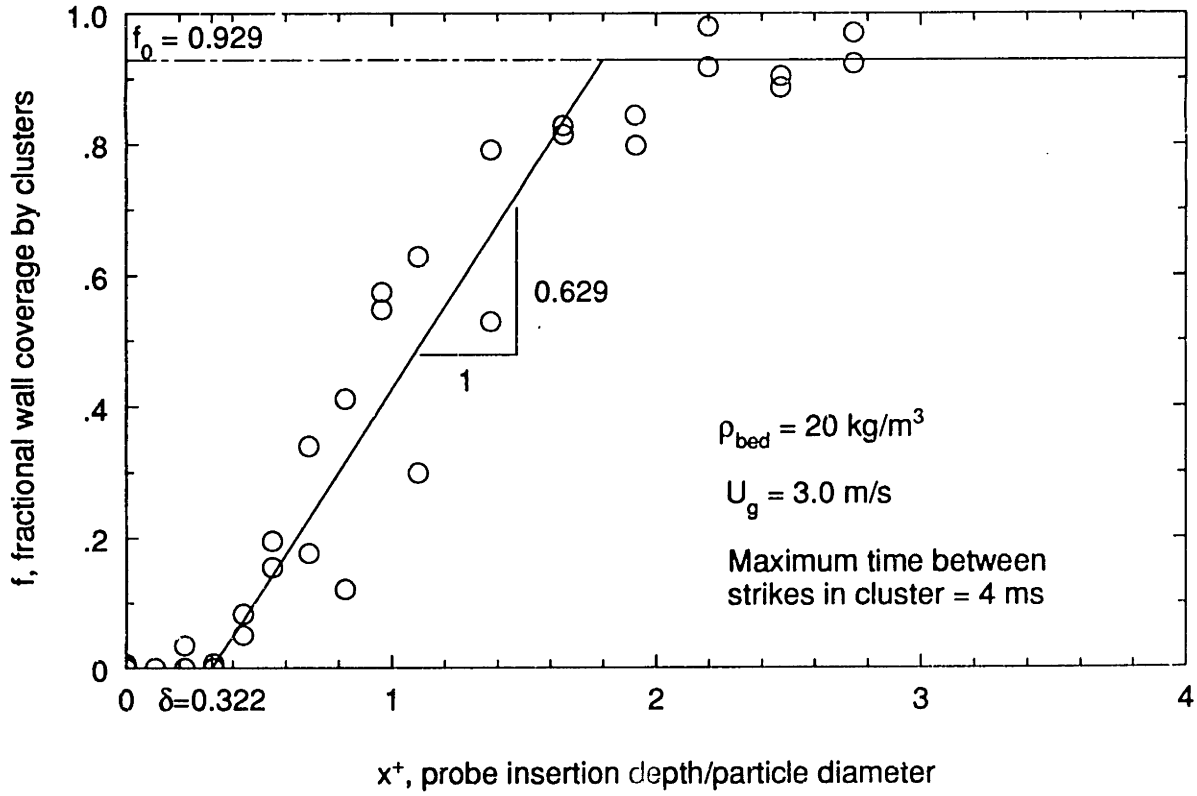

Figure D.8

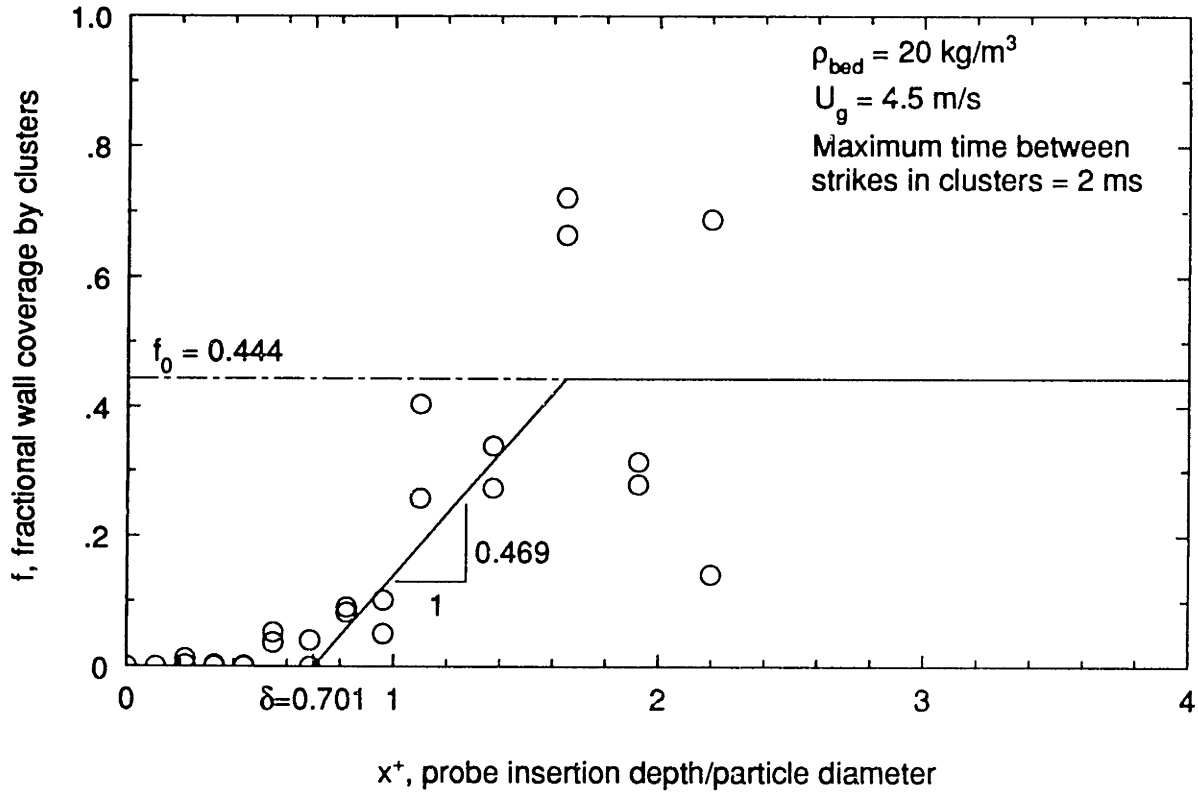

Figure D.9

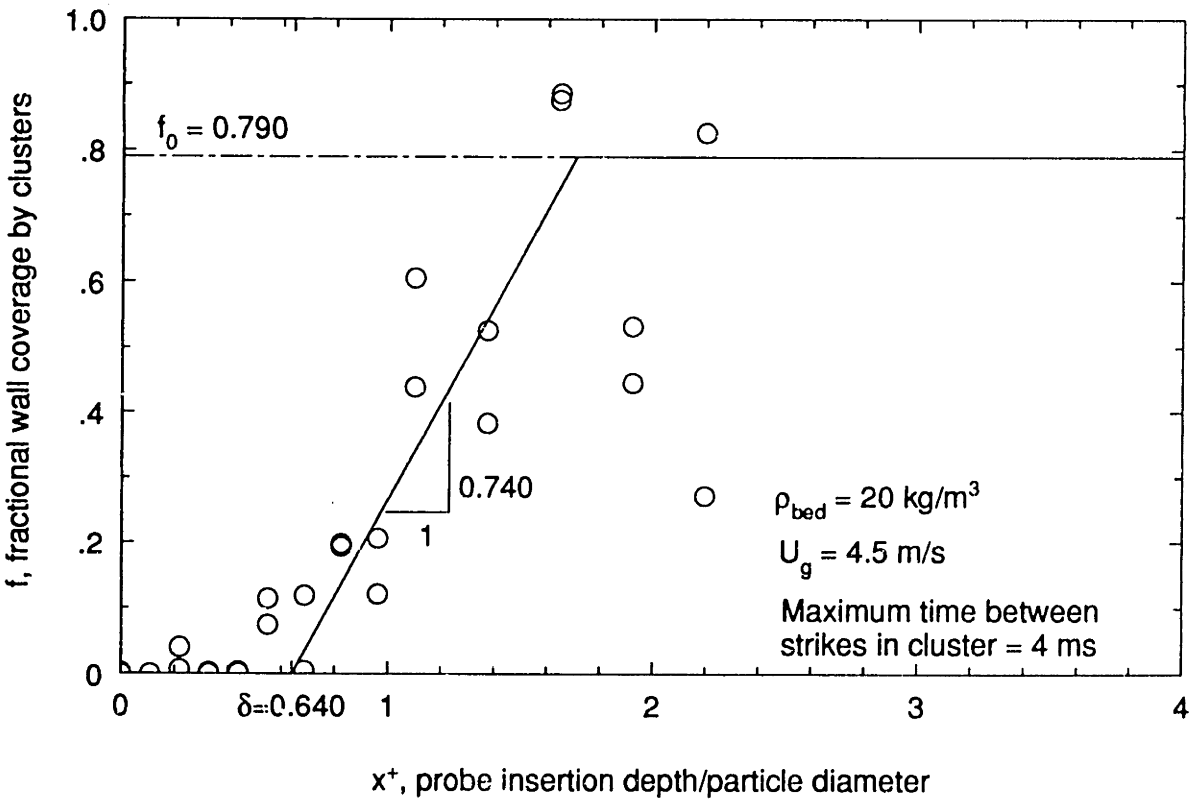

Figure D.10

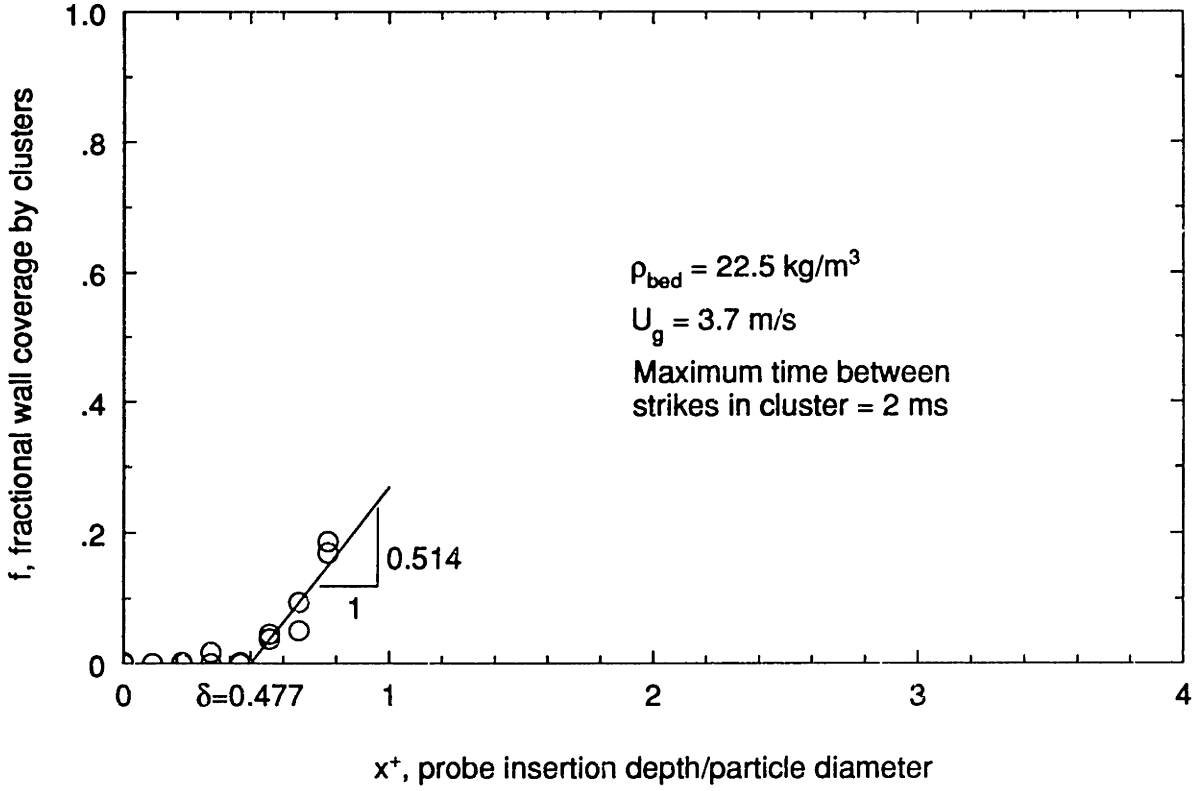

Figure D.11

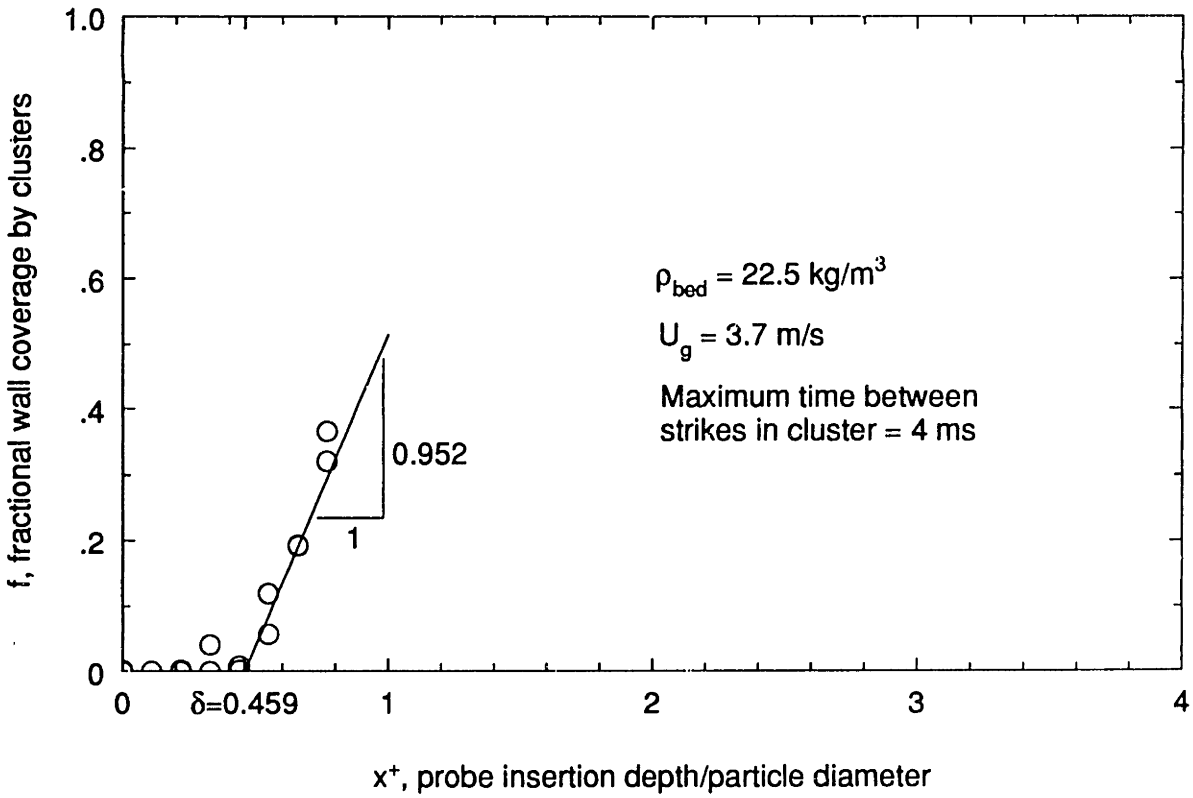

Figure D.12

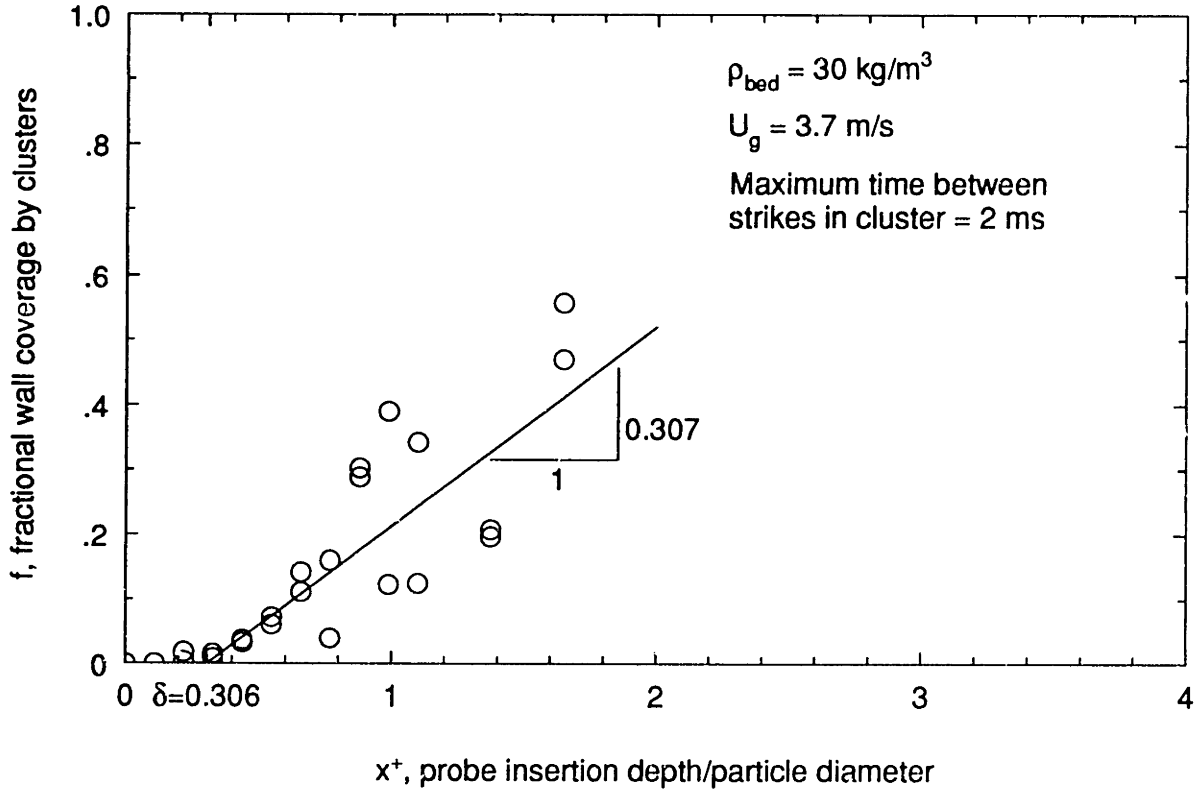

Figure D.13

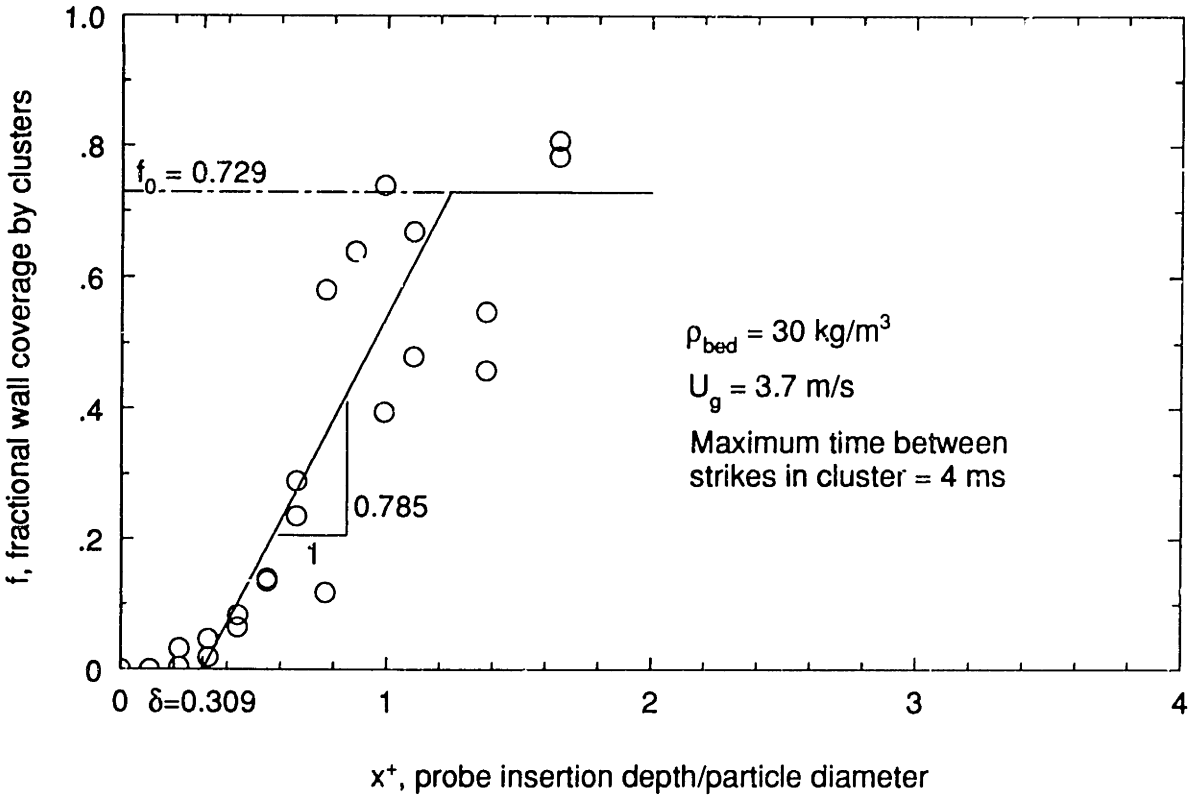

Figure D.14

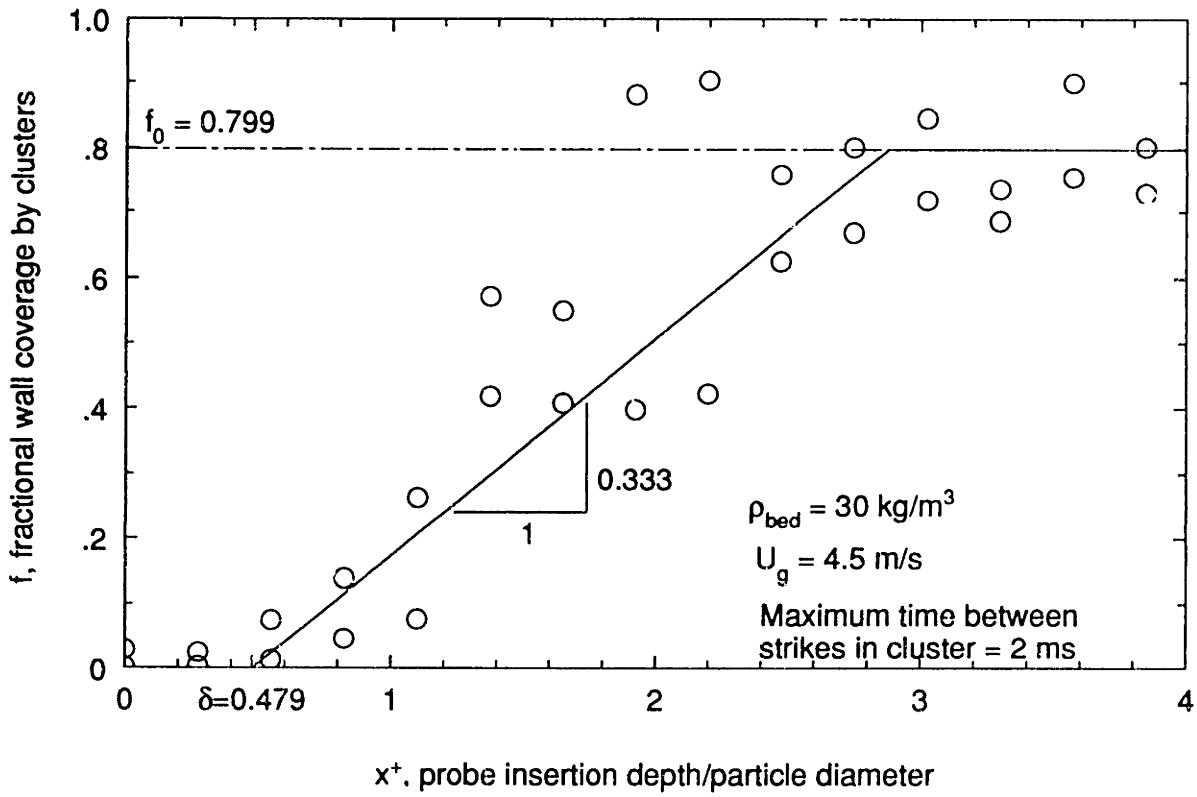

Figure D.15

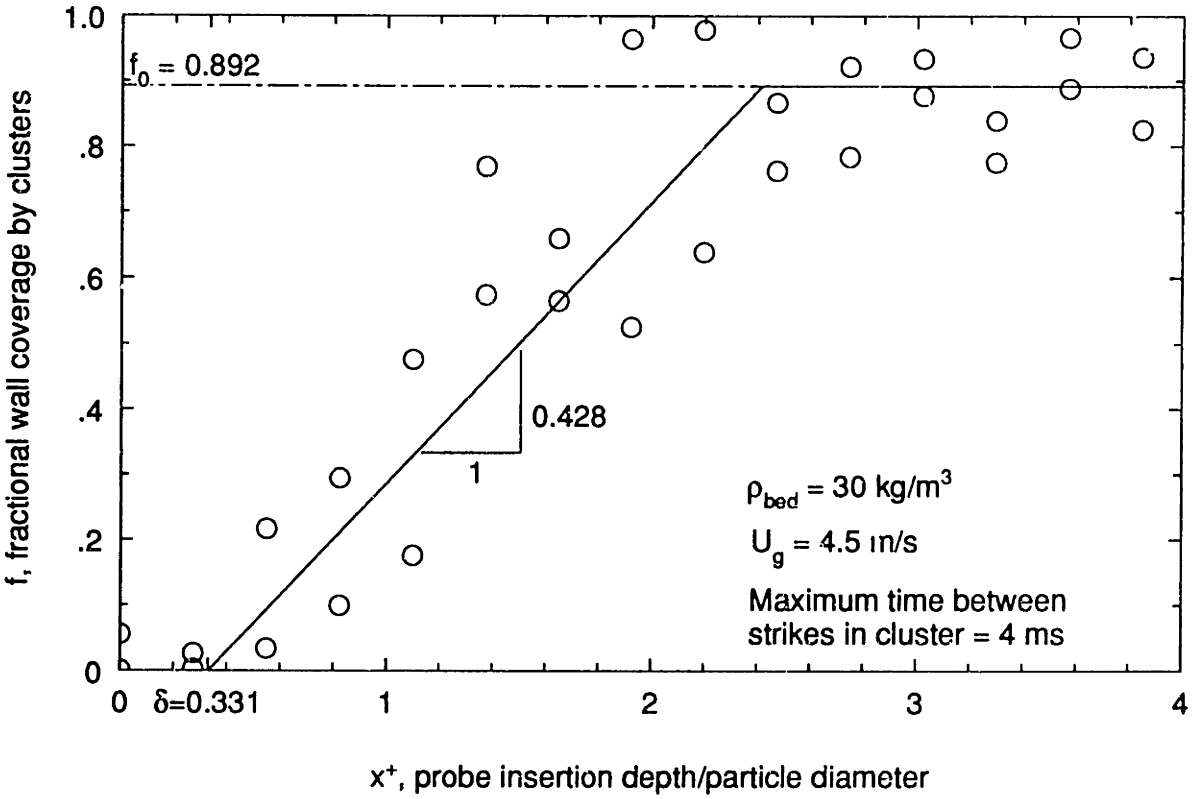

Figure D.16

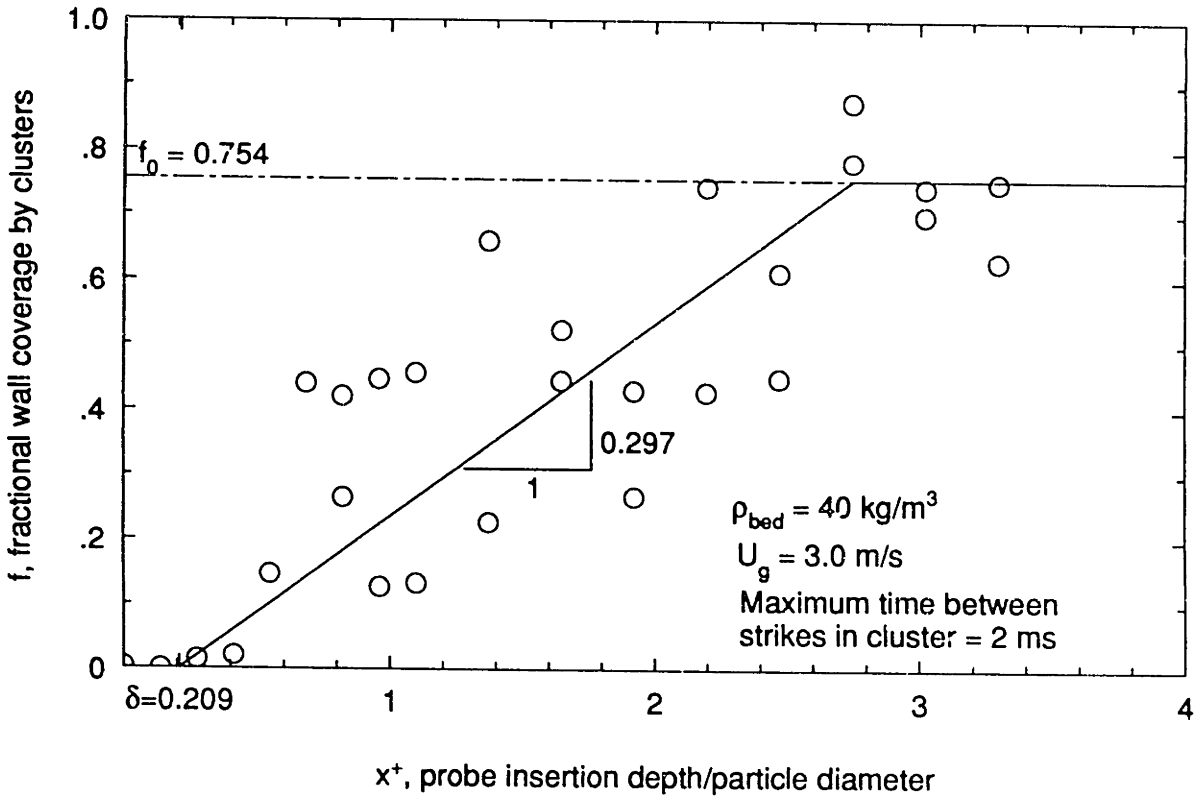

Figure D.17

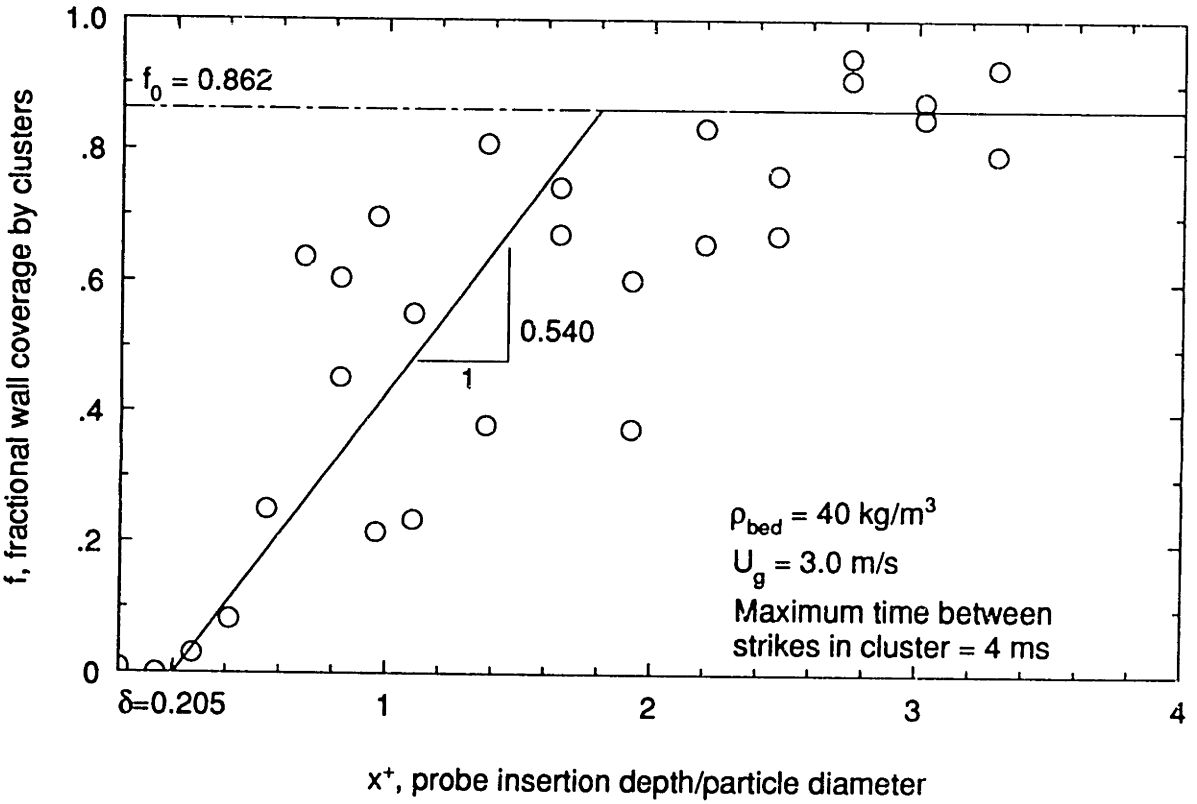

Figure D.18

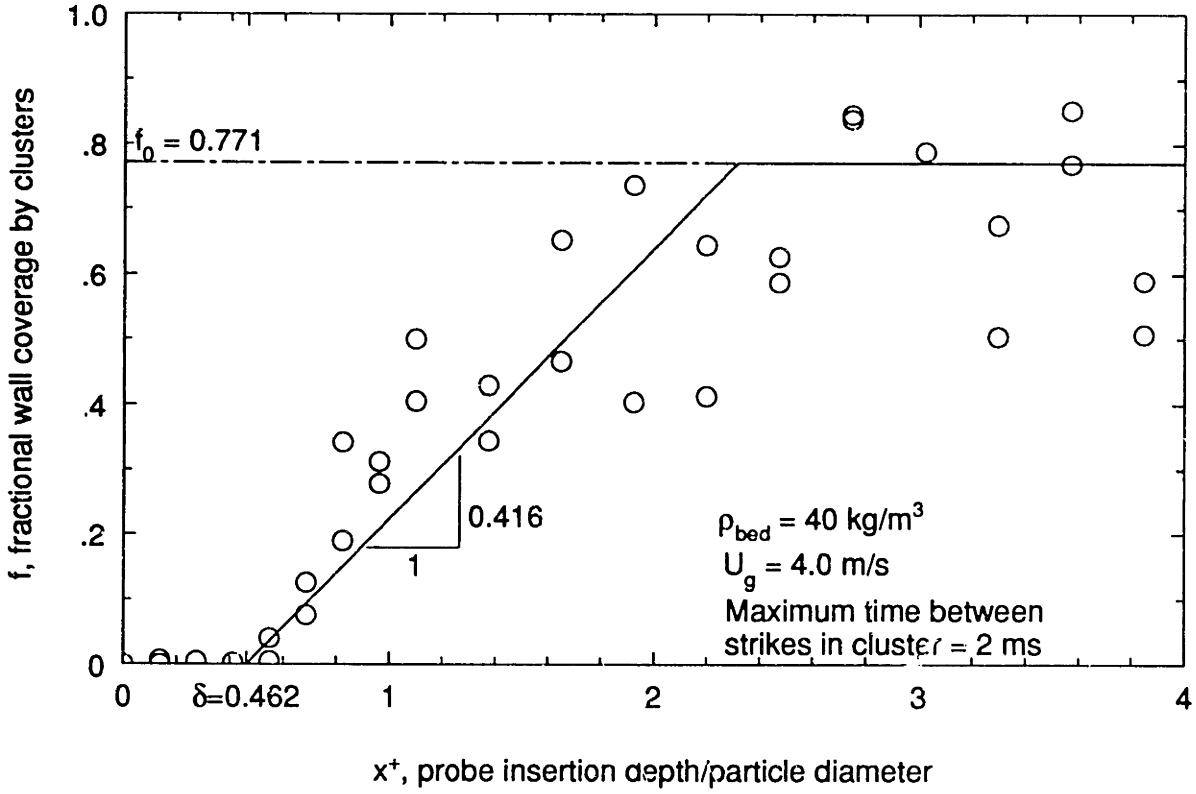

Figure D.19

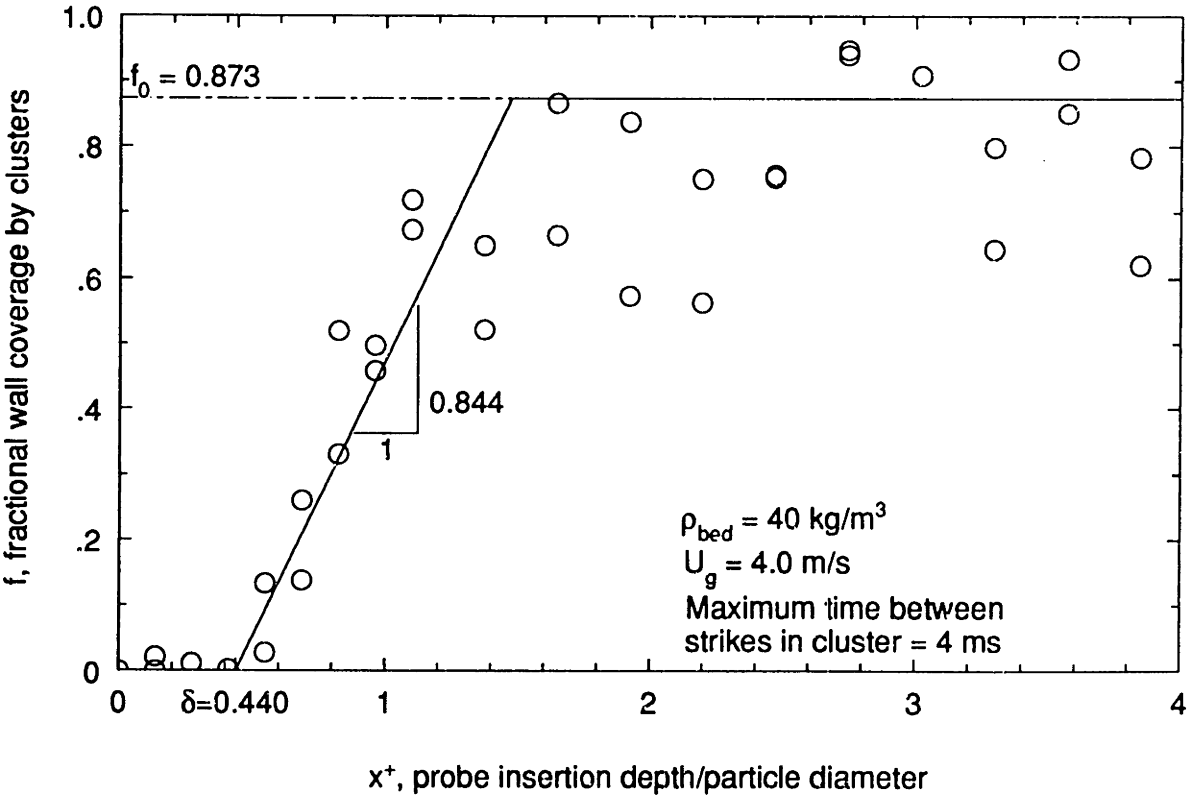

Figure D.20

Appendix E

Heat Transfer Coefficient for Homogeneous Clusters at Varying Distance from the Wall

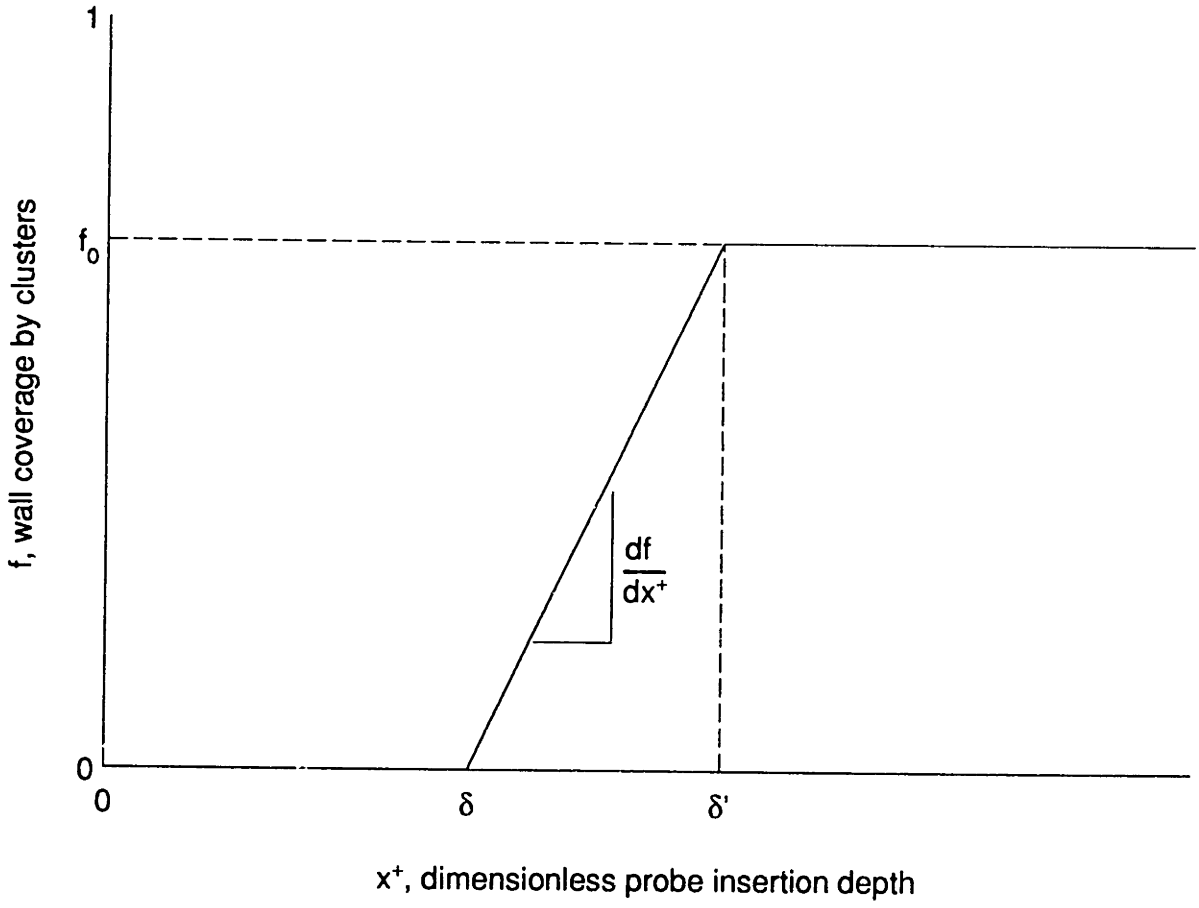

Figure 5.2 - Model of Cluster Wall Coverage

The average heat transfer coefficient is made up of the heat transfer from the areas of the wall which are covered by clusters and the areas which are covered by the dilute phase, where the heat transfer coefficient to the clusters is considered variable:

$$h = \frac{\int_0^{A_0} h_c \, dA_c + h_d (A_t - A_0)}{A_t} = \int_0^{f_0} h_c(f) \, df + h_d(1-f_0) \qquad \text{(E.1)}$$

where A_0 = area of wall covered by clusters,

A_t = total wall area,

A_c is a dummy variable of integration for the wall area covered by clusters, and the other variables are as previously defined. According to the model for cluster coverage in Fig. 5.2, reproduced above, $f = f(x^+)$, and the variable of integration can be changed:

$$h = \int_\delta^{\delta'} \frac{df}{dx^+} h_c(x^+) \, dx^+ + h_d(1-f_0) \qquad \text{(E.2)}$$

Substituting for $h_c(x^+)$ from Eq. 2.5 and integrating gives:

$$\begin{aligned} h &= \frac{df}{dx^+} \int_\delta^{\delta'} \left[\frac{x^+ d_p}{k_g} + \frac{1}{h_e} \right]^{-1} dx^+ + h_d(1-f_0) \\ &= \frac{df}{dx^+} \frac{k_g}{d_p} \left[\ln \left| \frac{x^+ d_p}{k_g} + \sqrt{\frac{\pi t}{4 k_c c_{p,s} \rho_s (1-\epsilon_c)}} \right| \right]_\delta^{\delta'} + h_d(1-f_0) \end{aligned} \qquad \text{(E.3)}$$

In this case, the factor of four has been included in h_e in order to give the average heat transfer coefficient, rather than the instantaneous value, for comparison with the measured average values.

The only remaining uncertainty is the value to use for df/dx^+ in Eq. E.3. The discrete values obtained by the statistical analysis of Chapter 5 are representative of the expected values, but show a large degree of stochastic fluctuation and will therefore give misleading results if substituted directly into Eq. E.3. One method of obtaining df/dx^+ as a continuous function of c is to fit the values of δ' from the statistical analysis as a

function of c; df/dx^+ is then given as a function of c by $f_0(c)/[\delta'(c)-\delta(c)]$. Figure E.1 shows the values of δ' from the results of the statistical analysis presented in Appendix D using a maximum time between strikes in the cluster of 4 ms plotted against c, and the least-squares power curve fit to the data:

$$\delta' = 0.4074\, c^{-0.329} \qquad \textbf{(E.4)}$$

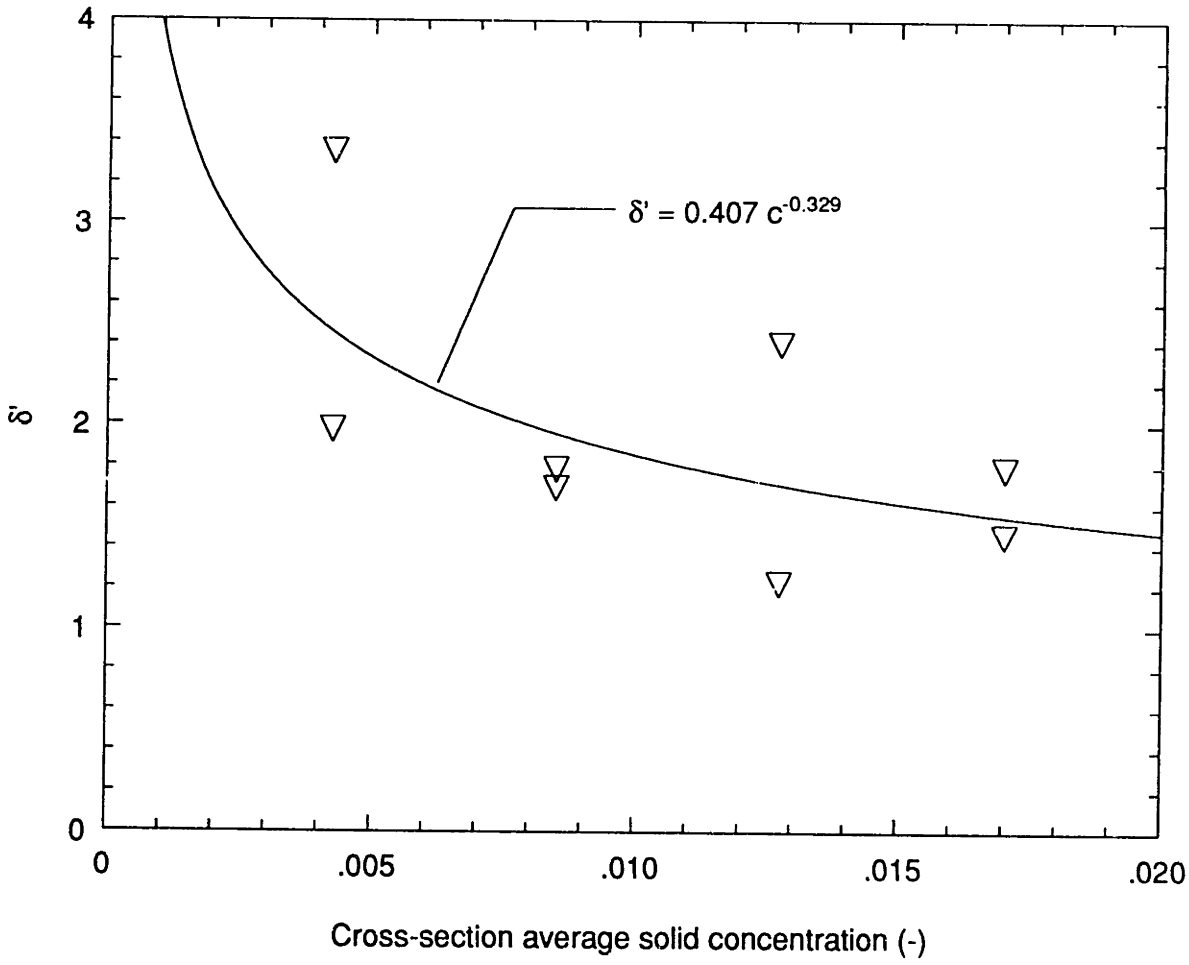

Figure E.1 - Experimental values for δ' and least-squares curve fit

The resulting functional relationship for the slope of the increase in fractional wall coverage with distance from the wall is:

$$\frac{df}{dx^+} = \frac{7\,c^{1/2}}{0.4074\,c^{-0.329} - 0.0287\,c^{-0.581}} \qquad \text{(E.5)}$$

Figure E.2 plots this relationship, and the discrete values of df/dx^+ taken from the results of the statistical analysis using a maximum time between strikes in the cluster of 4 ms. The function follows the general trend of the data, but tends to be somewhat lower than most of the experimental values. This tendency is consistent with the intended purpose of this analysis, i.e. to provide a lower bound estimate of the heat transfer coefficient (see Section 5.3).

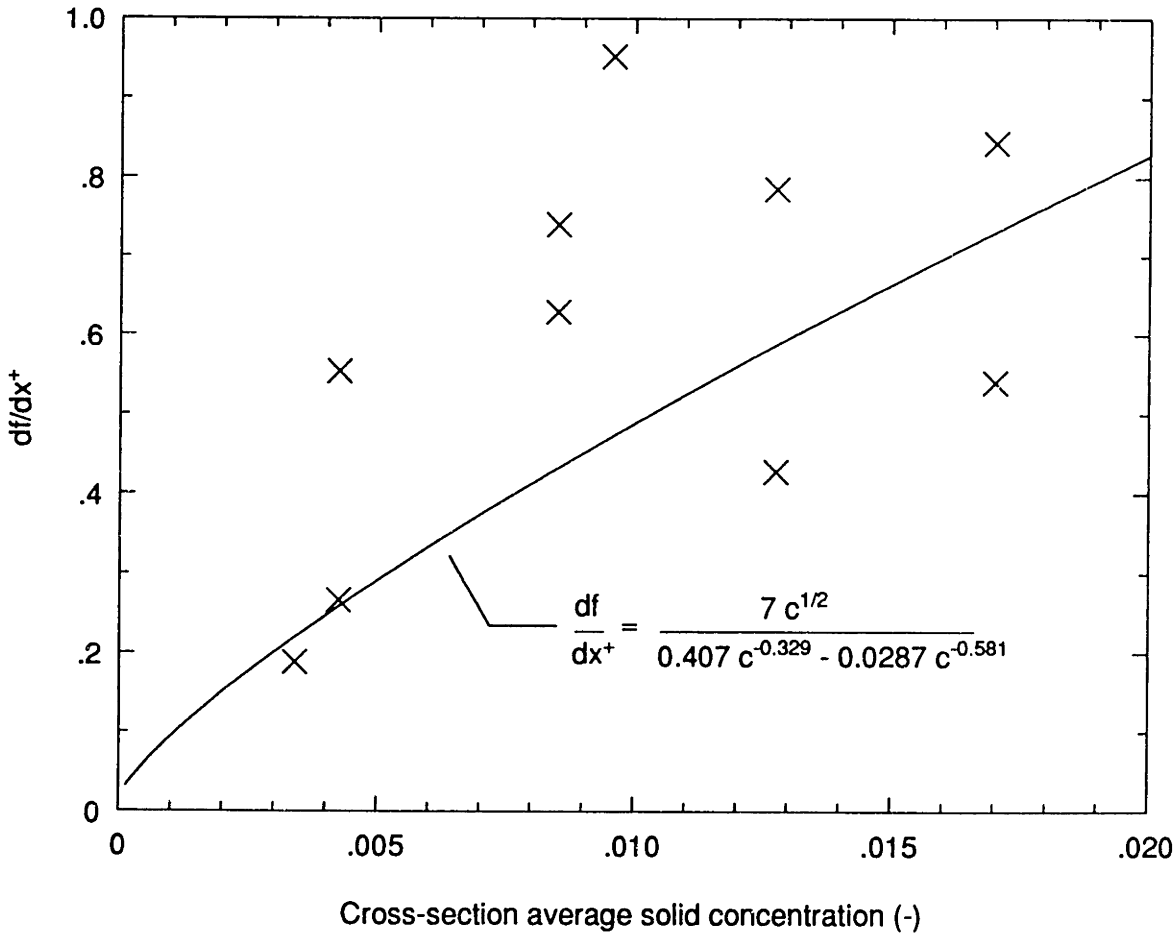

Figure E.2 - Functional relationship of df/dx^+ and experimental data